AC Electrokinetics and Electrohydrodynamics for the On-chip Particle Manipulation and Fluid Handling

Paresa Modarres

Doctor of Philosophy

Department of Biomedical Engineering

McGill University

Montreal, Canada

A thesis submitted to McGill University in partial fulfillment of the requirements of the degree of Doctor of Philosophy

ABSTRACT

The ever-increasing developments and advancements in the field of microfabrication technology for the past two decades have encouraged many applications geared towards miniaturized bioanalytical systems capable of performing independent or concurrent on-chip operations including, pumping, mixing, sample enrichment, thermal cycling and sensing. Reduced reagent consumption, enhanced spatiotemporal control over reaction conditions, the increased surface to volume ratios and ease of process parallelization are some key advantages of miniaturized bioanalytical systems over their counterpart conventional macroscale methods. Enabling physical mechanisms for many on-chip operations often include various gravitational, acoustics, magnetic and electric phenomena. Electrically-induced actuation mechanisms are becoming the method of choice for many specialized applications whereby low power, small footprint and absence of moving parts are desired. Applications of electrically induced actuation mechanisms encompassing classical electrokinetics and electrohydrodynamic forces are the subject of this thesis. Multiple novel biochips were designed, fabricated and characterized for performing cell enrichment, micromixing and nanoparticle synthesis. First, the principle of alternating current (AC) dielectrophoresis (DEP) was utilized for the tunable sorting of synthetic particles and cells. Next, the concepts of AC electroosmosis (ACEO) and electrohydrodynamic were investigated for the micromixing of monophasic and biphasic liquid systems. For the first time, the ACEO-induced fluid actuation mechanism was utilized for devising a phase-controlled field-effect micromixer. The phase-tunability of the micromixer was investigated experimentally and semi-analytically. Finally, electrohydrodynamic-based fluid instabilities were employed for the mixing of solvent and aqueous liquid phases in the context of nanoparticle synthesis. It was demonstrated that electrohydrodynamic-mediated micromixing can be leveraged for the synthesis of high-throughput

and highly monodispersed liposomal batches intended for drug delivery applications. The devised platform and methodology can be applied across many nanoparticle chemistries relying on the principle of nanoprecipitation. Overall, the novel ideas and methodologies introduced in this thesis validated the utility of electrical-based methods for on-chip operations and demonstrated new applications with many potentials for nanoparticle synthesis and drug encapsulation.

ABRÉGÉ

Les développements et les progrès sans cesse croissants dans le domaine de la technologie de micro-fabrication au cours des deux dernières décennies ont encouragé de nombreuses applications axées sur les systèmes bio analytiques miniaturisés capables d'effectuer des opérations sur puce indépendantes ou simultanées, y compris le pompage, le mélange, l'enrichissement et la concentration d'échantillon, le cycle thermique et la détection. La consommation réduite de réactifs, contrôle spatiotemporel amélioré des conditions de réaction, l'augmentation des rapports surface/volume et la facilité de parallélisations du processus sont quelques principaux avantages des systèmes bio analytiques miniaturisés par rapport à leurs méthodes macroscopiques conventionnelles. L'activation de mécanismes physiques pour de nombreuses opérations sur puce comprend souvent divers phénomènes gravitationnels, acoustiques, magnétiques et électriques. Les mécanismes d'actionnement induits électriquement sont les méthodes de choix pour de nombreuses applications spécialisées dans lesquelles une faible puissance, un faible encombrement et l'absence de pièces mobiles sont souhaités. Les applications des mécanismes d'actionnement induits électriquement englobant l'électrocinétique classique et les forces électro hydrodynamiques font le sujet de cette thèse. Plusieurs nouvelles bio puces ont été conçues, fabriquées et caractérisées pour effectuer l'enrichissement cellulaire, micro mélange et la synthèse de nanoparticules. Tout d'abord, le principe de diélectrophorèse CA (DEP) a été utilisé pour le tri accordable des particules synthétiques et cellules. Ensuite, les concepts d'électroosmose AC (ACEO) et d'électro hydrodynamique ont été étudiés pour le micro mélange de systèmes liquides monophasiques et bi phasiques. Pour la première fois, le mécanisme d'actionnement des fluides induit par l'ACEO a été utilisé pour concevoir un micro-mélangeur à effet de champ à phase contrôlée. L'accordabilité de phase du micro-mélangeur à été étudié expérimentalement et semi-

analytiquement. Enfin, des instabilités fluides électro hydrodynamiques ont été utilisées pour le mélange de phases liquides et aqueuses dans le cadre de la synthèse de nanoparticules. Il a été démontré que le micro mélange à médiation électro hydrodynamique peut être utilisé pour la synthèse des lots liposomiques de haut débit et hautement mono dispersés destinés à des applications d'administration de médicaments. La plate-forme et la méthodologie mises au point peuvent être appliquées à de nombreuses chimies de nanoparticules en s'appuyant sur le principe de la nano précipitation. Dans l'ensemble, les nouvelles idées et méthodologies introduites dans cette thèse ont validé l'utilité des méthodes électriques pour les opérations sur puce et ont démontré de nouvelles applications avec de nombreux potentiels pour la synthèse de nanoparticules et l'encapsulation de médicaments.

ACKNOWLEDGEMENTS

I would like to express my utmost gratitude to my advisor, Professor Maryam Tabrizian, for her guidance and support throughout the course of my PhD study. I will always be grateful for her encouragements, vision and trust that helped me to grow as a curious researcher and critical thinker. I am very thankful to my PhD advisory committee, Dr Satya Prakash and Dr Xinyu Liu, for their valuable insights and guidance at different stages of my PhD program.

I am very grateful to all the current and former staff of the McGill Nanotools Microfab for their diligent response to inquiries as well as their help and guidance during the fabrication of microchips. I would also like to thank Pina Sorrini, Nancy Abate and Daniel Caron in the Biomedical Engineering department for always being available and resourceful. Finally, I would like to express my appreciation to Vanessa Kairouz at Université de Montréal for her help with the NSERC-CREATE Continuous Flow Science (CFS) program.

I was fortunate to have the company of Biomat'X lab members and I am very thankful for their friendship and support throughout the years. Especially, I like to thank Mina, Saber, Amir, Sameera, Khalil, Laila, Feriel, Rosey, Saadia, Sultan, Meltem, Brandon, Michael, Celine, Antoine, Kaushar, Nick, Reza, Rafael, and Timothy Johns for all the memorable moments we had together. I would also like to extend my gratitude to Rafael and Khalil for their helpful technical discussions on various subjects and Celine for her help with the French translation of thesis abstract.

I would like to express my dearest appreciation to my family. I am very grateful to my husband, Dr Aboli, for his unconditional support and encouragement. I also like to thank him for his technical advice and discussions on various topics pertinent to my thesis. Last but not the least, I would like to thank my mother for her endless love and support.

Finally, I would like to acknowledge various grants and funding sources that made this work possible including, Natural Sciences and Engineering Research Council of Canada (NSERC), NSERC-CREATE Integrated Sensor Systems program, NSERC-CREATE Continuous Flow Science program and McGill's biomedical engineering department.

CONTRIBUTIONS OF AUTHORS

In accordance with the “Guidelines for Thesis Preparation”, this thesis is presented as a collection of manuscripts written by the candidate. The candidate envisioned, designed, and performed experiments. All data collection and analysis were conducted by the candidate. Dr Maryam Tabrizian appears on all publications for partaking in the manuscripts and her guidance and supervisory role throughout the execution of this work.

TABLE OF CONTENTS

LIST OF FIGURES

LIST OF TABLES

LIST OF ABBREVIATIONS

2D	Two dimensional
3D	Three dimensional
AC	Alternating current
ACEO	AC electroosmosis
ACET	AC electrothermal
BAW	Bulk acoustic wave
CMOS	Complementary metal oxide semiconductor
CTC	Circulating tumor cell
DC	Direct current
DEP	Dielectrophoresis
DLD	Deterministic lateral displacement
EDL	Electrical double layer
FACS	Fluorescence-activated cell sorter
FET	Field-effect transistor
FFF	Field flow fractionation
HFF	Hydrodynamic flow focusing
iDEP	Insulating dielectrophoresis
LAMP	Loop-mediated isothermal amplification buffer
LSPR	Localized surface plasmon resonance
MACS	Magnetic-activated cell sorter
MI	Mixing index
nDEP	Negative dielectrophoresis
PCR	Polymerase chain reaction
pDEP	Positive dielectrophoresis
RBC	Red blood cell
RT-PCR	Reverse transcription polymerase chain reaction
SAW	Surface acoustic wave
SEM	Scanning electron microscopy

SPR	Surface plasmon resonance
TEM	Transmission electron microscopy

Chapter 1. Introduction

1.1 Objectives

The subject of electrically-induced particle and fluid motion has been studied for well over a century in colloidal sciences. However, much recent interest in this classical subject has been promoted by the development of microfabrication technology and microfluidics. Scaling down to microscale is favorable to many electrically-driven phenomena which require the application of only small voltages to enable particle and fluid actuation. Electrokinetic techniques including AC dielectrophoresis and AC electroosmosis have extensively been implemented in microfluidic chips for many bioanalytical applications. However, in most cases, the strategies to improve performance are limited to geometrical optimizations and methods involving various electric field signaling schemes are rather sparse. Furthermore, many microdevices that utilize electric fields for fluid actuation have not shown wider applicability to real-world bioanalytical applications.[1-10] In this thesis, two novel platforms were introduced that include an electrically tunable cell sorter using hopping frequency dielectrophoresis and a micromixer employing phase-controlled AC electroosmosis. Finally, the concept of electrohydrodynamic-mediated micromixing, which has solely been explored within the context of theoretical modeling and experimental characterizations, was implemented for the synthesis of organic nanoparticles suitable for drug delivery applications. Accordingly, three major objectives were pursued during the course of this thesis as follows:

Objective 1: For this objective, we designed, fabricated and characterized a dielectrophoresis platform to enable a tunable and reconfigurable particle and cell sorting operation by using a frequency hopping signaling scheme. The characterization experiments were performed using

polystyrene microspheres and the platform was further validated by the separation of MCF-7 cancerous cells that were spiked in diluted blood samples.

Objective 2: An AC electroosmotic microfluidic mixer was designed, fabricated and tested to demonstrate a tunable micromixing mechanism by introducing a phase-lag on the excitation electrodes. The experimental observations were analyzed with an analogical comparison to field-effect transistors operation and validated through electric field simulations.

Objective 3: Electrohydrodynamic-assisted micromixing was characterized and validated for the synthesis of monodisperse liposomal batches. The platform was fully characterized to understand the effect of various parameters including the electric field excitation frequency, flow ratios/rates and reagent concentration.

1.2 Thesis Outline

This thesis is written in three broad sections that include: 1) the background knowledge and literature review, 2) the main body of the research study, 3) concluding remarks, limitations and future perspectives. The background knowledge entails the fundamental concepts underlying the main ideas and methods explored in this thesis that is presented in **Chapter 2**. Accordingly, chapter 2 covers active and passive microfluidic techniques for realizing particle sorting/enrichment and micromixing. Furthermore, the main concepts pertinent to the nanoprecipitation technique for nanoparticle synthesis are discussed in chapter 2. The relevant literature was reviewed in **Chapters 3** and **4**. **Chapter 3** provides a comprehensive overview of recent advances in microfluidic devices that are driven by electric fields. This chapter is broadly focused on the macroscale particle and fluid actuation through various electrically actuated microfluidic platforms. **Chapter 4** extends the major topics in chapter 3 to discuss the dielectrophoresis of biomacromolecules and the interplay

of other electrokinetic effects that may exist concurrently in many platforms. The literature review presented in Chapter 4 was published in the Journal of *Sensors and Actuators B: Chemical*.

Chapters 5, **6** and **7** cover the main research objectives. **Chapter 5** introduces the concept of frequency hopping dielectrophoresis for particle and cell separation. The results presented in this chapter were published in the Journal of *Sensors and Actuators B: Chemical*. **Chapter 6** reports on the concept of phase-controlled field-effect micromixing exploiting AC electroosmotic-induced flows. The results provided in Chapter 6 were published in the Journal of Microsystems and Nanoengineering. **Chapter 7** introduces the concept of electrohydrodynamic-mediated micromixing and how it can be utilized for the synthesis of nanoscale liposomes. The content of Chapter 7 was published in the Journal of ACS Applied Nano Materials. **Chapter 8** delivers the general conclusion, the summary of the main research objectives and the original contributions of this thesis to the knowledge advancements in the field of electrokinetic-/electrohydrodynamic-based microfluidic platforms. **Chapter 9** presents a detailed analysis of the limitations of presented methods followed by opportunities and future work that complement the objectives of the current thesis.

Chapter 2. Background Knowledge

2.1 Cell Separation and Enrichment

The purification and isolation of cells using microfluidic platforms have been a significantly active research area for the past decade. Much of the demand in the design of microfluidic devices for cells isolation is driven by needs in clinical diagnostics and therapeutic monitoring. The differentiation of cells generally relies on either labeled or label-free techniques. In labeled techniques, the cells are identified based on their unique membrane protein expressions that are targeted by fluorescent ligand tags or functionalized magnetic beads that are subjected to electrical or magnetic fields, respectively. On the contrary, label-free methods rely on the intrinsic mechanical and physical characteristics of the cells such as size, stiffness, deformability, density, polarizability, charge density, etc. The labeled techniques are often very specific but may potentially alter the fate and function of the separated cells due to the attachment of antibodies, prohibiting downstream applications. Conversely, separation techniques based on physical properties of cells do not require any pre-processing of the sample and are less prone to adverse effects on cell functionally albeit they may not be as specific as labeled techniques.

The labeled or label-free sorting of cells in a heterogeneous population is achieved through either passive strategies leveraging the channel geometry and inherent hydrodynamic forces or active methods utilizing an external force field to maneuver cells for spatial or temporal separation. The basics and main principles of various active and passive methods are briefly discussed in the following sections to present an overview of existing methods for cell separation and enrichment.

2.1.1 Active Methods

A. Fluorescence-activated Cell Sorting (FACS)

FACS is the most popular method for cell identification and separation meeting many scientific communities' needs due to its mature technology as well as high sensitivity and throughput.[11] In FACS, cells that are stained using fluorophore-conjugated antibodies are interrogated individually by flowing in a laminar stream and passing a focused laser beam that scatters into a detector (Fig. 2.1A).[12] Then, the specific light scattering and fluorescent characteristics of each cell are analyzed to identify the target cells. For separating the cells, various actuation mechanisms may be used. Conventionally, single cells are ejected in liquid droplets, analyzed by the detector and deflected into different bins using an electric field. The FACS systems can analyze and process cells with high throughputs in the order of 100, 000 cells/s.[13] Although FACs system may comprise cell viability and be costly, their single-cell level sensitivity, high throughput and ability to track multiple parameters have made them ubiquitous in many research settings.

B. Magnetic-activated Cell Sorting (MACS)

The MACS methods operate by first labeling cells with magnetic beads that are functionalized with the recognition molecules or antibodies.[14] Then, the cells are exposed to a magnetic field gradient and those target cells with the conjugated magnetic beads are separated from the population. The magnetic sorting can analyze cells individually in continuous flow or in a batch mode allowing higher throughput of up to 10^{11} cells per 30 min.[13] Furthermore, magnetic-based manipulation methods are not affected by the cell's surface charge or medium's ionic strength or pH as it is the case for electrical-based sorting such as dielectrophoresis discussed later in this chapter.

C. Dielectrophoresis

In the presence of a non-uniform electric field, cells can get polarized and be actuated by the action of the electric field.[15] This phenomenon is termed dielectrophoresis (DEP) and often generated by

the fabrication of microelectrodes embedded in microfluidic channels. The direction of particle movement is determined by the relative polarizability of the cell with respect to that of the surrounding liquid. For cells more polarizable than the suspension medium (positive DEP), they are directed towards the highest electric field intensities and for cells that are less polarizable than the suspension medium (negative DEP), they are moved towards lowest electric field intensities. The intensity of the dielectrophoresis force is dependent on particle volume and the relative permittivity of the cells and the medium. Thus, by engineering electrode geometry, target cells can be either trapped or spatially deflected to realize separation. DEP sorting methods do not require any labeling and the separation is solely based on the cell size and its unique electrical parameters. However, DEP force is most effective when cells are suspended in low conductivity buffers that are not ideal for cell viability and survival.

D. Acoustic

Ultrasonic acoustic resonance (standing waves) induced by piezoelectric materials can produce radiation forces to spatially manipulate cells and molecules for sorting applications.[16] The standing acoustic waves (SAW) generate fixed pressure nodes (minimum pressure) and antinodes (maximum pressure). The direction of the acoustic force is governed by the acoustic contrast factor $(\frac{5\rho_p-2\rho_m}{2\rho_p+\rho_m}-\frac{\beta_p}{\beta_m})$, which depends on the density (ρ) and compressibility (β) of the particle (subscript *p*) and medium (subscript *m*). For a positive contrast factor, that is generally the case for solid particles, acoustic radiation force moves the particles towards the pressure nodes. Conversely, a negative contrast factor, that is generally the case for bubbles, results in the movement of particles towards pressure antinodes. Furthermore, the intensity of the acoustic force has a linear relation with the particle volume that can be leveraged for particle sorting. Since most particles of interest have a positive contrast factor, the spatial separation of particles into different

bands at nodes and antinodes is not feasible. Instead, most acoustic sorting methods operate by generating a narrow stream of sample particles that are exposed to acoustic radiation (Fig. 2.1B and C).[17-18] Then, the lateral displacement of particles according to their size results in spatial particle sorting.

E. Optical

In optic-based sorting, a highly focused laser beam is utilized to provide attractive or repulsive forces to manipulate microscopic particles. The method is often referred to as optical tweezers following the pioneering work by Ashkin and colleagues.[19] Optical tweezers can manipulate cells according to their size, shape, refractive index and polarizability.[19] The highly focused laser beam induces two types of forces, the scattering force produced by photons striking the particle along their propagation direction and the gradient force generated by a gradient in field intensity (Fig. 2.1D).[20] The scattering and gradient forces depend on the laser beam wavelength (λ) and the particle size (r). Particle trapping by optical tweezers can assume three distinct regimes, Mie regime ($r \gg \lambda$), Rayleigh regime ($r \ll \lambda$) and the intermediate regime ($r \sim \lambda$).

In the Mie regime where the particle size is significantly larger than the beam wavelength, both the magnitude and the direction of the force depend on the particle shape, and the trapping is generally limited to spherical or ellipsoidal particles. In this mode, the conservation of momentum model or ray optics governs the particle movement.[21] For particles substantially smaller than the beam wavelength (Rayleigh regime), the force direction is independent of the particle shape and its magnitude changes with the particle orientation. In this regime, the electromagnetic field of light pulls particles towards the brightest part of the beam, where the induced dipole on particle minimizes its energy. When the particle size is comparable to the beam wavelength, neither the

ray optics nor the dipole moment is valid. In this case, more elaborate electromagnetic theories must be considered to analyze particle motion in this intermediate size range.[22]

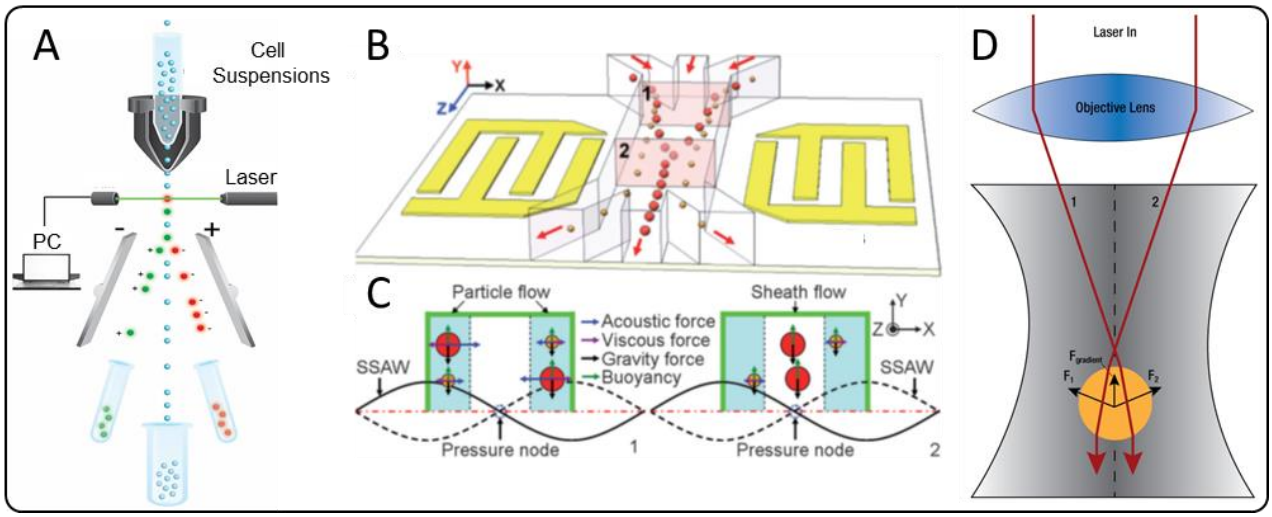

Figure 2.1. Active separation methods. **A.** Schematic illustrating the working principle of fluorescence-activated cell sorting**.** Reprinted with permission from Ref.[12] Copyright (2015) MDPI. **B.** Setup for a SAW-based acoustic sorter with interdigitated electrodes generating the SAW across the fluidic chamber. **C.** Forces acting on the incoming particles at two different sites (1 and 2) corresponding to the acoustic sorter in B. Reprinted with permission from Ref.[18] Copyright (2009) RSC. **D.** Schematic illustrating an optical tweezer and the net gradient force on a particle that is larger than the wavelength of light.

2.1.2 Passive Methods

A. Deterministic Lateral Displacement

The use of periodic arrays of micro-pillars is a popular passive technique to sort out cells based on size referred to as deterministic lateral displacement (DLD).[23-25] In DLD methods, as shown in Fig. 2.2A, cells of varying size navigate through an array of posts either deflected sideways or unaffected. Control over sorting is achieved by the design of array features (i.e., radius, distance and row offset) such that cells smaller than a critical radius ($a < R_c$) move with the convective flow and cells larger than a critical radius ($a > R_c$) move in a deterministic direction imposed by the row offsets in the micropillar array.

B. Pinched Flow Fractionation

As the name suggests, in pinched flow fractionation methods, a dilute sample stream is pinched in a narrow microfluidic channel that connects to a much broader channel (Fig. 2.2B). A sheath flow is used to pinch the sample stream such that the cells are constrained and aligned against one sidewall of the narrow microfluidic channel. As a result, the center of inertia for the larger cells is farther from the wall surface than the smaller cells such that cells of different sizes attain slightly different flow trajectory upon broadening of the channel. The cells are separated latterly with smaller cells closer to the channel wall and larger cells farther away from the channel wall.[26]

C. Microfiltration

Microfiltration is perhaps the most well-known method for separating particles according to their size and deformability. These methods typically employ weir microstructures,[27] pillars,[28] or membrane filters[29] whereby larger cells remain trapped and smaller cells pass through the open spaces or pores. Microfiltration can also be realized using hydrodynamic filtration whereby the sample stream is pumped through a channel with multiple side-branching outlets (Fig. 2.2C).[30] The side channels drain the liquid continuously that results in the alignment of all particles along the main channel's sidewalls. Thus, the smaller cells that are aligned closer to the channel walls elute earlier from the channel compared to the larger cells.

D. Inertia

Inertial lift forces on particles moving in microchannel flow can be exploited to precisely position them within the channel for sorting applications.[31] Lateral displacement of particles in microchannels happens due to the superposition of two inertial lift forces: the shear-induced lift force and the wall-induced lift force. The balance of these two forces displaces particles at distinct positions within the microchannel cross-section according to their size relative to the microchannel

dimensions, resulting in their lateral sorting. The inertial forces become appreciable when a particle's Reynolds number ($R_p = R_c \frac{a^2}{D_h^2}$) is on the order of 1 or higher. The particle's Reynold number (R_p) is dependent on the particle's diameter (a), the channel Reynold number (R_c) and the hydraulic diameter (D_h). For the case of curved microchannels, a secondary flow pattern also emerges due to the centrifugal force. This flow is termed Dean flow that is rotational in a perpendicular direction to the main flow. As a result of Dean flow, an extra drag force is exerted on the particles, enabling size-based separation.[32]

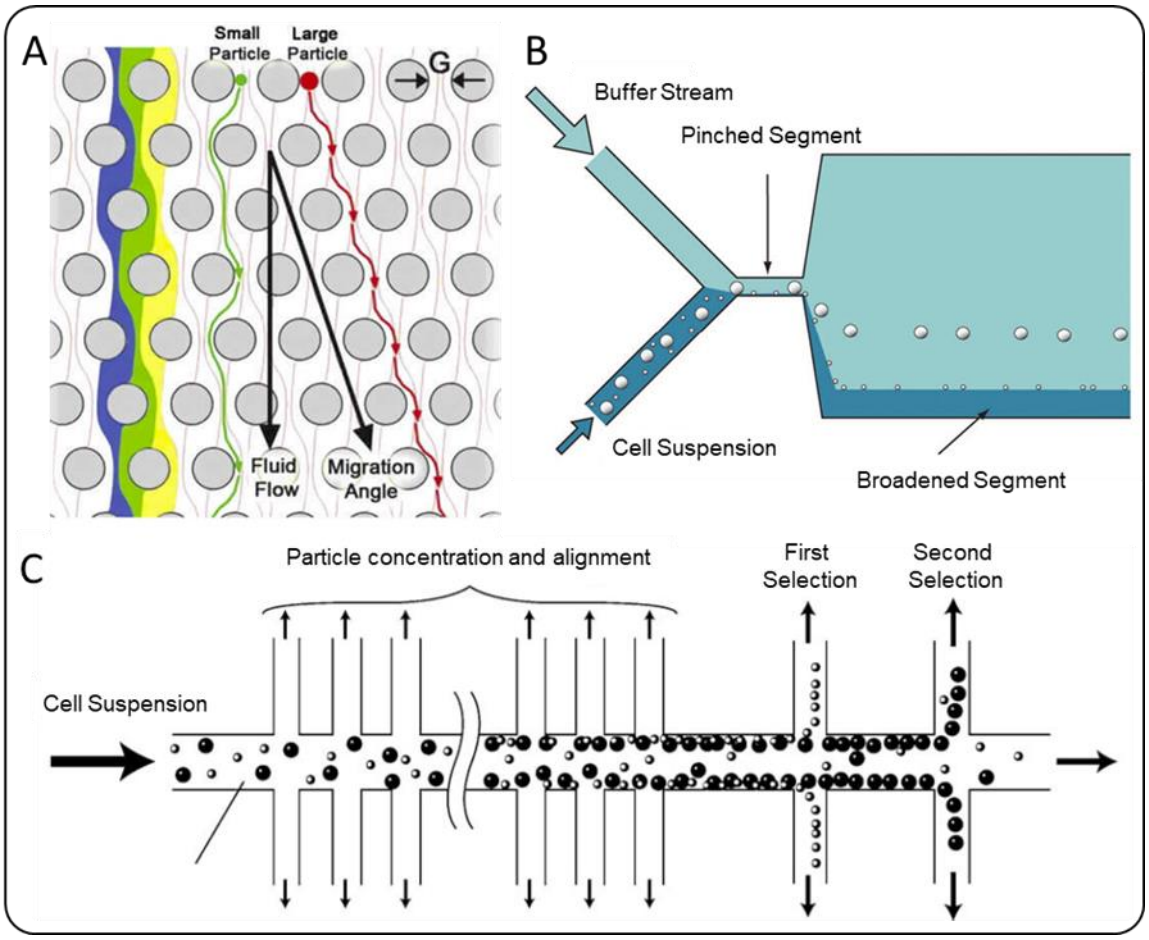

Figure 2.2 Passive separation methods. **A.** Schematic illustrating the working principle of particle separation for deterministic lateral displacement. Reprinted with permission from Ref.[25] Copyright (2009) AIP Publishing. **B.** Schematic depicting a pinched flow fractionation device. Reprinted with permission from Ref.[33] Copyright (2010) RSC. **C.** Schematic illustrating the working

principle of hydrodynamic filtration. Reprinted with permission from Ref.[30] Copyright(2005) RSC.

Table 2.1 Active and passive methods for cell sorting and enrichment

	Method	Actuation Mechanism	Differentiation Markers	Ref
Active	FACS	Various forces including electrostatic deflection	Light scattering	[11]
	MACS	Homogenous or inhomogeneous magnetic fields	Size, magnetic susceptibility	[14]
	Dielectrophoresis	Inhomogeneous fields	Size, polarizability	[15]
	Acoustics	Acoustic radiation pressure	Size, density, compressibility	[16-17]
	Optical tweezers	Optical scattering and gradient forces	Size, polarizability, refractive index	[19-21]
Passive	DLD		Size, deformability	[23-24]
	Pinched flow fractionation	Hydrodynamic force	Size	[26]
	Microfiltration		Size, deformability	[27-30]
	Inertia	Shear-induced and wall-induced lift	Size, shape	[31-32]

2.2. Mixing at Microscale

The dominance of viscous to inertial forces in microchannel flows often lead to laminar streams such that the mixing of the streams is only feasible by molecular diffusion. However, diffusive mixing is extremely slow and ineffective, especially when considering many bioanalytical applications that demand a rapid mixing environment such as in chemical synthesis. Thus, many active and passive methods have emerged to enhance mixing in microfluidic channels. Active mixers employ external energy sources such as magnetic, electric, or acoustic to disturb the flow patterns. These methods often have simple channel geometries that are easy to fabricate but they require external force generators that add to their bulkiness and cost. Conversely, the passive mixers utilize no external energy input and solely rely on the pressure head used to drive the fluid flow. The mixing is achieved by increasing the contact surface and contact time between the species flows. The passive mixers are simple to operate; however, the channel design and fabrication may become complex depending on the specific mixing mechanism. This section

attempts to cover the principles of operation describing various active and passive micromixers as a prerequisite to the remainder of this thesis.

2.2.1 Active Methods

A. Magnetic-field Driven Microstrring

Magnetic micro-stirrers are essentially the miniaturized version of macroscale magnetic bars in a rotating electric field. Similar to bulk stirring, this type of active mixing employs a rotating magnetic field to rotate one or multiple microbars within the fluidic channel.[34] The microbars are made of a ferromagnetic material. When an external rotating magnetic field is applied, the microbar will magnetize and experience a torque through interaction between its internal magnetization and the external field.

B. Acoustic-field Driven Micromixing

Both bulk acoustic waves (BAW) or surface acoustic waves (SAW) have shown feasibility for improving the mixing of laminar flows in microfluidic channels. The most common and efficient acoustic-driven micromixers leverage BAW to actuate elastomeric sharp edges or trapped bubbles in contact with flow streams. The BAW is generated using commercial piezoelectric transducers. The piezoelectric transducer is put in contact with PDMS microfluidic channels that embed sharp features, bubbles, or both (Figure 2.3A). This setup translates the acoustic field to the vibrational motion of sharp features or bubbles to generate acoustic microstreams for a strong agitation of flow to enhance mixing.[35-36]

C. Electric-field Driven Micromixing

Various electric-field driven flow actuation mechanisms may be utilized for the mixing of laminar streams.[37] Those mechanisms often involve AC electroosmosis, AC electrothermal and electrohydrodynamics. The AC electroosmosis fluid flow is driven by the interaction of a non-

uniform electric field with the induced electrical double layer on the surface of embedded electrodes. For ACEO-induced flow micromixing, electrodes are embedded within the microfluidic channel such that they generate counter-rotating rolls transverse to the incoming flow. ACEO micromixers are applicable to fluids of low ionic conductivities. With increasing ionic conductivity, the ACEO flow vanishes making these micromixers ineffective for most biological buffers. On the other hand, at high ionic conductivities, the ACET can induce flow agitation using the same electrode design criteria for ACEO mechanism. The ACET is driven by Joule heating that leads to a temperature gradient within the contained fluid. The temperature gradient is the source of conductivity and permittivity gradients creating volume charges that are acted on by the electric field resulting in fluid agitation.

Finally, electrohydrodynamic-driven micromixers are concerned with multiphase flows or flow systems with liquids of distinct electric permittivities, conductivities or both. Here, the source of fluid agitation is the interaction of the electric field with the monopolar charges at the interface of liquids. Unlike ACEO and ACET, the electrohydrodynamic-driven micromixing is applicable across larger liquid types so long as a disparity in phase or electrical parameters exist.[38] Figure 2.3B illustrates particle trajectors in an electrohydrodynamic micromixer employing liquid solutions of different conductivities under different biasing conditions.[39] The electric field is applied perpendicular to the flow direction.

2.2.2 Passive Methods

A. Flow Focusing/Injecting Micromixers

Focusing or injection mixer rely solely on diffusion to improve mixing. These mixers are essentially very effective at diluting the sample stream into another stream. In the hydrodynamic focusing methods, the sample stream is focused into a very narrow stream by the sheath streams

that are injected through the microfluidic channel at much higher flow rates than the sample stream (Figure 2.3C).[40] The sub-micron width of the sample stream allows for the rapid diffusion of species form the sheath streams into the focused stream. Mixing time (t_{mix}) of hydrodynamic focusers depends on the width of the focused stream (w_f) and is approximated as $t_{mix} \sim w_f^2/D$, with D being the diffusion coefficient.

In injection mixers, a small aperture is employed to inject a thin stream into another stream. These mixers allow multiple streams to be injected and may be desired in situations where the flow rate cannot be controlled. Furthermore, the injection mixers require the construction of small apertures that adds to the fabrication complexity. The mixing time for injection mixers is highly dependent on the device geometry and the method of injection.[41]

B. Lamination Micromixers

Lamination mixers generally split the streams to be mixed into multiple streams that are then interdigitated and recombined.[42-43] Splitting the main streams into several streams reduces the striation length and thus enhances mixing. Here, the striation length (l_{st}) refers to the length scale over which diffusion must act in order to homogenize the concentration. In the absence of turbulence, the striation length is in the order of the channel size (l). If each stream is split into N streams, the striation length is decreased by a factor of N, which reduces the mixing time by a factor of N^2. Here, the mixing time is approximated by $t_{mix} \sim (l/N)^2/D$, with D being the diffusion coefficient.

C. Chaotic Advection Micromixers

Chaotic advection micromixers can be engineered to result in the exponential thinning of the striation length. Continuous flow chaotic advection micromixers typically consist of repeating units which perform stretching and folding or splitting and recombining operations. Passing each unit, the striation length reduces by a constant factor and the exponential reduction in the striation

length is attained as the fluid stream traverses multiple units. The chaotic advection micromixers often require three-dimensional designs with unites consisting of ridges, grooves, or protruding features. A well-studied example of such mixers is the staggered herringbone mixer that employs grooves on the channel floor to drive transverse flows (Figure 2.3D). A periodic and asymmetric herringbone groove structures yield two asymmetric circulation flows that alternate periodically along the channel.[44]

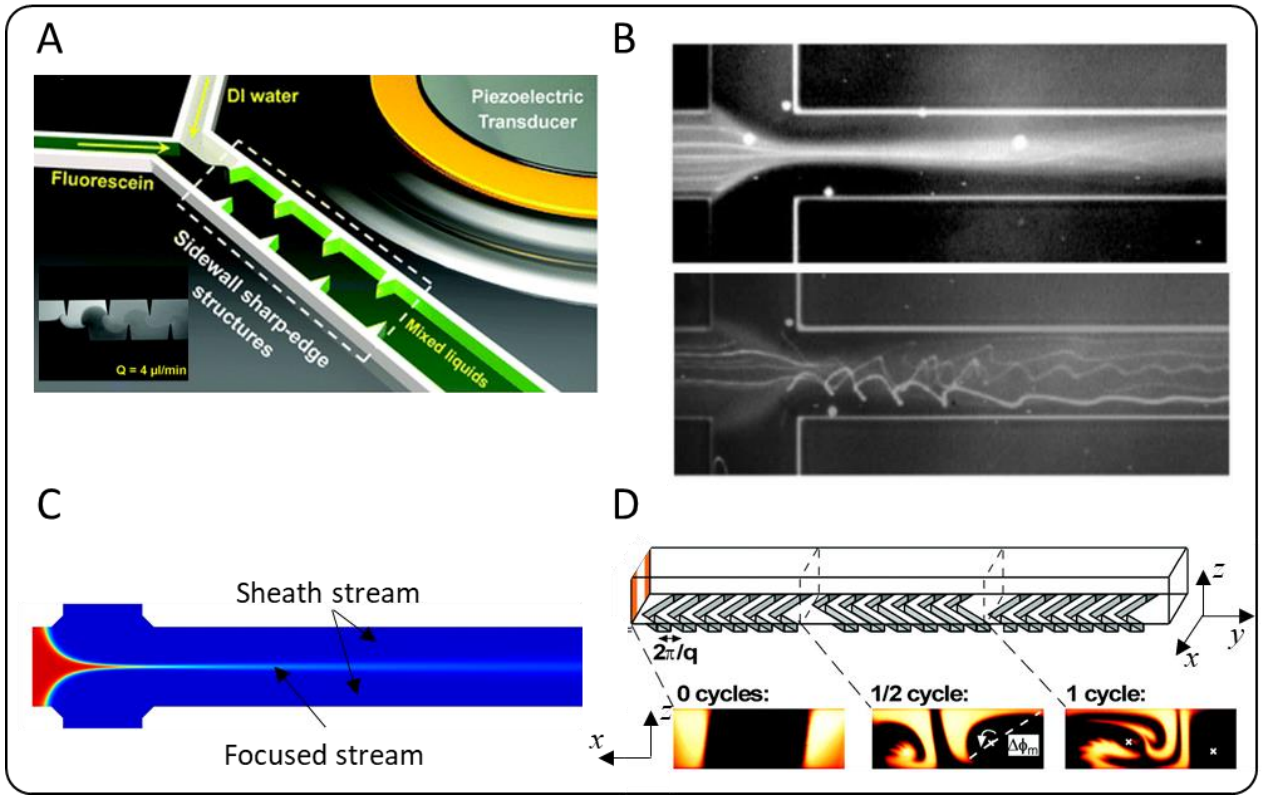

Figure 2.3. Active and passive mixing methods. **A.** Schematic illustrating the device structure for generating microstreams at sharp-edge structures through bulk acoustic waves. The inset shows the mixing of water and dyed water. Reprinted with permission from Ref.[36] Copyright (2013) RSC. **B.** Electrohydrodynamic mixing and particle trajectors for fluids of different conductivities. The sheath and center streams are 1 mM and 10 mM sodium chloride solutions. Reprinted with permission from Ref.[39] Copyright (2004) IOP Publishing. **C.** Computer simulation showing the mixing of water and isopropyl alcohol in a hydrodynamic flow focuser. Reprinted with permission from Ref.[45] Copyright (2010) ACS. **D.** Schematic diagram of one-and-a-half cycles of a staggered herringbone micromixer. The insets are confocal micrographs of the vertical cross-section of the

channel in **A** showing two streams of fluorescent solution. Reprinted with permission from Ref.[44] Copyright(2002) AAAS.

2.3 Nanoprecipitation of Nanoparticles

Among various methods for nanoparticle preparation,[46] the nanoprecipitation method (or solvent displacement) is a simple and fast process differing from emulsion-based methods in that no precursor emulsion is required. Starting from a multi-component system in single-phase, the precipitation (or phase separation) takes place at the onset of supersaturation when the system is perturbed by modifying conditions such as temperature or concentration.[47] Upon system perturbation, the solute concentration is raised beyond the saturation limit or solubility limit and reaches a critical concentration at which the precipitation process is initiated. The process of nanoparticle formation involves an initial nucleation phase followed by a growth phase. The nucleation phase happens when the solute concentration reaches a threshold limit, which results in the formation of a large number of nuclei. The nuclei form by condensation of solute molecules until they approach a critical size at which they are stable against dissolution. The nucleation phase ceases as the concentration of the solute falls below the critical nucleation limit. However, this concentration is sufficient for the growth of the formed nuclei. The growth phase continues until the concentration of the remaining dissolved solute reaches the equilibrium concentration (i.e. the bulk solubility).

In practice, the amphiphilic solute (polymer or lipid molecule) is dissolved into a polar organic solvent that is mixed with a large amount of an antisolvent (usually water).[48] The antisolvent and solvent liquids are miscible in all proportions and the vesicle formation is driven by the self-assembly process. Here, the amphiphile first forms a bilayer, which subsequently closes to form a vesicle. For the synthesis of homogenous nanoparticle batches with narrow size distributions, it is critical 1) to have a nucleation phase that occurs in a short period compared to

the time length required for the growth phase, 2) to generate a homogenous environment in terms of temperature and species concentration.[47]

Chapter 3. Recent Advances on Electrically-Driven Biomicrofluidics

This chapter discusses electrical based actuation mechanisms for fluid and particle handling and introduces recent advances in electrically-driven Biomicrofluidics.

3.1 Introduction

Electrokinetics and electrohydrodynamic phenomena, that involves particle and fluid actuation in response to electric fields, have been the subject of studies in colloidal science for decades due to the rich fundamental science and potent applications. In particular, the integration and application of electrokinetic effects in microfluidics have attracted intensive research interest owing to their advantageous attributes, including low hydrodynamic dispersion, non-moving parts, ease of automation and integration, and efficient and multifold actuation of liquids and particles for pumping, mixing and entrapment.[49-52]

Electrokinetic effects can broadly be classified into two groups based on the type of applied voltages, direct current (DC) versus alternating current (AC). The use of AC electric fields offers many advantages over DC electric fields. Particle aggregation and protein sedimentation is a major drawback of DC fields.[53] Additionally, Joule heating and Faradaic reactions at the electrode-electrolyte interface can cause bubble and ion contaminant generation as well as electrode degradation over time. Therefore, DC-operated microfluidic devices often isolate electrodes from the working channels in a separate compartment, not in contact with the analytes. This, however, limits the potential of such schemes for miniaturization and defeats the particle manipulation and flow control advantages of electrokinetic devices with internal electrodes.[53]

Application of AC electric fields to fluids and colloidal suspensions can lead to a dynamic range of field-induced effects.[54] A polarizable particle in an inhomogeneous field undergoes dielectrophoresis, which pushes the particle towards field minima or maxima depending on the relative permittivity of the particle with respect to the medium.[55] Fluids in AC electric fields can experience various type of instabilities depending on the electrical properties of the fluids, monophasic or multiphasic fluids in laminar microfluidic streams, and the applied voltage

frequency. AC electroosmosis fluid motion results in response to the electric field interaction with its self-induced electrical double layer (EDL) on the surface of electrodes in contact with an electrolyte.[56] On the other hand, AC electrothermal flow arises due to spatial inhomogeneities in fluid electrical conductivity and permittivity that are sourced by local Ohmic heating at the electrode surface.[57] While AC electroosmosis is most pronounced for low ionic solutions with AC voltages at low frequencies, AC electrothermal is most effective at high ionic solutions at higher signal frequencies. Finally, electrohydrodynamic fluid instabilities occur in multiphasic liquid systems in which the electric field drives the built-up charges at the interface of liquids with different electrical conductivities or permittivities or both.[58]

Those aforementioned phenomena have found applications in numerous on-chip operations involving particle manipulation and assembly, fluid mixing and pumping. Yet, new applications are still emerging tailoring the material-dependent (i.e. conductivity and permittivity) behavior of electrokinetic/electrohydrodynamic effects. In this review, we aim to provide a comprehensive treatment of recent advances in electrically-driven microfluidic platforms with applications to bioanalytical systems. We cover novel developments in particle manipulation based on the dielectrophoresis force followed with advances in fluid actuation mechanisms by AC electric fields and their emerging applications.

3.2 Dielectrophoresis

3.2.1 Theoretical Background

Dielectrophoresis is the motion of dielectric or polarizable particles induced by a non-uniform electric field. Charged molecules such as DNA, RNA and protein as well as neutral particles such as cells can polarize in an inhomogeneous electric field and undergo a net dielectrophoretic force. In a medium with finite polarizability, under an applied field, the bound charges temporarily

redistribute to induce a dipole or many poles within the medium. If the field is uniform, the Coulomb force due to charge redistribution balances out to a zero average. However, if the field is non-uniform, the charge distribution is uneven, leading to a non-zero Coulomb force. The dielectric force acting on a dipole moment p with polarizability α in an inhomogeneous field with a non-zero gradient tensor ∇E is:

$$F_{DEP} = (p.\nabla)E \tag{3.1}$$

$$p = \alpha E \tag{3.2}$$

An immediate observation of this equation reveals that no net force acts on a dipole when $\nabla E = 0$, or when the electric field is uniform. For an idealized spherical particle of radius *r* with electrical permittivity of ε_p suspended in a medium of electrical permittivity of ε_m, the time average DEP force is given by eq. 3.3:

$$\langle F_{DEP} \rangle = 2\pi\varepsilon_0\varepsilon_m r^3 Re[f_{cm}]\nabla|E|^2 \tag{3.3}$$

$$f_{cm} = \frac{\varepsilon_p^* - \varepsilon_m^*}{\varepsilon_p^* + 2\varepsilon_m^*} \tag{3.4}$$

$$\varepsilon^* = \varepsilon - j\frac{\sigma}{\omega} \tag{3.5}$$

where f_{cm} is the Clausius-Mossotti or Maxwell-Wagner factor, ε^* the complex permittivity, σ the conductivity and ω the angular frequency. The presence of the dielectric force is strongly dependent on the relative polarizability of the medium with respect to that of the suspending particle represented by the Clausius-Mossotti factor. The sign of the real part of f_{cm} determines force domination towards maximum or minimum of an electric field. If this factor is positive, the DEP force is referred to as positive DEP (pDEP), and the particle is moved towards the maximum

of the electric field. If it is negative, the DEP force is referred to as negative DEP (nDEP), and the particle is repelled away from regions of the highest field intensity.

A key observation of the analytical solution in eq. 3.3 is that the time average DEP force is dependent on particle volume, non-uniformity of the electric field and relative polarizability of particle compared to the medium. The electric field amplitude square dependence implies that both DC and AC fields can induce a DEP force. However, under DC conditions, the existence of electrophoretic motion may be an undesired effect. Furthermore, DC currents are more likely to cause Faradaic reactions at the electrode-electrolyte interface leading to the generation of bubbles and unwanted reactions.

It is important to note that the average DEP force in eq. 3.3 only applies to homogeneous spherical particles. For structurally inhomogeneous bioparticles such as cells, the complex structure of the cell, in single-shell models, is reduced to a homogenous cytoplasm and a membrane with effective permittivity and conductivity values.[59] Furthermore, the polarization mechanism of macromolecules is a complex subject, rendering modeling and estimating a dielectric constant very challenging. This difficulty is mainly attributed to the complex dependency of polarization mechanism on the macromolecule's conformational and topological variations.[60] For many practical situations, however, precise knowledge of the dielectric constant is not necessary.[61] Average polarizability values that entail major conformational contributions and solvent-macromolecule interfacial effects will suffice. Average polarizability values in the bulk solution are determined using dielectric and impedance spectroscopy,[62-64] dielectrophoresis[65-67] and time domain reflectometry[68] techniques.

3.2.2 Dielectrophoresis Applications

Dielectrophoretic induced motion of particles has extensively been employed to move particles in micro-/nanoscale settings to realize multipurpose manipulations involving concentrating and trapping, focusing, sorting, precision positioning and assembling. For those operations, parameters such as electrodes and fluidics enclosure geometries, the strength of background flow field and the liquid properties in which particles are suspended are of utmost importance for achieving optimized performance. Particle motion is generally achieved by invoking either pDEP or nDEP at the appropriate frequencies applied to planar electrodes to selectively capture or release particles. pDEP captures particles at the edges of electrodes where the field intensities are the strongest while nDEP repels particles away from electrodes. On the other hand, electrode-less or insulating DEP (iDEP) enables dielectrophoretic particle manipulation by embedding insulating microstructures within the fluidic channel to disturb electric field intensities with voltages applied across the channel. The iDEP approach eliminates electrochemical reactions and bubble generation at the electrodes by removing them from the main microfluidic channels. To compensate for the loss of electric field strength, the iDEP devices typically require voltages in the range of hundreds of volts making them most appropriate for use in laboratory settings.

With a fundamental understanding of dielectrophoretic theory and device operations, the following sections aim to cover the latest advances in bioanalytical systems employing various dielectrophoresis approaches for micro- and nanoscale particle manipulations.

A. Trapping and Concentrating

In recent years, many genomics, proteomics and transcriptomics studies demand assessing cells and biomolecules as single entities.[69-71] Single-cell analysis reveals biology that is masked when cells in populations or within tissues are considered.[70] For most single-cell analysis investigations,

microfluidic-based techniques provide unique capabilities to precisely manipulate and locate cells in large numbers utilizing droplets,[72-74] hydrodynamic traps,[75] valve traps,[76] electric traps[77] and acoustic traps.[78] Electrical techniques providing on-demand capture and release of cells are advantageous in several manufacturing and performance criteria. Dielectrophoretic device fabrication is routinely executed by conventional microfabrication techniques with single-layer electrode patterning and microfluidics that are simple to fabricate unlike designs with multi-layer structures involving valves and micromixers. Furthermore, on-demand capture and release of cells provide another level of flexibility with the dielectrophoretic platforms.

Single-cell trapping is mostly achieved by combining pDEP force with physical constrictions such as well-like[79-81] or filter-like features.[77] The pDEP force pulls the cells towards the field maxima and the physical constriction prevents the entrapment of additional cells at the occupied spot. For instance, Qin et al. devised a microfluidic setup with two parallel channels interconnected by a series of reaction chambers with inlets consisting of filters of a specified size.[77] As shown in Fig. 3.1A and B, the fluidic setup also included two electrodes that extend the length of the fluidic channel at the periphery. Upon voltage excitation, the PDMS filter groves provided pDEP traps and cells were drawn to these traps. The cell release to each reaction chamber was then followed by flowing the loop-mediated isothermal amplification buffer (LAMP) and turning off the voltage. Finally, the isolation of a cell microenvironment from other reaction chambers was achieved by injecting an immiscible oil phase. The platform enabled a single-cell capture efficiency of 92.7 %. The dimension of filter groves, the voltage amplitude, and fluid velocity are parameters that must be optimized for efficient single-cell trapping.

Other commonly employed designs for single-cell trapping by pDEP force are the implementation of interdigitated electrodes that are covered by microwells[79-81] or electrodes at the

substrate and cover levels whereby the electrode on the substrate is masked with microwells.[82-83] An example of such platforms is the work by Wu et al. for high throughput cell pairing utilizing an array of 3264 microwells to pair two different cell types.[79] In brief, the cell-pairing platform consisted of a two-layer interdigitated electrode arrangement on the substrate level and a two-layer SU-8 microwell design of different diameters (Fig. 3.1C). The two cell types were trapped consecutively by exciting each interdigitated electrode pair separately. Once both cell types were trapped, the cells paired through flow in a capillary channel and a physical barrier in the shape of a "U" micro-baffle.

While most cell trapping applications deploy pDEP force due to its greater holding force, nDEP force can also be very effective for confining cells away from electrode edges. However, the geometry of the electrodes must be optimized to generate efficient nDEP cages. Quadrupole electrodes[84-85] and concentric electrodes[86] are by far the most studied platforms for cell analysis at the single level. The quadrupole electrodes are generally best fitted for cellular characterization experiments in small numbers. High throughput cell trapping using a single layer electrode design with individually addressable electrodes is not feasible with quadrupole electrodes. On the other hand, few studies showed that concentric type electrodes may be utilized for high-density single-cell analysis. An example of such platforms is the work by Chung et al. that designed a 104 × 104 microarray with a complementary metal-oxide-semiconductor (CMOS) readout circuitry to record impedance measurements of individual cells that were positioned by nDEP on sensing electrode pads.[86]

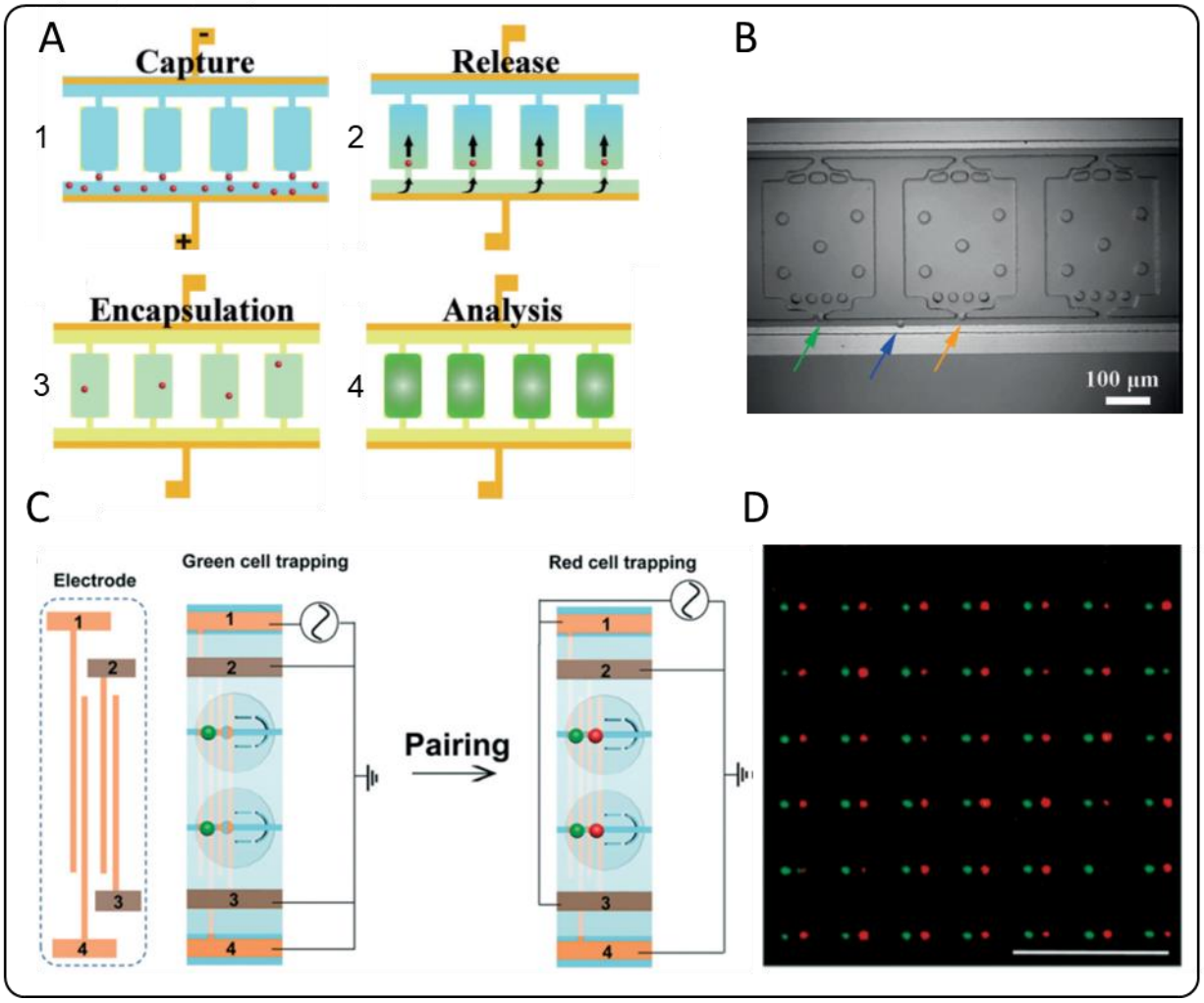

Figure 3.1 Platforms based on pDEP force for single-cell trapping. A. Process steps for single-cell capture by first flowing in cells and applying pDEP force at filter grooves (1), releasing trapped cells by turning off the voltage and injecting fresh LAMP reaction buffer (2), filling the channel with an immiscible phase to compartmentalize cells in chambers (3) and lysing cells for single-cell LAMP analysis (4). **B.** An optical image of the platform in A. Reprinted with permission from Ref.[77] Copyright (2018) Wiley. **C.** Single-cell trapping and pairing by invoking pDEP using two sets of interdigitated electrodes. **D.** Fluorescent image of Hella cell pairing. The scale bar is 500 μm. Reprinted with permission from Ref.[79] Copyright (2017) Royal Society of Chemistry.

So far, we discussed the utility of dielectrophoresis for the trapping of microscale cells in the context of lab-on-a-chip platforms. However, many molecular-scale studies have benefited from dielectrophoresis for manipulating nanoscale bioparticles either in population or at single-molecule precision. The dielectrophoretic handling of nano-bioparticles is largely driven by the

need to overcome the slow diffusion of biological species in many detection schemes and to advance the state-of-the-art techniques for the on-demand control of biomolecules. The principle of dielectrophoresis induction remains the same as the particles of interest approach nanoscale dimensions. However, the excitation electrodes in electrode-based DEP and the insulating features in insulating DEP must be scaled down with nanoscale features (i.e. gaps, pores, edges, surface roughness or etc.) to generate adequate DEP traps at small voltages. In recent years, the development and fabrication of nanotweezers,[87-89] nanopores,[90-93] nanogaps[94-95] and nanopipettes[96] have proven very effective for manipulating nanoscale bioparticles.

Recently, Nadappuram et al. reported on the development of a minimally invasive nanotweezer that can extract molecular species from individual cells with single-molecule precision without aspirating cytoplasmic fluid (Fig. 3.2A).[87] They fabricated nanotweezers utilizing nanopipettes made from double-barreled quartz capillaries via laser pulling with nanoelectrodes formed at the tip by pyrolytic deposition of carbon (Fig. 3.2B and C). The described nanotweezer was used for dielectrophoretic (pDEP) trapping and extracting fluorescently labeled DNA of various sizes ranging from 22-base single-stranded DNA to 48,502 base-pair double-stranded DNA as well as small proteins (monomeric α-synuclein (14.5 kDa)) in solution. Furthermore, the feasibility of the nanotweezer to perform single-cell biopsy was assessed by selectively sampling cellular components such as DNA, RNA and organelles.

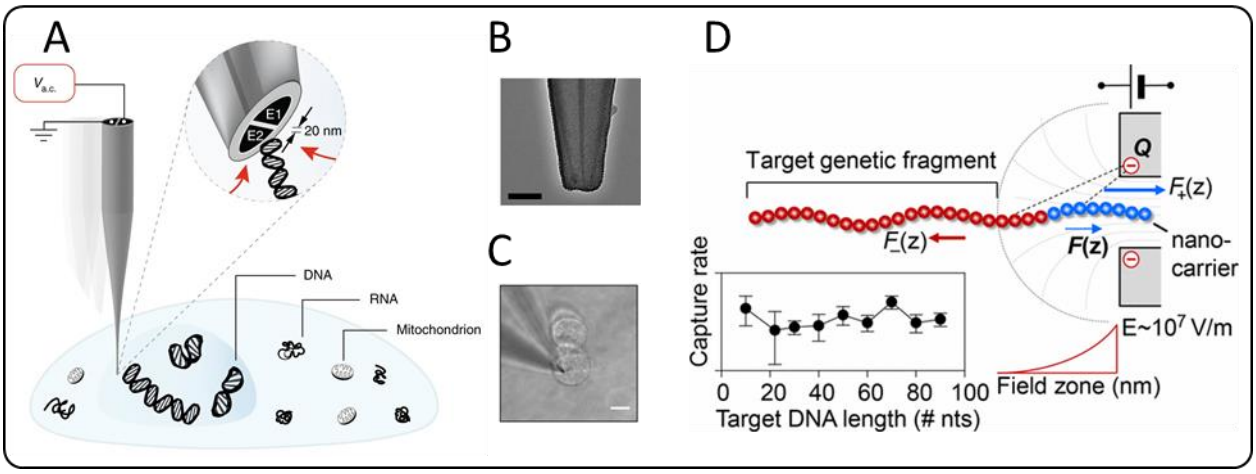

Figure 3.2. **Molecular dielectrophoresis**. **A.** Nanoscale tweezers for single-cell biopsies to capture and extract cellular components such as DNA, RNA and Mitochondria. **B.** Transmission electron microscopy micrograph of DEP nanotweezer. Scale bar is 20 nm. **C.** Bright-field image of a nanotweezer inside a cell. The DNA inside the nucleus was targeted with a voltage of 20 V_{pp} at 1 MHz frequency. Reprinted with permission from Ref.[87] Copyright (2019) Nature Publishing Group. **D.** The principle of operation for a synthetic dipole facilitated nanopore dielectrophoresis. Reprinted with permission from Ref.[90] Copyright (2017) Americal Chemical Society.

Nanopore sensing is another field of study that has exploited the dielectrophoretic-induced motion of nano-bioparticles to address the challenges of selectivity and long time-to-detection events in low concentration samples. Tian et al. demonstrated that by conjugating an engineered polycationic nanocarrier with target DNA or RNA molecules, a prescribed dipole moment can be imposed on the target molecules (Fig. 3.2D).[90] The engineered target-nanocarrier complex renders nanopore sensing sensitive and selective as opposed to the conventional sensing. In this manner, the tagged target molecules experience an enhanced dipole moment and are drawn to the nanopores by dielectrophoresis force while non-target molecules are electrophoretically repelled from the nanopores. The method was validated for the detection of single- and double-stranded DNA or RNA of any length and allows the simultaneous sensing of multiple targets.

B. Focusing

Many microfluidic applications such as flow cytometry and various sorting methods require processing cells and microparticles in a single stream whereby particles flow at the same speed and are positioned within the same streamline. Conventionally, single-stream particle focusing is performed by sheath-flow[97-98] or inertial focusing.[99-100] The limitation of sheath-flow focusing is the need for high flow rate ratios of sheath-to-sample streams resulting in substantial dilution of the sample. On the other hand, size-dependent focusing location and the need for high-speed flows in inertial focusers may be a hurdle in certain applications. As a result, active approaches may be a viable alternative to hydrodynamic-based flow focusing. Both pDEP and nDEP forces balanced with the hydrodynamic force have been utilized to perform cell focusing.[101-104] Kung et al. devised a microfluidic platform termed tunnel dielectrophoresis consisting of four independently addressable electrodes (two on device floor and two on device ceiling) to focus a randomly distributed cell population with nDEP forces (Fig. 3.3A).[104] As illustrated in Fig. 3.3B, tuning of the AC voltages on each electrode generated a single electric field minimum within the channel with control over its spatial position. Single-stream focusing at different locations within the channel was achieved in a physiological buffer noting that most cells will experience nDEP force at high ionic conductivity liquids and will displace to the field minimum. Positive dielectrophoretic-based cell focusing and impedance sensing of spiked *E. Coli* bacteria in drinking water was demonstrated by Kim and colleagues.[103] In their platform, slanted microelectrode pairs acted as guiding rails to focus cells in one end of the channel. The cell affinity to attach to electrodes by pDEP combined with the drag force drove the cells along the electrode edges to reach the opposite side of the channel. To avoid irreversible cell attachment to electrodes, a passivation layer was deposited on these electrodes.

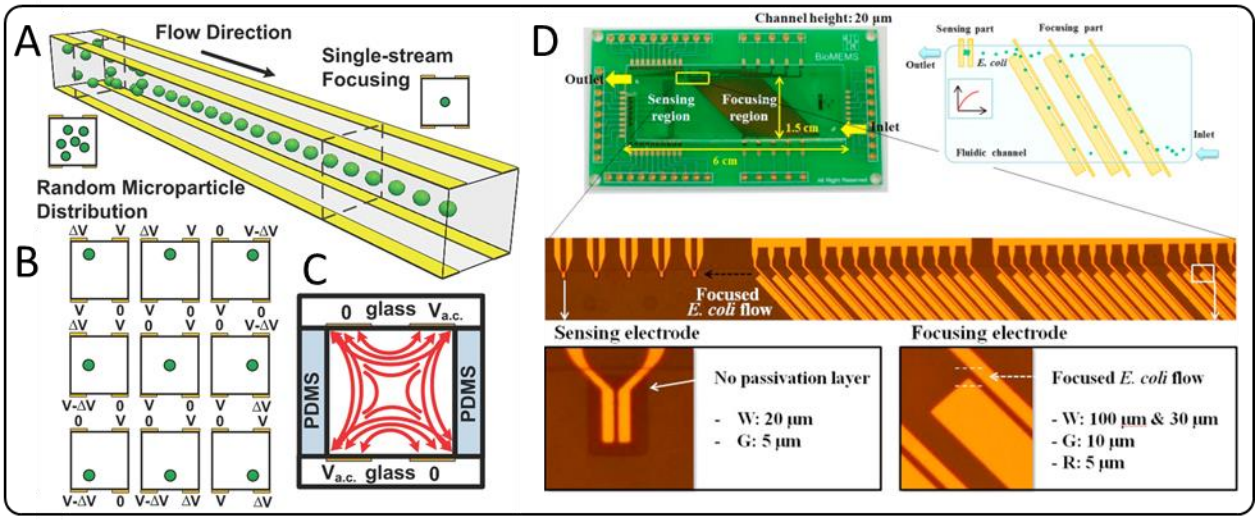

Figure 3.3. Dielectrophoretic particle focusing. **A.** Schematic illustration of tunnel dielectrophoresis using quadro-electrodes aligned with the longitudinal axis of the microfluidic channel to focus randomly distributed particles into a single stream. **B.** Tuning of stream location by the independent modulation of AC voltages on each electrode. **C.** Voltage combination and schematic of electric field distribution to locate the cell stream at the channel center. Reprinted with permission from Ref.[104] Copyright (2016) Wiley. **D.** Schematic illustration and photos of an integrated positive dielectrophoretic cell focusing and impedance sensing of *E. Coli* spiked in drinking water. Reprinted with permission from Ref.[103] Copyright (2015) Elsevier.

C. Sorting

Perhaps one of the most explored applications of dielectrophoresis is the sorting and separation of constituent components of a heterogeneous population. Generally, size and dielectric properties are considered as key differentiation factors amongst bioparticles in a population. One main approach to the dielectrophoretic separation of target species is to tarp a certain group of particles by pDEP and release the remaining particles that undergo nDEP force or experience a minimal pDEP force insufficient for their entrapment under the operating flow conditions. This approach is generally simple to implement but may suffer from the saturation of trap spots especially as the sample concentration increases. The issue with the saturation of trap locations is manifested in channel clogging with continuous flow platforms whereby the trap locations at the start of the separation channel will get filled and block the flow of incoming particles. Furthermore,

pearl-chaining due to electrostatic interaction between particles may aggravate the problem. Thus, this approach may be most suitable when the capture of rare species is considered such as circulating tumor cells (CTCs) or the isolation of nanoscale entities from the bulk liquid.

Recent sorting designs that rely on pDEP have deployed metal electrodes/probes,[105-109] insulating posts[110-111] and wireless bipolar electrodes.[112] Shim and colleagues devised a dielectrophoresis-based field flow fractionation (FFF) device for isolating CTCs from unprocessed blood leveraging the tumor cells' pDEP response differentiating them from blood cells.[109] The device consisted of multiple inlets and outlets to introduce the sample and the deionization solution and to remove tumor cells and untargeted cell. As depicted in Fig. 3.4A, one inlet carries in the sample and the other injects a deionization solution of low ionic conductivity at physiological osmolarity. The slow diffusion of two streams allows the cells to spend less time in the low conductivity solution that is required for an efficient DEP force. After a certain mixing length to equilibrize the diffusion process, the cells are exposed to a nonuniform electric field generated by interdigitated electrodes on the device floor. The CTCs are pulled down by pDEP force and are skimmed out at their dedicated outlet while remaining cells are repelled by nDEP force and are eluted from the channel to a separate outlet. The ability to process an undiluted blood sample by introducing a deionization step is an intriguing idea explored in the described study that appropriated the concept of DEP FFF.

Moreover, the separation of nanoscale suspensions in blood plasma by pDEP has proven feasible and utilized for discerning blood plasma of pancreatic cancer patients.[106-107] Heller and colleagues proposed a new device structure using a silicon substrate with platinum electrodes that were covered by a patterned layer of silicon dioxide covering the substrate except the electrode surfaces. The chip surface was further covered by a porous hydrogel layer to protect electrodes

from electrochemical reactions and possible bubble formation when media of high ionic conductivities such as blood plasma are being used (Fig. 3.4B). The spiked exosomes (glioblastoma), extracellular vesicles (EV) and aggregated protein particles suspended in blood plasma were isolated by dispensing a small sample volume (30 – 50 μL) onto the chip subject to an AC signal of 10 V_{pp} at 15 kHz frequency for 10 minutes. Those nanovesicles and protein aggregates were collected at high-field regions by the pDEP force while the larger entities such as cells were concentrated in the low-field areas that were washed away. The described platform and operating conditions have proven very efficient in isolating nanovesicle biomarkers validated through multiple characterization techniques including scanning electron microscopy (SEM) visualization, fluorescent labeling, and RT-PCR and end-point PCR on released RNA from glioblastoma exosomes and EVs (Fig. 3.4C-E). The method was also implemented for exosome separation from pancreatic and colon cancer patient samples with the subsequent immunofluorescent detection of specific exosome-associated protein biomarkers.[106] The on-chip immunofluorescent analysis of the biomarkers glypican-1 and CD63 readily discriminated a small cohort of pancreatic ductal adenocarcinoma (PDAC) patients (n = 20) from healthy individuals (n = 11).

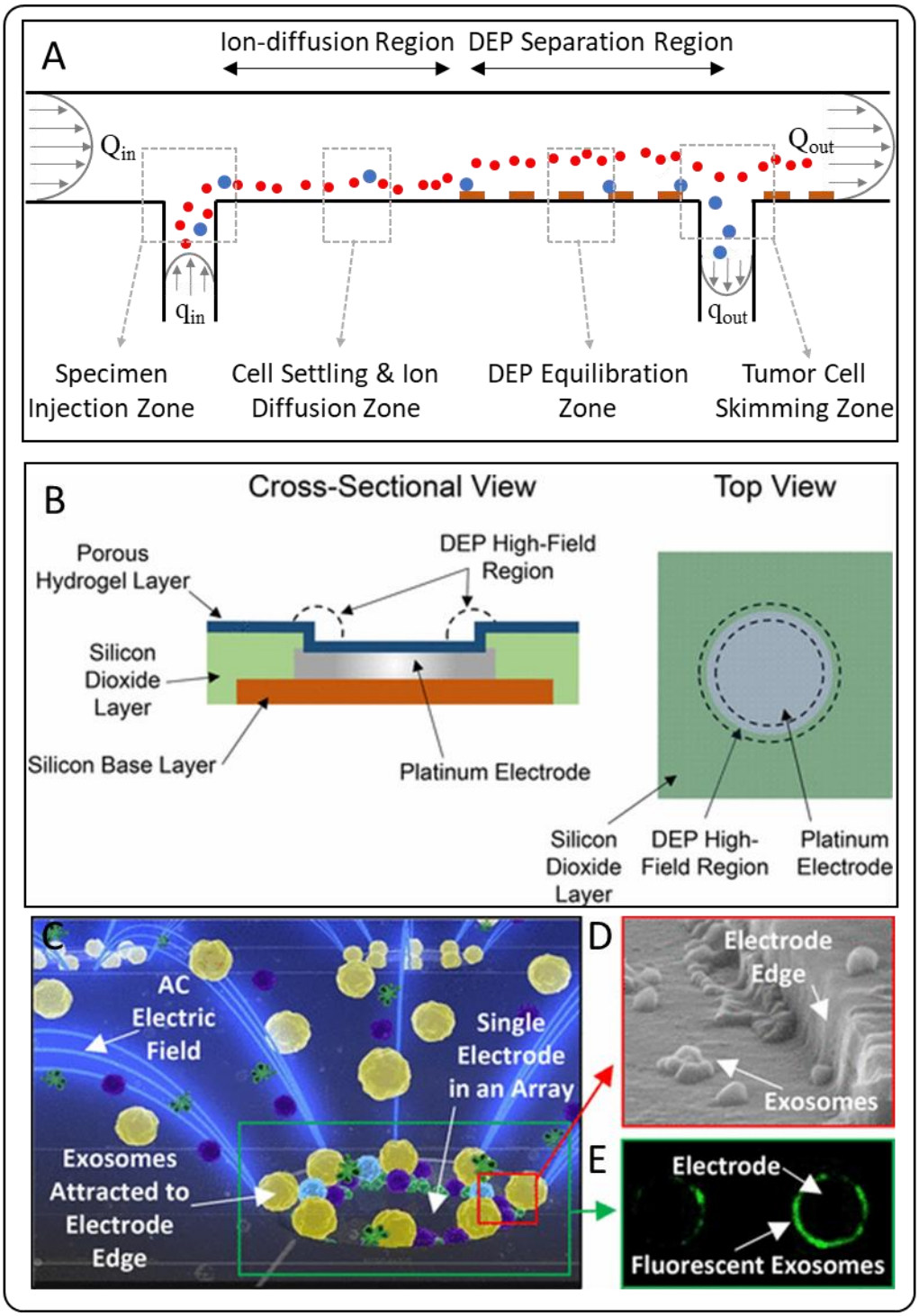

Figure 3.4. Dielectrophoretic cell and nanoscale particle enrichment. A. DEP-FFF separation of tumor cells from peripheral blood mononuclear cells (PBMNs) in a continuous-flow chamber. The separation chamber is composed of four major parts: specimen injection, cell settling and specimen deionization, height stabilization by force balance and isolation of the tumor cells and PBMNs at two separate outlets. Reprinted with permission with Ref.[109] Copyright (2013) AIP Publishing. **B.** Schematic drawing of the device structure for the collection of extracellular vesicles

using pDEP. **C.** Schematic illustration of exosomes and other nanoparticles collection at electrode edges. **D.** Top-view SEM image of a microelectrode after DEP collection of extracellular vesicles. **E**. Fluorescence image showing the on-chip labeling of glioblastoma exosomes. Reprinted with permission from Ref.[107] Copyright (2017) American Chemical Society.

Another major approach to dielectrophoretic particle separation is through the lateral displacement of particles so that different groups of particles are positioned at different streamlines. A basic element for many DEP-based lateral displacement platforms is the "guiding tracks" traversing the width of the channel at a certain angle θ with respect to the direction of flow. The DEP force generated by the guiding tracks at an oblique direction displaces particles laterally as they move through the separation channel. In that context, the particles that undergo larger DEP force are displaced further from their initial position while those unaffected or experiencing smaller DEP force remain close to their initial position. The guiding tracks generally include angled electrodes[113-116] in electrode-based platforms or offset microstructure posts[117-118] in iDEP designs. The concept of lateral displacement can also be realized using electrodes that are situated on one side of the channel exposing a stream of mixed particles to a non-uniform electric field.[119] The sorting of particles is then attained through the differential DEP force experienced by different groups of particles. In either case, the sample stream must be focused into a narrow stream by a sheath stream.

Lately, the lateral displacement by oblique interdigitated electrodes in combination with a pulsed signaling scheme (on/off) was investigated to effectively separate human mesenchymal stem cells (hMSC) and their differentiation progenies (osteoblasts).[114] The interdigitated electrodes were designed with an inclined angle of 45˚ relative to the flow direction, and the sample and buffer streams were introduced via two inlets of the same dimensions. The separation of the two cell types was achieved by electrode excitation with an AC signal frequency that induced appreciable pDEP force on osteoblast cells to deflect them from their original position along the

path of electrodes while the hMSCs cells remained relatively unaffected. To alleviate problems with irreversible particle attachment to electrodes under pDEP, a pulsed signaling scheme was utilized to break the continuity of the DEP force.

iDEP platforms can be leveraged for particle sorting in a manner analogous to conventional deterministic lateral displacement devices. For instance, Calero et al. implemented an iDEP DLD platform consisting of microstructured cylindrical posts in a transverse AC electric field that imposed an orthogonal field with respect to the direction of flow.[117] The AC electrokinetic DLD design can operate under two frequency-dependent modes that enabled a tunable particle separation. Those particles less than a critical diameter moved in the direction of flow in a zig-zag fashion much like the operation of a DLD design when no voltage was applied. At high AC frequencies (> 1kHz), for an adequate nDEP force that acted mainly orthogonal to the Stokes force by the fluid flow, particles started bumping along the posts and flowed in displacement mode. The posts that were misaligned at an angle θ from the longitudinal axis of the separation channel ensured the lateral distortion of particles. On the other hand, at low frequencies (<1 kHz), the particles also experienced electroosmotic and electrophoretic forces which generated a low frequency oscillation along the direction of electric field lines. This oscillation was superimposed onto a non-zero DEP force, which modified the effective particle diameter leading to the deviation of particles smaller than the critical diameter. Fig. 3.5F shows particle trajectories for 3 μm, 1 μm and 500 nm beads at the absence of an AC field, high- and low-frequency AC fields.

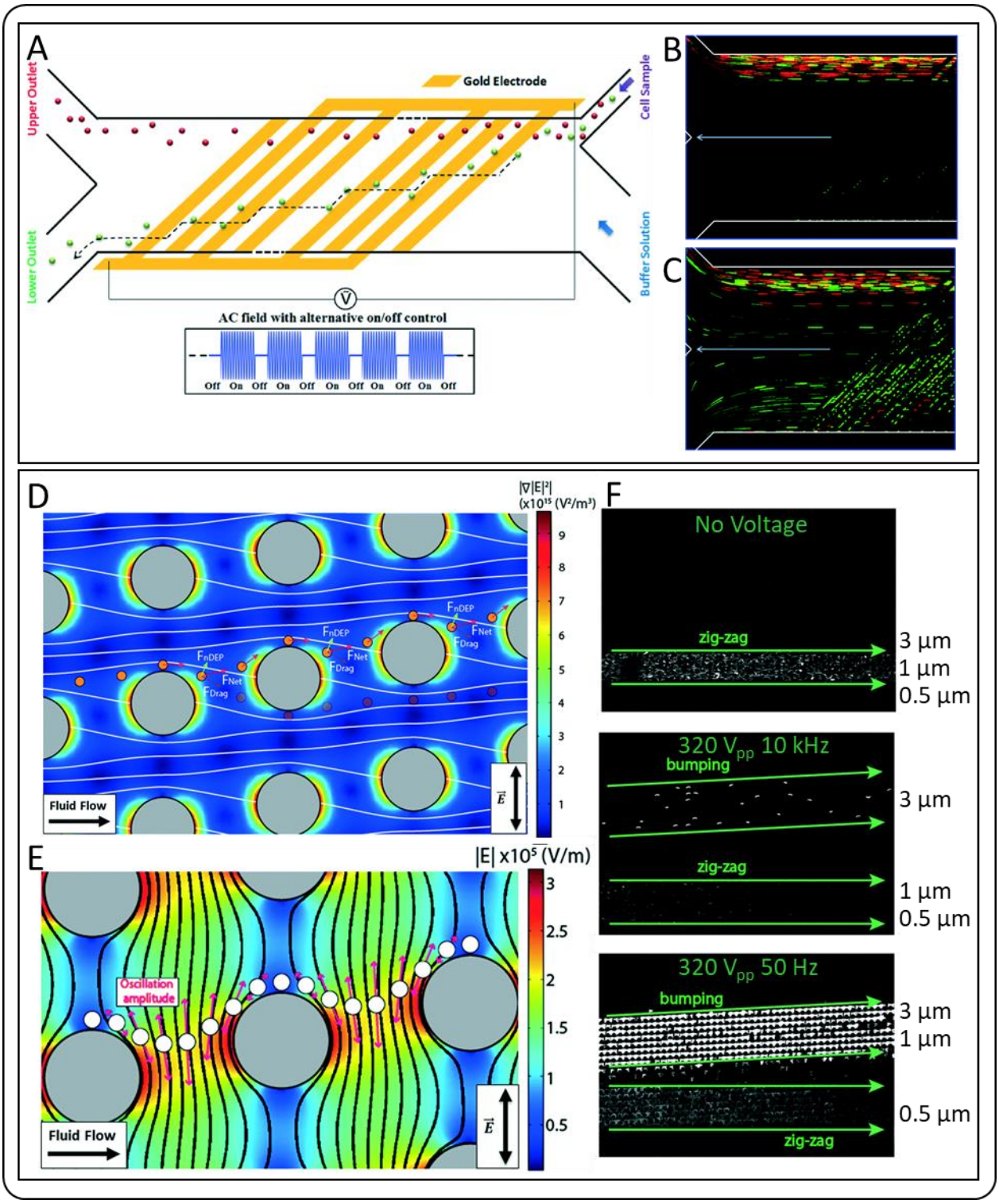

Figure 3.5. Dielectrophoretic lateral displacement sorting. A. Schematic illustration of the electrode/fluidic layout for the separation of hMSCs and their differentiation progenies (osteoblasts) using slanted electrodes as the guiding tracks. **B.** Superimposed trajectory of hMSCs (in red) and osteoblasts (in green) for an AC field of 7.2 V_{pp} at 3 MHz. **C.** The superimposed

trajectory of hMSCs and osteoblast for an AC signal of 15.4 V_{pp} at 3 MHz. Reprinted with permission from Ref.[114] Copyright (2015) Royal Society of Chemistry. **D.** Insulating posts in a transverse electric field for nDEP lateral displacement of cells. The nDEP force prevents particles from zigzagging when trying to pass between the posts of the same row. **E.** Diagram showing the deviation of a particle under the low-frequency signal. The oscillation of the particles along the field lines and perpendicular to the fluid flow due to electrophoresis and electroosmosis that change the effective diameter of the particles, leading to their deviation. **F.** Deviation of 3 μm, 1 μm and 500 nm microspheres suspended in 1.7 mS/m electrolyte. Reprinted with permission from Ref.[117] Copyright (2019) Royal Society of Chemistry.

3.3 AC Electrokinetic Fluid Actuation

Microelectrodes in contact with a liquid can generate fluid flow when excited with an electric potential. These types of flows are a strong function of electric potential (i.e. intensity and oscillation frequency) as well as electrical parameters of the liquid. This section covers AC field-driven fluid actuation mechanisms that include AC electroosmosis (ACEO) and AC electrothermal (ACET). While ACEO flow is bound to the electrode-liquid interface in response to an induced electrical double layer, the ACET flow is a volumetric flow mechanism corresponding to heat gradients and the subsequent conductivity/permittivity gradients in a non-uniform electric field. Another major distinction between the two fluid actuation mechanisms is the ionic conductivity of the liquid upon which the electric field is effective. The ACEO flow rapidly decays with increasing salt concentrations with almost no flow for bulk salt concentrations above ~10 mM.[120] On the other hand, the ACET flow is most appropriate for liquids of high ionic conductivity such as biological fluids and cell buffers.

3.3.1 Theoretical Background: AC Electroosmosis

Application of AC voltages to microelectrodes generate flow actuation by the action of the electric field on its self-induced charges at the electrode-electrolyte interface or the induced charges in the electrical double layer. This phenomenon is referred to as AC electroosmosis in an analogy to the conventional electroosmosis whereby an electric field acts on mobile charges at the interface of a

solid-liquid interface. The major difference here is that in AC electroosmosis, the applied field is responsible for both inducing the charges and pulling on them. A simple approach to understanding fluid flow generation by ACEO is to consider a pair of coplanar electrodes that are covered by an aqueous electrolyte. The electrodes are biased with a harmonic potential difference of amplitude V_0 and radial frequency ω, $V(t) = V_0 \cos(\omega t)$. Upon electrode excitation, counterions are migrated to the surface of electrodes and due to the nonuniform electric field, an electrical force pulls the liquid outward ($F = qE_t$) that is the source of fluid actuation on the surface of electrodes and within the bulk via viscous forces (Fig. 3.6). Here, E_t refers to the tangential component of the electric field. The generated flow remains stable despite the AC voltage excitation as in each half-cycle of the signal, both the tangential field and the induced charge change sign and thus, the force direction remains unchanged and the time-averaged force is non-zero.

An analytical formula was developed by Ramos et al. [56] to describe the time-average electroosmotic velocity at a distance x from the center of electrode gaps given by:

$$\langle v \rangle = \frac{1}{2} Re \left\{ \frac{\Delta\sigma_q E_t^*}{\mu k} \right\} = \frac{1}{8} \frac{\varepsilon V_0^2 \Omega^2}{kz(1+\Omega^2)^2} \frac{C_s}{C_s + C_d} \tag{3.6}$$

$$\Omega = \omega \frac{\varepsilon \pi z k}{2\sigma} \tag{3.7}$$

Where k is the reciprocal Debye length, and μ, σ and ε represent liquid viscosity, conductivity and dielectric constant, respectively. $\Delta\sigma_q(t)$ is the time-dependent excess charge in the diffuse double layer that varies with the frequency of applied voltage. The last right-hand-side term in eq. 3.6 is a correction factor with C_s being the Stern layer (or compact layer) capacitance and C_d being the diffuse layer capacitance.

The AC electroosmotic flow velocity peaks at a characteristic frequency and tends to zero at lower and higher frequency limits. At high frequencies (typically >100 kHz), the potential drop is across the entire electrolyte and thus, the induced potential across the double layer and the excess

charge tends to zero seizing the AC electroosmotic flow. At low frequencies, the potential is entirely dropped across the double layer and the electric field in the medium tends to zero. However, due to the continuity requirement in tangential field, E_t in the double layer is also zero yielding zero flow velocity.

3.3.2 Theoretical Background: AC Electrothermal

Electrothermal flow is another important electrokinetic phenomenon that is often observed in solutions of high ionic conductivities in combination with high applied voltages. ACET flow is primarily driven by dynamic variations in net charge density induced by gradients in fluid properties. The mechanism behind ACET flow is attributed to local Ohmic heating near the electrode surfaces which gives rise to local temperature increase. This, subsequently, leads to local conductivity increase and permittivity decrease. To maintain charge conservation, the local electric field must be lowered. However, according to Gauss's law, reduction in the local electric field necessitates the existence of a local charge density.[121] Hence, this leads to variations in net charge density generating an electrostatic body force.

The liquid temperature (T) increase yields permittivity and conductivity gradients within fluid bulk that are calculated as follows:

$$\nabla\varepsilon = (\frac{\partial\varepsilon}{\partial T})\nabla T \tag{3.8}$$

$$\nabla\sigma = (\frac{\partial\sigma}{\partial T})\nabla T \tag{3.9}$$

As described earlier, the variations in electrical and permittivity within the fluid produce a charge density (ρ_e). The charge density and the electric field are described by Gauss's law:

$$\rho_e = \nabla.(\varepsilon E) \tag{3.10}$$

$$\frac{\partial\rho_e}{\partial t} + \nabla.(\sigma E) = 0 \tag{3.11}$$

Considering the temperature dependence of σ and ε gradients, eq. 3.10 and 3.11 can be written as:[57]

$$\rho_e = \frac{\sigma\varepsilon(\alpha-\beta)}{\sigma+i\omega\varepsilon}\nabla T.\boldsymbol{E}_0 \tag{3.12}$$

Where

$$\alpha = \frac{1}{\varepsilon}\left(\frac{\partial\varepsilon}{\partial T}\right) \tag{3.13}$$

$$\beta = \frac{1}{\sigma}\left(\frac{\partial\sigma}{\partial T}\right) \tag{3.14}$$

The expression for the electrical force per unit volume is given by:

$$\boldsymbol{f}_E = \rho_q\boldsymbol{E} - \frac{1}{2}\boldsymbol{E}^2\nabla\varepsilon \tag{3.15}$$

The first term in eq. 3.15 represents the Coulomb force of volume charges and the second term is the dielectric force. To first order, the time-averaged electrical force per liquid unit volume is expressed as:

$$\langle \boldsymbol{f}_e \rangle = \frac{1}{2}Re\left(\frac{\sigma\varepsilon(\alpha-\beta)}{\sigma+i\omega\varepsilon}(\nabla T.\boldsymbol{E})\boldsymbol{E}^* - \frac{1}{2}\varepsilon\alpha|\boldsymbol{E}|^2\nabla T\right) \tag{3.16}$$

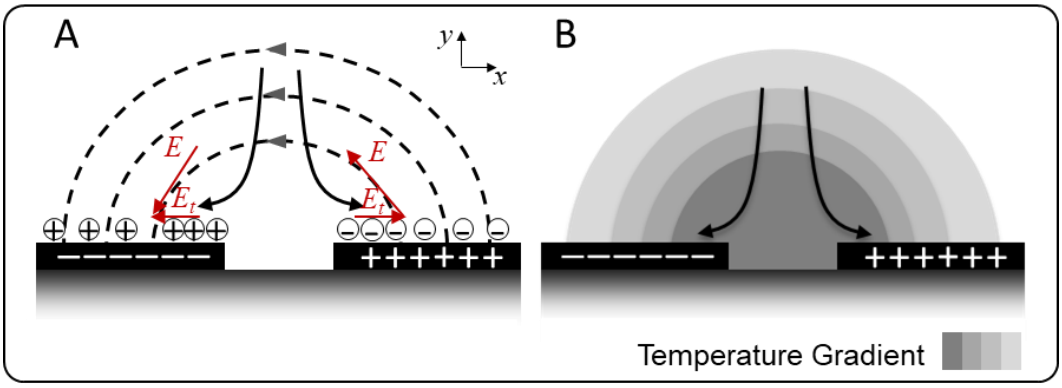

Figure 3.6 Diagram illustrating different mechanisms of AC electrokinetic flow actuation. **A.** Cross-section view of coplanar electrodes depicting electric field lines and generated field components acting on EDL in ACEO. **B.** Cross-section view of coplanar electrodes showing temperature gradients and the generated fluid flow streams in ACET.

3.3.3 AC Electrokinetic Fluid Actuation Applications

Both ACEO and ACET flows have been utilized in microscale and nanoscale fluidic platforms for applications in pumping, micromixing and particle concentration. While the pumping and mixing of fluids have been proven feasible in the context of theoretical studies and characterization experiments, their usefulness for lab-on-a-chip applications and niche problems in bioanalytical systems are still developing. This is largely due to the process variations and sensitivity of those techniques to the electrical properties of the liquid system of interest compounded by the need for the faster and more efficient pumping/mixing. Nevertheless, AC electrokinetic fluid flow engineering has functioned as a very effective method to enhance mass transport and analyte concentration involving many biosensing applications. Either ACEO or ACET flows are increasingly being exploited in conjunction with many biosensing mechanisms to improve time to detection and detection limits in various biosensing mechanisms.[50]

A. Pumping

The example of a symmetric coplanar electrode in Fig. 3.6 serves as a simple structure for understanding the mechanism of AC electrokinetic fluid actuation that yields local fluid mixing with no net pumping of fluid. With symmetrical electrodes, the generated flow streams roll on top of the electrodes that are identical and do not produce any net directional flow. However, if microelectrode or potential asymmetry is introduced, a net flow pumping can be achieved in microfluidics channels.[122] In the case of asymmetric microelectrode arrays as depicted in Fig. 3.7A, the counter-rotating convection rolls on top of the larger electrodes dominate and a net directional flow is generated. The theoretical prediction of ACEO-based liquid pumping using asymmetric electrode arrays was first laid out by Ajdari et al.[123] followed by several experimental validations by other researchers.[124-126] Pumping velocities over 100 μm/s were shown by planar

microelectrode arrays which are inefficient for many portable microfluidic applications. The performance of ACEO can be greatly improved by designing asymmetric 3D electrode structures. The general design idea behind 3D microelectrode structures is to reduce the effect of local reverse flows contributed by the smaller electrodes, which hinder the dominant forward flow. This is realized by designing asymmetric microelectrodes with the larger electrodes at significantly higher height compared to the smaller electrodes. With 3D electrodes, pumping velocities over 1 mm/s were achieved.[127]

Another strategy to break the symmetry for net fluid pumping is the application of a traveling-wave electric potential. Traveling-wave potentials are typically implemented by applying AC voltages with a 90˚ phase shift between adjacent electrodes to an array of equally sized electrodes. Since it takes a finite time for double layer charging, a delay exists between the time of maximum induced charge and the maximum applied voltage. Then, the electric field interacts with the charges pulling the liquid in the direction of the traveling-wave. Traveling-wave ACEO generally produces slower flow velocities compared to the standing-wave ACEO.

The ACEO flow with planar electrodes has shown to reverse flow direction with increasing voltage, usually above 2 V_{pp}, and the reverse flow is stronger than the forward flow that grows more rapidly with the voltage than the expected scaling $v \propto V_0^2$. Another limiting feature of ACEO is the strong decay of the flow with increasing salt concentration. For this reason, most experiments in literature have utilized either very dilute solutions or deionized water. Studies by Bazant et al. have suggested that ACEO flow vanishes beyond a bulk salt concentration of about C_{max} ~ 10 mM, which is an order of magnitude smaller than most biological solutions.[128]

Overall, the pumping speeds achieved with the ACEO phenomenon are not adequate for ACEO flow to be used as a standalone pumping mechanism in most microscale fluidic

applications. Other challenges such as flow reversal at high voltages and flow speed dependence on the liquid ionic conductivity impede the usability of ACEO-based flow for pumping applications.[122, 129-131]

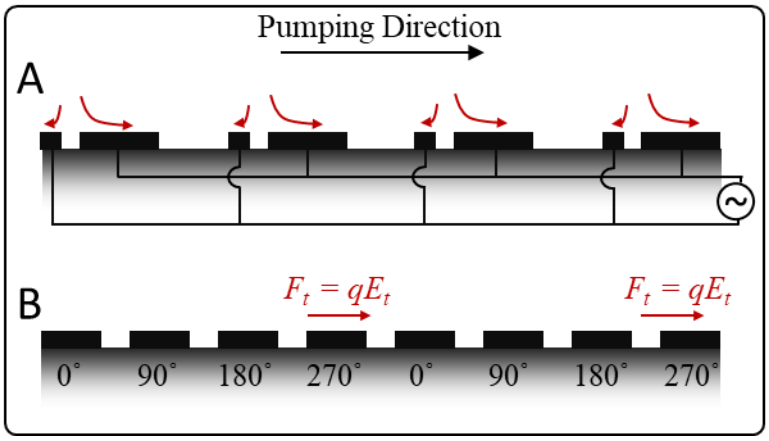

Figure 3.7. Schematic diagram illustrating breaking symmetry with **A.** asymmetric electrode arrays and **B.** traveling-wave electrode arrays.

Although the ACET flow mechanism is inherently different from ACEO flow, similar design concepts can be implemented to generate ACET directional flow pumping. Unlike, ACEO flow, ACET pumping can be functional with liquids of high ionic conductivity including biological buffers and liquids. Traveling-wave ACET for pumping was first illustrated by Fuhr et al. using an array of 16 equally sized electrodes (10 μm width and 10 μm spacing).[132] Flow velocities over 150 μm/s were obtained for DI water at 35 V_{pp} and 100 kHz. Later, the ACET phenomenon was further investigated to design micropumps with asymmetric electrode geometries[133-135] and external heating using thin-film resistive heaters[136] and light illumination.[137]

A specific ACET design consideration that must be taken into account is the degree of heat generation ensuring the biological entities remain viable and the buoyancy force does not overpower the electrical forces (i.e., high $\nabla T/\Delta T$). Also, similar challenges with respect to the use of ACEO as a global pumping mechanism remain valid for ACET pumping.

B. Micromixing

An immediate application of generating counter-rotating rolls over a pair of coplanar electrodes is in micromixing of laminar flows in a microfluidic channel.[138] Both ACEO and ACET mechanisms may be implemented to induce local fluid mixing that finds applications across many sensing platforms as means to overcome diffusion-limited transfer of target species to the recognition elements on the sensing surface. The counter-rotating rolls can help to facilitate mass transport to the sensing surface as well as mass removal of unbound species improving the sensor's sensitivity and decreasing detection time. In low conductivity analyte solutions, the presence of dielectrophoresis force along with ACEO flow may further assist the delivery of target species.

In recent years, various sensing mechanisms leveraged AC electrokinetic flow actuation for enhanced sensing performance. The suitable sensing platforms for assisted AC electrokinetic flow typically use sensing electrodes that are modified to generate either ACEO or ACET flow motion. Examples of such platforms include impedance sensing,[139-141] surface plasmon resonance, (SPR)[142-143] Raman spectroscopy,[144] quartz crystal microbalance (QCM),[145] field-effect transistors[146] and fluorescent immunosensing.[147]

For instance, AC electrokinetic fluid engineering has provided significant improvements in sensitivity and detection time for SPR sensing. Song et al. devised a localized surface SPR (LSPR) sensor based on gold nanorods (AuNR) that was supplemented with a pair of coplanar Pt electrodes that sandwich the sensing area (Fig. 3.8A).[143] In this platform, the analyte solution is introduced using a PDMS-based microfluidic setup that runs orthogonal with respect to the Pt electrodes. Application of a small AC voltage induces ACEO rolls that run from the center of electrode spacing over the surface of electrodes. The convective ACEO rolls break the diffusion-limited barrier for nanoscale molecules to reach the surface of antibody-functionalized nanorods.

The described ACEO-enhanced LSPR was utilized for sensing IL-1B (a pro-inflammatory cytokine biomarker) in diluted human serum by measuring the real-time binding events between IL-1B and anti-IL-1B on the surface of gold nanorods. The binding events on the surface of functionalized AuNR were reflected by a spectral shift of the scattering light from the AuNR surfaces, which translated into a far-field intensity increase of the optical signal detected by optics via a bandpass filter. Improving mass transfer by invoking ACEO flow resulted in a significant increase in recorded change in scattering intensity when compared to incubation-based readings (Fig 3.8B).

Another instance of mass transfer improvement by AC electrokinetics flow engineering was demonstrated for a Carbon nanotube field effect transistor (FET) biosensor.[146] Fig. 3.8C shows the structure of a single FET that consists of an island electrode (drain), an enclosing electrode (source) and a carbon nanotube network (with p-type semiconducting behavior) decorated with gold nanoparticles that bridge the source and drain electrodes. The gold nanoparticles were conjugated with Tro6 aptamer molecules with high affinity and specificity to cTnI target molecules, which is a specific cardiac biomarker for the diagnosis of acute myocardial infarction. The FET sensor was exposed to cTnI molecules spiked in PBS buffer and was excited with a 5 V_{pp} AC signal at 1 MHz frequency to generate ACET flow. The sensor's performance was evaluated by measuring drain-source current (I_{DS}) versus drain-source voltage (V_{DS}) and reporting sensitivity defined as the ratio of the difference in channel current before and after probe-target binding to the channel current before probe-target binding. As illustrated in Fig. 3.8D, transient response of the sensor with and without the AC bias showed significant improvements when AC bias and the subsequent ACET are present.

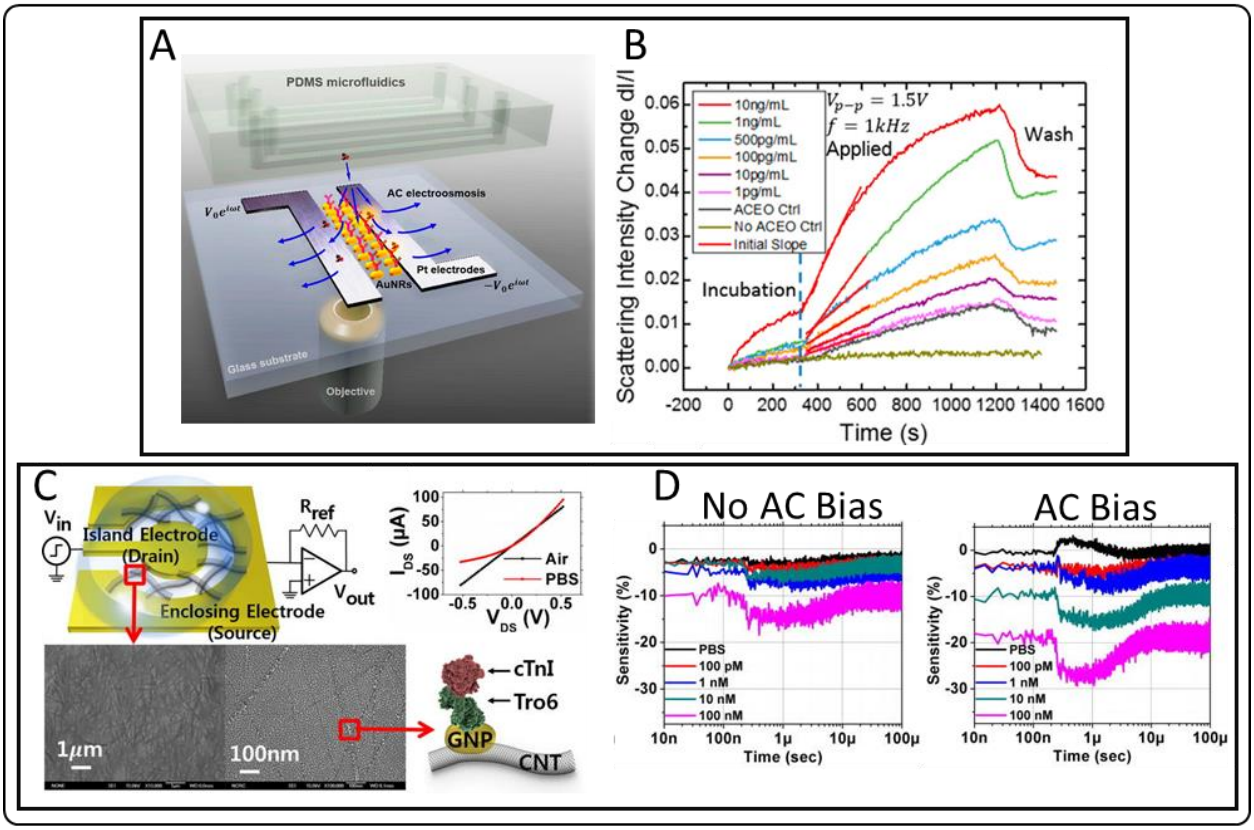

Figure 3.8. AC electrokinetic for mixing and mass transfer enhancement in biosensing platforms. A. Schematic illustrating ACEO-enhanced LSPR imaging. **B.** Real-time scattering light intensity signals for 50% human serum matrix spiked by IL-1β at concentrations of 1 pg/mL to 10 ng/mL. The AC signal was applied after an incubation period of 5 min. Reprinted with permission from Ref.[143] Copyright (2017) American Chemical Society. **C.** Schematic diagram of the carbon nanotube network (CNN) FET sensing platform. The SEM images show the CNN (thick black lines) decorated with gold nanoparticles (small white dots). **D.** Experimental results of the transient measurements of cTnI solutions under no AC bias and AC bias. Reprinted with permission from Ref.[146] Copyright (2016) American Institute of Physics.

3.4 Electrohydrodynamics

Despite studying the same subject of electrically induced flows, electrokinetics and electrohydrodynamics concepts have developed separately, focusing on different types of liquids and interfaces. Indeed, the "electrohydrodynamic" term has interchangeably been used to broadly refer to various electrokinetic phenomena discussed in the earlier sections. Electrokinetic studies generally focus on the fluid motion that arises from the electroosmotic slip of a liquid electrolyte across a neutral dipolar interface called electrical double layer. On the other hand,

electrohydrodynamic effects involve multiphasic systems with poorly conducting neutral fluids and solids, whose interface accumulates a net charge corresponding to the applied electric field.[148-149] Alternatively, it can be said that the field of electrohydrodynamics is concerned with charged monopolar interfaces and neutral fluids of constant permittivity and (small) conductivity.[58]

The theoretical foundations of electrohydrodynamics were first laid out by Taylor and Melcher in their "Leaky dielectric" model and experiments performed on oil droplets in a uniform electric field.[58] The Taylor-Melcher model describes electrohydrodynamic phenomena in poorly conducting liquids in the absence of any volumetric charges. The liquids are analyzed as dielectric materials that nevertheless possess finite ohmic conductivities. Consequently, rather than satisfying the interfacial condition of electric-displacement continuity, relevant to dielectric liquids, the electric-field distribution is set at steady-state by the condition of electric-current continuity. With the jump in the electric displacement, the field distribution satisfying the latter condition is generally accompanied by a non-zero surface-charge distribution at the interface. The electrical shear forces acting on the charged interface then give rise to fluid motion. The governing equations describing electrohydrodynamics emerge from equations describing the conservation of mass and momentum, coupled with Maxwell's equations. A detailed mathematical description of the leaky dielectric model is described in pioneering texts by Taylor and Melcher[58] and Saville.[150]

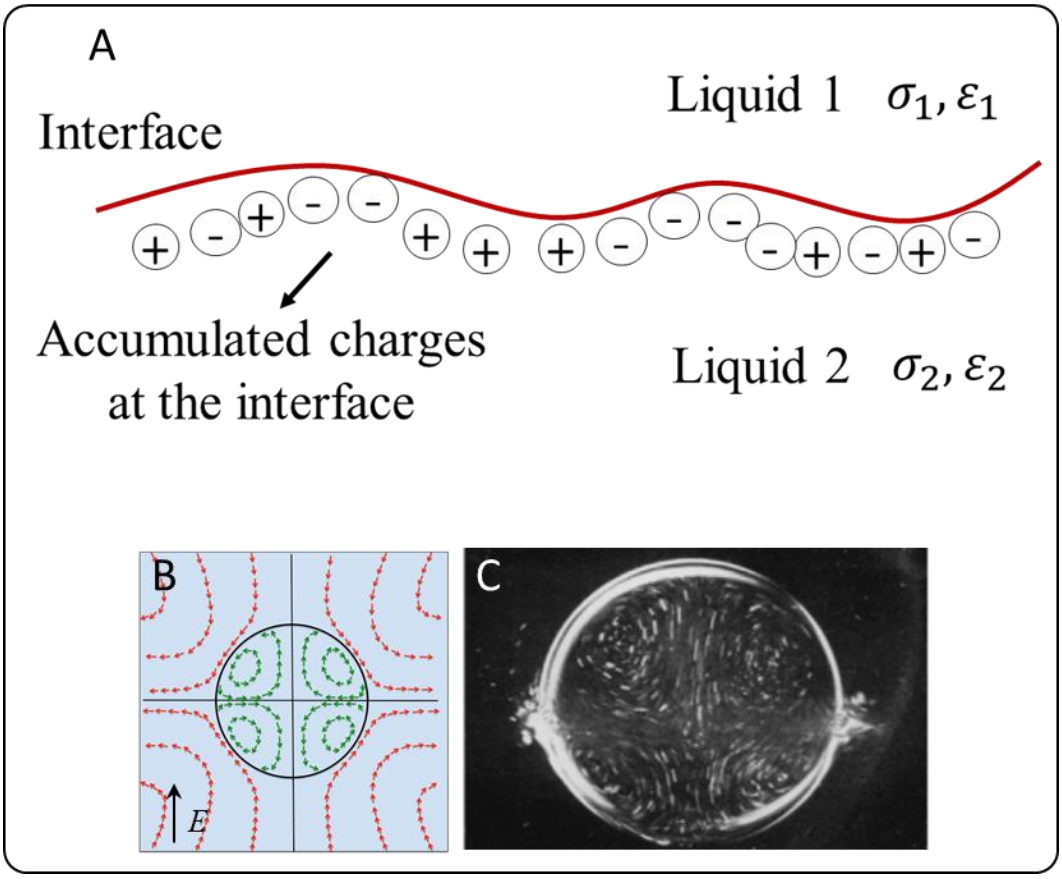

Figure 3.9 A. Schematic depiction of a generic interface between two fluids of different electrical parameters. **B.** Predicted theoretical and **C.** experimental flow patterns in an oil droplet in the presence of a uniform electric field. Reprinted with permission from Ref.[151] Copyright (1966) Royal Society of London.

3.4.1 Electrohydrodynamic Applications

Applications of electrohydrodynamics are abundant such as electrospraying and electrospinning,[152-155] micromixing,[3, 156-160] coalescence of droplets,[161] inkjet printing,[162] and enhancement of heat and mass transfer.[163] Perhaps the most investigated electrohydrodynamic processes are electrospinning and electrospraying for wide applications in tissue engineering,[154, 164] drug delivery systems,[153, 155] food industries,[152] and direct writing.[165] Both electrospinning and electrospraying processes use similar setup consisting of a spinneret (a nozzle coupled with a syringe containing a polymer solution), a high voltage source and a counter electrode collector. As the solution in the syringe is pumped out, a DC high voltage is applied between the nozzle and the

collector electrode. Application of a large DC voltage (1 ~ 30 kV or 0.5 ~ 3 kV/cm) generates a cone-shaped deformation of the solution drop due to surface tension, known as Taylor cone. The large electrostatic force then produces electrically charged jets out of the polymer solution. As the solvent evaporates in time, the nano/microscale structures are deposited on the collector. The physical characteristics of the polymer solution determines whether the electrified jet breaks up into drops (electrospraying) or remains as filament (electrospinning). Electrospraying and electrospinning have mostly relied on high voltage DC power sources to fabricate micro or nanostructures with a body of literature describing and exploiting the effect of various parameters like syringe flow rate, voltage amplitude, ambient temperature, humidity and solution's concertation, viscosity and conductivity. Although the use of AC electric fields for electrospinning/spraying is sparse, it can provide the means for the synthesis of electroneutral microscale drops with potential applications in pulmonary drug delivery bioparticles.[166-167]

Micromixing is another prominent application of electrohydrodynamics that has been implemented for mixing of laminar streams with differing electrical parameters by several studies. Those studies showed experimental validation for the mixing of liquid systems with different conductivities and permittivities.[3, 157, 168] However, the experimental characterizations have remained limited to the theoretical understanding of flow behavior. Further studies are required to explore the electrohydrodynamic effect for the true on-chip applications.

Chapter 4. Alternating Current Dielectrophoresis of Biomacromolecules: the Interplay of Electrokinetic Effects

The theoretical concepts in dielectrophoresis, AC electroosmosis and AC electrothermal discussed earlier were published in the Journal of *Sensors and Actuators B: Chemical* that are presented in the current chapter. Furthermore, this chapter elaborates on the utility of dielectrophoresis and other electrokinetic phenomena for the manipulation and handling of biomacromolecules.

Journal publication:

Modarres, Paresa, and Maryam Tabrizian. "Alternating current dielectrophoresis of biomacromolecules: The interplay of electrokinetic effects." *Sensors and Actuators B: Chemical* 252 (2017): 391-408.

4.1 Abstract

Dielectrophoresis is a powerful technique for the handling of bioparticles ranging in size and structure from cells to proteins. The surge in experimental research on dielectrophoretic manipulation of biomacromolecules in recent years demands a renewed consideration of tools leveraging micro- and nanofabrication for dielectrophoresis. One aspect of such platforms that is less explored in literature is the volumetric electrokinetic flows generated in response to an alternating current potential at the electrode-electrolyte interface such as AC electroosmosis and AC electrothermal flows. Those electrokinetic flows may interfere with the dielectrophoretic force in certain experimental conditions. Hence, we provide a concise overview of the theory behind those phenomena and point out the key parameters for consideration and optimization. We further summarize experimental techniques for dielectrophoresis of the two most extensively studied biomacromolecules, DNA and protein molecules, and elaborate on their potential applications in separation and mass transport for biosensing devices.

Keywords *- AC Dielectrophoresis, AC Electrokinetics, Biomacromolecule Dielectrophoresis*

4.2 Introduction

Transport of biomacromolecules within microfluidic channels is central to many state-of-the-art lab-on-a-chip devices. Among many techniques that exist for on-chip processing of molecules including optical, [169-170] acoustics[171-172] and magnetics,[173-174] electrical methods remain an indispensable tool for studying the physics of biomacromolecules and for applications in separation, mass transport and sensing. Application of electric fields to an analyte gives rise to several phenomena collectively referred to as electrokinetics. Electrokinetic techniques, especially those that operate under AC conditions, can potentially enable very robust and accurate platforms for particle handling and sorting. AC excitation mitigates or eliminates many challenges inherent to DC fields including particle aggregation and bubble and ion contaminant generation due to Joule heating and Faradaic reactions at the electrode-electrolyte interface.

An important electrokinetic effect that emerges due to the application of inhomogeneous electric fields to polarizable particles is dielectrophoresis, first introduced by Pohl.[175] Since the early explorations by Pohl, the development of dielectrophoretic platforms for bioparticle manipulation has enormously increased, particularly with the progress in instrumentation and microfabrication technologies. In early experiments, mostly microscale cells were the subject of dielectrophoretic experiments. However, with the advancements in the fabrication technology and the development of new nanomaterials providing the capability for the generation of highly magnified electric fields, dielectrophoretic manipulation of biomacromolecules has gained renewed attention. As an indicator, Fig. 4.1 illustrates a notable uptrend in journal publications on the topic of biomacromolecule dielectrophoresis since the first demonstration of DNA DEP in 1990. The majority of early publications were aimed at the experimental validation of gaining control over molecules by trapping, orienting and stretching of molecules on pre-defined surfaces.

Most recent publications, however, tend to favor applying DEP for sensing applications overcoming diffusion-limited transport of analytes. Regardless of detection type, DEP-mediated analyte concentration enables significant improvement of the limit of detection (LOC) at much shorter timescales compared to the incubation techniques.

Aside from dielectrophoresis that acts on particles, other electrokinetic phenomena, such as AC electroosmosis and AC electrothermal flows, may coexist in a system. Those phenomena that induce volumetric hydrodynamical flows can be comparable to or even overpower the dielectrophoresis force in certain experimental conditions. Thus, the presence and significance of such volumetric flows must be considered in the design of dielectrophoretic experiments. In this chapter, we reviewed the available literature exploring dielectrophoresis of DNA and protein molecules, the two extensively studied biomacromolecules. Additionally, the theory behind ACEO and ACET flows is introduced and further elaborated on within the framework of discussed applications.

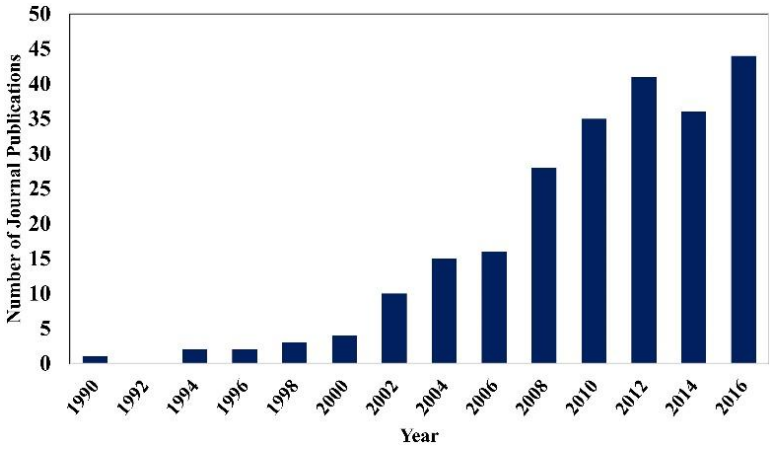

Figure 4.1 Biannual journal publication trend on dielectrophoresis of biomacromolecules. The data represents publications on and before December 1, 2016.

4.3 AC Electrokinetics Theory

Microfluidic platforms leveraging the DEP force for bioparticle manipulation are often complex systems with a multifaceted interaction of body and volumetric fluid forces. As most dielectrophoretic platforms contain electrodes in contact with an electrolyte, one must be aware of other electrokinetic forces taking place at the interface of a conducting surface and a liquid. Two important electrokinetic phenomena often encountered in DEP experiments are 1) fluid motion due to double layer polarization or ACEO, and 2) fluid flow due to Joule heating or ACET. Neglecting such bulk fluid actuation results in the erroneous and skewed interpretation of observed effects in DEP experiments. In this section, we concisely cover such electrokinetic dynamics and relate their significance to practical applications concerning the dielectrophoresis of biomacromolecules. For a more comprehensive treatment of the subject, one should refer to texts by Morgan and Green,[52] Chang and Yeo[53] and Jones.[176]

4.3.1 AC Dielectrophoresis: Particle Polarization Induced

Dielectrophoresis is the motion of dielectric or polarizable particles induced by a non-uniform electric field. Charged molecules such as DNA, RNA and protein as well as neutral particles such as cells can be polarized in an inhomogeneous electric field and undergo a net dielectrophoretic force. In a medium with finite polarizability, under an applied field, the bound charges temporarily redistribute to induce a dipole or many poles within the medium. If the field is uniform, the Coulomb force due to charge redistribution balances out to a zero average. However, if the field is non-uniform, the charge distribution is uneven, leading to a non-zero Coulomb force. The dielectric force acting on a dipole moment p with polarizability α in an inhomogeneous field with a non-zero gradient tensor ∇E is:

$$F_{DEP} = (p.\nabla)E \tag{4.1}$$

$$p = \alpha E \tag{4.2}$$

An immediate observation of this equation reveals that no net force acts on a dipole when $\nabla E = 0$, or when the electric field is uniform. For an idealized spherical particle of radius r with electrical permittivity of ε_p suspended in a medium of electrical permittivity of ε_m, the time average DEP force is:

$$\langle F_{DEP} \rangle = 2\pi\varepsilon_0\varepsilon_m r^3 Re[f_{cm}]\nabla|E|^2 \tag{4.3}$$

$$f_{cm} = \frac{\varepsilon_p^* - \varepsilon_m^*}{\varepsilon_p^* + 2\varepsilon_m^*}, \varepsilon^* = \varepsilon - j\frac{\sigma}{\omega} \tag{4.4}$$

where f_{cm} is the Clausius-Mossotti or Maxwell-Wagner factor, ε^* the complex permittivity, σ the conductivity and ω the angular frequency. The presence of the dielectric force is strongly dependent on the relative polarizability of the medium with respect to that of the suspending particle represented by the Clausius-Mossotti factor. The sign of the real part of f_{cm} determines force domination towards maximum or minimum of an electric field. If this factor is positive, the DEP force is referred to as positive DEP and the particle is moved towards the maximum of the electric field. If it is negative, the DEP force is referred to as negative DEP and the particle is repelled away from regions of the highest field intensity.

A key observation of the analytical solution in eq. 4.3 is that the time average DEP force is dependent on particle volume, non-uniformity of the electric field and relative polarizability of particle compared to the medium. The electric field amplitude square dependence implies that both DC and AC fields can induce a DEP force. However, under DC conditions, the existence of electrophoretic motion may be an undesired effect. Furthermore, DC currents cause Faradaic reactions at the electrode-electrolyte interface leading to the generation of bubbles and unwanted

reactions. Additionally, the dipole moment assumption may not hold for certain conditions. In reality, significant higher-order moments may occur for non-spherical particles or highly non-uniform electric fields, which lead to observable differences in particle motion.[177-178]

It is important to note that the average DEP force in eq. 4.3 only applies to homogeneous spherical particles. For structurally inhomogeneous bioparticles such as cells, the complex structure of the cell is reduced to a homogenous cytoplasm and a membrane with effective permittivity and conductivity values.[59] Unlike cells, the polarization mechanism of macromolecules is a complex subject, rendering modeling and estimating a dielectric constant very challenging. This difficulty is attributed to the complex dependency of polarization mechanism on the macromolecule's conformational and topological variations.[60] For many practical situations, however, precise knowledge of the dielectric constant is not necessary. Average polarizability values that entail major conformational contributions and solvent-macromolecule interfacial effects will suffice. Average polarizability values in the bulk solution are determined using dielectric and impedance spectroscopy, [62-64] dielectrophoresis[65-67] and time domain reflectometry[68] techniques.

For negatively charged DNA molecules, the widely accepted polarization mechanism is the counter-ion polarization.[179] Counter-ions are positively charged ions within the solvent that are recruited to the DNA's surface. Upon application of an electric field, the negative DNA molecule and positively charged counterions atmosphere move in opposite directions aligning with electric field lines giving rise to DNA-counterion polarization (Fig. 4.2). This polarization exists only on time scales shorter than the relaxation time of counterions. At longer times, migration of oppositely charged ions neutralizes the DNA-counterion structure and a dipole moment ceases to exist. In proteins, a dipole moment is generated due to polar bonds and charged groups in the polypeptide

backbone and the amino acid side chains.[64] Moreover, solvent-protein interactions and polarization of electrical double layer attribute to the protein's overall dipole moment.

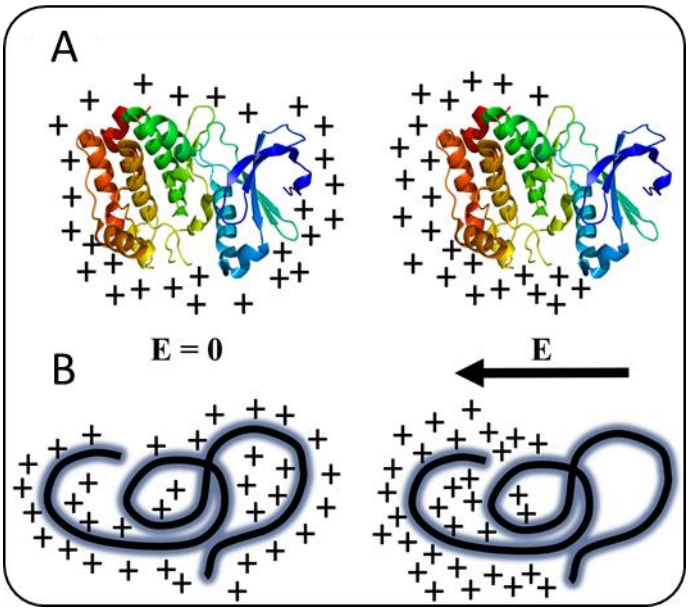

Figure 4.2 Schematic illustration of counterion distribution around a macromolecule in the absence and presence of an electric field. **A**. A negatively charged protein, and **B**. A DNA molecule. Upon application of an electric field, the counterion cloud redistributes to align in the direction of the electric field causing the counterion-macromolecule complex polarization. For clarity, negative charges on the macromolecules are not shown.

4.3.2 AC Electroosmosis: Double Layer Polarization Induced

AC electroosmosis lies under the broader category of induced-charge electro-osmosis (ICEO), where net fluid flow is generated by the polarization of electrical double layer due to the potential at a conducting surface. A simple approach to understanding ACEO flow is to consider a pair of planar electrodes that are biased at positive and negative AC voltages. In one half-cycle, the electric potential at electrodes drives counter-ions by electro-migration from the bulk electrolyte to the surface of electrodes. As the double layer charges, the electric field lines start to have an oblique angle to the electrode surface (especially at the edges) as opposed to being perpendicular before charging takes place. Thus, the tangential electric field component produces flow within

the double layer fluid that generally points inward from electrode edges. In the next half-cycle, the force magnitude and direction remain unchanged since both electrode potential and double layer change polarity. As a result, a time-averaged Maxwell force is generated which points from the inner electrode space at the edges to the electrode surface, giving rise to an electro-osmotic slip velocity.[180-181]

In many experimental studies, asymmetric electrode pairs or very wide symmetric electrodes are exploited to converge particle from fluid bulk to a stagnation point near the electrodes. At the stagnation point, the application of a low-range force field like positive dielectrophoresis can trap particles. The stagnation point of a symmetric pair of electrodes of width *L*, separated by a distance *d* is obtained using:[53]

$$x = \pm\sqrt{\frac{1}{2}\left[\left(L + \frac{d}{2}\right)^2 + \left(\frac{d}{2}\right)^2\right]} \tag{4.5}$$

For the case of very wide electrodes (Fig. 4.3), for which the electrode width is much larger than the inner electrode spacing ($L \gg d$), the stagnation point is at the golden mean, $x = \pm L/\sqrt{2}$ from the edge of the inner electrode spacing.[53]

There are some key features of ACEO flows that need to be considered for the design of electrokinetic devices. First, the AC electro-osmotic vortices can change directions under certain conditions. This phenomenon referred to as flow reversal ACEO typically happens at moderate to high voltages (several volts) at a frequency range of 10-100 kHz.[182] One explanation for flow reversal at lower frequencies is Faradaic charging as opposed to capacitive charging, where ions are generated or consumed at the electrolyte-electrode interface.[183] The mechanism for flow reversal at high frequencies, however, is attributed to steric effects of ion crowding in the double layer.[182] Secondly, the ACEO flow rapidly decays with increasing salt concentration with almost

no flow for bulk salt concentrations above ~10 mM.[120] Thus, only very dilute solutions or water is used in AC electroosmotic experiments.

4.3.3 AC Electrothermal Flow: Joule Heating Induced

Electrothermal flow is another important electrohydrodynamic phenomenon that often competes with ACEO flow. Electrothermal flow arises due to induced spatial inhomogeneities in fluid electrical conductivity and permittivity. In ACEO flow, the net charge density at the electrolyte-electrode interface is in equilibrium. However, in ACET, the flow is primarily driven by dynamic variations in net charge density induced by gradients in fluid properties. The mechanism behind ACET flow is attributed to local Ohmic heating at the electrode surface which gives rise to local temperature increase. This, subsequently, leads to local conductivity increase and permittivity decrease. To maintain charge conservation, the local electric field must be lowered. However, according to Gauss's law, reduction in the local electric field necessitates the existence of a local charge density.[121] Hence, this leads to variations in net charge density generating an electrostatic body force. For an incompressible fluid, the expression for the electrical force per liquid unit volume is: [51]

$$\bar{f_E} = \rho_q \bar{E} - \frac{1}{2}\bar{E}^2 \nabla \varepsilon \tag{4.6}$$

where ρ_q is the volume charge density and ε is the media permittivity. Considering Gauss law $\rho_q = \nabla \varepsilon . \bar{E}$ and using electric field perturbation expansion ($\bar{E} = \bar{E}_0 + \bar{E}_1$) with $\bar{E}_0$ as the applied field and $\bar{E}_1$ as the perturbation field, the time-average force becomes:[51]

$$\langle \bar{f_E} \rangle = \frac{1}{2} Re \left[\frac{(\sigma \nabla \varepsilon - \varepsilon \nabla \sigma).\bar{E}_0}{\sigma + j\omega\varepsilon} \bar{E}_0^* - \frac{1}{2}|E_0|^2 \nabla \varepsilon \right] \tag{4.7}$$

$$\bar{E}_0(t) = Re\left(\bar{E}_0 e^{j\omega t}\right) \tag{4.8}$$

There are some key points to note for ACET flows. Most importantly, the flow is strongly dependent on media conductivity and is significant for electrolyte conductivities exceeding 100 mS/m.[53] At high enough conductivities, higher voltages lead to stronger flows due to a stronger temperature gradient. Comprehensive ACET studies by Green and colleagues suggest that there is a crossover frequency (f_c) for planar electrode pairs with infinitesimal gaps where the ACET flow reversal takes place. At low frequencies ($f < f_c$), the flow moves from the inner electrode gap to the center of the metal surface similar to ACEO flows. At higher frequencies ($f > f_c$), the flow is reversed and streams up in the center of the gap. The crossover frequency is given by:[51]

$$\omega_c = 2\pi f_c \approx \frac{1}{\tau}\left(2\frac{\left|\frac{\partial\sigma}{\sigma\partial T}\right|}{\left|\frac{\partial\varepsilon}{\varepsilon\partial T}\right|}\right)^{\frac{1}{2}} \tag{4.9}$$

where $\tau = \frac{\varepsilon}{\sigma}$ is the relaxation time of liquid and T the temperature. For most protein/DNA dielectrophoretic experiments operating at a few mS/m conductivities, ACET flow is negligible at low frequencies (<100 kHz). However, at high conductivities (in the range of S/m), the existence of ACET flow should be considered.

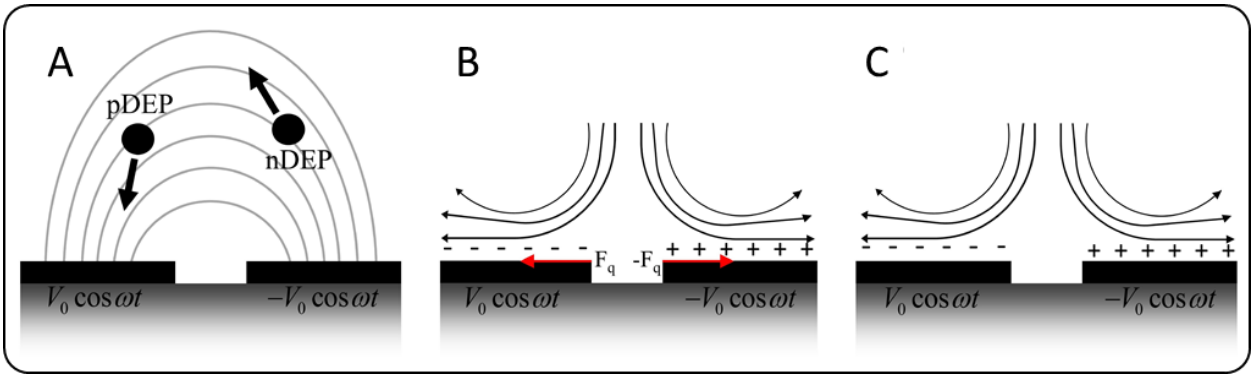

Figure 4.3 A. Dielectrophoresis mechanism demonstrating pDEP and nDEP. **B**. AC electroosmosis flow near the electrode surface. **C.** AC electrothermal flow near the electrode surface for frequencies below the crossover frequency defined by eq. 4.9. At higher frequencies, the flow reverses moving up from inner electrode spacing.

4.4 Biomacromolecule Manipulation Using AC Dielectrophoresis

Dielectrophoretic manipulation of micron-scale bioparticles such as cells is well established and critiqued by several reviews.[15, 184-189] Scaling down to sub-micron biomacromolecule dimensions, however, poses challenges for employing dielectrophoresis. The main challenge arises from the fact that the DEP force has a cube relation with the particle's radius. Thus, influencing sub-micron particles demands very intense electric fields restricting device scaling to a few micrometers or nanometer dimensions when small voltages are desired. Furthermore, the lack of complete understanding of biomacromolecules' polarization mechanism and its relation to conformational variations within analytes subjected to electric fields add to the complexity of the problem. Nevertheless, advances in micro/nanofabrication technology have resolved many difficulties for the generation of highly magnified electric fields either through the employment of nanomaterials or nanofabrication techniques. However, the polarization mechanism of biomacromolecules remains the subject of many ongoing studies and reviewed for DNA[179] and protein molecules.[64-65]

Two major platforms are adopted for DEP of biomacromolecules relying on either embedded electrodes (electrode-based or eDEP) or insulating structures (insulating DEP or iDEP). In eDEP designs, electrodes are in direct contact with the analytes and are often operated under AC conditions. Metallic electrodes, however, are prone to electrolytic reactions at the electrodes and generation of bubbles causing clogging of the fluidic channel. Although high-frequency voltages significantly reduce electrolytic reactions and bubble generation, such problems are eliminated by the placement of electrodes outside of the working fluidic channel. This method is referred to as electrodeless or insulating DEP. In iDEP platforms, insulating structures made of SU-8, PDMS, or glass are spaced in between the electrodes to disturb the field lines and generate

field gradients.[190] The placement of electrodes outside the working fluidic channels nevertheless demands excitation with voltages in the order of a few hundred volts for adequate field intensities.

In this section, we review microfluidic platforms for the manipulation of DNA and protein molecules that mostly involve trapping, stretching (for DNA molecules) and the differential motion of the molecules leading to separation. In this text, we use the words trapping, focusing and concentrating interchangeably, which refer to localized attraction or collection of molecules. Furthermore, we mostly refrain from reporting specific values of voltage parameters as the optimum operating conditions strongly depend on the device geometry and media properties. Instead, a comprehensive list of the reported dielectrophoretic platforms is tabulated in Table 4.1, reporting the type of devices and molecules as well as voltage and media parameters.

4.4.1 Trapping and Focusing

Trapping and focusing, in this context, refers to reversible capturing of molecules as opposed to permanent anchorage or immobilization achieved with certain surface chemistries. Movement and dislocation of molecules are typically visualized by fluorescent microscopy using dyes like YOYO-1, TOTO-1, DAPI, PicoGreen, Rhodamine Green and Alexa-647. Both positive and negative DEP are demonstrated for the accumulation of biomacromolecules. However, the application of AC electric fields at positive DEP frequencies is by far the most common approach for trapping of DNA and protein molecules.

A. Micro- and Nanoscale Planar Electrodes

Washizu et al. pioneered early experiments on dielectrophoresis of biomacromolecules exploiting planar metal strips and interdigitated electrodes using Aluminum (Al) or Gold (Au) material.[191-195] Planar microelectrodes are fabricated using conventional photolithography and thin film deposition techniques such as e-beam evaporation. Remarkably, protein and DNA molecules

accumulated only at the edges of planar electrode strips due to very high-intensity electric fields present at the sharp electrode boundaries. Planar microelectrodes may not provide the strongest field gradients necessary for trapping of sub-micron particles. However, the effective DEP force can substantially be increased by combining DEP with the long-range ACEO or ACET flows. The ACEO and ACET flows generate volumetric fluid actuation to transport molecules to the proximity of electrodes, where the trapping DEP field is strong enough to capture the molecules. For instance, the coupling of ACEO and dielectrophoresis is demonstrated to enhance DNA/Protein concentration in asymmetric concentric electrodes,[196-198] very wide symmetric electrodes[199] and T-shaped electrodes.[200-201]

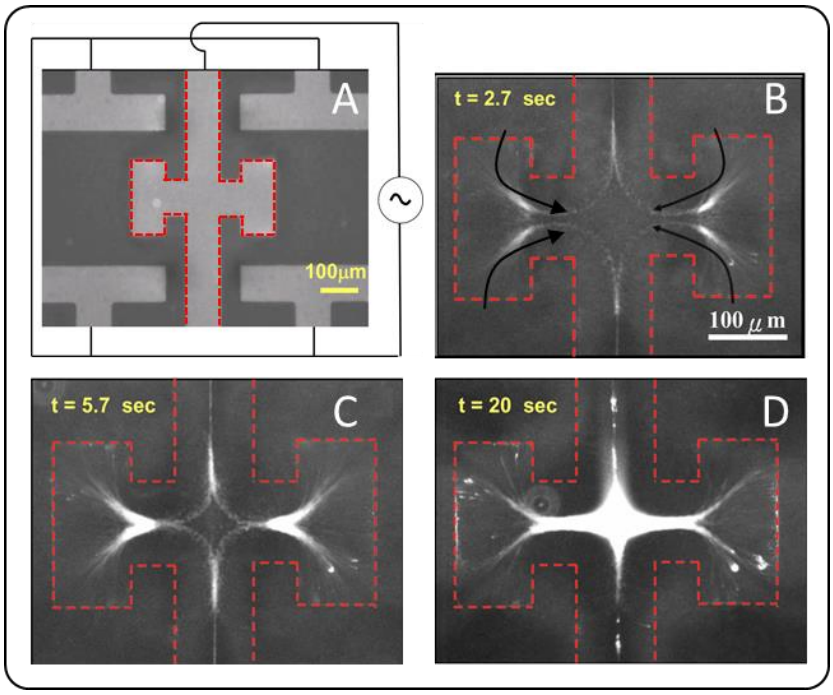

Figure 4.4 DNA focusing with asymmetric T-shape Au electrodes using 1 μg/mL DNA solution with 20 V_{pp} @ 1 kHz voltage: **A.** unbiased electrodes **B-D** snapshots of DNA focusing due to converging ACEO flows (illustrated in B with black arrows) and pDEP. Reprinted with permission from Ref.[201] Copyright (2010) American Chemical Society.

Nanoscale electrodes/nanogaps mitigate the challenge of generating high-intensity field gradients without the use of high voltages demanding costly amplifier instruments. Noting the

DEP force scaling with the systems characteristic length as $F_{DEP} \sim V^2/L^3$, it is evident how scaling down will help in enhancing the DEP force without increasing the voltage. Nanoscale electrodes/gaps are commonly fabricated using e-beam lithography.[202-204] For instance, Tuukkanen et al. studied trapping efficiency of nano- and microscale DNA molecules ranging in length from 27 to 8400 base pairs (bp) using nano-fingertips with nanogaps of 100 nm separation.[205] Trapping efficiency of the DNA fragments signifies that longer DNA molecules undergo larger DEP forces, consistent with the theory. Thus, smaller voltages are needed to influence larger DNA molecules.

B. Micro- and Nanoscale Conducting Tips

Freestanding tips are manufactured using IC compatible bulk micromachining of silicon and the subsequent metallization of the tip using conventional thin film deposition techniques. Kalyanasundaram et al. fabricated gold-coated microtips and utilized them for the extraction of human genomic DNA from the buccal swab and saliva samples. The extracted DNA yield characterized by qPCR was comparably the same as a commercial kit. However, DNA extraction using the microtip was much faster with fewer steps and no need for centrifugation and use of toxic reagents.[206-207]

Nanotweezers are another exciting candidates for precise manipulation of biomolecules. A nanotweezer consists of two opposing tips with an adjustable nanogap. Unlike single tip structures, the two opposing tips help to capture and release bioparticles of various dimensions by electrostatically actuating the tips. For the first time, Hashiguchi et al. demonstrated the fabrication and application of Si nanotweezers with aluminum-coated tips for DNA manipulation.[208-211] While one tip was fixed, the second tip was electrostatically actuated for a tunable gap with a maximum displacement of 2.5 microns and a resolution of 0.2 nm. The DNA molecules were attracted to the nanotweezer gap and formed bundles of DNA with diameters ranging from 10 nm to more than

100 nm for DEP duration of ~10 s and ≥ 1 min, respectively. Formation of DNA bundles within the nanotweezer gap produced a pronounced shift in the resonance frequency and Q-factor of the device.[208] For single-molecule manipulations, however, the presence of strong ACET flows diverging from the nanotweezer gap onto the nano-tip surfaces prevented DNA capture in very dilute DNA samples. Electrothermal flows require a longer time to fully develop compared to dielectrophoresis, which is an instantaneous effect. Therefore, keeping the voltage on at periods smaller than the electrothermal response time in a pulsatile fashion enables single-molecule trapping at the nanotweezer tip. The electrothermal response time can be estimated experimentally by measuring the velocity of fluorescently labeled DNA molecules in response to DEP signal period.

One-dimensional materials like carbon nanotubes and nanowires are also utilized to structure nanotips of various dimensions and compositions.[212-217] Nanofibrils of different lengths and diameters are constructed from other nano-fiber dispersions by the application of AC dielectrophoresis to the solution and pulling a metallic tip in contact with the dispersion.[218-219] AC dielectrophoresis assists in the aligned assembly of pre-formed nano-fibers dispersed in water at the tip of the metallic coil while the coil is slowly pulled out of the solution. The diameter of the fibril is controlled by adjusting the drawing rate, the electric field gradient, the diameter of the metallic tip and the concentration of the nanofibers in dispersion.[219] The length of the nano-fibril is adjusted by varying the distance the metallic tip travels. Yeo et al. used a composite nano-fibril made of silicon carbide (SiC) nanowires and single-walled carbon nanotubes (SWCNTs) for capturing Au nanoparticles, oligonucleotides and DNA molecules leveraging positive dielectrophoresis and capillary action. The carbon nanotubes within the nanowire bundle provide structural integrity and mechanical stability of the nano-fibril.[220] Furthermore, the authors reported

non-specific binding of DNA molecules onto the carbon nanotube, which hinders the application of bare carbon nanotube as reusable bio-probes. One solution to prevent non-specific binding involves the coating of the nanotip with PDMS, for which DNA molecules readily desorb from the tip in boiling water.

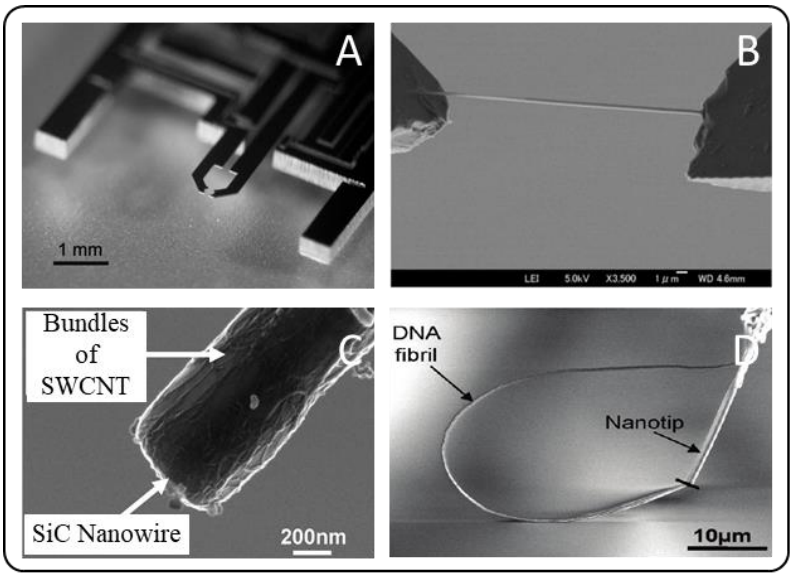

Figure 4.5 SEM images of **A**. Si nanotweezer. Reprinted with permission from Ref.[221] Copyright (2011) IOP Publishing, **B**. DNA bundle with a mean diameter of 380 nm at the nanotweezer gap. Reprinted with permission from Ref.[210] Copyright (2008) Elsevier, **C**. Single SiC nanowire wrapped by SWCNT bundles and **D**. DNA fibril at the end of nanotip in C. Reprinted with permission from Ref.[213] Copyright (2009) American Chemical Society.

C. iDEP Platforms

Electrodeless AC DEP is employed for concentrating of single- and double-stranded DNA molecules,[222] trapping DNA molecules for polarization studies[66] and separation applications.[67] Dielectrophoretic trapping of protein molecules within gaps of insulating microstructures is mainly explored under DC conditions[223-226] and recently under AC fields.[227-228] Unlike DNA molecules, the need for highly magnified electric fields is more pronounced for protein molecules due to their smaller dimensions and polarizability. Thus, various iDEP platforms have emerged benefiting

from nanoscale fingertip insulators with nanogaps for protein concentration at the vicinity of the nanogaps.[226-230]

Chou and colleagues validated a new approach for fast and highly amplified protein focusing utilizing nanoscale insulating fingertips with 30 nm gaps operating under AC only and DC offset AC signals.[228] Fig. 4.6 illustrates the device structure and operation under various excitation conditions. Under pure AC signal, proteins were either attracted to or dispersed from the nanogaps due to positive and negative DEP, respectively. However, when the AC voltage was offset with a DC voltage, fast and highly amplified streptavidin protein enrichment to more than 10^5-fold in 20 seconds was realized (higher amplification compared to pure AC signal). Competition of the DEP force and electroosmosis flow with electrophoresis (EP) created a damming effect for protein concentration. While the negative DEP and electroosmosis were pushing the molecules away from the constriction, the electrophoretic force was towards the constriction, giving rise to a focusing band within the proximity of a highly-concentrated field at the center of constriction.

Nanopipettes used in conventional scanning ion conductance microscopy (SICM) are also explored as an electrodeless tool for programmable capture and release of biomolecules.[231-235] Glass nanopipettes with nanoscale inner radii (~50 nm) are fabricated using laser-based pipette pullers. Similar to SICM, a reference electrode inside the nanopipette and a working electrode within the bulk electrolyte generate an electric field with the highest field gradient present at the conical nanopipette tip. The nanopipette is backfilled with DNA solution and brought into contact with a bath solution in a glass-bottomed dish. DNA molecules are retained or released by pulsing the voltage at low frequencies. For example, pulsing at 10 Hz with a positive voltage duration of 30 ms results in the release of 150 ± 20 DNA molecules with each pulse.[231] Studying electrokinetic

forces involved in the release of DNA molecules reveals a combination of electrophoretic, electroosmotic and dielectrophoretic flows at play at the tapered tip of nanopipettes.[232] While the DEP flow is always towards the tip of the nanopipette due to positive DEP, the combined electrophoresis and electroosmosis flows change direction with the positive and negative cycles of the AC frequency (Fig. 4.7). At the negative half cycle, the DEP force and the resultant electrophoresis and electroosmosis force are in the opposite direction at the tip inside the pipette leading to accumulation of molecules at the tip. However, at the positive half cycle, all flows are directed towards the tip driving the release of molecules.

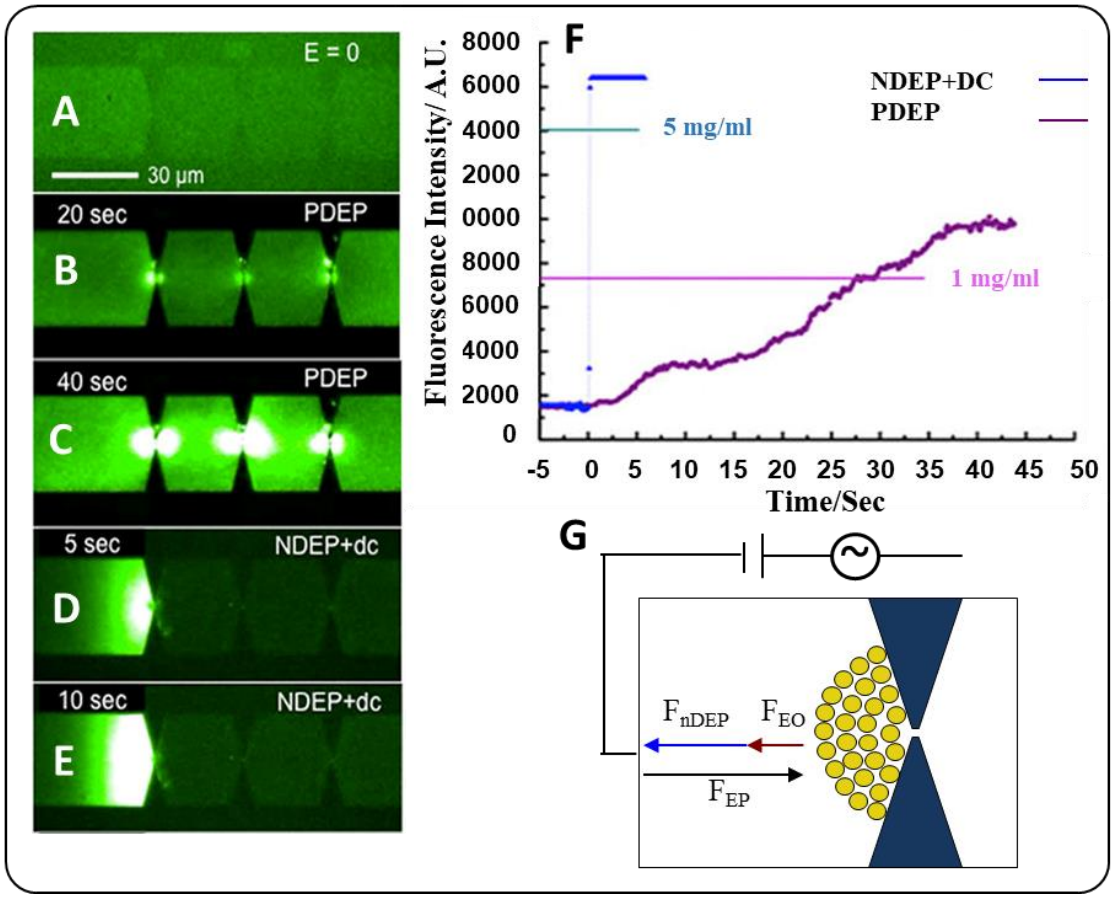

Figure 4.6 Protein concentration through the balance of electrokinetic forces: **A.** Alexa-488 streptavidin (10 µg/mL) loaded in the chip by capillary force. Trapping with pDEP **B**. 20 and **C**. 40 s after application of 473 V_{pp}/cm at 10 kHz (signal amplified 4 × 10^4- fold to 3.3 × 10^9 V_{pp}/m at the constriction). Trapping with nDEP + DC using V_{AC} + V_{DC} **D**. 5 and **E**. 10 s after application

of 214 V_{pp}/cm at 1 MHz with 1.5 V/cm DC bias (with the positive voltage at the right side of the channel). **F**. Protein enrichment intensity plot corresponding to operating conditions as for fluorescent images with the same initial concentration of 10 μg/mL. Reprinted with permission from Ref[228]. Copyright (2012) American Chemical Society. **G**. Force balance when DC offset AC signal is applied with EO and EP representing electroosmosis and electrophoresis forces, respectively. Adapted with permission from Ref.[228] Copyright (2012) American Chemical Society.

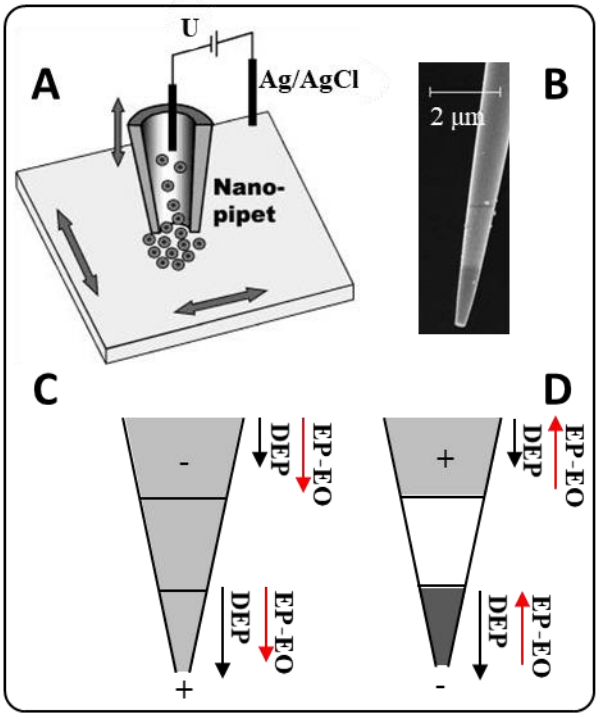

Figure 4.7 . A. Nanopipette setup with reference and working electrodes inside the pipette and bath, respectively. Reprinted with permission from Ref.[233] Copyright (2002) American Chemical Society. **B.** SEM image of nanopipette tip. Electrokinetic forces at **C.** negative cycle causing the release of molecules and **D**. positive cycle leading to the depletion (white section) and capture zones near the tip. Adapted with permission from Ref.[232] Copyright (2004) Elsevier.

D. Carbon Electrodes

Carbon and glass-like carbon are attractive candidates for leveraging the advantages of the electrode-based and insulating DEP platforms. Platforms relying on carbon electrodes require much lower voltages compared to iDEP devices and have better electrochemical stability compared to metals. A few tens of volts is sufficient for generating adequate DEP fields in contrast to hundreds of volts in iDEP platforms. Additionally, carbon has excellent mechanical properties

and biocompatibility.[236] Martinez-duarte et al. implemented a 3D carbon microfluidic platform for dielectrophoretic manipulation of DNA molecules demonstrating both pDEP and nDEP.[237-238] The carbon electrodes are fabricated by pyrolyzing a patterned organic precursor like SU-8. Pyrolysis refers to high temperature (~900° C) decomposition of an organic substance in an inert ambient like nitrogen, forming gas, or vacuum. Pyrolysis of widely used photoresists such as SU-8 and AZ positive tone resists offers a cost-effective and simple approach to fabricate 3D and planar carbon electrodes, respectively.

The increased surface area of the 3D carbon electrodes enables the presence of sufficiently strong AC electroosmotic flows. As Green and colleagues reported, it is possible to generate AC electroosmotic flow using asymmetrical 3D carbon electrodes.[239] The potential use of ACEO microvortices in symmetric and asymmetrical 3D carbon electrodes can be explored for more efficient capture of molecules under the influence of DEP force.

E. Light-activated Electrodes

Another method to deviate from conventional dielectrophoretic platforms is light-activated electrode patterns that provide a reconfigurable approach to electrode design.[240-242] The general device structure includes an aqueous medium sandwiched between two electrode layers on glass facing the medium. One electrode layer is a conductive thin film such as Platinum[240] or Indium tin oxide (ITO),[242] and the other metal layer is a photoconductive film like hydrogenated amorphous silicon (a-Si:H) deposited on a conductive film such as highly doped ZnO[240] film or ITO.[242] Local illumination of hydrogenated amorphous silicon increases the conductivity of illuminated area by several orders of magnitude creating a virtual electrode. Selective illumination of the photoconductive surface and application of an AC field between the conductive film contacts on each layer produce a field gradient and drives the electrokinetic motion of molecules.

Hoeb et al. demonstrated positive dielectrophoresis of λ-DNA implementing this technique.[240] Furthermore, Wu and colleagues provided large scale patterning of nanoparticles on the photoconductive surface benefiting from long-range ACEO and electrothermal flows and local trapping force by DEP. As described, the device structure involved an ITO layer and a photoconductive layer. The photoconductive layer consisted of a glass substrate covered with ITO, n+ a-Si:H and undoped a-Si:H. Nanoscopic particle recruitment and concentration were achieved by applying an AC signal to the two ITO layers at charge relaxation frequency of the double layer and light-patterning of the photoconductive surface using a digital micromirror device. The slip velocity due to the interaction of electric field lateral component with the double layer and local heat gradient generated due to absorption of light in the a-Si:H film gave rise to ACEO and electrothermal flows helping to recruit nanoparticles in the bulk.

4.4.2 Stretching

Inside cells, DNA-protein interactions require constant twisting, bending and stretching for regulatory, enzymatic and structural functions. Insight into the mechanical and elastic properties of DNA helps to uncover the underlying mechanism behind such ubiquitous DNA-protein interactions as well as improving current DNA's physical models. Electrostatic stretching of DNA using non-uniform electric fields involves two steps: 1) immobilization and anchorage of fluorescently dyed DNA onto microfabricated surfaces, and 2) elongation and stretching of DNA along field lines.

Electrode-based platforms with embedded planar electrodes are commonly utilized for stretching of DNA molecules between adjacent electrode fingers. Washizu and colleagues pioneered immobilization and dielectrophoretic stretching of DNA molecules on microfabricated aluminum electrodes. In their early work, they demonstrated DNA stretching along field lines and

recoiling at the presence and absence of electric fields (0.1-2 MHz, 10^6 V/m), respectively.[191, 193, 243-244] Furthermore, they demonstrated enzymatic cutting of freestanding λ-DNA bridged in between floating aluminum electrodes. In floating electrodes structure, metal strips were placed in between two large periphery electrodes that were connected to a power supply. This structure subsided the electrothermal flows and enhanced the chance of DNA bridging between metal strips. The dielectrophoretic DNA stretching provided a platform for deterministic enzymatic dissection where the desired enzyme is fixed on a latex microsphere, and optical tweezers are employed for enzyme-bead complex manipulation and pressing against the loosely stretched DNA.[245] This method could offer an improvement to conventional biochemistry experiments where DNA-cutting enzymes and DNA molecules are mixed in a solution, and the enzymatic cutting of DNA is purely a stochastic process.

While aluminum electrodes are successful for DNA stretching, the binding mechanism and location-specific immobilization of DNA molecules to untreated aluminum surfaces are not well understood and characterized. Conversely, chemical immobilization of DNA molecules provides orientation-specific anchorage of DNA.[246] Other groups performed similar electro-stretching of DNA molecules using alternative immobilization techniques.[247-250] These immobilization techniques include: (a) thiol-modified DNA in conjunction with gold electrodes,[247, 250] (b) (3-aminopropyl) triethoxy silane-functionalized DNA with silicon dioxide surfaces,[250] and (c) biotinylated DNA in conjunction with asymmetrically modified interdigitated gold electrodes (interdigitated fingers are alternatively treated with streptavidin and electro-polymerized poly-scopoletin film).[248] Long λ-DNA molecules commonly used for DEP experiments, however, do not readily conform to thiol-gold or avidin-biotin chemistries. The steric hindrance significantly diminishes the binding efficiency of long DNA strands (> 2 kbp). To enhance DNA binding

efficiency, the gold electrode surface is functionalized with short single-stranded DNA oligonucleotides bound to the surface via a thiol group. Then, the λ-DNA molecules with a single-stranded overhang sequence complementary to the surface-bound oligonucleotide are hybridized and thus immobilized on the surface.[249]

Electrostatic DNA elongation is a strong function of voltage and frequency. As illustrated in Fig. 4.8, higher voltages reinforce DNA elongation. Furthermore, elongation increases with increasing frequency until it reaches a plateau at which further frequency increase suppresses stretching.[251-253] Aside from electrical signal frequency and intensity, surface and bulk solution properties play a significant role in DNA stretching within microfabricated devices. Highly hydrophilic surfaces decrease the stretching efficiency while surfaces treated with high silane (trimethylchlorosilane) concentrations improves DNA elongation. This effect is most likely due to decreased nonspecific adsorption of DNA on the silane-treated surfaces compared to their more hydrophilic counterparts.[254] Surface roughness is another factor to consider; rough surfaces hinder the DNA immobilization and its ability to stretch. Annealing the electrodes at high temperatures (~450° C) alleviates surface roughness and enhances DNA stretching.[254]

In many DNA's electrostatic stretching studies, DNA elongation parallel to field lines is purely attributed to polarization-induced forces. However, one might speculate other mechanisms being involved such as AC electroosmosis and electrothermal fluid flows in parallel strip microelectrodes that reinforce DNA's stretching. This speculation arises from the fact that the free end of DNA has a higher chance of falling back (i.e. antiparallel to field lines) towards the electrode with tethered end under positive DEP, where the electric field intensities are maximum.[255] Thus, the existence of a supplementary bias force provided by electric-field-induced fluid flow parallel to the electric field lines appears essential for DNA's elongation and bridging

between parallel strips.[251] More studies are required to understand the role of AC-induced flows in the initiation of dielectrophoretic stretching of DNA molecules. Furthermore, the influence of AC-induced flows on the frequency-dependent stretching of DNA molecules can be the subject of further investigations.

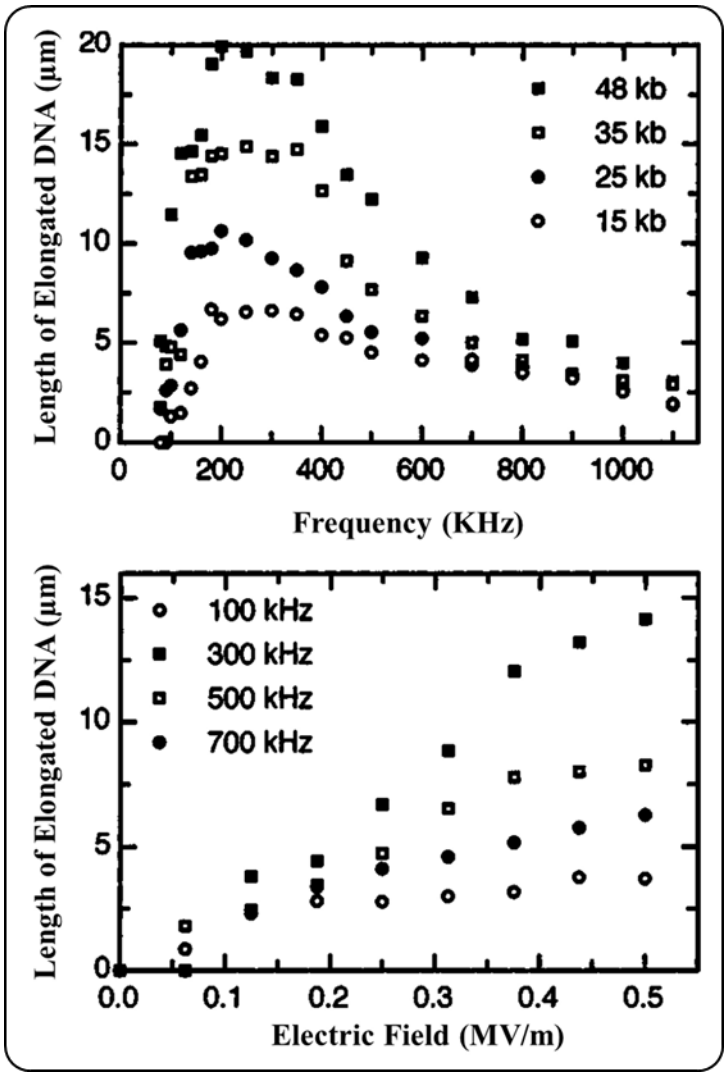

Figure 4.8 DNA elongation across a 40 μm wide gap: (**Top**) frequency vs. elongation at a field intensity of 0.5 MV/m for various lengths DNA molecules and (**Bottom**) electric field intensity vs. elongation for a 35 kb DNA molecule. Each value is the average of three experiments. Reprinted with permission from Ref.[252] Copyright (2004) AIP Publishing LLC.

4.5 Applications of Biomacromolecule Dielectrophoresis

Separation and mass transport are the two mainstream applications of biomacromolecules manipulations. Most reported separation platforms demonstrated sorting of DNA molecules, and protein separation is less explored. This is most likely due to smaller protein dimensions, making device design and operation much more challenging. Additionally, protein molecules must significantly vary in dimension to observe a discernable dielectrophoretic response. Nevertheless, the dielectrophoretic sorting of protein molecules could be an interesting and stimulating area of research. Surface patterning is an emerging application of dielectrophoretic capture and release of molecules utilizing nanopipettes. Glass nanopipettes discussed in section 4.4.1 are promising tools for direct patterning and programmed delivery of DNA and protein molecules down to single-molecule level.[233]

4.5.1 Separation

Separation of biomacromolecules using novel passive or active microfluidic techniques is gaining considerable attention within the scientific community in recent years. Active techniques like dielectrophoresis can potentially introduce new modes of separation based on polarizability rather than electrophoretic mobility in conventional electrophoresis techniques enabling size-based separation and detecting conformational variations. Washizu and colleagues first introduced the concept of dielectrophoretic chromatography for the separation of DNA molecules with a 22 bp-48 kbp size range.[256-257] Their device was made of a long chain of corrugated interdigitated electrodes on a glass substrate with a flow channel on top. The samples were fed in with constant flow velocity and were exposed to the DEP field along the channel. The separation mechanism relied on the repeated trap and release of molecules in response to positive and negative DEP.

After many cycles, particles of different size and polarizability elute from the device at different times.

More recently, several studies demonstrated the feasibility of dielectrophoretic DNA separation by coupling of electrophoresis and dielectrophoresis adapting electrodeless DEP platforms. In such techniques, an AC signal is superimposed on a DC signal. While the DC signal provides a net propelling force based on electrophoresis, the AC signal generates DEP traps at insulating microstructures. The key mechanism for differentiation is the competition between the polarization-dependent trapping and thermal randomization leading to the escape of molecules from the DEP traps. For instance, Ros and colleagues demonstrated the bimodal separation of DNA molecules employing an electrodeless DEP platform consisting of arrays of insulating PDMS microstructures.[66-67] The DNA molecules were driven through the main channel containing microstructures by application of a small DC voltage of 12 V. An AC signal of much higher amplitude (~200 V) was superimposed on the DC voltage for the dielectrophoretic trapping at the gaps between microstructures. The separation mechanism depended on average escape times from the DEP traps due to thermal activation. The average escape times and hence the average migration velocities were polarization-dependent and vary for different length DNA molecules. Using this technique, λ-DNA and T2-DNA, as well as ccc 7-kbp plasmid and its 14-kbp dimer, were separated longitudinally along the channel (Fig. 4.9A and 9B).

In a different study (Fig. 4.9C and 4.9D), bimodal and continuous-flow separation of DNA molecules and DNA-protein complexes were realized using an electrodeless platform with an insulating curved ridge crossing the width of a microfluidic channel.[258-259] This device was similarly biased with a DC offset AC signal. The molecules were driven straight through the channel by the application of appropriate DC voltages. At the ridge, the molecules either passed

over the ridge unaffected or deflected sideways. The deflection mechanism stemmed from the polarization-induced DEP traps at the ridge and the gradual escape due to the Brownian or thermal motion. In this platform, the molecules were separated laterally across the channel, facilitating collection at different output channels.

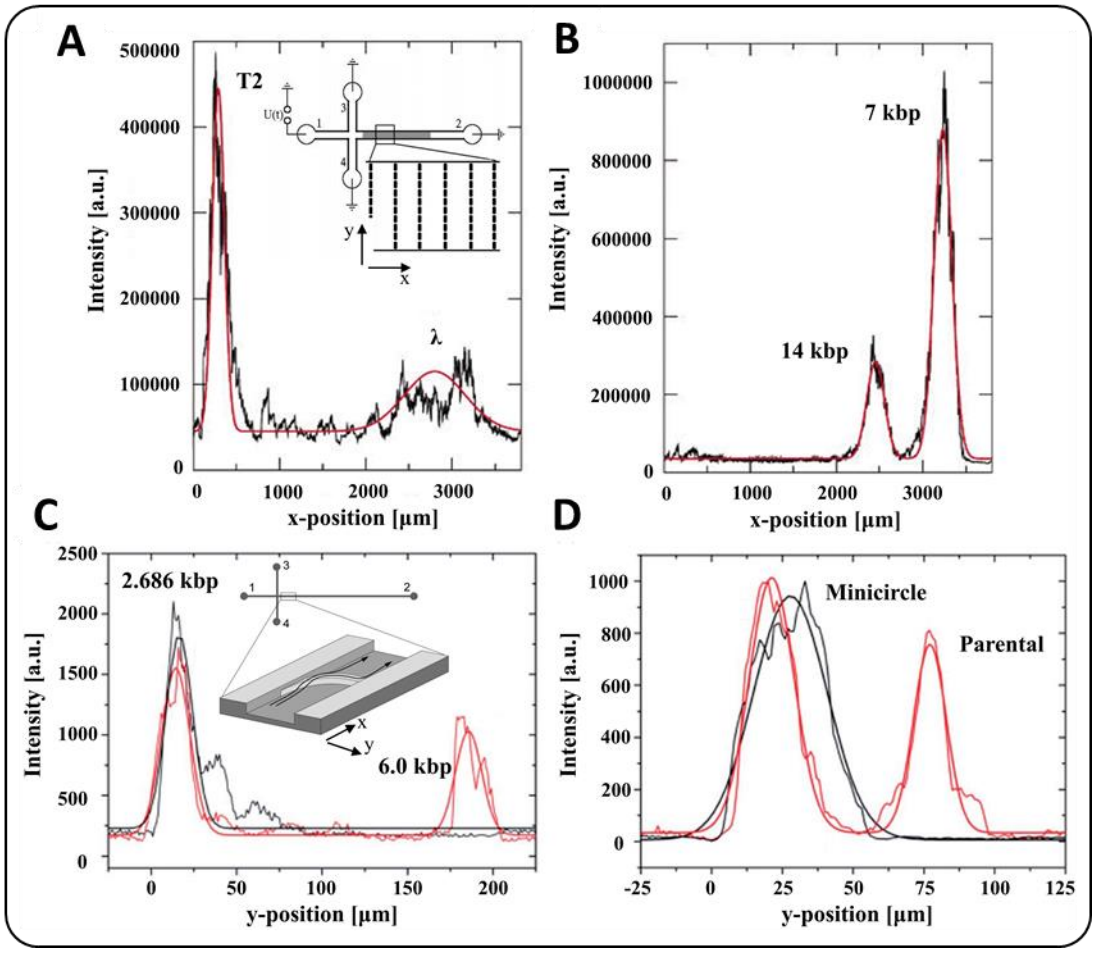

Figure 4.9 Steady-state electropherograms showing the bimodal separation of DNA molecules based on thermally-activated escape time from dielectrophoretic traps in constriction gaps in the direction of the electrophoretic force. **A**. Separation of λ- and T2-DNA (V_{DC} = 12V, V_{AC} = 189 V, $\boldsymbol{\omega}$ = 60Hz). The inset shows the device with the array of microstructures in the gray region. **B**. Separation of 7-kbp ccc-plasmid DNA and its 14-kbp dimer (V_{DC} = 12V, V_{AC} = 240 V, $\boldsymbol{\omega}$=60Hz). Reprinted with permission from Ref.[67] Copyright (2007) American Chemical Society. **C**. Separation of 2.686 kbp and 6.0 kbp DNA molecules (V_{AC} = 650 V, $\boldsymbol{\omega}$ = 350 Hz). The inset shows the device with the curved ridge crossing the channel. **D**. Separation of Minicircle (2.247 kbp) and parental (6.766 kbp) DNA (V_{AC} = 200 V, $\boldsymbol{\omega}$ = 350 Hz). Reprinted with permission from Ref.[258] Copyright (2012) Royal Society of Chemistry.

4.5.2 Mass Transport

The ever-increasing trend in miniaturization of microfluidics and sensor devices, while favorable in many aspects, poses serious limitations in mass transport, especially at the nanoscales. Diffusion-limited accumulation of molecules at the sensing element adversely affects the advantages of miniaturization for reducing sample volume and enhancing the signal-to-noise ratio. Analytical studies and experimental validation of steady-state flux to a sensing surface suggest two important findings: 1) analyte transport limitations are more significant than signal transduction limitations for femtomolar detection limits reported for bioassays, 2) directed transport of analytes is needed for detection limits beyond picomolar for practical timescales.[260]

Assisted delivery of molecules to the sensing surface can be achieved through magnetic or electrical fields. In magnetic techniques, the target molecules are labeled with magnetic beads and transported to the sensing element using magnetic field gradients. However, magnetic labeling adds to the device complexity and processing time. In recent years, dielectrophoresis has been widely exploited as the method of choice for assisted delivery of target analytes to overcome limitations of diffusive transport without additional processing or labeling steps. Both setups with embedded electrodes or insulating structures are leveraged for directed delivery of molecules. In DEP platforms with embedded electrodes, planar electrodes are typically located nearby the sensing surface and operation under positive DEP frequencies facilitates analyte accumulation. Similarly, in iDEP or electrodeless platforms, an insulating constriction is structured within the vicinity of the sensing element and a voltage is applied to electrodes at the periphery of the device or the inlet/outlet.

Dielectrophoretic or hybrid electrokinetic delivery platforms with electrodes improve detection limit and time in many biosensing devices including surface-enhanced Raman spectroscopy,[95] impedance sensing,[261-263] capacitive sensing,[264] plasmonic sensing,[265-266] nanopore

sensing ,[92] SWCNT-based immunosensing,[267] Silicon nanowire field-effect transistor (FET)[268] and fluorescent immunosensing.[269] Likewise, iDEP platforms with insulating constrictions are adapted for improved delivery of analytes in poly-silicon nanowire field-effect transistors[270] and electrochemical immunoassays.[271]

Impedance spectroscopy sensors employing concentric or interdigitated electrodes can generate a DEP field without design modifications to implement electrodes or insulating structures. In addition, other AC electrokinetic flows can be coupled with DEP with the proper choice of frequency and medium conductivity. ACEO and ACET flow vortices potentially improve the transport of analytes and dispersion of non-target molecules. Cheng et al. utilized one circular sensing electrode and two concentric rings as the electrochemical counter and reference electrodes for the application of DC biased AC signal to facilitate analyte concentration followed by multiple AC frequencies to observe impedance shifts.[261] Analytes were brought into a stagnation point with a long-range ACEO flow, where the DEP force retained the analytes at the sensing surface. IgG-protein A detection time of about 90 seconds was 100 times faster than conventional incubation on the same device. Additionally, detection limits down to 200 pg/mL were 30 times lower than the incubation method. Similarly, Chuang et al. implemented concentric interdigitated electrodes for the dielectrophoretic trapping of antibody-conjugated nanoprobes to the electrodes followed by antigen detection using impedimetric electrochemical sensing.[262] In a different study, Kim et al. utilized parallel interdigitated electrodes and biased the electrodes for negative dielectrophoresis.[263] By employing negative dielectrophoresis, Amyloid-beta 42 and prostates specific antigen molecules concentrated at the functionalized electrode's inner spacing. Active concentration of molecules led to a resistance shift and enhanced detection sensitivity and limit of detection.

Directed delivery utilizing DEP and ACEO has greatly reduced the detection time in novel plasmonic sensing platforms. For instance, Barik et al. demonstrated the modification of a plasmonic nanohole array to apply an AC signal for electrokinetic delivery of analytes to the rim of nanoholes (Fig. 4.10A). The device consisted of a gold nanohole array on a glass substrate topped with a tape spacer and an ITO cover glass. An AC signal (6 V_{pp} @ 1 kHz) applied between the gold nanoarray and the ITO electrode provided field gradients for the entrapment of bovine albumin serum (BSA) at the nanoholes. DEP-mediated accumulation of BSA molecules enabled exceptionally fast detection times with concentrations as low as 1 pM within a few minutes. The detection time is estimated about 1000 times faster compared to a purely diffusive transport mechanism.

Another exciting and emerging application of DEP-assisted analyte transport is in surface-enhanced Raman spectroscopy (SERS).[95] Fabrication of Ti nanoelectrodes with 10 nm gaps provides a platform for delivery of analytes to the nanogaps using AC DEP (Fig. 4.10C). The nanogaps act as hotspots for Raman spectra recording, current/conductance measuring, as well as fluorescence imaging. The AC signal is mainly responsible for dielectrophoretic recruitment of molecules, and a small DC bias contributes to the net current. Electrical excitation of nanogap generates a significant shift in Raman spectra which is virtually non-existent in the absence of an electric field (Fig. 4.10D).

Finally, DEP is leveraged for enhancing DNA hybridization kinetics.[272-274] For instance, Swami et al. fabricated a constriction-based device to localize DNA hybridization at the constriction.[272] The method was capable of enhancing DNA hybridization kinetics by ten folds for concentrations as small as 10 pM. The DNA hybridization was monitored in real-time utilizing a two-potential electrochemical probe. Cheng et al. applied a similar concept of localized DNA

hybridization and assisted DNA transport to amplify hybridization kinetics.[273] First, carboxylated silica nanobeads were functionalized with oligonucleotides complementary to the target DNA. Then, the nanobeads assembled into a cusp-shaped nano-colloid by a focusing dielectrophoretic force using converging electrodes. Lastly, hydrodynamic flow and dielectrophoretic focusing accelerated transport of fluorescently-tagged target DNA to the cusp-shaped nano-colloid for hybridization.

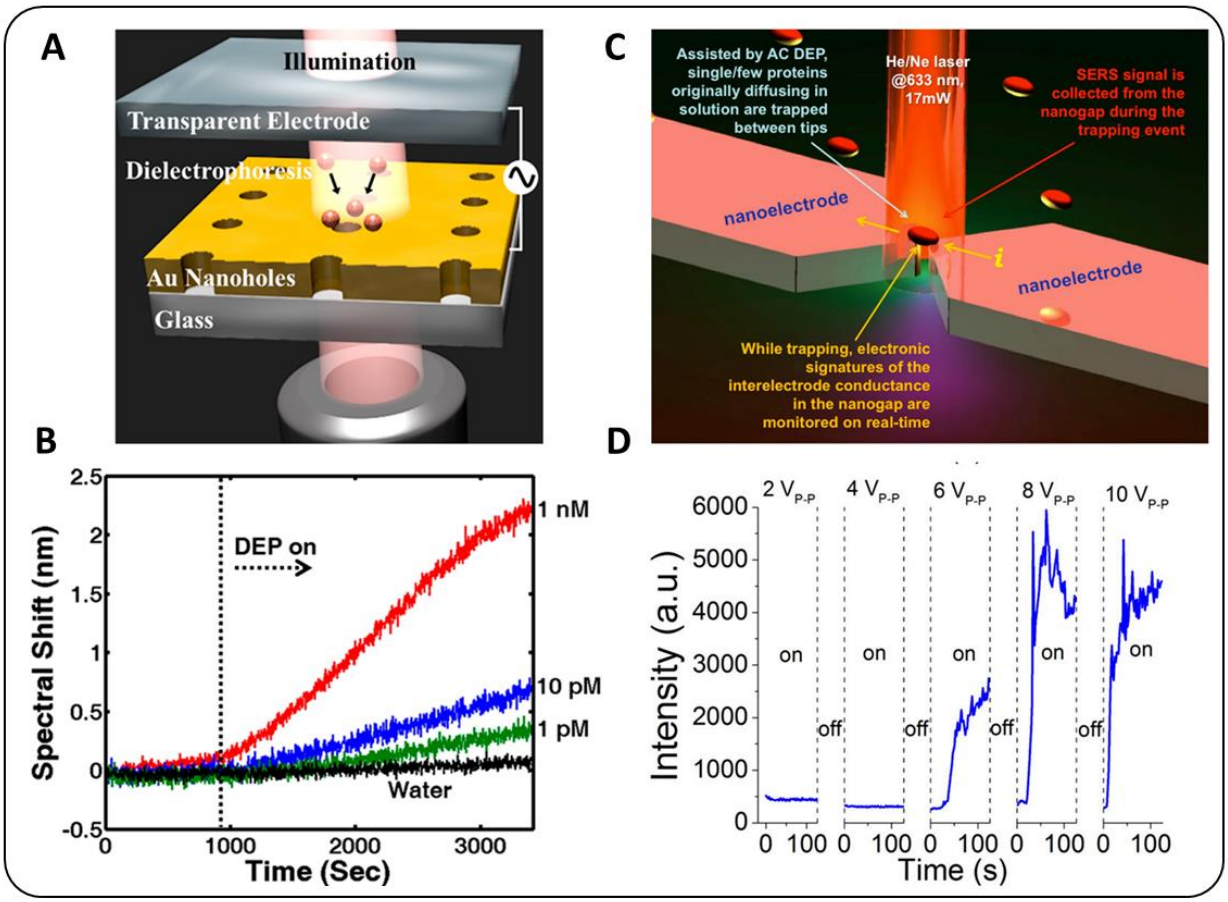

Figure 4.10 A. Experimental setup for gold nanohole array plasmonic sensing. By application of an AC voltage between the ITO electrode and the gold array, analytes were concentrated at the rim of nanoholes. The setup was illuminated with a tungsten-halogen lamp and the transmitted light through nanoholes was collected with a 2× objective. **B**. The time-resolved spectral shift for various concentrations of BSA and control experiment (water). A voltage of 6 V_{pp} with a frequency of 1 kHz was applied after 15 min of baseline. Reprinted with permission from Ref.[266] Copyright (2014) ACS. **C**. Nanoelectrodes with a nanogap as a hotspot for SERS. **D**. Raman spectral shift

for different AC voltages at 1 MHz frequency and DC bias of 100 mV. At off state, both AC and DC components of voltage were off. Reprinted with permission from Ref.[95] Copyright (2014) American Chemical Society.

4.6 Effects of Electric Fields on DNA and Protein Molecules

Application of high-intensity electric fields raises important concerns related to exposure of biomolecules to electric fields which may lead to either structural changes in biomolecules or altering the binding affinity of molecules affecting immunosensing platforms. While there is plenty of research articles exploring DNA and protein handling under electric fields, there are not many fundamental studies on the effect of electric fields on these biomolecules. The effects of electric field on biomolecules are of two nature: direct electric field interaction and the secondary electric field effect of Joule heating. Based on the current literature, typical electric field intensities of the order of 10^6 V/m employed in dielectrophoretic platforms are not large enough to trigger structural damage to DNA or protein molecules. For instance, several theoretical studies indicated the mutagenic effects of high-intensity electric fields on DNA but those changes are reported to happen at field intensities in the order of 10^9 V/m.[275-276] Additionally, there is evidence for protein conformational variations under intense electric fields, which may alter their binding affinity.[277-279]

Passage of electric currents through a conductive medium leads to power dissipation causing Joule heating. Temperature elevation due to Joule heating is an important parameter affecting antibody-antigen interaction kinetics. Temperatures a few degrees beyond the physiological temperature of 37˚C will lead to protein denaturation. Additionally, temperature variations below the denaturation temperature can alter the dissociation constant of protein-protein interactions.[280] The temperature dependency is mainly dominated by weak bonds involved in the interaction. For instance, temperature increase reduces the binding affinity of antibody-antigen

interactions that are exothermic (formation of hydrogen bonds and polar bonds). In contrast, for non-polar bonds or hydrophobic interactions, the strength of interaction increases with temperature increase.[281]

The Joule heating effect is more pronounced in insulating DEP platforms where the application of high voltages (a few hundreds of volts) across the medium is essential for observing electrokinetic effects. As suggested by recent studies, the temperature increase in iDEP devices employing high conductivity media can be a source of concern and special attention must be paid to the applied voltage, the size of constrictions, and media conductivity when designing such platforms.[227, 282]

4.7 Discussions and Future Direction

In this paper, we provided an overview of devices for DNA and protein dielectrophoresis. Table 4.1 compiles a comprehensive list of these platforms and their operating conditions. Most devices generate field intensities of the order of 10^6 V/m, and media conductivities vary extensively from a few μS/cm to 10^4 μS/cm. Moreover, a wide variety of dsDNA, ssDNA and protein molecules are represented in this table. λ-DNA (48 kbp), BSA (66 kDa) and streptavidin (52.8 kDa) are the most frequently explored model molecules in literature. Nevertheless, there is a growing trend for the dielectrophoretic manipulation of other submicron bioparticles like RNA,[283-284] DNA origami, [285-288] DNA templates[289] and neuropeptides,[290] and subcellular components such as microtubules [291-293] and actin filaments.[294-296] For example, Giraud et al. demonstrated collection and repulsion of 16S and 23S subunit ribosomal DNA, extracted from *E. Coli*, onto interdigitated microelectrodes over a wide frequency range of 3 kHz to 50 MHz.[283] Furthermore, a commercially available AFM tip was chemically and structurally modified to extract messenger RNA (mRNA)

from a single living cell.[284] This novel technique finds applications in the extraction of high purity mRNA for RT-qPCR experiments where access to pure and fresh mRNA is crucial.

Fabricating and handling DNA origami structures is an exciting and growing research field with potential applications in targeted drug delivery and molecular nanoelectronics. Any processing technique must preserve DNA origami's shape and structure and provide a template for orientation-specific positioning. For the first time, Kuzyk et al. demonstrated dielectrophoretic trapping of 2D rectangular DNA origami in nanogaps between nano-finger gold electrodes with optimal capture efficiency above 10 MHz at conductivities well below 1 mS/cm.[286] Additionally, thiol-gold chemistry and thiol modification of DNA origami facilitated the orientation-specific trapping. In a different study, an iDEP platform with an elliptical post array was developed for trapping of two DNA origami structures with identical sequences but very different topologies (6 helix bundle versus triangle). The triangular topology required higher field strength for trapping indicating lower polarizability. The study suggests that polarizability of DNA origami structures is dependent on many factors such as orientation parallel/perpendicular to the field, particle-particle interactions within the traps and DNA origami's geometrical configuration.

Likewise, dielectrophoresis has proven very useful in precise confinement and alignment of microtubules and filaments enabling novel platforms for investigating the interaction of microtubules and molecular motors in vitro. Experimental studies suggest that microtubules and actin filaments align themselves along the electric field lines. Aggregation of actin filaments in an end-to-end fashion was also noted in experiments by Asokan et al., signifying dipole-dipole interactions among filaments.[296] Also, the same study reported that DEP forces in the order of ~ 0.4 pN did not stall the motility of actin-myosin motor system.

While in most dielectrophoretic platforms, the dominant effect originates from the polarization-induced motion of particles, the presence of ACET and ACEO flows should also be taken into consideration for proper interpretation of observations. Like dielectrophoresis, the presence and magnitude of ACEO and ACET flows are a strong function of frequency, medium conductivity and electrode configuration. ACEO and ACET flow velocities as a function of media conductivity and frequency were calculated for planar electrodes (of the type presented in Fig. 4.3) and illustrated by Green and colleagues in Fig. 4.11.[297] In relative terms, ACET flow is often observed at high media conductivities or high frequencies (> 100 kHz) and ACEO is present at lower frequencies (<100 kHz) and media conductivities. For most biomacromolecule dielectrophoretic experiments, media conductivities in the order of μS/cm (refer to Table 4.1) undermine the existence of ACET flows. Thus, ACET strength is insignificant unless for high frequencies and voltages. Furthermore, ACET flow direction reverses at crossover frequency f_c (eq. 4.9) which is of the order of the inverse of charge relaxation time of the liquid [51]. Accordingly, ACET flow can act as a reinforcing or opposing force along with dielectrophoresis depending on the applied frequency and the device geometry.

As discussed, dielectrophoresis is rapidly emerging as a ubiquitous tool for the handling of biomacromolecules and subcellular components. It is expected that research studies undergo a surge in the application of dielectrophoresis to the less-explored nano-bioparticles based on the growing trend in published research on DNA/protein dielectrophoresis. Furthermore, the insightful inclusion of electrokinetic forces with dielectrophoresis can potentially be very useful for many novel applications. As evident from recent studies, DEP or hybrid electrokinetic systems have proven remarkably valuable to lower the limit of detection at much faster timescales in biosensing platform. Most importantly, AC electrokinetic effects are generated with a simple and inexpensive

implementation of electrodes with minimal analyte pre-processing steps to concentrate, separate and sense particles.

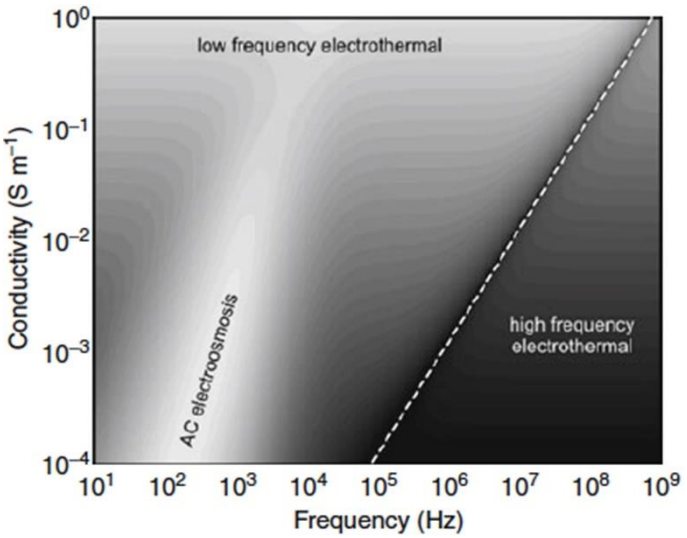

Figure 4.11 AC electroosmosis and AC electrothermal flows as a function of frequency and media conductivity. The white dotted line indicates when ACET changes direction. The velocities are plotted on a log grayscale and were calculated at 10 μm distance from the inner edge of a planar electrode pair at 1 V. Reprinted with permission from Ref.[297] Copyright (2012) Springer Science.

Acknowledgements

We would like to acknowledge the financial support from Natural Science and Engineering Research Council of Canada (NSERC) through CREATE training programs in ISS (Integrated Sensors and Systems) and CFS (Continuous Flow Systems) and CGS doctoral fellowship.

Table 4.1 Dielectrophoretic platforms for biomacromolecule manipulation.

Device	Type of Manipulation	Molecule	Media (μS/cm)	Frequency	Ref.
Al interdigitated microelectrodes	Trapping	Avidin, Concanavalin, Chymotrypsinogen, Ribonuclease A	Several	1 kHz - 1MHz	[192]
Au floating microelectrodes	Trapping	λ-DNA	1.8	30 Hz	[194]
Au interdigitated microelectrodes	Trapping	T2 phage, λ-DNA, Adenovirus, pBR322	NA	30 Hz	[195]
Au microelectrodes	Trapping	T4 DNA	150	1 kHz	[298]
Au microelectrodes	Trapping	λ-DNA	NA	1 kHz -1MHz	[299]
Au asymmetric microelectrodes	Trapping*	T4 DNA	150	1 kHz	[201]
Au microelectrodes	Trapping	Plasmid DNA pAT250 Avidin	800 14	20 MHz nDEP <9 MHz pDEP >9 MHz nDEP	[300]
Au quadruple microelectrodes	Trapping	λ-DNA BSA	10 10	100 kHz - 30 MHz 50 kHz - 5 MHz	[301]
Pt microelectrodes coated with a polyacrylamide hydrogel layer	Trapping	ss-DNA 40-45 kb, dsDNA >10 kbp 23-mer oligonucleotide	4400-11500	10 kHz	[302]
Pt microelectrodes coated with a polyacrylamide hydrogel layer	Trapping	Cell-free circulating DNA	7400 11500	10 kHz	[303]
Au sawtooth electrodes	Trapping	λ-DNA	70	100 kHz - 1MHz	[202]
Au electrodes	Trapping	R-phycoerythrin	20	1 MHz	[203]
Al interdigitated microelectrodes	Trapping	Circular pBlueScript dsDNA	250	10 kHz - 20 MHz	[304]
Au interdigitated microelectrodes	Trapping	pTA250 plasmid DNA	50	100 kHz – 20 MHz	[305]
Au fingertip nanoelectrodes	Trapping	dsDNA fragments: 27, 145, 444, 1065, 5141 and 8461 bp	20	1 MHz	[205]
Au fingertip nanoelectrodes	Trapping/ Stretching	dsDNA 414 bp	NA	750 kHz	[204]
Cylindrical W nanoelectrodes array embedded in SiO2	Trapping	BSA R-phycoerythrin IgG	NA 1 1	10 kHz 500 kHz 100 kHz	[306-307]
W interdigitated nanoelectrodes embedded in SiO2	Trapping	eGFP	<1	10 kHz -1MHz	[308]
ITO electrodes with SU-8 microcavities	Trapping	Gal-1 functionalized nano-probes LDH-B functionalized nano-probes	380~552 477~617	16~20 kHz 9~12 kHz	[269]
Pt interdigitated microelectrodes	Trapping/ Concentrating	Amyloid beta 42	NA	1 MHz (nDEP) 50 MHz (pDEP)	[263]
Ti nanoelectrodes (sub 10 nm gaps)	Trapping	R-phycoerythrin	15	1 MHz	[95]
Silicon Nanowire FET with coplanar Ti microelectrodes	Trapping*	PSA, CTB, BSA	NA	200 Hz (1mM PBS media) 47 Hz (10 μM PBS media)	[268]
SWCNT immunosensor with coplanar Au microelectrodes	Trapping*	cTnl	10	100 kHz	[267]
Concentric Au interdigitated electrodes	Trapping	Gal-1 functionalized nano-probes	0.9	100 kHz	[262]
Concentric Pt and Au electrodes	Trapping*	Protein A	150	800 Hz	[198]
Plasmonic Au nanohole array	Trapping	BSA	2.8	1 kHz	[266]
Gold nanocones	Trapping	BSA	NA	2.5 MHz	[265]
High aspect ratio Au microtips coated with poly-L-lysine (PLL)	Trapping*	λ-DNA	NA	V_{DC}/V_{AC}/V_{DC}+V_{AC} Most efficient at: V_{DC}+V_{AC} (10 MHz)	[206]

Carbon nanotube conjugated with a microelectrode	Trapping	dsDNA 145 and 1065bp	20	0.1-10 MHz	[212]
Nanotip (single SiC nanowire wrapped with SWCNTs)	Trapping	λ-DNA spiked in saliva Human genomic DNA in blood	NA	5 MHz	[217]
Nanotip (single SiC nanowire wrapped with SWCNTs)	Trapping	24b oligonucleotides (biotinylated)	960-1025	5 MHz	[214]
SiC and MWCNT Nanofibril tip	Trapping	λ-DNA	NA	5 MHz	[213]
Silicon nanotweezers	Trapping	λ-DNA	NA	1 MHz	[208]
Silicon nanotweezer	Trapping	λ-DNA	1.1	50 ms pulses of 1MHz	[211]
Nanopipette	Trapping/ Releasing*	Protein G ssDNA	NA	NA	[233]
Nanopipette	Trapping/ Releasing*	ssDNA 20-mer	NA	10 -1000 Hz pulses	[231]
Nanopipette	Trapping/ Releasing*	ssDNA 40-mer ssDNA 1kb Single-nucleotide triphosphate dCTP	NA	0.5 Hz	[232]
Gold-coated Nanopipette	Trapping*	dsDNA 10 Kbp	NA	V_{DC}+V_{AC} (0.5-0.4 MHz)	[92]
3D carbon electrodes	Trapping	λ-DNA	6	75 - 250 kHz (nDEP) <75 kHz (pDEP) Most efficient at: 10 kHz	[237]
Floating Au electrode coupled with insulating constrictions	Trapping*	ssDNA 150 bp	10^4	1 kHz	[309]
Poly-silicon nanowire FET coupled with insulating constrictions	Trapping	dsDNA 20 bp	1350	100 Hz - 2 MHz	[270]
Electrodeless (2.2 µm gaps)	Trapping/ Separation	λ-DNA, T2 phage, 7 and 14 kbp plasmid DNA	NA	V_{DC}+V_{AC} (60 Hz)	[67]
Electrodeless (1-20 µm gaps)	Trapping	T5 dsDNA, ssDNA (200bp)	10^6	500 Hz	[272]
Electrodeless (microscale gaps)	Trapping	Streptavidin	10^3 - 10^4	100 kHz	[227]
Electrodeless with 30 nm gaps	Trapping	Streptavidin PSA	16 ×10^4	V_{AC} (10 kHz) V_{DC}+V_{AC} (1 MHz) V_{DC} + V_{AC} (6 MHz)	[228]
Electrodeless with 150 nm gaps	Trapping	Streptavidin Phycoerythrin	700	60 Hz 20 Hz	[230]
Al interdigitated electrodes	Separation	6.6 kbp-48 kbp	250	1 MHz	[257]
Electrodeless with side ridges	Separation	6 kbp and 2.686 kbp Actinomycin D and 6 kbp DNA E.coli RNAP core Enzyme and 6 kbp DNA	NA	350 Hz 550 Hz 300 Hz	[310]
Electrodeless with insulating side ridges	Separation	Parental plasmid (6.766 kbp) Miniplasmid (4.509 kbp) Minicircle DNA (2.257 kbp)	NA	V_{DC}+V_{AC} (350 Hz)	[259]
Electrodeless with insulating side ridges	Separation	2.686 kbp and 6 kbp Minicircle (2.257 kbp) and parental DNA (6.766 kbp)	NA	V_{DC}+V_{AC} (350 Hz)	[258]
Photoconductive electrodes	Trapping	λ-DNA	0.8	100 kHz	[240]
Al microelectrodes	Stretching	λ-DNA T4 phage DNA	2	1 MHz	[191]
Al floating microelectrodes	Stretching	λ-DNA	NA	1 MHz	[245]
Al microelectrodes	Stretching	λ-DNA and its fragment (25 kbp)	1000	0.1 - 1MHz	[311]
Au microelectrodes	Stretching	λ-DNA	NA	1 MHz	[247]
Au microelectrodes	Stretching	λ-DNA	0.05	300 kHz	[249]
Au microelectrodes	Stretching	λ-DNA	2	1 MHz	[254]

Au microelectrodes	Stretching	λ-DNA	1000	200 kHz -1MHz	[255]
Au microelectrodes	Stretching	λ-DNA fragments: 15, 25, 35 and 48 kb	1000	100 kHz -1MHz Most efficient at: 200 kHz - 300 kHz	[252]
Al interdigitated electrodes	Stretching	Linear M13 dsDNA	0.1	1 MHz	[248]
Au microelectrode conjugated with Au-coated optical fiber	Stretching	λ-DNA	0.4 ×, 0.5 ×, 0.67 ×, 1 ×, 2 × 10^3	1 MHz	[312]

* Hybrid electrokinetic platforms that also employ ACET, ACEO, or electrophoresis.

Chapter 5. Frequency Hopping Dielectrophoresis as a New Approach for Microscale Particle and Cell Enrichment

The following chapter introduces the concept of frequency hopping dielectrophoresis and its application to the sorting of synthetic particles and the enrichment of circulating cancer cells spiked in diluted blood samples. The results presented in this chapter were published in the Journal of *Sensors and Actuators B: Chemical*.

Journal publication:

Modarres, Paresa, and Maryam Tabrizian. "Frequency hopping dielectrophoresis as a new approach for microscale particle and cell enrichment." *Sensors and Actuators B: Chemical* 286 (2019): 493-500.

5.1 Abstract

In the present study, we introduce a new concept termed frequency hopping dielectrophoresis (DEP) to enable a tunable microfluidic platform for microscale particle sorting. Frequency hopping DEP is used to provide a modulating force field leveraging the frequency-dependent response of polarizable particles to a non-uniform electric field. The proposed DEP platform operates by adjusting the signal parameters where a sinusoidal/square wave hops between two frequencies with a constant voltage amplitude. The two frequencies are selected such that one provides maximal DEP force (trapping frequency) and the other induces the minimal DEP force (release frequency). Analogously, the proposed DEP signaling scheme acts like the conventional microfluidic filters in which the filter size is tuned by modifying the DEP magnitude through the frequency-dependent behavior of particles. To this end, the proof-of-concept experiments were performed for the sorting of polystyrene particles of 3, 5 and 10 micrometers in diameter in a mixture with very high sorting efficiencies (98.7%). The protocol was then applied for the enrichment of MCF7 cells spiked in diluted blood samples to achieve capture efficiencies as high as 82.2%.

Keywords— Dielectrophoresis, Frequency Hopping Dielectrophoresis, Microfluidic Particle Sorting/Separation, Circulating Tumor Cell Enrichment.

5.2 Introduction

Sorting, purification and enrichment of synthetic or biological particles are essential processing steps in many lab-on-a-chip platforms with broad applications in the food industry, defense and diagnostics. An application of particular interest is the identification and isolation of circulating tumor cells (CTC) for diagnostics or analytical purposes. CTCs are malignant cells that have detached from the primary tumor and migrated in blood vessels. With CTCs as a fundamental prerequisite to metastasis, the enumeration of CTCs is pertinent for diagnosis, prognosis and assessment of drug resistance.[313] Isolation of CTCs from whole blood, as the first step of the overall analysis, is a very challenging task stemming from the extremely low number of these cells, and wide heterogeneity in size, deformability and protein expression. Despite these challenges, many techniques have been explored for CTC recognition and enrichment including immunoaffinity-based,[314-315] immunomagnetic-based[316-319] and micro-filtration.[320-324] Immunoaffinity- and immunomagnetic-based methods target membrane proteins expressed by CTCs to isolate them from blood cells. However, the major limitation of these methods is their incapability to isolate CTCs that inherently do not express targeted proteins. [326-325] Using a cocktail of antibodies enhances the capture efficiency, but the process is time-consuming and cost-ineffective. Label-free techniques like micro-filtration rely on physical properties of CTCs for differentiation. Micro-filtration techniques utilize microscale features like pillars, weirs, or pores to retain desired cells based on size and deformability. However, filtration approaches are prone to clogging, and the subsequent change in flow rate increases shear stress which potentially can damage CTCs.

In recent years, dielectrophoresis (DEP), translational motion of polarized bodies in response to a non-uniform electric field, has found numerous applications in microscale and nanoscale particle handling.[50, 327] DEP techniques rely on both size and dielectric properties of

cells for separation that are not addressable with other labeled- or label-free methods. Besides the cell size that significantly affects the DEP force magnitude, dielectric properties are sensitive to structural composition and morphological variations among cells providing additional criteria for differentiating CTCs from normal cells.[328-329] Furthermore, DEP devices, especially those operating under AC fields, can easily be adapted for highly automated and miniaturized platforms owing to simple and inexpensive electrode fabrication and experimental setup.

DEP microfluidic platforms generally function based on the competition of hydrodynamic and DEP forces resulting in either capture/release or deflection of desired particles. For instance, Alazzam et al. implemented channel-side planar electrodes to laterally separate MDA-MB-231 breast cancer cells from blood cells achieving 81% capture efficiency.[330] However, the throughput and the lateral displacement was limited due to restrictions on channel width since the DEP force has an inverse relation with the cube of length characterizing electric-field variations ($F_{DEP} \sim V^2/L^3$). Li et al. demonstrated the separation of MDA-MB-231 cancer cells from Jurkat E6-1 T cells using an array of wireless bipolar electrodes.[112] Bipolar electrode geometry was helpful for achieving parallelization to enhance throughput; however, additional channels demanded higher voltages, up to 248 volts for a 32-channel configuration. Application of such high voltages necessitates the use of voltage amplifiers which are prohibitively expensive and bulky. Shim et al. devised a continuous flow microfluidic chamber with a slow injection of unprocessed blood that was subjected to deionization by diffusion followed by DEP exposure that was balanced out with sedimentation and hydrodynamic lift forces.[109] Equilibrium of these forces led to the transport of cancer cells to the chamber floor to be skimmed out and blood cells to an elevated height to be eluted from the channel, providing 75% sorting efficiency. This approach provides an elegant solution to process whole blood, a challenge with DEP platforms due to

limitations with media conductivity. However, the deionization and levitation process require a large fluidic chamber (200 mm (L) x 25 mm (W)) and two syringe pumps, making the device fabrication and operation complicated.

Moreover, to date, most dielectrophoretic platforms are optimized based on different geometrical configurations of electrodes or exploiting various sorting strategies that mostly rely on the application of a continuous-time force field.[186] Few studies have considered tuning electrical signal parameters for realizing new modes of dielectrophoresis operation for particle sorting and manipulation. For instance, Cui et al. demonstrated size-specific elution of polystyrene particles in a mixed population using a discontinuous force field generated by a pulsed signal.[331] The pulsed signaling scheme provided a tunable mechanism for sorting a mixture containing more than two population of particles with various sizes. However, the throughput was strictly limited since the average force in time was reduced by half due to the use of a pulsed signal with 50% duty cycle. Guo et al. implemented a quadruple electrode array for moving individual cells by modulating the phase difference between electrode pairs.[332] Similarly, Zemánek et al. devised a novel microelectrode array consisting of four sectors with parallel electrodes to control movement of individual polystyrene particles within the plane of electrodes by changing the phase shift between electrodes. The phase modulation approach provided a mean for manipulating individual synthetic or biological particles in a stationary fluid. However, the applicability of this technique to particle sorting in larger scale is lacking. Furthermore, Rohani et al. applied a wave sequencing technique to induce nDEP and electrorotation (ROT) fields at different time points in order to enhance the spatial extend and frequency range for ROT characterizations.[333] Using this technique, they performed highly parallelized ROT characterization of *Cryptosporidium Parvum* after exposure to varying degrees of heat treatment. Finally, Urdaneta et al. employed a three-electrode geometry

platform where two AC signals with different frequencies were applied on two electrodes while a third electrode was grounded.[334] The effective DEP force contributed from the three electrodes led to the patterning of dead and live yeast cells at separate locations between electrodes. The use of multiple frequencies at multiple electrodes was most useful for patterning different type of cells rather than dynamically sorting out a mixed population.

In the present study, we introduce a new concept termed frequency hopping DEP to enable a tunable platform for microscale particle sorting. Frequency hopping DEP is employed to provide a modulating force field leveraging frequency-dependent response of particles to a non-uniform electric field. The frequency is continuously shifted between two frequencies which induce different DEP force magnitudes on the suspending particles of various sizes and dielectric properties. By carefully choosing the frequencies and the shift rate between frequencies, particles in a multi-particle mixture can be eluted from the system according to their size and frequency-dependent signature. To this end, we present the design of a microfluidic platform to achieve sorting based on the principle of frequency hopping. For the proof of concept, separation of polystyrene microspheres based on size is presented. High captures efficiencies up to 99.8% were achieved for sorting a mixed population containing 3, 5 and 10 μm microspheres quantified via flow cytometry. Furthermore, the efficacy of the platform and the frequency hopping mechanism were validated by the enrichment of MCF7 cancer cells that were spiked in diluted blood samples where cancer cells were captured at electrodes, and blood cells were eluted from the channel.

The proposed frequency hopping DEP platform proved useful for sorting of synthetic particles and isolation of CTCs with the simple implementation of planer electrodes and application of small voltages (up to 20 V_{pp}). Moreover, the platform can easily be augmented with parallel channels for enhancing the throughput. Finally, the concept of frequency hopping DEP

opens new avenues for exploring the effect of combining multiple frequencies for new DEP applications.

5.3 Materials and Methods

5.3.1 Microfluidic Platform Fabrication

The microfluidic platform consisted of gold interdigitated electrodes on the device floor with 30 μm width and 30 μm spacing, and the fluidic channel was made in SU-8 with a thickness of 30 μm, a width of 3 mm, and a length of 2.3 cm. The device fabrication involved patterning gold electrodes on a Borosilicate glass slide (SCHOTT North America, Inc., Elmsford, NY). The glass slide was first cleaned using acetone, isopropyl alcohol (IPA) and deionized water (DI) water. Next, photoresist AZ5214E was spin coated to form a 1.5 μm thick layer followed by soft baking at 110 ˚C. Then, the sample was undergone UV exposure with a dose of 20 $mJcm^{-2}$ and reversal bake at 110 ˚C for 2.5 min. Flood exposure was followed at 450 $mJcm^{-2}$ and developing was done in MIF720 developer for 30 sec. Following the photolithography, 20 nm of Ti and 80 nm of gold was deposited using e-beam evaporation. The electrode fabrication was completed by sonication in Microposit Remover 1165 at 70 ˚C for 30 min.

Next, the glass substrate was cleaned with acetone, IPA and rinsed with DI water followed by one-hour dehydration bake at 150 ˚C in a vacuum oven. The fluidic channel was then formed by patterning a 30 μm thick SU-8 2015 layer. First, SU-8 2015 was spin coated and soft baked at 67 ˚C and 97 ˚C for 5 and 10 min, respectively. The substrate was then UV exposed at 100 $mJcm^{-2}$ and baked at 67 ˚C for 2 min and 97 ˚C for 5 min. The sample was developed for 75 sec in the SU-8 developer to form the fluidic channel and hard baked at 150 ˚C for 10 min to relieve surface cracks and to further harden the SU-8 film.

Finally, the flow channel was sealed by bonding a PDMS layer with inlet/outlet vias to the SU-8 coated substrate. First, (3-Aminopropyl) triethoxysilane (APTES) was vacuum-deposited onto the substrate with the SU-8 layer for 1 hour.[335] The PDMS layer was plasma treated to activate the surface with oxygen groups. Then, the PDMS layer and the substrate were bonded. The bonding completed by heating the assembly on a hotplate at 100 ˚C for 5 hours under 20 N force.

5.3.2 Microsphere Sample Preparation

To mimic the bacterial and mammalian cells size, fluorescent polystyrene microspheres with nominal diameters of 3.1 µm, 5 µm and 9.9 µm were purchased form Magsphere (Magsphere, Inc., Pasadena, CA). For the ease of reading, round numbers 3, 5 and 10 µm are used as nominal diameters for the remainder of this article. All microspheres were in aqueous suspensions of 2.5% w/v. The microspheres were diluted by taking 1 µL of 3 µm, 4.6 µL of 5 µm and 37 µL of 10 µm microspheres and re-suspending them in 5 mL of DI water resulting in approximately 10^3 particles per µL.

5.3.3 Cell Culture Sample Preparation

The working buffer for cell suspension was prepared by adding phosphate buffer saline (PBS) solution to DI water to bring the conductivity to 280 μScm^{-1}, measured using a conductivity meter (HI98303, Hanna Instruments, Woonsocket, RI). The osmolarity of the working buffer was adjusted with the addition of 8.5% sucrose, 0.1% dextrose and 1% (w/v) bovine serum albumin (BSA). MCF7 cells (ATCC, Manassas, VA) were cultured in DMEM/High Glucose media, supplemented with 10% FBS and 1% antibiotics (v/v), and maintained in 5% CO_2 at 37 ˚C in 25 cm^2 culture flasks. Cells were harvested at 85% confluency using 0.05% trypsin-EDTA. The cell suspension was centrifuged for 3 min at 1500 rpm. Then, the media was replaced and washed twice with 2 mL of the working buffer.

5.3.4 Red Blood Cell Sample Preparation

Blood samples were collected from healthy volunteers in accordance with the guidelines of the ethical committee of the Montreal Heart Institute (Montreal, Canada). The blood withdrawn from the antecubital vein through a 19-gauge butterfly needle was collected in syringes containing acid citrate dextrose (Baxter Corporation, Mississauga, Canada) acting as an anticoagulant. The blood/acid citrate dextrose part ratio was 5 to 1. The collected blood was centrifuged at 3000 rpm for 15 min at room temperature. The plasma and the buffy coat were removed by aspiration. Then, 20 μL of sediments was washed with the working buffer and re-suspended in 2 mL of the working buffer containing MCF7 cells.

5.3.5 Cell Counting and Size Measurements

The number of cells in the final sample was counted using a hemocytometer, and the average cell radius was obtained from 30 cells measurements using light microscopy (TE-2000E, Nikon). The average red blood cell (RBC) and MCF7 radii were measured to be 4.57 ± 0.23 μm and 12.17 ± 2 μm, respectively.

5.3.6 Microsphere and Cell Separation Protocol

For the experiments with microspheres, the device was pre-washed with 0.1% solution of Tween 20, and the microsphere solution was continuously withdrawn into the device using a standard infuse/withdraw syringe pump (11 Elite Programmable Syringe Pump, Harvard Apparatus, Inc.). The device operation was monitored using an inverted microscope (TE-2000E, Nikon) to assess particle trajectories. The frequency hopping signal (output mode: high impedance) was generated by a function generator (AFG3200C, Tektronix, Inc.). For MCF7 cell enrichment experiments, the device was pre-washed with the working buffer for 5 min followed by continuous withdrawal

of cell suspensions in working buffer using a standard infuse/withdraw syringe pump as mentioned above.

To quantify the sorting efficacy of polystyrene microspheres, 80 μL of the mixed solution was withdrawn through the fluidic chamber and collected in a glass syringe used with the pump. The collected sample was transferred to a 1.5 mL vial while raising the volume to 500 μL. With the dilution parameters stated in section 2.2, 80 μl volume corresponds to approximately 80×10^3 microspheres. For flow cytometry (BD FACSCalibur™) measurements, the sample was transferred to a flow cytometry tube and mixed well with a vortex mixer. To identify the percentage of microsphere within the output population, side scattered cytometry (SSC) versus forward scattered cytometry (FSC) dot plots were attained and the reported numbers within each identified gate for fluorescent microbeads were used for percentage calculations. Flow cytometry data were expressed as the mean ± standard deviation (SD) of three replicates.

The enrichment efficiency of MCF7 cells was calculated by counting the number of captured cells and eluted cells and taking the ratio of captured cells to the sum of all cells by analyzing acquired videos at the outlet and consecutive images acquired from electrodes. For each experimental condition, a five-minute video (50 frames per second (fps)) was captured at the outlet while continuously withdrawing the cell solution followed by a cell-free buffer wash. Since the MCF7 cells were significantly different in size and shape from red blood cells and very low in number, they were easily distinguished from red blood cells and were counted on-chip by analysing captured images of electrodes. The capture efficiency data were reported as the mean ± standard deviation (SD) of three replicates.

5.4 Results and Discussions

5.4.1 Theory and Principle of Operation

Dielectrophoresis is the translational motion of polarized bodies in the presence of an electric field. In an electric field with intensity *E*, the average force exerted on a homogeneous spherical particle of radius *r* and electrical permittivity of ε_p in a media of electrical permittivity of ε_m is formulated as:

$$F = 2\pi\varepsilon_0\varepsilon_m r^3 Re[f_{cm}]\nabla|E^2| \tag{5.1}$$

$$f_{cm} = \frac{\varepsilon_p^* - \varepsilon_m^*}{\varepsilon_p^* + 2\varepsilon_m^*} \tag{5.2}$$

$$\varepsilon^* = \varepsilon - j\frac{\sigma}{\omega} \tag{5.3}$$

where ε_0 is the permittivity of free space, *Re* [f_{cm}] is the real part of the Clausius-Mossotti (CM) factor, σ is the conductivity, ω is the radial frequency and ε^* is the complex permittivity. The CM factor determines the polarity and strength of the induced dipole in a particle and thus provides a mean for understanding how a particle behaves in a non-uniform electric field. For positive values of *Re*[f_{cm}], a polarized particle is attracted to the regions of the highest electric field (or electrode edges), and for negative values of *Re*[f_{cm}] factor, a particle is repelled from electrodes to the field minima. For polystyrene microspheres, the cross-over frequency (the frequency at which the DEP force is zero) is strongly dependent on the size of particles assuming all other parameters are constant. The size-dependent behavior of cross-over frequency for these particles directly stems from the conductivity (σ_p) relation with size revealed through the following relation:[336-337]

$$\sigma_p = \sigma_{bulk} + 2\frac{K_s}{r} \tag{5.4}$$

where σ_{bulk} denotes the bulk conductivity, and K_s is the surface conductance. Eq. 5.4 was derived assuming the electrical double layer (EDL) is much thinner than the particle diameter. The

parameters for polystyrene surface and bulk conductivity and permittivity values were obtained from published literature.[336, 338-339]

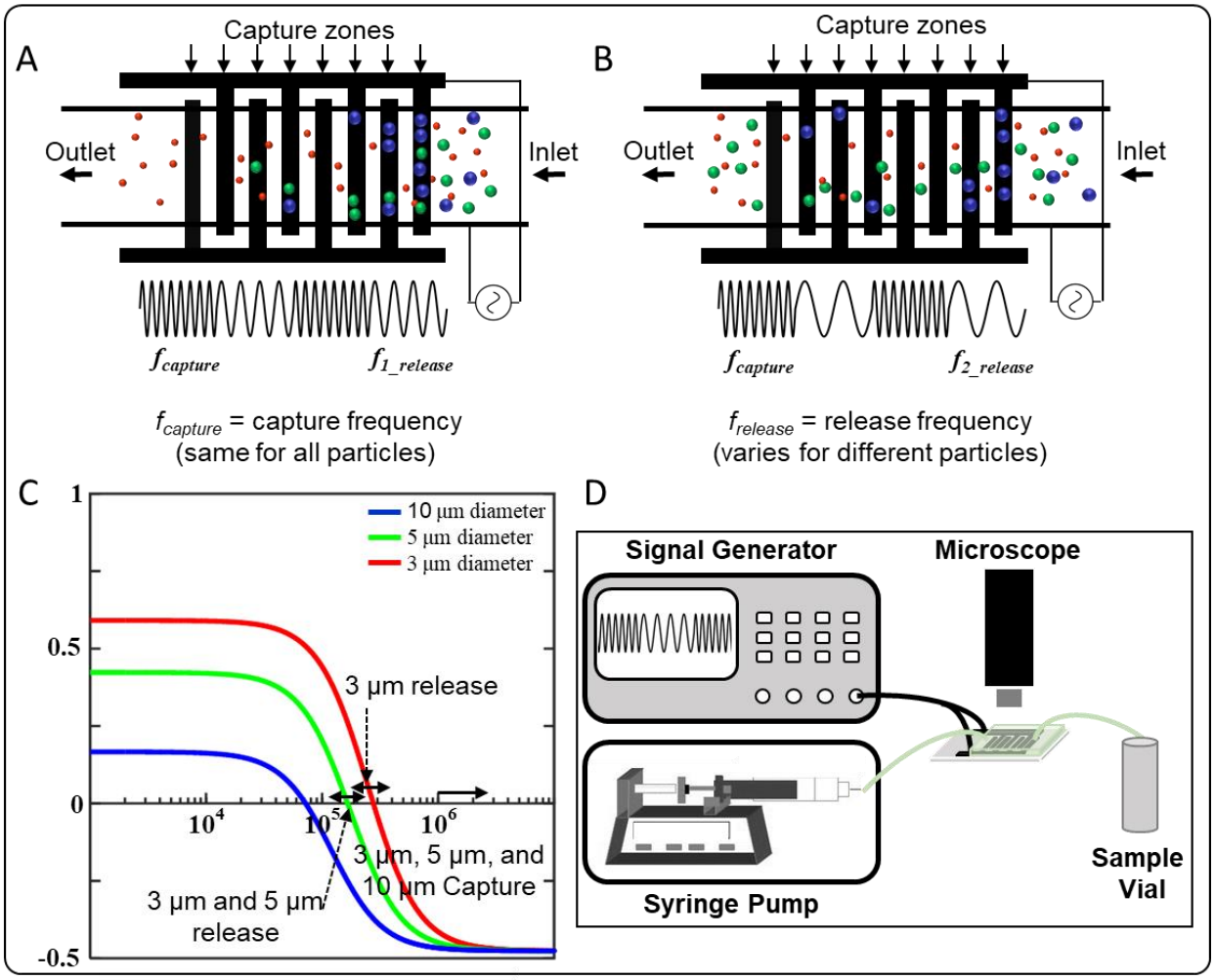

Figure 5.1 Schematic illustration of device operation using frequency hopping dielectrophoresis demonstrating size-based sorting of particles in a heterogenous polystyrene population. **A.** 10 µm (blue) and 5 µm (green) microspheres are retained while 3 µm (red) particles are flowing down the channel. **B.** 10 µm particles are retained while 3 and 5 µm microspheres are released. **C.** The real part of the CM factor versus frequency for polystyrene microspheres of 10, 5 and 3 µm diameter showing the cross-over frequency. **D.** Experimental setup.

The size- and frequency-dependent behavior of particles in a non-uniform electric field were utilized to sort out a mixture of polystyrene microspheres of various sizes by manipulating the frequency of the applied voltage. To this end, two frequencies were identified for capturing

and releasing particles. The capture frequency ($f_{capture}$) was selected such that all particles experienced either a maximum negative DEP (nDEP) force or a maximum positive DEP (pDEP) force. The release frequency ($f_{release}$) was chosen based on the cross-over frequency for each particle size such that the DEP force was reduced leading to release from the DEP capture zones.

To leverage the frequency hopping DEP for particle sorting, the proposed platform consisted of interdigitated electrodes (trap locations) to generate sinusoidally varying field intensities. Thereby, the application of capture frequency displaced all particles to the field traps above the nearest electrode digits (nDEP) or at electrode edges (pDEP). By adjusting the release frequency, the target particles were released from the DEP capture zones based on their cross-over frequency (Fig. 5.1A and 1B).

5.4.2 Electric Field Distribution Simulations

The electric field inside the channel was simulated using COMSOL 5.2 (Burlington, MA) to find the location of field minima and maxima where the DEP capture zones are. The 2-D cross-section of the device including the channel floor (glass), the fluid and the channel top (PDMS) was modeled using the AC/DC module physics. The electric field square (E^2) versus location along the longitudinal axis of the device (x-direction) is illustrated in Fig. 5.2A. As seen in this figure, the field capture zones operating under nDEP and pDEP lie above each electrode digit (black bars) near the ceiling and electrode edges, respectively. The magnitude and spatial variation of E^2, one particle radius away from the channel top and floor, are shown in Fig. 5.2B and 2C.

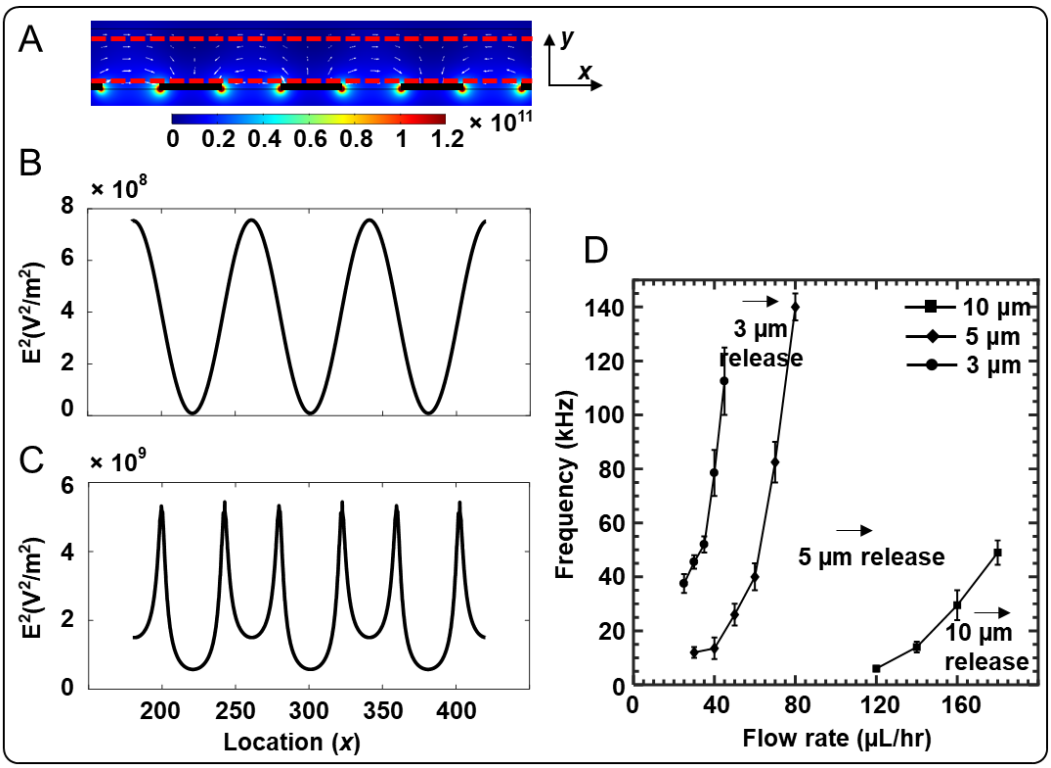

Figure 5.2 A. 2-D cross-section simulation of electric field intensity square (E^2) for a 20 V_{pp} signal. E^2 versus location along x-axis indicating field capture zones, **B.** under nDEP (corresponding to cut-line at 2.5 µm below the top), and **C.** under pDEP (corresponding to cut-line at 2.5 µm above the device floor). **D.** Experimental flow rate vs. threshold frequency for polystyrene particles.

5.4.3 Sorting of Polystyrene Microparticles

The theoretical calculation of CM curve using reported parameters in literature is illustrated in Fig. 5.1C. According to CM plot, an appropriate frequency to capture all polystyrene particles found to be 1 MHz. The release frequency was experimentally identified by lowering frequency to near cross-over frequency for the target particles which fell within 20 – 100 kHz range for 3 µm and 5 µm diameter microspheres.

To experimentally identify and optimize the parameters for microparticle sorting protocol in a mixed population, first, each microsphere size was withdrawn into the device at the maximum flow rate at which the nDEP force traps all incoming microspheres. The capture frequency for a maximum nDEP force was set at 1 MHz for all microsphere sizes (Fig. 5.1C). To find the release

frequency, the frequency was lowered from 1 MHz in 1 kHz steps until microspheres started eluting from the channel. This experiment was repeated with several flow rates to have a plot of flow rate vs. threshold release frequency. Fig. 5.2D illustrates the threshold frequency at which particles start escaping the DEP traps for certain flow rates. As the flow rate decreases, the release frequency reduces approaching the cross-over frequency. Based on these experiments, a volumetric flow rate of 40 µL/hr was chosen to retain all microspheres. To sort a mixed population, the electrical signal and flow rate parameters were initially set to these values to capture all incoming microspheres followed by varying the release frequency for reducing the nDEP force to elute microspheres of different diameters.

The sorting efficiency of the platform was determined by analyzing the size distribution of collected microparticles before and after the voltage application using flow cytometry. For a mixed population of 3, 5 and 10 µm diameter microspheres, the mixed solution was withdrawn into the device in a continuous fashion at a flow rate of 40 µL/hr. The composition and the percentages of microspheres in a mixed solution are shown in Fig. 5.4A and Fig 5.4D, respectively. Initially, all microspheres were trapped by applying a 20 V_{pp} sinusoidal signal ($f_{capture}$ = 1 MHz, $f_{release}$ = 1 MHz, f_{rate} = 1 Hz). To elute 3 µm microspheres and capture 5 and 10 µm particles, the release frequency was set at 85 kHz. As seen in Fig. 5.4B and Fig. 5.4E, 3 µm microspheres (red color) consisted 99.7% percent of retrieved microspheres at the output. To elute 3 and 5 µm microspheres with 10 µm microspheres trapped, the release frequency was further lowered to 20 kHz. The result of this elution is illustrated in Fig. 5.4C and 4f where 98.7% of collected microsphere were 3 and 5 µm (green color) beads with 1.3% of 10 µm beads (blue color).

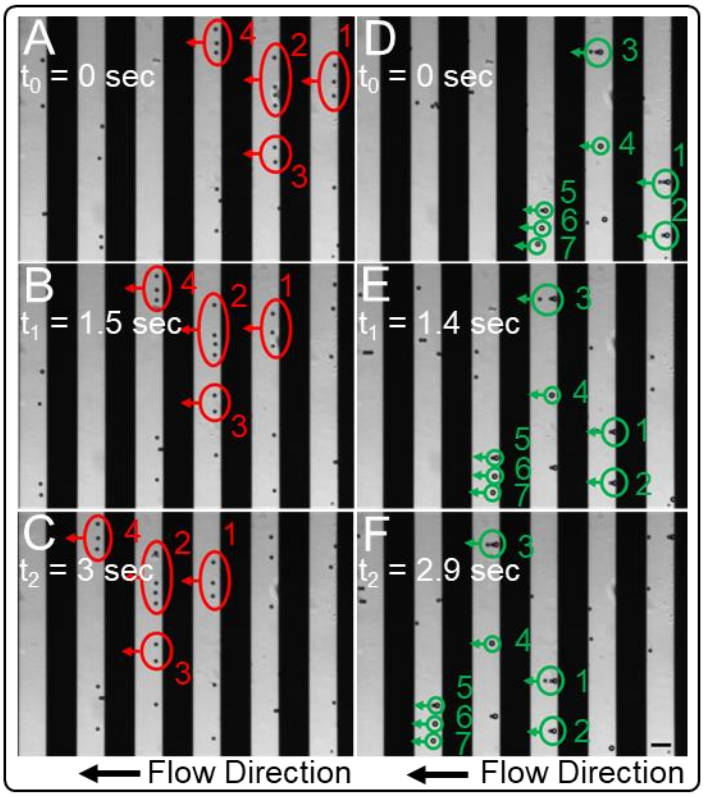

Figure 5. 3 Time-lapse images showing (**A**, **B**, **C**) free-flowing 3 µm microspheres (circled red) with 5 and 10 µm microspheres being trapped. The 5 and 10 µm microspheres are entirely above gold electrodes and are not visible in these images. (Signal and flow parameters: $f_{capture}$ = 1 MHz, $f_{release}$ = 85 kHz, f_{shift} = 1 Hz, V_{pp} = 20 V, V_{flow} = 40 µL/hr). (**D**, **E**, **F**) free-flowing 3 and 5 µm microspheres (green circles) while 10 µm microspheres are retained. (Signal and flow parameters: $f_{capture}$ = 1 MHz, $f_{release}$ = 20 kHz, f_{shift} = 1 Hz, V_{pp}=20, V_{flow} = 40 µL/hr). The scale bar is 20 µm.

During the sorting experiments, particle pearl-chaining was observed as the number of captured particles increased. Pearl-chaining of polarized particles happens due to electrostatic interactions between particles as a mean to reduce their electrical potential energy.[340] While the dielectrophoretic behavior of these chain-like particles is different from single microspheres,[341] we noted that doublet and triplet microspheres were also released along with single microspheres of the same size. Thus, the formation of pearl-chain microspheres did not prohibit elution of these assembled particles from the channel. However, attachment of the smaller sized microspheres to the larger ones, which formed dissimilar pearl-chain assemblies, prevented the smaller sized

particles to be removed from the channel when intended unless they were dissociated from the larger particles by interrupting the voltage. Moreover, the electrodes at the beginning of the stream collected all incoming particles which led to the saturation of these electrodes, the capture of unwanted microparticles, and exacerbation of pearl-chain formation. To relieve these issues, it was necessary to disrupt the electric field by turning off the voltage in intervals to avoid the saturation problem and to allow the grouped particles to dissociate and move down the channel.

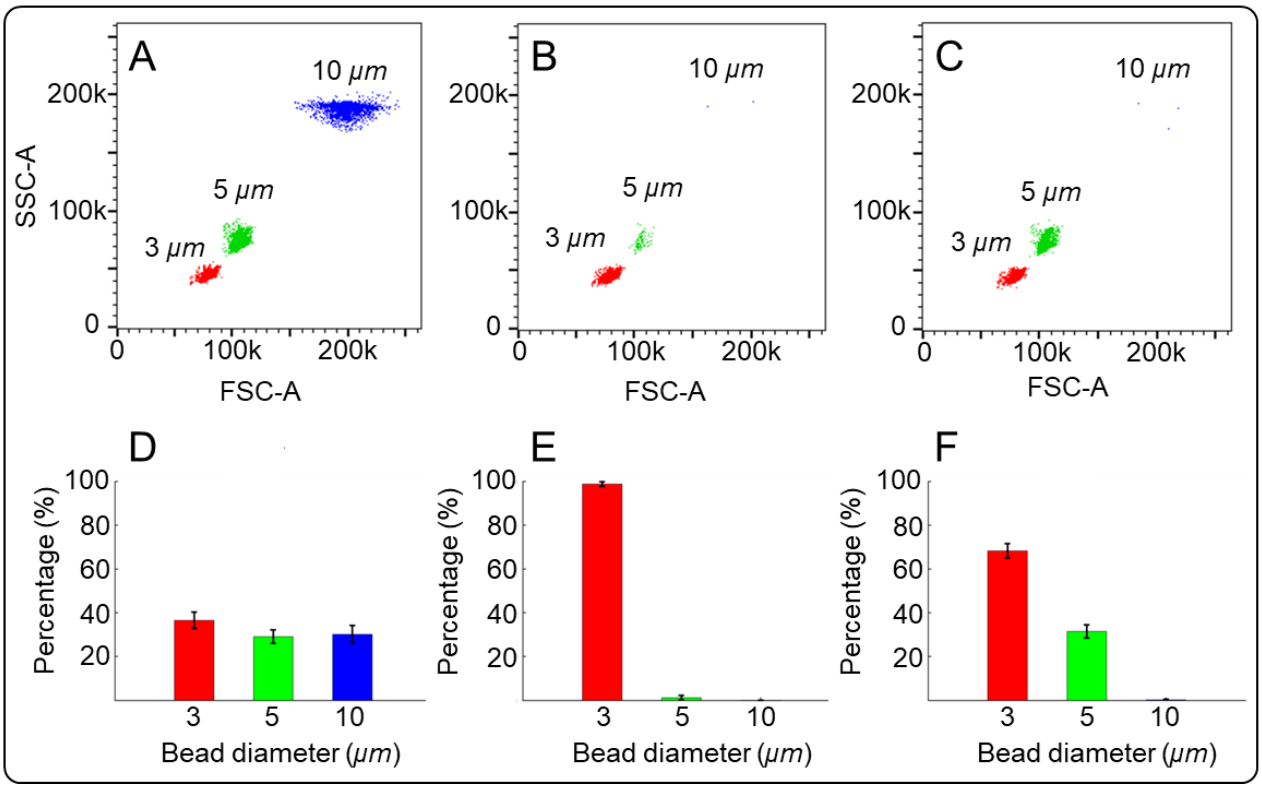

Figure 5. 4 Quantitative analysis of collected samples. Dot plots of flow cytometry and the percentages of microspheres showing the sample composition **A**, **D** before voltage application, **B**, **E** after applying voltage and eluting 3 µm microspheres and **C**, **F** after applying voltage and eluting 3 and 5 µm microspheres. (n=3)

5.4.4 Enrichment of MCF7 Cells as a Model for CTCs

To test the feasibility of frequency hopping DEP for the cell enrichment, label-free capturing of MCF7 cells (a breast cancer cell line used as a model for CTC) was performed with MCF7 cells

spiked in diluted blood, approximately one MCF7 cell for every five hundred RBCs. Both MCF7 and RBCs showed a strong pDEP response collecting these cells at electrode edges for approximate frequency ranges of 350 kHz - 20 MHz and 200 kHz - 14 MHz, respectively. At frequencies below 200 kHz, a weak nDEP force was observed for both cell types. The $Re(f_{cm})$ versus frequency plot based on dielectric parameters reported in the literature for MCF7 and RBCs is illustrated in Fig. 5.5A. The experimental observation of frequencies corresponding to pDEP and nDEP forces for MCF7 cells and RBCs were slightly different from that of predicated by the theoretical calculations. This can be explained considering the variations in cell dielectric parameters reported in the literature and the cells used in experiments as well as the simplifications that were assumed in deriving the theoretical cell models and DEP force.

To isolate MCF7 cells, the cell suspension was continuously withdrawn into the channel at 80 µL/hr with 1 MHz capture frequency and 150 kHz release frequency. With these flow and signal parameters, the MCF7 cells were captured at electrodes by pDEP force, and RBCs were eluted from the channel experiencing a weak nDEP force. The enrichment efficiency was calculated by counting the number of captured cells and eluted cells and taking the ratio of captured cells to the sum of all cells by analyzing acquired videos at the outlet and consecutive images acquired from electrodes (Fig. 5.5B). An enrichment efficiency as high as 82.2% was obtained for a 20 V_{pp} sinusoidal signal. At lower voltages, the sorting performance remained relatively similar down to 16 $V_{pp,}$ below which the trapping efficiency was appreciably reduced. The trapping efficiency of MCF7 cells was largely affected by inhomogeneities in shape, size and structure of cancer cells which explain the lower capture rate of CTCs compared to that of polystyrene microparticles. For instance, individual and cluster cells with sizes considerably deviate from the

average cell size were not effectively trapped. Such problems can be compensated for by designing channels with larger depth and increasing the voltage amplitude.

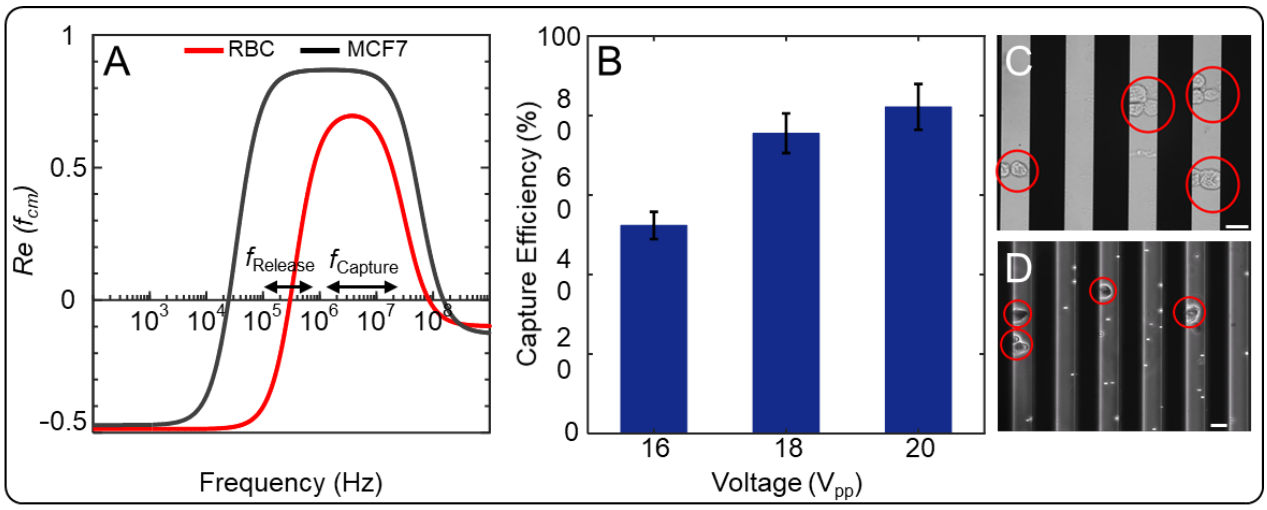

Figure 5. 5 A. Real part of the Clausius-Mossotti factor versus frequency for RBC and MCF7 cells. **B.** Enrichment efficiency of MCF7 cells vs. different voltage amplitudes (n=3). **C.** Light microscopy image of captured MCF7. **D.** Phase-contrast image of captured MCF7 cells at electrode edges with blood cells flowing down the channel. The scale bar is 20 µm.

5.5 Conclusion

In this article, we demonstrated the efficacy of frequency hopping DEP for the sorting of polystyrene microspheres with excellent purities as high as 98.7%. The applicability of the proposed DEP platform to enrich CTC-like cells was also achieved with a separation efficiency of 82.2%, comparable to that reported in DEP-based devices so far.[109, 330] The introduced platform was proposed as an analytical technique for assessing the presence of CTCs in diluted blood samples. As such, further viability assays were not performed, and the study remained focused on quantitively measuring the capture efficiencies of CTCs. The current study can further be improved by spiking white blood cells in diluted blood and examining the ability of the technique for differentiating CTCs from white blood cells. Our results convey that the concept of frequency hopping DEP is effective for sorting of particles based on variations in size only or a combination

of size- and frequency-dependent response of particles to an electric field. Additionally, in the present study, we employed a signaling scheme where frequency shifted with a 50% duty cycle. Further experiments are required to study the effect of duty-cycle on capture efficiency. Finally, frequency hopping provides a tunable platform by which multiple parameters can be altered to accomplish separation based on the size and inherent dielectric properties of cells of interest. Once a certain electrode and fluidic channel geometry is adapted, the presented DEP scheme can be leveraged for sorting of other micron-sized particles.

Acknowledgements

The authors gratefully acknowledge the financial support from Natural Sciences and Engineering Research Council of Canada (NSERC) through CREATE training programs in ISS (Integrated Sensors and Systems) and CFS (Continuous Flow Systems) and CGS doctoral fellowship. Additionally, the authors acknowledge the kind support of colleagues, Nickolas Distasio, Kaushar Jahan and Saadia Shoaib, for assisting with flow cytometry and cell culture experiments.

5.6 Supplementary Information

5.6.1 Release Frequency and Flow Rate Dependency

The release frequency and flow rate dependency were analyzed for hopping and single frequency modes of operation using polystyrene beads. For frequency hopping operation, the capture and release frequencies were initially set to 1 MHz for a maximum nDEP force for all microsphere sizes. To find the release frequency, this frequency was lowered from 1 MHz in 1 kHz steps until microspheres started to elute from the channel. For the single-frequency operation, the frequency was first set to the capture frequency (1 MHz). Next, this frequency was lowered in 1 kHz steps until microspheres released from the DEP traps. The obtained release frequencies versus flow rates are shown in Fig. S5.1 for three different size particles. Results in Fig. S5.1 suggest two outcomes:

1) the release frequency shifts to lower frequencies in the case of frequency hopping, and 2) for the same frequency, larger flow rates can be sustained under frequency hopping compared to single-frequency signaling.

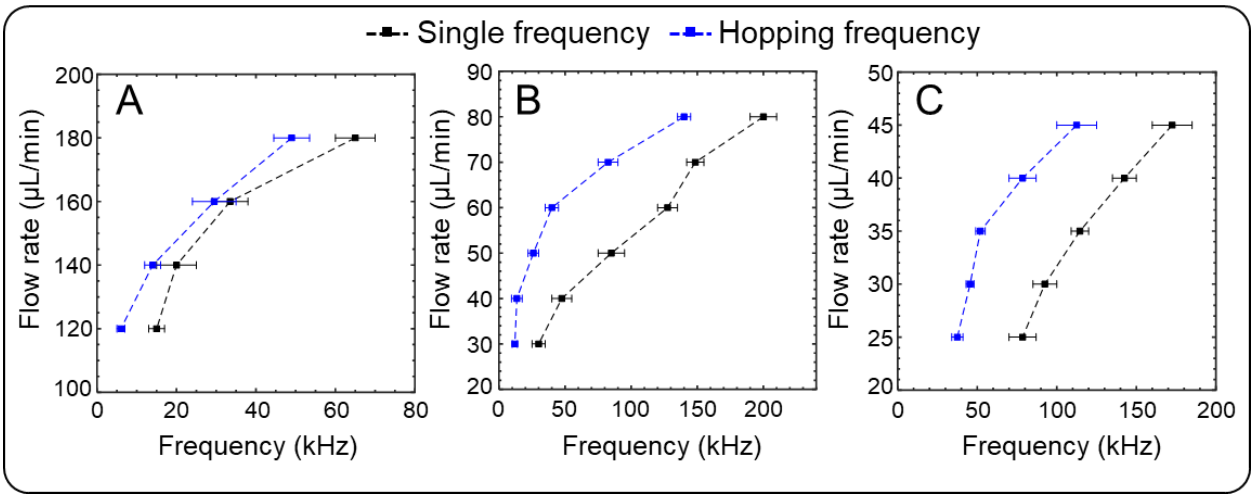

Figure S5.1 Experimental flow rate versus threshold release frequency for single and hopping frequency operation (20 V_{pp}, $f_{capture}$ = 1 MHz, f_{shift} = 1 Hz) for **A.** 10 µm diameter particle, **B.** 5 µm diameter particle and **C.** 3 µm diameter particle.

5.6.2 Dielectric Properties of Polystyrene Microspheres

For homogeneous polystyrene microspheres, the dielectric parameters are listed in table S5.1 and illustrated in Fig. S5.2.

Table S5.1 Dielectric properties of polystyrene.

Material	ε	K_s(S/m)	σ_{bulk}	Ref
Polystyrene	2.55	1.2e^{-9}	0	336, 338-339

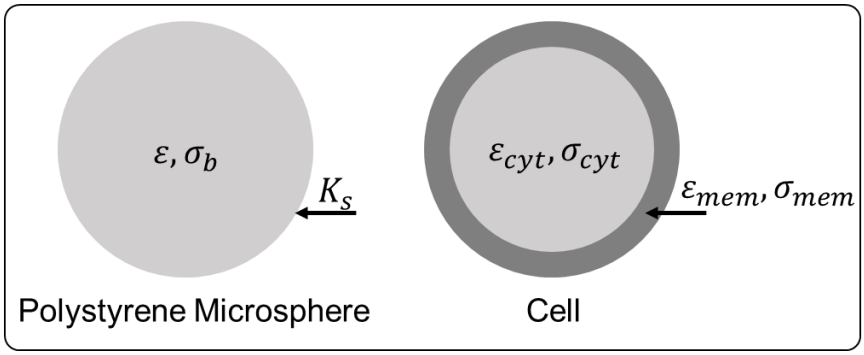

Figure S5.2 Schematic illustration of polystyrene and cell structure with dielectric parameters.

5.6.3 Dielectric Properties of Red Blood Cells and MCF7 Cancer Cells

Biological cells are complex and heterogeneous structures with multiple layers of different dielectric properties. One of the most common models used to take account of the multi-layered structure of the cells is the multi-shell model.[59] The heterogeneous structure of a cell can progressively be simplified to a homogenous body with an effective cell permittivity ε_p^*, which, in theory, polarizes as the original heterogeneous body in the presence of an electric field. To model red blood cells (RBCs) and MCF7 cells, the single-shell model was used where the entire cell structure was reduced to a cytoplasm of an effective permittivity ε_{cyt} and conductivity σ_{cyt} and a membrane of effective permittivity ε_{mem} and conductivity σ_{mem}. The effective cell permittivity is formulated as follows:

$$\varepsilon_p^* = \varepsilon_{mem}^* \frac{(\frac{r_{out}}{r_{in}})^3 + 2(\frac{\varepsilon_{cyt}^* - \varepsilon_{mem}^*}{\varepsilon_{cyt}^* + 2\varepsilon_{mem}^*})}{(\frac{r_{out}}{r_{in}})^3 - (\frac{\varepsilon_{cyt}^* - \varepsilon_{mem}^*}{\varepsilon_{cyt}^* + 2\varepsilon_{mem}^*})} \tag{5.5}$$

$$\varepsilon^* = \varepsilon - i\frac{\sigma}{\omega} \tag{5.6}$$

where r_{out} and r_{in} are the outer and inner cell radius, respectively. ε^*_{cyt} is the complex cytoplasm permittivity, ε_{mem}^* is the complex membrane permittivity, and ω is the radial frequency. The membrane and cytoplasm dielectric properties were extracted from the available literature and are listed in table S5.2. The membrane permittivity was deduced from the membrane capacitance (C_{mem}) that was mostly reported in literature through the following relation:

$$\varepsilon_{mem} = \frac{C_{mem}.d}{\varepsilon_0} \tag{5.7}$$

where d is the membrane thickness and ε_0 is the permittivity of free space.

Table S5.2 Dielectric properties of red blood cells and MCF7 cell line.

Cell type	r (μm)	d_{mem}(μm)	ε_{cyt}	ε_{mem}	σ_{cyt} (S/m)	σ_{mem} (S/m)	Ref
RBC	4.57	$9e^{-3}$	59	4.44 ± 0.45	0.31 ± 0.03	$1e^{-6}$	[342]
MCF7	12.17	$7e^{-3}$	50	14.7	1	$1e^{-6}$	[343]

Chapter 6. Phase-controlled Field-Effect Micromixing Using AC Electroosmosis

The following chapter concerns the design and validation of a phase-controlled micromixer based on AC electroosmotic induced flows. The chapter provides a thorough introduction to the concepts and existing literature followed by analytical and experimental results. The presented results were published in the Journal of Microsystems and Nanoengineering.

Journal publication:

Modarres, Paresa, and Maryam Tabrizian. "Phase-controlled Field-Effect Micromixing Using AC Electroosmosis" *Microsystems and Nanoengineering* (2020).

6.1 Abstract

The exploration and application of electrokinetic techniques in micro total analysis systems have become ubiquitous in recent years, and scientists are expanding the use of such techniques in areas where comparable active or passive methods are not as successful. In this work, for the first time, we utilize the concept of AC electroosmosis to design a phase-controlled field-effect micromixer that benefits from a three-finger sinusoidally shaped electrodes. Analogous to field-effect transistor devices, the principle of operation for the proposed micromixer is governed by the source-gate and source-drain voltage potentials that are modulated by introducing a phase-lag between the driving electrodes. At an optimized flow rate and biasing scheme, we demonstrate that the source, gate and drain voltage phase relations can be configured such that the micromixer switches from an unmixed state (phase-shift of 0˚) to a mixed state (phase-shift of 180˚). High mixing efficiencies beyond 90% was achieved at a volumetric flow rate of 4 µL/min corresponding to approximately 13.9 mm/s at optimized voltage excitation conditions. Finally, we employed the proposed micromixer for the synthesis of nanoscale lipid-based drug delivery vesicles through the process of electrohydrodynamic-mediated nanoprecipitation. The phase-controlled electrohydrodynamic mixing utilized for the nanoprecipitation technique proved that nanoparticles of improved monodispersity and concentration can be produced when mixing efficiency is enhanced by tuning the phase-shifts between electrodes.

Keywords— AC Electroosmosis, Micromixing, AC Electrokinetics.

6.2 Introduction

For the past two decades, one of the foremost applications of microfabrication technology in biomedical sciences has been the advent of microfluidic devices for handling minute amounts of biological liquids with broad applicability to analytical and diagnostic devices. While miniaturization is beneficial in many aspects such as low volume consumption, portability and accessibility, it poses new challenges due to fluid physics at the microscale. At the microscale, the dominance of viscous to inertial forces leads to laminar flows wherein mixing is only possible by diffusion. However, with diffusion coefficients ranging from 10^{-9} m^2/s to 10^{-11} m^2/s depending on molecule size, mixing by diffusion is extremely slow and inefficient. Consequently, many passive and active micromixers have emerged to enhance mixing within microfluidic channels. Passive micromixers rely on the fluid transport mechanism to promote mixing by stretching the interface between the liquids and reducing the striation length across which diffusion takes place. Examples of passive micromixers include hydrodynamic focusers,[344] lamination-based designs[43, 345] and those implementing geometrical obstacles.[44, 346-348] Passive micromixers are simple to operate but the fabrication process can get very complex especially for the three-dimensional designs.[349] Furthermore, many passive techniques suffer from sample dispersion and dilution by spreading it out longitudinally compromising assay sensitivity for sensing applications and yield for chemical synthesis.[350] Active micromixers do not suffer from the dilution problem since these mixers maintain a constant volume during the mixing process by the use of an external force source such as magnetic,[351-355] acoustic[35-36, 356] and electrical[2, 10, 357-362] to drive local fluid flow. Amongst active micromixers, electrical-based methods offer unique properties such as the ease of electrode implementation, the absence of any moving parts and use of small voltages making them an attractive mixing mechanism for many bioanalytical applications. Most significantly, electrical-

based mixing is an excellent choice for mixing in droplet-based microfluidics[2, 363] and sensitivity enhancement by overcoming diffusion-limited analyte transport in several sensing platforms[50] like impedance sensing,[139, 198, 262] plasmonic sensing[364] and quartz crystal microbalance[365] by fabricating additional electrodes or modifying the sensing electrodes.

Microfluidic-based electrokinetic mixers typically embed electrodes within microfluidic channels that cause fluid motion upon voltage excitation. The mechanism of fluid motion and the strength of induced flow streams are highly dependent on the electrical parameters of the fluid (i.e., conductivity and permittivity), monophasic or multiphasic nature of the liquid system and voltage parameters (i.e., AC frequency and voltage amplitude). Application of low-frequency AC voltages to a pair of co-planar electrodes in contact with an electrolyte generates steady (non-zero time-averaged) fluid motion that is driven by the interaction of electric field on its self-induced charges in the electrical double layer (EDL).[366] This type of flow is referred to as AC electroosmosis (ACEO) and is a strong function of the tangential electric field and the zeta potential.[56] In this context, zeta potential is defined as the voltage at the edge of the shearing plane on the surface of electrodes to the bulk medium. The ACEO fluid velocity is strongest for fluids with low ionic conductivities, and peaks at frequencies below the reciprocal charge relaxation time of the fluid (typically in the range of hundreds of Hz to tens of kHz).[180] On the contrary, fluids with high conductivities (1>M) can undergo Joule heating when AC voltages of high frequency (>100 kHz) with large amplitudes are utilized. The temperature gradients as a result of Joule heating cause local conductivity and permittivity gradients creating volume space charges that are the source of AC electrothermal (ACET) fluid actuation in the presence of a non-uniform electric field.[51] The ACEO and ACET flows are well characterized for liquid systems of homogenous compositions. On the other hand, when electric fields are applied across media consisting of

multiple liquid phases or liquids of distinct electrical permittivity/conductivity parameters, the Maxwell stresses acting on the accumulated monopolar charges at the interface derives fluid motion.[149-150] This type of flow is referred to as electrohydrodynamics, and it has developed separately from electrokinetic phenomena although both electrokinetics and electrohydrodynamics are concerned with electric-field induced fluid motion.

The integration and implementation of AC electrokinetic techniques within microfluidic channels initiated with the pioneering studies by Green and colleagues that experimentally and theoretically investigated fluid actuation by ACEO.[180, 366-367] Later on, ACEO induced flows were implemented in applications involving pumping,[368] mixing[369] and analyte transport[370] for various bioanalytical systems. Within the domain of micromixing, coplanar electrodes generating transverse electric fields with respect to the incoming flow direction were utilized for efficient mixing of low conductivity fluid streams by ACEO.[359-361, 371-372] Those micromixers mostly employed co-planar electrode pairs, which are limited in providing flow control capability and field enhancement through various biasing configurations. If an additional electrode at fixed potential is added, the magnitude and direction of flow can further be controlled by introducing potential or phase imbalances between electrodes to realize a rich variety of effects that do not occur when only one electrode pair is used. The tuning of AC signals in a three-electrode micromixer is analogous to the operation of field-effect transistors (FETs) whereby the gate, source and drain voltages are set to have a conducting/non-conducting channel in linear mode. Likewise, in an electrokinetic micromixer with electrodes in contact with a solution, the voltage on each electrode defines the electric field intensity and distribution that enable different levels of fluid mixing.

The FET concept for fluid handling has mostly been applied in conventional electroosmosis for directional flow control and pumping by the application of a perpendicular electric field to the channel surface enabling modification of zeta potential.[373-376] However, field-effect electroosmotic flows are very sensitive to the pH of the solution and are ineffective at pH values higher or lower than the value at which the native zeta potential of the surface is zero. Moreover, they mostly operate by the application of large DC voltages across the channel that are prohibitively prone to electrolysis and bubble formation. Recently, Wu et al. demonstrated a FET-based AC electroosmotic micromixer using two sets of three-electrodes in a tandem configuration.[10] They demonstrated that by tuning the gate electrodes voltages, asymmetric vortices are generated, and mixing degree can be adjusted by a small degree. However, the use of six electrodes unnecessarily complicates device biasing and analysis. Furthermore, the mixing performance in a voltage-tuned micromixer is compromised when the maximum allowed voltage is limited.

Herein, we provide the first demonstration of a phase-controlled electrically-powered micromixer whereby the phase shift between electrodes regulates the mixing extent from an unmixed state to a mixed state similar to that of a FET in switching mode (Fig. 6.1A). Applying voltages of the same amplitude with a phase lag offers flow control capability without compensating the electric potential intensities by unbalancing voltage amplitudes. We define different biasing conditions for the proposed micromixer and lay out the governing rules for achieving the best mixing by considering the source-gate and the source-drain voltages. The insightful operational analogy between the field-effect micromixer and a FET device, delivered in this work, greatly simplifies the analysis of the proposed micromixer. Finally, we utilize the proposed micromixer for the generation of nanoscale lipid-based vesicles (liposomes) employing

the process of nanoprecipitation (or solvent displacement). We show that rapid mixing of reagents, when optimized AC signals are applied, yields highly monodisperse nanoparticle populations.

6.3 Theoretical Background

The ACEO liquid motion is driven by the interaction of a nonuniform electric field with the induced charges in the diffuse double layer. A double layer forms at electrodes by the electric potential that moves counter-ions by electro-migration from the bulk electrolyte to the surface of electrodes. As the double layer charges, the tangential electric field component produces flow within the thin double layer that is the source of long-range flow patterns via the viscous forces. In an AC field, the flow velocity and direction remain unchanged in each half-cycle as both the electrode and the double layer reverse polarity, simultaneously. Thus, a time-average Maxwell force is generated giving rise to a steady electro-osmotic slip velocity, which typically points from the inner electrode spacing over the surface of electrodes when a coplanar electrode pair is considered. In a liquid of permittivity, ε, conductivity, σ and viscosity, μ, the time-averaged electroosmotic velocity at distance x from inner electrode spacing is given as follows:[56, 126, 180]

$$\langle v \rangle = \frac{1}{2} Re\left\{\frac{\Delta\sigma_q E_x^*}{\mu k}\right\} = \frac{1}{8}\frac{\varepsilon V^2 \Omega^2}{\mu x(1+\Omega^2)^2}\frac{C_s}{C_s+C_d} \tag{6.1}$$

$$\Omega = \omega \frac{\varepsilon}{\sigma}\frac{\pi}{2} x\kappa \tag{6.2}$$

Where V is the amplitude of AC potential, κ^{-1} is the Debye length of the double layer, ω is the angular frequency and Ω is the non-dimensional characteristic frequency. E_x is the tangential electric field component, and $\Delta\sigma_q$ is the time-dependent excess charge in the diffuse layer. The last right-hand-side term in eq. 6.1 is a correction factor with C_s being the Stern layer (or compact layer) capacitance and C_d being the diffuse layer capacitance. At high frequencies, the applied potential is entirely dropped across the media, while at low frequencies the voltage drop is across

the EDL. Thus, at high frequencies, $\Delta\sigma$ tends to zero resulting in no ACEO flow. At low frequencies, the electric field in the bulk media tends to zero; however, since the tangential electric field must be continuous, the E_x approaches zero in the double layer, which stops the ACEO flow. Accordingly, the ACEO flow peaks at an intermediate characteristic frequency, and ceases at high and low frequency limits.

6.4 Principal of Operation

The proposed micromixer consists of a Y-shaped microchannel with three-finger gold electrodes that are shaped sinusoidally (s-shape) running parallel to the main channel (Fig. 6.1A). The center electrode is denoted as the gate electrode, and side electrodes are interchangeably designated as the source and drain electrodes. Two coflowing streams of deionized water (DI) and dyed water solution are introduced to the mixing channel. Upon voltage excitation, the ACEO-generated transverse flows with an asymmetric pattern along the mixing length lead to the mixing of the streams.

To understand the phase-actuating mechanism, Fig. 6.1B-E schematics illustrate the physical system at a given time in the first half-cycle of AC signals looking at a 2D cross-section of the device. The voltages assigned to the source, gate and drain electrodes are designated as V_s, V_g and V_d, respectively. With one electrode grounded, two biasing schemes can be assumed for the mixer. In the first biasing scheme (Fig. 6.1B and 6.1C), the drain electrode is grounded, and the source and gate electrodes are biased with two AC signals of the same amplitude with the gate electrode imposing a phase difference. In the second biasing scheme (Fig. 6.1D and 6.1E), the gate electrode is grounded, and the source and drain electrodes are given two AC signals of the same amplitude with the source electrode introducing the phase shift. In both biasing conditions, the

driving electrodes are given voltages of the same frequency, and only the phase difference is modulated.

Mixing takes place at the interface of the two liquid streams by the microvortices generated at the electrode gaps that are extended over the electrode surfaces. The intensity of those microvortices dictates the degree of mixing. The micromixer in biasing scheme 1 acts like a FET in switching mode or linear regime with no mixing when the phase difference is zero ($\Delta\theta_{Vgs} = 0^{\circ}$) and maximized mixing when the signals are anti-phase ($\Delta\theta_{Vgs} = 180^{\circ}$). In biasing scheme 2, similar but the opposite response to phase modulation is observed with less intensity. The difference between the two biasing schemes and the overall mixing mechanism can be explained by considering the potential difference between electrodes and electric field intensity distribution when the phase lag is modulated. For instance, when $\Delta\theta_{Vgs} = 0^{\circ}$ for the first biasing condition (Fig. 6.1B), the potential difference between the source and gate electrodes is zero at all times leading to minimal mixing due to the lack of flow at the source-gate electrode gap. Conversely, at $\Delta\theta_{Vgs} = 180^{\circ}$ (Fig. 6.1C), the potential difference between the source and gate electrode is maximized providing optimal mixing for the given potentials. Table 6.1 shows the device operation under different biasing schemes considering the peak voltage in the first half-cycle of AC signals.

At any flow rate and regardless of the biasing scheme, the best mixing takes place when the potential difference between the gate and source electrodes ($|V_{gs}|$) is higher than the potential difference between the source and drain electrodes ($|V_{ds}|$). In contrast, the mixing is minimized when $|V_{ds}|$ is larger than $|V_{gs}|$. Furthermore, the larger the $|V_{gs}|$ potential is, the stronger the microvortices at the source-gate electrodes are due to the stronger field intensities. This explains why the operating conditions (Table 6.1) corresponding to Fig. 6.1C lead to the best mixing performance as semi-quantitatively and experimentally established in the future sections. The

field-effect micromixer is insensitive to the voltage polarity and thus, only absolute potential differences are important. Additionally, the source and drain electrodes are essentially symmetric and can be interchanged. Hence, $|V_{gd}|$ potential difference shall be considered (instead of $|V_{gs}|$) to predict micromixer behavior if the alternate electrode assignment is assumed.

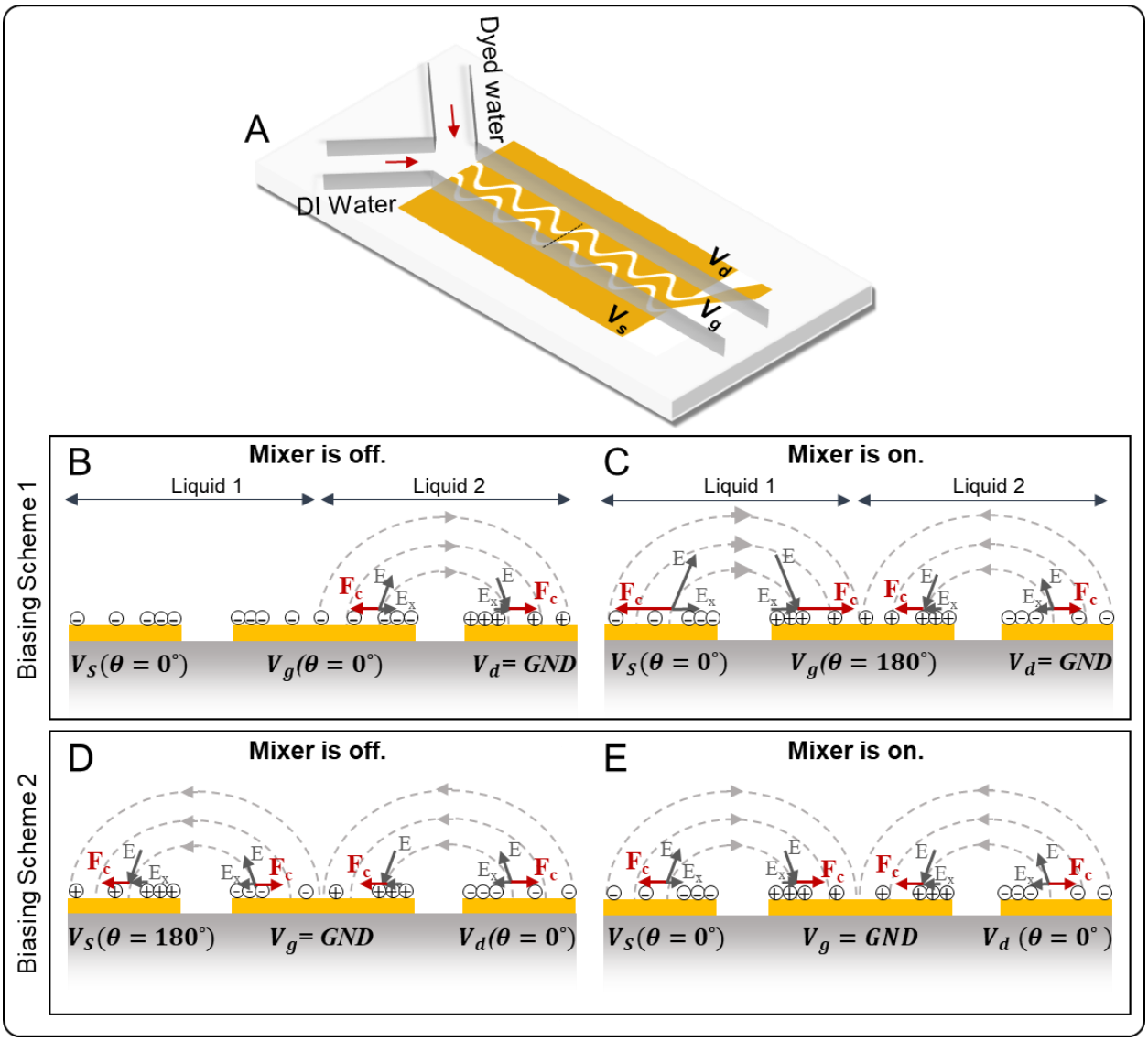

Figure 6.1 A. Schematic illustration of the micromixer. **B.** Minimized and **C.** maximized mixing occur in biasing scheme 1 when $\Delta\theta_{Vgs} = 0^\circ$ and $\Delta\theta_{Vgs} = 180^\circ$, respectively. For the biasing scheme 2, **D.** minimized and **E.** maximized mixing take place when $\Delta\theta_{Vds} = 180^\circ$ and $\Delta\theta_{Vds} = 0^\circ$, respectively.

Table 6.1 Phase-controlled FET mixing under different biasing schemes.

	V_s	V_g	V_d	$\|V_{gs}\|$	$\|V_{ds}\|$	Phase Difference	Biasing Condition	State
Fig. 2B	5	5	0	0	5	$\Delta\theta_{V_{gs}} = 0^{\circ}$	$\|V_{gs}\| < \|V_{ds}\|$	Off
Fig. 2C	5	-5	0	10	5	$\Delta\theta_{V_{gs}} = 180^{\circ}$	$\|V_{gs}\| > \|V_{ds}\|$	On
Fig. 2D	-5	0	5	5	10	$\Delta\theta_{V_{ds}} = 180^{\circ}$	$\|V_{gs}\| < \|V_{ds}\|$	Off
Fig. 2E	5	0	5	5	0	$\Delta\theta_{V_{ds}} = 0^{\circ}$	$\|V_{gs}\| > \|V_{ds}\|$	On

6.5 Materials and Methods

6.5.1 Microfluidic Platform Fabrication

The microfluidic platform consisted of gold electrodes on the device floor and a SU-8 fluidic channel with a thickness of 30 μm, width of 160 μm and length of 8 mm. The device fabrication involved patterning gold electrodes on a Borosilicate glass slide (SCHOTT North America, Inc., Elmsford, NY). The glass slide was cleaned using acetone, isopropyl alcohol (IPA) and DI water. Next, photoresist AZ5214E was spin coated to form a 1.5 μm thick layer followed by soft baking at 110 ˚C. Then, the sample was undergone UV exposure with a dose of 20 mJcm^{-2} and reversal bake at 110 ˚C for 2.5 min. Flood exposure was followed at 450 mJcm^{-2}, and developing was done in MIF720 developer for 30 sec. Following the photolithography, 20 nm of titanium and 80 nm of gold was deposited using e-beam evaporation. The electrode fabrication was completed by sonication in Microposit Remover 1165 at 70 ˚C for 30 min.

Next, the glass substrate was cleaned with acetone and IPA, and rinsed with DI water followed by one-hour dehydration bake at 150 ˚C in a vacuum oven. The fluidic channel was formed by patterning a 30 μm thick SU-8 2015 layer. First, SU-8 2015 was spin coated, and soft baked at 67 ˚C and 97 ˚C for 5 and 10 min, respectively. The substrate was then exposed at 100 mJcm^{-2} and baked at 67 ˚C for 2 min and 97 ˚C for 5 min. The sample was developed for 75 sec in

the SU-8 developer, and hard baked at 150 ˚C for 10 min to relieve surface cracks and to further harden the SU-8 film.

Finally, the flow channel was sealed by bonding a flat PDMS piece with inlet/outlet vias to the SU-8 layer on the substrate. First, (3-Aminopropyl) triethoxysilane (APTES) (Sigma Aldrich, St. Louis, MO) was vacuum-deposited onto the substrate with the SU-8 layer for 1 hour. The PDMS layer was plasma treated to activate the surface with oxygen groups immediately before bonding with the substrate. The bonding completed by heating the assembly on a hotplate at 100 ˚C for 8 hours under 20 N force.

6.5.2 Experimental Setup

The mixing experiments were performed by infusing DI water and Fluorescein dye solution using a standard infuse/withdraw syringe pump (11 Elite Programmable Syringe Pump, Harvardapparatus, Inc.). The Fluorescein solution was prepared by dissolving 2 mg of Fluorescein powder (Sigma-Aldrich, Inc.) in 1 mL of Acetone and supplementing with 300 mL of DI water followed by filtration using a 0.4 μm membrane syringe filter (Corning, Inc.). The Fluorescein solution had a conductivity of 20 μScm^{-1} measured with a conductivity meter (HI98303, Hanna Instruments, Woonsocket, RI). The image acquisition setup consisted of an inverted microscope (TE-2000E, Nikon) equipped with a CCD camera (Retiga-2000R, Nikon) and Nikon NIS-Elements D software. The voltages were applied by a 2-input/2-output function generator (AFG3200C, Tektronix, Inc.).

The lipid solutions for making liposomes as a proposed application for the micromixer were prepared by dissolving 2 mg of DPPC (1,2-dipalmitoyl-sn-glycero-3-phosphocholine) and 0.5 mg of Cholesterol in 10 mL of reagent alcohol (90% ethanol, 5% methyl alcohol and 5% isopropyl alcohol) giving a final concentration of 0.2 mg/mL of DPPC with a 1:0.25 (DPPC :

Cholesterol) ratio. This ratio remained constant throughout all experiments. All lipid formulations were stored in glass vials (VWR International Radnor, PA, USA) with aluminium covered caps and stored at 4 ˚C until use. The lipid solutions and DI water were brought to room temperature before use in the microfluidic device.

6.5.3 Mixing Characterization

The mixing performance was characterized by measuring pixel intensities across the width of the channel (150 µm from where electrodes end) and calculating the mixing index (MI) where 1 and 0 represent perfectly mixed and unmixed states, respectively. The MI was computed by taking the ratio of the standard deviation of pixel intensities, σ, to the average of pixel intensities in the mixed state, $\bar{I}$, according to the formula below:[377]

$$MI = 1 - \frac{\sigma}{\bar{I}} = 1 - \frac{\sqrt{\frac{1}{N}\sum_{i=1}^{N}(I_i - \bar{I})^2}}{\bar{I}} \tag{6.3}$$

Where I_i represents the local pixel intensities, and N is the total number of pixels.

6.6 Results and Discussion

6.6.1 Mixing performance: frequency and voltage effect

The ACEO flow velocity is a strong function of frequency and voltage amplitude (eq. 6.1).[180] To find the optimal frequency for mixing, the mixing indices for the frequency range of 600 Hz – 200 kHz were considered for each biasing scheme. Fig. 6.2A presents the frequency response of the micromixer when two streams of DI water and Fluorescein solution were infused at a confluent flow rate of 4 µl/min with an excitation voltage of 10 V_{pp}. At low frequencies (< 1 kHz), unsteady and unpredictable flow patterns were observed. Moreover, prolonged operation in the order of minutes generated gas bubbles due to electrolysis and Faradaic reactions. At larger frequencies (>1 kHz), the mixing of streams was stable and peaked at 40 kHz – 60 kHz frequency range. The

mixing dependence on voltage was also evaluated by biasing the micromixer at the optimal frequency (40 kHz) and stepping up voltage from 2 V_{pp} to 10 V_{pp} in 1 V steps (Fig. 6.2B). The mixing degree increased as the voltage level increased which is in agreement with the theoretical prediction (eq. 6.1) and previous literature.[180] An operating voltage of 10 V_{pp} (limited by the function generator) was selected for the rest of the experiments.

At the peak voltage of 10 V_{pp}, bubbles were observed at frequencies below 1 kHz reaching the DC limit. These bubbles were large enough to clog the channel and severely disturb the flow streams, which required a high-pressure flow to remove them from the mixing channel. The source of these bubbles is the Faradaic reactions that generate ions periodically in time at the electrodes following Faraday's law. Although the presence of bubbles is a strong indicator of Faradaic reactions taking place on the electrodes, Faradaic reactions do not necessarily result in gas formation. Reversible electrode dissolution and deposition often do not cause gas bubbles.[183] Moreover, it is possible that the gas molecules generated in each half cycle are insignificant such that they get dissolved without nucleating macroscopic bubbles. Negligible pH gradients as a result of Faradaic process may also not materialize as the reaction products can be consumed in the reverse reaction within the next half-cycle of an AC signal. With this understanding of the Faradaic process, it is evident that macroscopic bubbles and intensely unstable flows observed at frequencies below 1 kHz were triggered by strong Faradaic reactions. To mitigate these problems, AC signals at frequencies much higher than the inverse Faradaic reaction time should be applied to induce capacitive charging on electrodes for realizing ACEO flow, the theory of which was described earlier.[378] However, since it is possible to have Faradaic reactions without discernable physical manifestations, further understanding of flow mechanism under each phenomenon (Faradaic charging vs capacitive charging) is required.

The time-periodic Faradaic charging is qualitatively different from capacitive charging. Coions are produced at the electrodes by electrochemical reactions instead of counterions moving from the bulk to the surface of electrodes by electromigration. As a result, in a Faradic reaction, coions which have the same polarity as the electrodes amplify the external field instead of screening it. Due to this effect, it is expected that Faradaic charging produces flow velocities that increase monotonically and approach a constant asymptote at low frequency with the assumption that the reaction is reversible and reaches equilibrium within a half-cycle.[183] This behavior is different from ACEO flow based on capacitive charging, where the fluid velocity peaks at a characteristic frequency. In other words, the frequency dependence of the velocity has a bell-shaped profile in capacitive charging.[180] As can be seen in Fig. 6.2A, the frequency dependence of the MI has a bell-shaped curve with a characteristic frequency at which optimized mixing is achieved, an indication that ACEO streams are at their peak velocity. Based on this analysis, it is reasonably safe to assume Faradaic reactions are not significant in this study.

Aside Faradaic charging, Joule heating and the subsequent ACET flow may also be present in certain experimental conditions. The Joule heating produces a temperature field that depends on liquid conductivity and the voltage amplitude through $\Delta T \sim \sigma V^2/2k$, with k being the fluid heat conductivity.[379] The increase in temperature produces temperature gradients, which lead to conductivity ($\nabla\sigma = (\partial\sigma/\partial T)\nabla T$) and permittivity ($\nabla\varepsilon = (\partial\varepsilon/\partial T)\nabla T$) gradients within fluid bulk. The conductivity and permittivity gradients lead to variations in net charge density generating an electrostatic body force. Studies by Green et al.[57] and Castellano et al.[379] suggest that, for voltages smaller than 10 V (20 V_{pp}) and conductivities less than approximately 10^{-2} Sm^{-1} (10^{-4} S/cm^{-1}), Joule heating is insufficient for the generation of temperature gradients to account for observed flow velocities attributed to ACEO flow. Another theoretical and experimental investigation of

ACET flow by Loire et al. also indicates that, at a conductivity of 40 × 10^{-4} Scm^{-1} and voltages less than 10 V_{pp}, insignificant flow velocities less than 0.25 μms^{-1} are generated.[380] Noting that the liquid conductivities in these studies are at least two orders of magnitude larger than the current study, it is reasonable to assume that observed flows are solely sourced by ACEO and not ACET phenomenon.

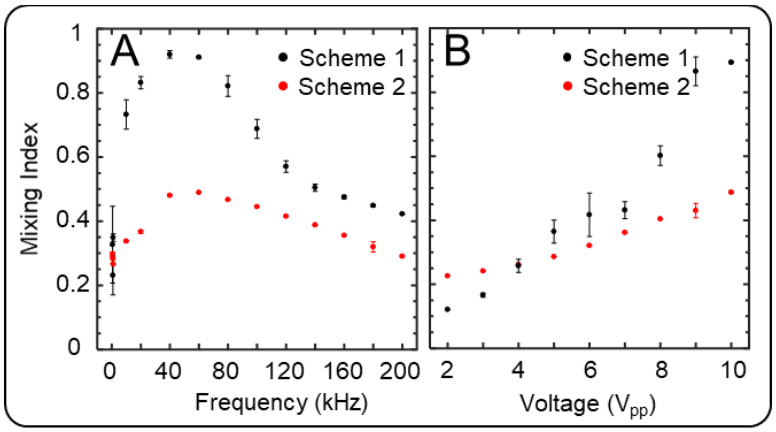

Figure 6.2 Mixing dependence on frequency and voltage**. A.** Frequency and **B.** voltage versus MI for the two biasing schemes. All experiments were performed with a 10 V_{pp} at the optimal phase lag and a confluent flow rate of 4 µl/min.

6.6.2 Phase-controlled mixing

In the proposed electrode setup, the electric field intensity and distribution can be tunned by imposing a phase lag between electrodes, which directly impact the ACEO flow velocities and the mixing degree. Thus, the electric field distribution was studied by simulating a 2D cross-section of electrodes including the glass substrate, gold electrodes, fluid (DI water) and the PDMS cover using COMSOL 6.2 (Burlington, MA). The simulations were performed by employing the Electric Current module in the frequency domain for which ac signals (10 V_{pp} at 40 kHz) were applied according to the biasing schemes introduced earlier (Fig. 6.1B-E). The logscale electric field intensities were evaluated for better visualization of electric field variations across electrodes. For each biasing scheme, the phase shifts of 0˚, 90˚ and 180˚ were assumed. Fig. 6.3A shows phasor

analysis of electric field intensity with current density streamlines corresponding to the biasing scheme 1. The electric field simulations qualitatively elucidate the mixing dependence on the phase lag between the driving voltages. As shown in this figure, when the gate and source electrodes are in-phase ($\Delta\theta_{V_{gs}}$= 0˚), the electric field intensity is very weak at the source-gate electrode gap. This leads to small fluid velocities at this gap, which effectively put the micromixer in an off state. However, as the phase lag between the source-gate electrodes is increased, the field intensity increases that induces stronger flow fields. This is evident in Fig. 6.3A when a phase lag of 90˚ ($\Delta\theta_{V_{gs}}$= 90˚) is imposed on source-gate electrodes. Finally, when the gate and source electrodes are completely out of phase ($\Delta\theta_{V_{gs}}$= 180˚), the electric field intensity is maximized for the given potentials and hence, maximized mixing performance is expected.

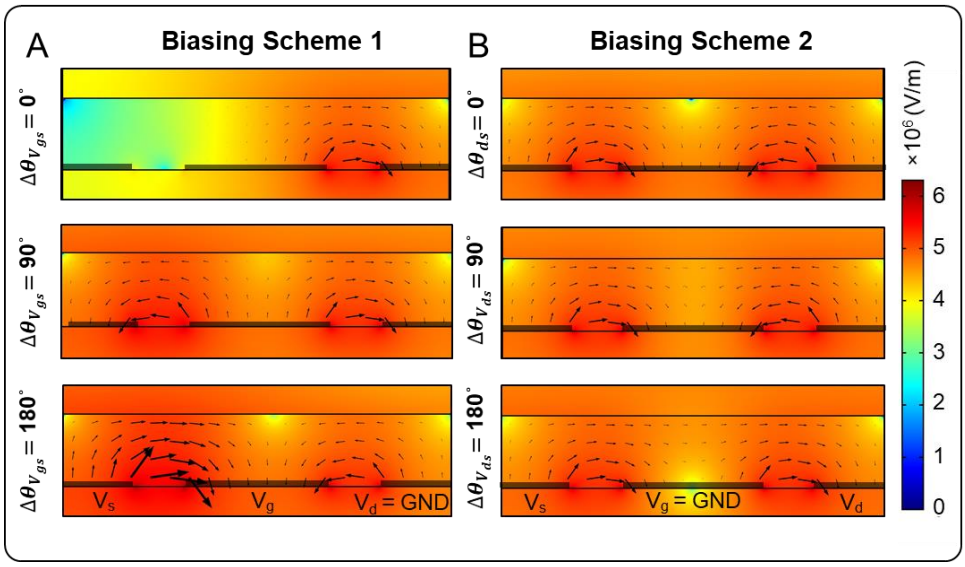

Figure 6.3 Electric field phasor analysis. **A.** logscale electric field intensity for biasing scheme 1 at different phase lag values on the source-gate electrodes. **B.** logscale electric field intensity for biasing scheme 2 at different phase lag values on the source-drain electrodes.

Similarly, the micromixer behavior for the biasing scheme 2 can be explained by analyzing the filed intensities at different phase lags between the source and drain electrodes. The electric field phasor analysis in Fig. 6.3B indicates that electric field intensity peaks for in-phase voltages

($\Delta\theta_{V_{ds}}$= 0˚). At a phase lag of 90˚, the field intensity slightly decreases especially on the center electrode. For the anti-phase voltages ($\Delta\theta_{V_{ds}}$= 180˚), however, the reduction in electric field strength on the center electrode is more pronounced while the field intensities at the source-gate and drain-gate electrodes are relatively unchanged. Accordingly, it is expected to observe optimal mixing when the applied voltages are in-phase and minimal mixing with anti-phase voltages.

The findings from the electric field simulations and the mixing dependency on the imposed phase lag were experimentally validated for various flow rates. Fig. 6.4 shows the mixing indices versus phase lag for the two discussed biasing schemes. For the biasing scheme 1, the mixing performance enhanced as the imposed phase lag on the driving electrodes was increased from 0˚ to 180˚ for all flow rates (Fig. 6.4A). The increase in mixing indices by increasing the phase lag is in agreement with the simulation analysis presented previously. Fig. 6.4B illustrates the grayscale fluorescent images of the actual device for phase-lags of 0, 90, 180 degrees corresponding to the confluent flow rate of 4 µL/min in Fig. 6.4A. At 0˚ phase-lag, barely any mixing occurs between the two streams. At 90˚phase-lag, partial mixing takes place. When the voltages are anti-phase, the two streams are completely mixed.

For the biasing scheme 2 (Fig. 6.4C), an opposite response to phase-lag with less intensity is observed which agrees with the electric field simulation analysis. Fig. 6.4D provides the grayscale fluorescent images of the micromixer representing the confluent flow rate of 4 µl/min in Fig. 6.4C. At 0˚ phase lag, the best mixing performance was achieved. The mixing slightly decreases for 90˚ phase lag and reaches the lowest level at 180˚ phase lag.

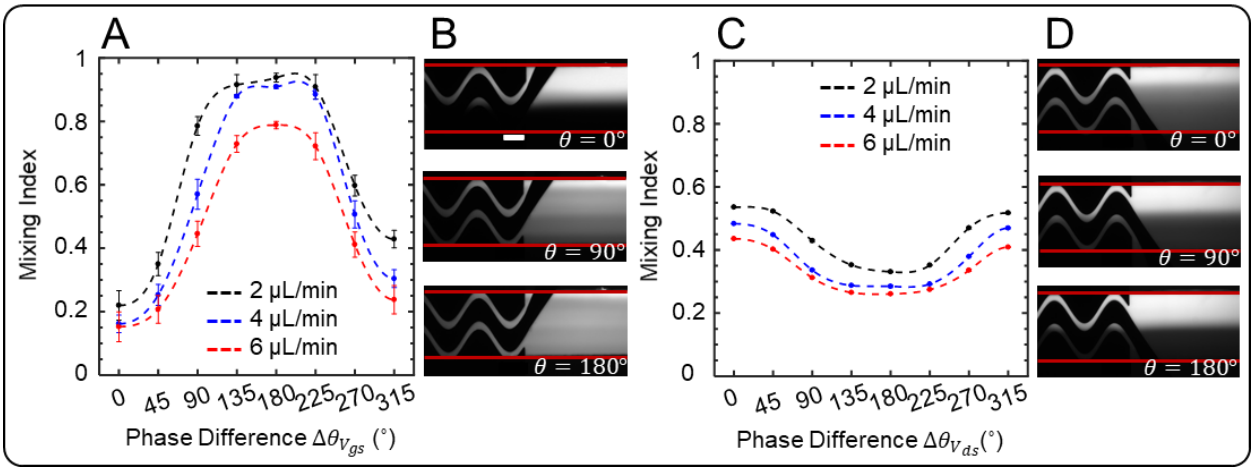

Figure 6.4 Phase-controlled mixing. **A.** MI versus phase difference for the biasing scheme 1 with $\Delta\boldsymbol{\theta}_{\boldsymbol{V_{gs}}}$ changing. **B.** Grayscale fluorescent images of the channel output showing the mixing of DI water (dark) and fluorescein solution (bright) corresponding to plot in **C.** for the confluent flow rate of 4 µl/min. MI versus phase difference for the biasing scheme 2 with $\Delta\boldsymbol{\theta}_{\boldsymbol{V_{ds}}}$ altering. **D.** Grayscale fluorescent images of DI water and fluorescein solution corresponding to plot in C for the confluent flow rate of 4 µl/min.

The performance of the proposed micromixer was compared with the existing electrokinetic micromixers based on ACEO induced flow actuation. Since different studies vary widely in the design of the microfluidic channels, the maximum volumetric flow rates sustaining MIs of 0.8 or higher reported in the literature were converted to average linear velocities for a meaningful comparative analysis. Accordingly, micromixers that can operate at larger velocities to attain a threshold mixing performance are better mixers. Table 6.2 lists various ACEO micromixers with pertinent reported channel and voltage parameters. As seen in this table, the proposed micromixer (a) achieves the highest linear velocity compared to other micromixers. Moreover, the applied voltage is the same as or smaller than other micromixers except that of micromixer in (d). Thus, a true comparison between the current study and the micromixer in (d) is not feasible. However, it is notable that the micromixer in (d) operates at the low frequency of

1Hz, which makes it very likely to cause Faradaic reactions at slightly higher liquid conductivities or prolonged voltage excitation.

Table 6.2 Comparison of the proposed micromixer with the existing electrokinetic micromixers based on ACEO fluid actuation.

Mixer	Channel Width (µm)	Channel Height (µm)	AC Voltage Parameters	Volumetric Flow Rate (µL/min)	Average Linear Velocity (mm/s)
A	160	30	10 V_{pp} at 40 kHz	4	13.9
b [362]	120	40	20 V_{pp} at 1 kHz	2	6.9
c [360]	100	44	20 V_{pp} (-2.5 DC) at 100 kHz	2	7.6
d [359]	140	60	5 V_{pp} at 1 Hz	1.25	2.5
e [361]	400	100	20 V_{pp} at 2 kHz	2	0.83
f [10]	180	100	10 V_{pp} at 500 Hz	NA	2

6.6.3 Application of phase-controlled mixing in nanoparticle synthesis

To assess the applicability of the proposed micromixer in chemical synthesis applications, fabrication of nanoscale liposomes was carried out. Liposomes are drug delivery agents that consist of a lipid bilayer shell and an aqueous core that can encapsulate various drugs and nutrients.[381] Microfluidic-based liposome synthesis is achieved through the process of nanoprecipitation (or solvent displacement) when coflowing streams of aqueous phase mix with the reagent-containing solvent.[382] The liposomes are formed by hydrophobic forces through the process of self-assembly of lipid precursors into liposomes. The most widely used and studied microfluidic platforms for liposome synthesis involve hydrodynamic flow focusing wherein a center stream containing the precursors is narrowed by sheath streams in order to enhance diffusion-based mixing at the liquid

boundaries.[383] However, effective mixing at the boundaries necessitates very high flow rate ratios of sheath streams to sample streams (up to 50), which limits the product throughput and yield. Thus, recent studies have investigated nanoparticle synthesis employing other types of passive or active mixers to achieve improved throughput and homogeneous batches with improved mixing. In-droplet mixing[384] and acoustic streaming[385] are two examples of such mixers. While both techniques are effective methods for on-chip nanoparticle synthesis, they suffer from drawbacks that limit their application. The droplet-based techniques (mostly oil-based) demand the use of surfactants for droplet stabilizations that may contaminate the products. The separation of water and oil phases further adds to the post-processing steps. On the other hand, acoustic-based methods require the use of elastomer-based microchannels for the vibration of protruding fingers to introduce acoustic microstreaming, which require the application of high voltages (tens of volts) for decent throughputs. In that context, electrokinetic-based methods can provide a viable approach for nanoparticle synthesis that operate with low voltages without any moving parts or addition of extra chemicals. Most importantly, the nanoprecipitation technique generally employs DI water and low conductivity solvents (eg., ethanol, isoproponal, acetonitrile and etc.) that are ideal for electrokinetic techniques since the likeliness of Faradaic reactions and product contamination at small voltages is very slim.

Accordingly, the proposed micromixer was modified to accommodate three microfluidic inlets to introduce two streams of an aqueous phase (DI water) and a stream of a solvent (ethanol) containing lipid precursors (Fig. 6.5A). Liposomes were formed through the process of self-assembly of hydrophobic lipid tails when streams of lipid-containing ethanol and DI water mixed. For such biphasic liquid systems, the mixing mechanism is no longer based on ACEO, instead, electrohydrodynamic instabilities facilitate the mixing of ethanol and DI water streams. This is due

to the existence of a sharp discontinuity in electrical parameters of DI water and ethanol in the presence of an electric field that accumulates monopolar charges at their interface. The electrical shear forces acting on the charged interface then give rise to fluid motion [150]. Since the flow actuation mechanism is different from ACEO, the micromixer frequency response at the peak voltage of 10 V_{pp} was characterized by considering different flow rate ratios (FRR) of sheath streams to sample stream of 10:1, 5:1 and 2.5:1 (Fig. S6.4A). Although the electrohydrodynamic mixing mechanism is distinct from that of ACEO flow, the principle of phase-controlled tunning of electric field intensity and mixing degree is still valid.

The liposomal batches were synthesized by operating the micromixer at optimal biasing conditions (scheme 1) and the frequency (1 MHz) at three different FRRs of water to lipid-containing solvent. The average size and size distribution of batches were measured using a Nanoparticle Tracking Analysis (NTA) equipment. Fig. 6.5B shows the liposome size versus different FRRs, and Fig. 6.5C is a TEM image of synthesized liposomes at a FRR of 5:1. The effect of mixing enhancement on the size characteristic of liposomal batches was considered by operating the micromixer at optimal mixing with a phase shift of 180° and minimal mixing with a phase shift of 0°. Fig. 6.5D shows size distributions of batches produced at different FRRs considering phase lags ($\Delta\theta_{V_{gs}}$) of 180° and 0° for each FRR. In this figure, it is observed that the monodispersity and concentration of batches were significantly improved when the micromixer is run with optimal mixing at a 180° phase shift.

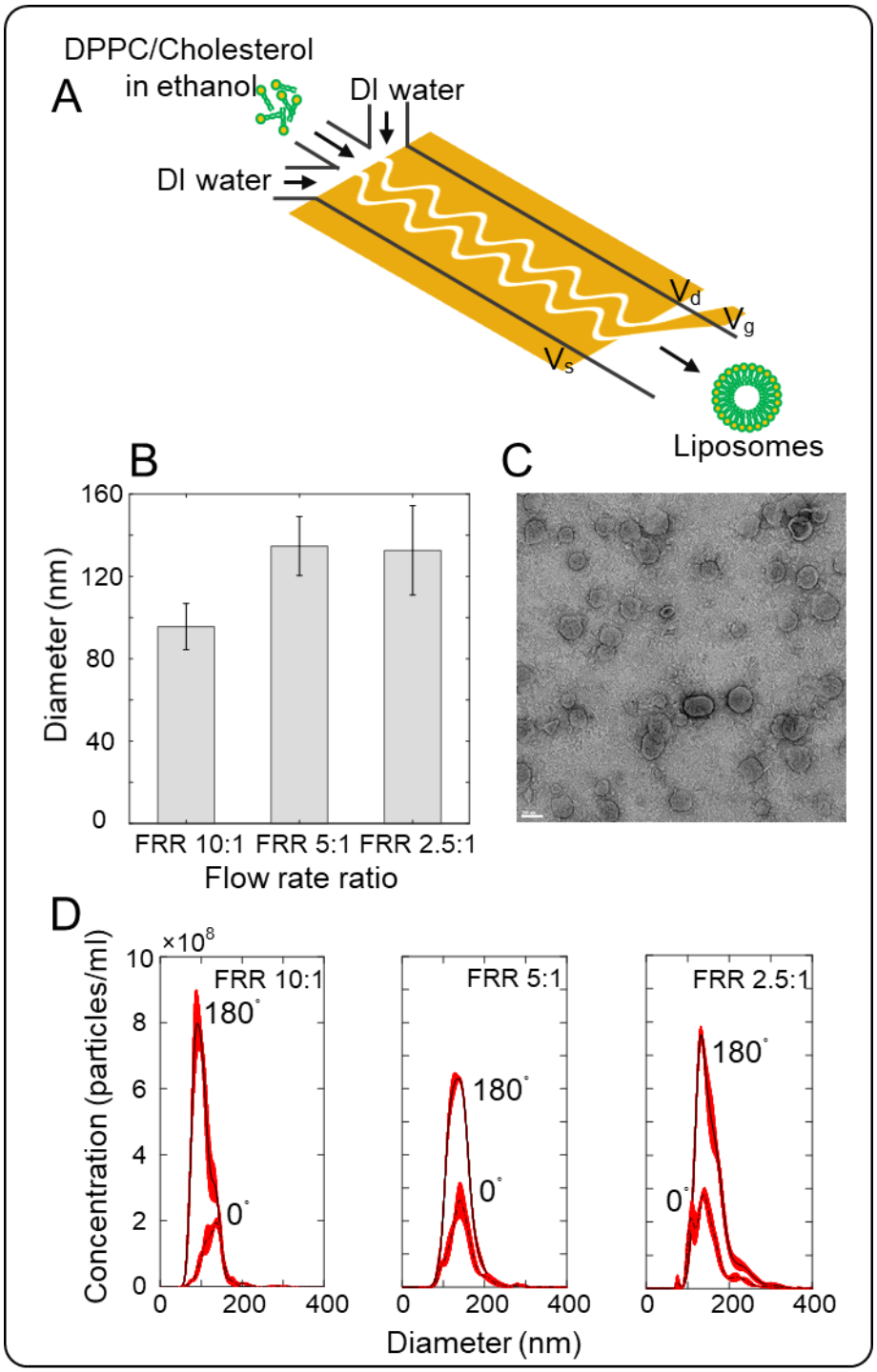

Figure 6.5 Nanoscale liposome synthesis. A. Schematic illustration of the modified device for nanoparticle synthesis. **B.** Liposome size versus different FRR **C.** TEM image of synthesized liposomes (FRR 5:1). The scale bar is 100 nm. **D.** Size distribution of synthesized nanoparticles at different FRRs for phase shifts of $\Delta\boldsymbol{\theta}_{\boldsymbol{V_{gs}}}$=180˚ and $\Delta\boldsymbol{\theta}_{\boldsymbol{V_{gs}}}$= 0˚. (n=3, Total flow rate: 200 µL/min)

6.7 Conclusion

In this article, a novel phase-controlled electrokinetic micromixer based on ACEO-generated microflows was introduced and the working mechanism was elaborated and analyzed based on electric field simulations. By modulating the phase lag between the driving voltages at constant amplitudes, the electric field distribution and intensity can be altered leading to different AC electroosmotic slip velocities and mixing performance. It is essential to note that the phase relation that leads to the best performance is a strong function of electric field distribution, which can be specified by the electrode orientation and biasing layouts. The utility of the proposed micromixer was extended to the mixing of reagents in the process of nanoprecipitation to produce lipid nano-vesicles. We only presented the preliminary results of this novel micromixer for nanoparticle synthesis, and those early results have shown promising outcomes to benefit from electrokinetic techniques for nanoparticle formation. Further studies are being carried out to fully characterize the mixing mechanism for water-solvent-water coflowing streams and nanoparticle synthesis applying the electrohydrodynamic mixing.

6.8 Supplementary Information

6.8.1 Device Geometry

The proposed micromixer consists of a Y-shaped microchannel with three-finger electrodes that are shaped sinusoidally (s-shape) running parallel to the main channel (Fig. S6.1A). To compare the efficacy of the proposed electrode geometry to that of rectangular-shaped (r-shape) electrodes, a micromixer with straight electrodes (Fig. S6.1B) was also fabricated and evaluated. For both designs, L, W and H correspond to the electrode length, channel width and channel height, respectively. The gate, source and drain electrodes widths are designated as w_g, w_s and w_d,

respectively. The spacing between each electrode pair is d. The design parameters for the s-shape and r-shape micromixers are listed in table S6.1.

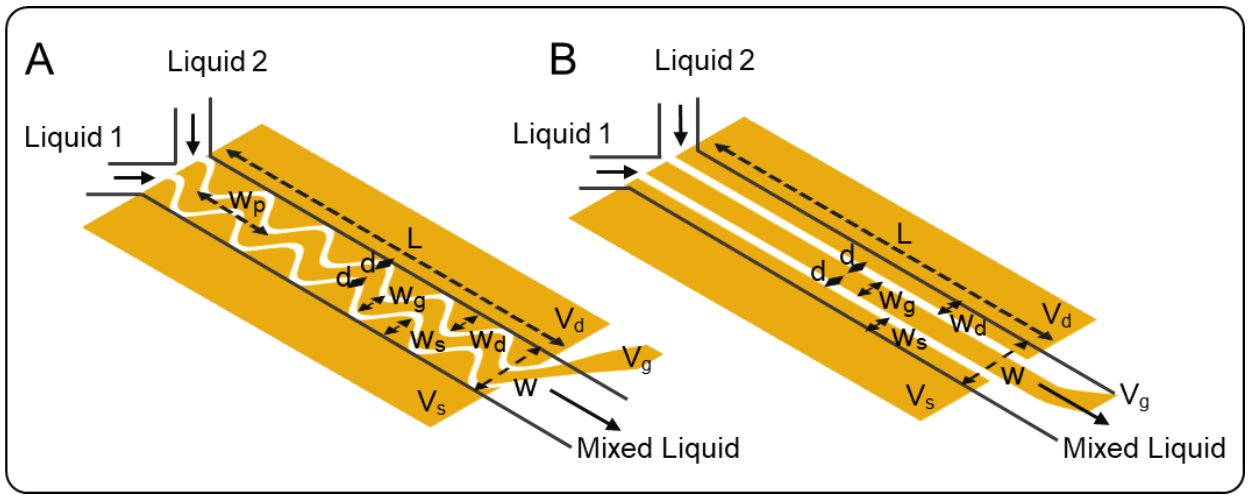

Figure S6.1 S-shape (**A**) and r-shape (**B**) electrode micromixer design parameters.

Table S6.1 Geometrical parameters for the s-shape and r-shape electrodes and the microfluidic channel.

	S-shape	R-shape	
w_g	60	60	Gate electrode width
w_d	0 – 60 (variable)	30	Drain electrode width
w_s	0 – 60 (variable)	30	Source electrode width
w_p	160	-	Electrode periodicity
d	20	20	Electrode spacing
w	160	160	Channel width
h	30	30	Channel height
L	3000	3000	Electrode length

6.8.2 Mixing Performance: Device Geometry

Unlike the majority of prior electrokinetic-based micromixers that encompassed rectangular electrode patterns symmetric to the flow direction, the altering configuration of the sinusoidally shaped electrodes introduces asymmetric vortices with respect to the interface of the incoming

fluid streams along the mixing length. To assess the mixing enhancement attained with the sinusoidal electrode geometry, a micromixer with parallel rectangular electrodes was fabricated and characterized (Fig. S6.1B). All parameters including electrode length, channel width, channel height, electrode spacing, and gate electrode width remained constant for both designs for a proper comparison.

Fig. S6.2A shows the mixing indices versus frequency for a confluent flow rate of 4 µL/min and excitation voltages of 10 V_{pp} using biasing scheme 1. As it is observed in this figure, the maximum mixing for the r-shape electrode geometry is obtained at a frequency range of 10-20 kHz. Thus, for the r-shape electrode, the mixing variation with voltage was characterized at 10 kHz and is shown in Fig. S6.2B. Overall, it can be concluded that in r-shape electrode geometry the mixing was significantly reduced corresponding to an average of 187% decrease in the peak mixing index with the biasing scheme 1.

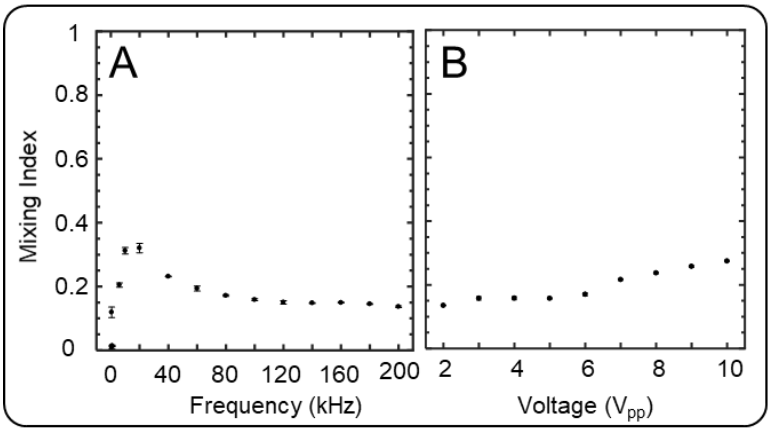

Figure S6.2 A. Mixing index versus frequency for r-shape electrode geometry (V = 10 V_{pp}, biasing scheme 1). **B.** Mixing index versus voltage for r-shape electrodes. All experiments were performed with a total flow rate of 4 µl/min.

6.8.3 Device Geometry for Nanoparticle Synthesis

The device geometry was modified to allow the injection of two aqueous streams and a precursor-containing solvent to demonstrate the applicability of the proposed micromixing mechanism and platform for nanoparticle synthesis. The modified geometry consists of the same s-shape electrode pattern with a widened microfluidic channel with three inlets. The schematic illustration of the modified design is shown in Fig. S3 and the relevant geometrical parameters are listed in Table S6.2.

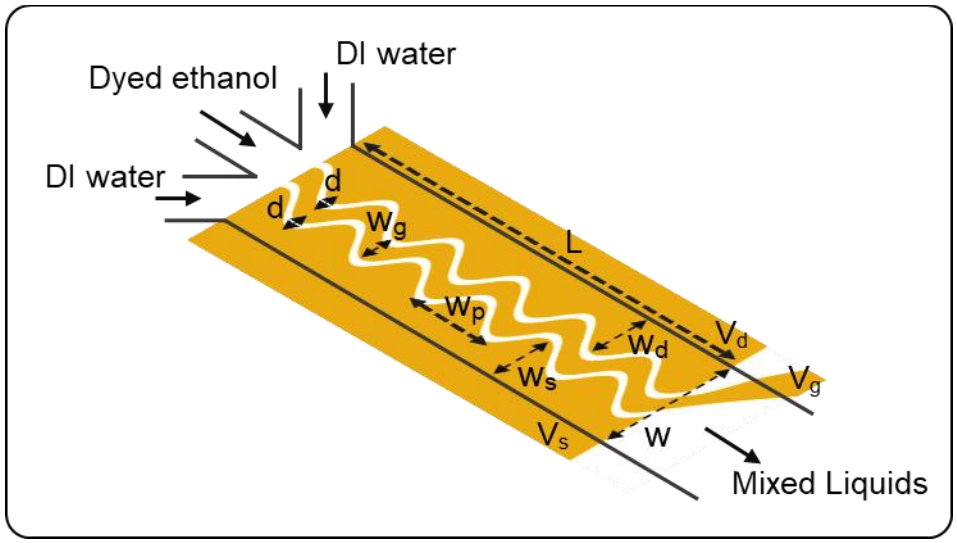

Figure S6.3 The modified platform for nanoparticle synthesis.

The frequency response of the micromixer for a water/ethanol/water flow system was assessed by injecting Rhodamine-B dyed ethanol solution and DI water. The excitation voltages remained constant at 10 V_{pp} and the frequency was varied ranging from 1 kHz to 20 MHz. Furthermore, the mixing quality for three different flow rate ratios (FRR) of water to ethanol stream was examined. The frequency response and the effect of FRR on the mixing performance are presented in Fig. S4A. According to mixing indices in Fig. S4A, frequencies above 100 kHz for all FRRs result in optimized mixing. Next, the effect of the total flow rate (TFR) on the mixing index was evaluated by operating the mixer at the optimized frequency of 1 MHz and a voltage of

10 V_{pp}. Fig. S4B shows the mixing performance corresponding to TFR values ranging from 10 µL/min to 400 µL/min at different FRRs.

Table S6.2 Geometrical parameters of the electrodes and the microfluidic channel for the modified platform.

Parameter	Value (µm)	Description
w_g	60	Gate electrode width
w_d	0 – 120 (variable)	Drain electrode width
w_s	0 – 120 (variable)	Source electrode width
w_p	160	Electrode periodicity
d	20	Electrode spacing
w	280	Channel width
h	60	Channel height
L	3000	Electrode length

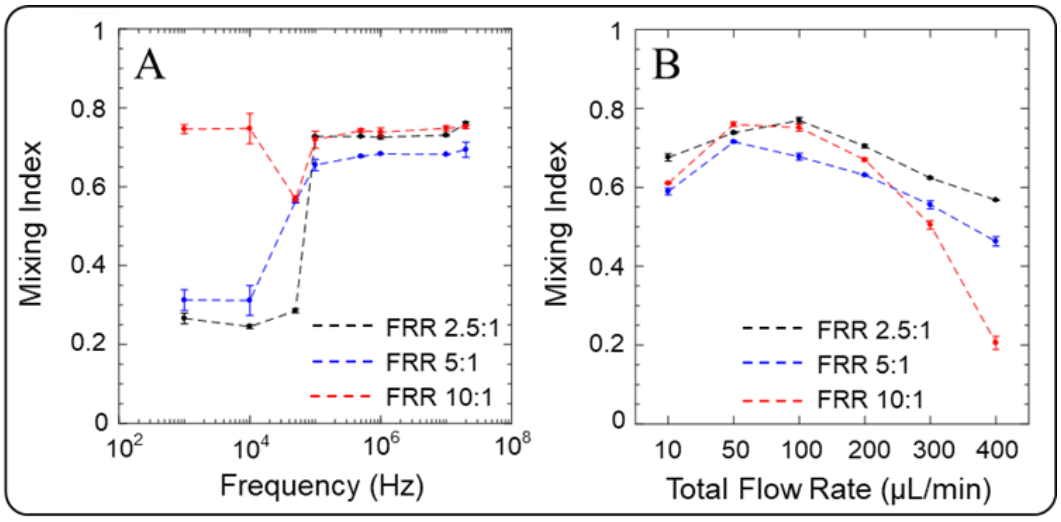

Figure S6.4 A. Mixing index versus frequency at different FRRs of DI water to ethanol. (V: 10 V_{pp}, TFR: 50 µL/min) **B.** Mixing index versus total flow rate at different FRRs of DI water to ethanol. (V: 10 V_{pp} at 1 MHz)

Chapter 7. Electrohydrodynamic-Driven Micromixing for the Synthesis of Highly Monodisperse Nanoscale Liposomes

This chapter introduces an electrohydrodynamic-assisted micromixer that was characterized and validated for the synthesis of liposomes or lipid-based vesicles. The chapter develops by presenting the micromixing characterization experiments followed by nanoparticle synthesis. The results provided in this chapter were published in the Journal of ACS Applied Nano Materials.

Journal publication:

Modarres, Paresa, and Maryam Tabrizian. "Electrohydrodynamic-driven Micromixing for the Synthesis of Highly Monodisperse Nanoscale Liposomes." *ACS Applied Nano Materials* (2020).

7.1 Abstract

Microfluidic-based chemical synthesis is uniquely suited for the fabrication of reproducible and monodisperse nanoparticle batches due to the highly controlled reaction environments in microscale dimensions. With many passive and active micromixers emerging for the on-chip chemical synthesis needs, electrically driven fluid actuation is yet an unexplored technique with much-unrealized potentials. Accordingly, in this study, we propose a micromixer based on electrohydrodynamic-driven fluid instabilities for the synthesis of liposomes using the nanoprecipitation principle. The mixing channel embeds microelectrodes to impose a transverse electric field upon coflowing reagent-containing solvent and antisolvent streams. The sharp discontinuity in electrical parameters of solvent and antisolvent at their interfaces is the source of fluid motion when low ac voltages are applied to the electrodes. The fluid instabilities at the interfaces lead to efficient mixing and nanoprecipitation of nanoparticles producing highly monodisperse liposomes for the unprecedented flow rates up to 400 μL/min and small voltages up to 10 V_{pp} compared to its counterpart active micromixers. The liposome characteristics were studied by systematically evaluating the flow parameters, initial lipid concentrations and surface charge. The obtained results and the working mechanism of the proposed micromixer can readily be extended to the production of nanoparticles of different chemistries relying on mixing of biphasic liquids.

7.2 Introduction

Liposomes have been the subject of studies for many drug delivery applications since its discovery in the sixties. A liposome consists of an aqueous core entrapped by one or more concentric phospholipid layers (lamellas), which are uniquely employed as carriers of both lipophilic and water-soluble molecules due to their lipid bilayer shell.[381] They also provide many advantages to their counterpart non-organic drug delivery systems by offering biocompatibility, biodegradability, high encapsulation efficiency, protection and sustained release of the encapsulated drugs and high intracellular uptake.[386-388] To leverage these properties of liposomes, they need to be synthesized in a highly controllable manner to tailor desired physicochemical properties such as size, polydispersity, charge and stability. Conventional bulk methods of liposome synthesis typically require multiple steps involving pipetting, injecting and vortexing under environments with characteristic dimensions in millimeter and centimeter scales.[388] This leads to uneven concentration profiles yielding heterogenous liposomes and large batch to batch variations. Techniques like sonication[389] and extrusion[390] are then necessary to produce liposomes of a certain size and high monodispersity, which make the bulk methods prohibitively time-intensive and cost-ineffective.

Microfluidic-based methods can produce monodisperse and reproducible batches by providing precise control over the reaction parameters using a minute amount of reagents in microscale reaction environments.[391-396] The formation of liposomes in microfluidic channels is facilitated by the self-assembly of hydrophobic lipid tails when streams of lipid-dissolved solvent and antisolvent mix through different mixing mechanisms. In this process, the quality and the pace of mixing are key elements affecting the size and homogeneity of nanoparticles.[382] The most widely implemented microfluidic mixing platforms for nanoparticle synthesis are hydrodynamic

flow focusers (HFF),[383] droplet-based platforms,[384] and those with embedded microstructures and baffles in mixing channels.[397] HFF methods, while widespread and simple to operate, demand high flow rate ratios of the sheath to sample streams for an efficient boundary limited diffusive mixing to produce nanoparticles of desired size and monodispersity.[45, 383, 398-399] As a result, these methods often suffer from low throughput and limited reagents that can be mixed simultaneously. On the other hand, droplet-based techniques (particularly water-in-oil systems), which mix reagents based on chaotic advection and recirculation within droplets, require the use of surfactants for droplet stabilization that can potentially contaminate the products. Furthermore, water and oil phase separation necessitates additional post-processing steps. Other passive mixers based on chaotic advection with embedded microstructures have also proven effective for liposome synthesis with high throughputs.[400-404] These methods do not require the extreme dilution of the sample for an effective micromixing, and they can operate without the addition of any surfactants. However, complete mixing takes place over millimeter-scale and the initial partial mixing introduces an uncontrolled reaction environment that may lead to unaccounted heterogeneity in the final product.[405] Some of these micromixers based on micro-grooves are also prone to the aggregation of products or contaminants that can clog the channel. On the contrary, microfluidic platforms based on active mixing mechanisms can overcome these challenges by rapid and complete mixing of reagents in geometrically simple channel designs.

Recently, few studies employed acoustic streaming via vibration of elastomeric sharp edges in contact with flow streams for rapid mixing.[385, 406] While acoustic streaming is a powerful mixing technique, the vibrational amplitude of sharp edges rapidly diminishes as the flow rate increases limiting the throughput of these methods. Achieving higher throughput necessitates the use of power amplifiers for the application of high voltages that contribute to the complexity and

the cost of acoustic micromixers. Consequently, other active micromixing techniques based on electrical or magnetic forces may be utilized to address the drawbacks of passive mixing and limitations of those acoustically powered methods.

Microfluidic platforms exploiting electrically driven fluid handling often rely on the principles of AC electrokinetics that involve AC electroosmosis (ACEO)[180] and induced-charge electroosmosis (ICEO).[54] Although a large body of literature covers various theoretical and modeling aspects of AC electrokinetics, studies on the true applications of those fluid handling methods are rather sparse, and only recently have become popular as means to facilitate mass transfer in various sensing platforms.[50, 407] However, both phenomena become progressively inefficient as the ionic conductivity of the working liquid increases and approaches the conductivity of physiological buffers limiting their broader applicability. At large liquid conductivities, AC electrothermal (ACET) flow in response to Joule heating becomes dominant.[380] An increase in temperature generates conductivity and permittivity gradients within the fluid bulk that feed variations in net charge density producing an electrostatic body force. ACET flows have similarly been employed for micromixing[9, 408] and mass transport of analytes in various biosensing applications.[409-411]

The aforementioned phenomena, that are often treated under the subject of electrokinetics, work on liquid systems with homogeneous electrical properties except for the ACET with the heat-induced modulation of fluid's electrical parameters. On the contrary, electrohydrodynamics studies the fluid behavior in liquid systems of multiphase nature or stratified liquids of differing electrical conductivities or permittivities.[58, 150, 157] Applications of macroscale electrohydrodynamics abound including electrospinning or electrospraying for tissue engineering[154] and drug delivery nanoparticle synthesis.[153, 155] Yet, electrohydrodynamic effects

haven't been leveraged for microfluidic-based processes. El Moctar et al. were among the first demonstrating the electrohydrodynamic-driven micromixing by the application of a perpendicular electric field across the interface of oil phases of different electrical conductivities and permittivities.[3] However, they did not extend their study to explore biologically-relevant applications. Recently, Lee et al. utilized rapid electrohydrodynamic mixing as opposed to turbulent mixing to synthesize block copolymer nanoparticles in bulk mode using excitation voltages up to 2.5 kV.[412] To the best of our knowledge, neither the electrohydrodynamic-driven mixing of miscible solvent-aqueous solutions nor the electrohydrodynamic-assisted synthesis of nanoparticles in microfluidic devices has been investigated before.

In this study, we present an electrohydrodynamic micromixer for homogenizing a two-phase liquid system consisting of laminar streams of solvent and antisolvent (deionized water (DI)). The proposed micromixer comprises a mixing microchannel with embedded electrodes aligned parallel to the direction of flow (Fig. 7.1A). The sharp discontinuity in fluid electrical parameters at water/solvent interfaces is the source of electrical body forces and fluid instability in the presence of an electric field that facilitate the mixing of incoming streams (Fig. 7.1B). The significance of water and solvent mixing comes into play when considering the formation of liposomes or other nanoparticle chemistries through the process of nanoprecipitation, which requires mixing of a solvent (with dissolved reagents) and an antisolvent solution.[413]

The proposed electrohydrodynamic-driven fluid mixing was fully characterized by considering the AC signal frequency, total flow rate (TFR) of combined streams and flow rate ratio (FRR) of water to solvent streams. Next, the micromixer was applied for the fabrication of nanoscale liposomes with DPPC (1,2-dipalmitoyl-sn-glycero-3-phosphocholine) as the lipid precursor. The synthesis of liposomes was rigorously characterized to study the effect of TFR,

FRR and initial lipid concentration on size, monodispersity distribution and concentration of liposomes. Furthermore, cationic and anionic liposomes were synthesized by the addition of appropriate precursors of DDAB (didodecyl-dimethylammonium bromide) and DOPG (1,2 dioleoyl-sn-glycero-3- phosphoglycerol), respectively.

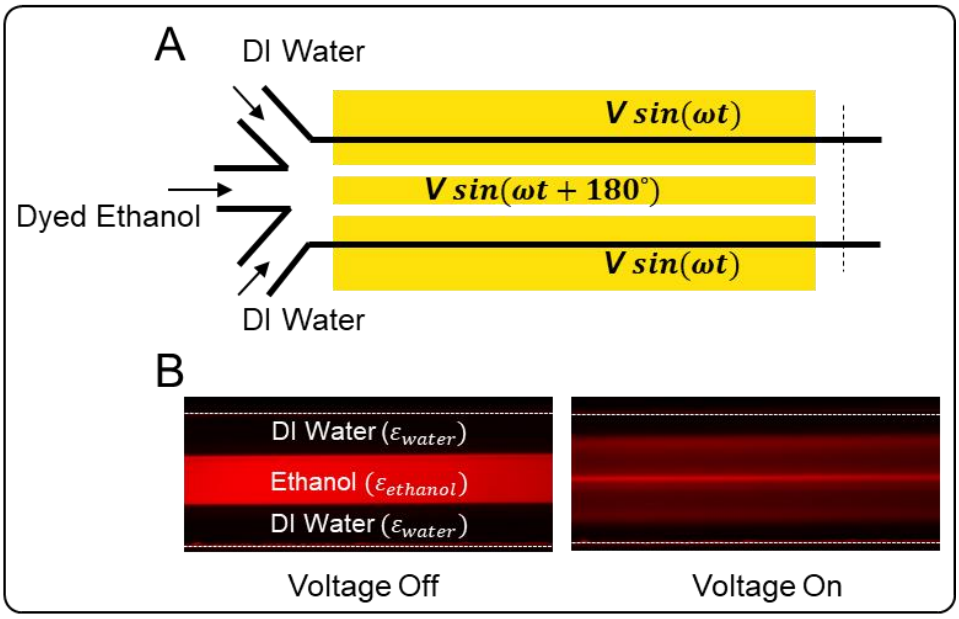

Figure 7. 1 A. Schematic illustration of device geometry, electrode setup and excitation voltages. Electrodes were excited by voltages of the same amplitude (V) and frequency (ω) with the center electrode at a 180˚ phase shift. **B.** The fluorescent images (taken at the dashed line) showing laminar streams of DI water and ethanol (dyed with Rhodamine B) when the voltage is off and on.

7.3 Results and Discussions

7.3.1 Principle of Operation

The proposed micromixer consists of electrodes on a glass substrate and a microfluidic setup with three input channels and one output channel. The flow streams are introduced by pressure-driven flow with side channels at higher flow rates in order to focus the middle stream as performed in conventional HFF methods. To synthesize liposomes, ethanol with dissolved lipids/cholesterol and DI water are introduced in the middle and side streams, respectively. The liposome formation is governed by the nanoprecipitation principle (also termed solvent displacement) when precursor-

containing ethanol mixes with the DI water.[413] In general, nanoprecipitation procedures rely on the generation of a supersaturated solution by imposing a temperature change or solvent shifting, that eventually leads to the formation of precipitates.[47] As the ethanol solution mixes with DI water, the solute (lipid molecules) concentration increases above a saturation or solubility threshold and reaches a critical concentration at which the precipitation process is initiated. Nanoparticle formation involves a nucleation phase at which seed (or nuclei) particles precipitate spontaneously followed by a growth phase, where the seeds grow by capturing remaining dissolved solute. To obtain nanoparticle batches of narrow size distribution, the nucleation phase must take place at a short timescale compared to the time length for the growth phase. Furthermore, a homogenous environment with respect to the temperature and solute concentration is necessary throughout the nanoparticle formation process. Consequently, it is crucial to have a rapid and spatially homogenous supersaturation signifying the importance of fast and complete mixing of the reagents.

Without any source of fluid agitation, the mixing of streams is solely based on diffusion at the boundaries of the streams and is enhanced by narrowing the middle stream using very high flow rate ratios (up to 15 – 50) of buffer to sample stream. However, the mixing of reagent and buffer streams can be increased by multiple folds even at low flow rate ratios if strong convective fluid instabilities are imposed onto the streams. In that respect, one method to force such fluid instabilities is through electrohydrodynamic-driven fluid flow at fluid interfaces by the application of electric fields perpendicular to the interfaces. In the present study, this is realized by exciting electrodes that are patterned parallel to the longitudinal axis of the microfluidic channel (Fig. 7.1A). The electrodes are biased with antiphase AC signals of the same frequency and amplitude for the optimal electric field intensities yielding maximized mixing performance.

According to the existing literature on microfluidic-based nanoprecipitation techniques, we expect that the liposomes mean diameter and distribution strongly correlate with the flow rate ratio of water to ethanol streams and the initial lipid concentration.[414] Furthermore, we speculate that the size characteristics of liposomes are affected by the total volumetric flow rate due to the improved mixing for smaller flow rates and vice versa. Finally, the electrohydrodynamic fluid actuation is a strong function of the AC signal frequency; thus, the characteristic frequency at which optimized mixing is attained must be considered for liposome synthesis. Accordingly, a comprehensive assessment of these parameters was carried out through mixing characterization experiments followed by liposome synthesis considering the aforementioned flow parameters and lipid concentrations.

7.3.2 Electrohydrodynamic Force Origin

The foundations of electrohydrodynamic phenomena were first introduced by Taylor & Melcher in their "Leaky Dielectric Model" and experiments with oil droplets in uniform electric fields.[58] The leaky dielectric model describes the behavior of poorly conducting liquids of distinct electrical parameters, whose interfaces acquire net charge in response to electric fields. In this description, the leaky dielectric liquids, rather than satisfying the interfacial condition of electric-displacement continuity pertinent to dielectric liquids, meet the condition of electric-current continuity. With an inevitable jump in the electric displacement, the field distribution that must satisfy the electric-current continuity results in a non-zero surface charge distribution at the interface.[415] Then, the electric shear forces acting on the charged interface give rise to fluid motion. The electrohydrodynamic flow motion is governed by the conservation of mass and Navier-Stokes equation:

$$\nabla . \boldsymbol{u} = 0 \tag{7.1}$$

$$\rho\left[\frac{\partial \boldsymbol{u}}{\partial t} + \boldsymbol{u}.\nabla\boldsymbol{u}\right] = -\nabla p + \mu\nabla^2\boldsymbol{u} + \boldsymbol{F}_e \tag{7.2}$$

where ρ and μ denote the density and dynamic viscosity of the fluid, respectively. $\boldsymbol{u}$ is the velocity field vector and p is the pressure. Here, the gravitational force term ($\rho\boldsymbol{g}$) is neglected. Also, for small Reynolds numbers ($Re \ll 1$), the inertial term ($\boldsymbol{u}.\nabla\boldsymbol{u}$) can be ignored. The electric force, $\boldsymbol{F}_e$, acting on the liquid is expressed as:

$$\boldsymbol{F}_e = \rho_q\boldsymbol{E} - \frac{1}{2}\boldsymbol{E}^2\nabla\varepsilon + \frac{1}{2}\nabla\left(\rho\frac{\partial\varepsilon}{\partial\rho}\boldsymbol{E}^2\right) \tag{7.3}$$

where ρ_q is the volume charge density, $\boldsymbol{E}$ is the electric field, and ε denotes the electrical permittivity of liquid. The last term in eq. 7.3 can be ignored for an incompressible fluid as it does not affect the dynamics (gradient of a scalar), reducing the electric force to:

$$\boldsymbol{F}_e = \rho_q\boldsymbol{E} - \frac{1}{2}\boldsymbol{E}^2\nabla\varepsilon \tag{7.4}$$

In eq. 7.4, the first term is the force acting on the fluid due to the presence of volume charges, and the second term defines the force acting on the bound polarized charges at liquid interfaces due to permittivity differences. In the current study, it can be assumed that the constituent liquids (i.e. DI water and ethanol) have the same conductivities with distinct permittivities ($\varepsilon_{DI\ water}$ = 80, $\varepsilon_{ethanol}$ = 24.5). Moreover, both liquids are considered leaky dielectrics with small conductivities. Thus, both terms in eq. 7.4 attribute to the electrohydrodynamic flow motion. The significance of the electric force terms depends on the relaxation time for free charges that is described by the ratio $\tau = \varepsilon_0\varepsilon/\sigma$ with ε_0 being the permittivity of free space.[416] If the frequency f of the AC signal is much larger than the inverse charge relaxation time ($f \gg 1/\tau$), then the free charges do not have time to build up in the fluid at the interfaces, and hence cannot be acted upon by the electric field. In this case, the term $\frac{1}{2}\boldsymbol{E}^2\nabla\varepsilon$ dominates while the term $\rho_q\boldsymbol{E}$ can be neglected. On the other hand, if $f \ll 1/\tau$, including DC electric fields, the term $\rho_q\boldsymbol{E}$ becomes dominant. There

can also be an intermediate range of frequencies over which both forces contribute comparably to the overall flow.

7.3.3 Mixing Characterization

The mixing performance of the device was evaluated by infusing DI water at the side inlets and dyed ethanol solution at the center inlet. The three electrodes were biased with the same voltage amplitudes and frequencies with the center electrode at a 180˚ phase difference. The cross-section of the output channel was imaged and pixel intensity readings were utilized for the mixing quality assessment. Fig. 7.2A provides normalized pixel intensity profiles across the output channel for different frequencies at three FRRs of 2.5:1, 5:1 and 10:1. Note that unmixed streams show a sharp change in intensity profile with lowest and highest intensities representing unmixed DI water and dyed ethanol solution, respectively. At small FRRs of 2.5:1 and 5:1, the homogenization of DI water and ethanol improved as the AC signal frequency increased from 1 kHz to 20 MHz. For the FRR of 2.5:1, mixing at frequencies beyond 100 kHz provides comparable intensity profiles. Similarly, for the FRR of 5:1, no significant change was observed in the intensity profiles for frequencies above 50 kHz. Conversely, for the FRR of 10:1, the intensity distribution across the width of the channel remained relatively unchanged with changes in AC frequency except at 50 kHz frequency.

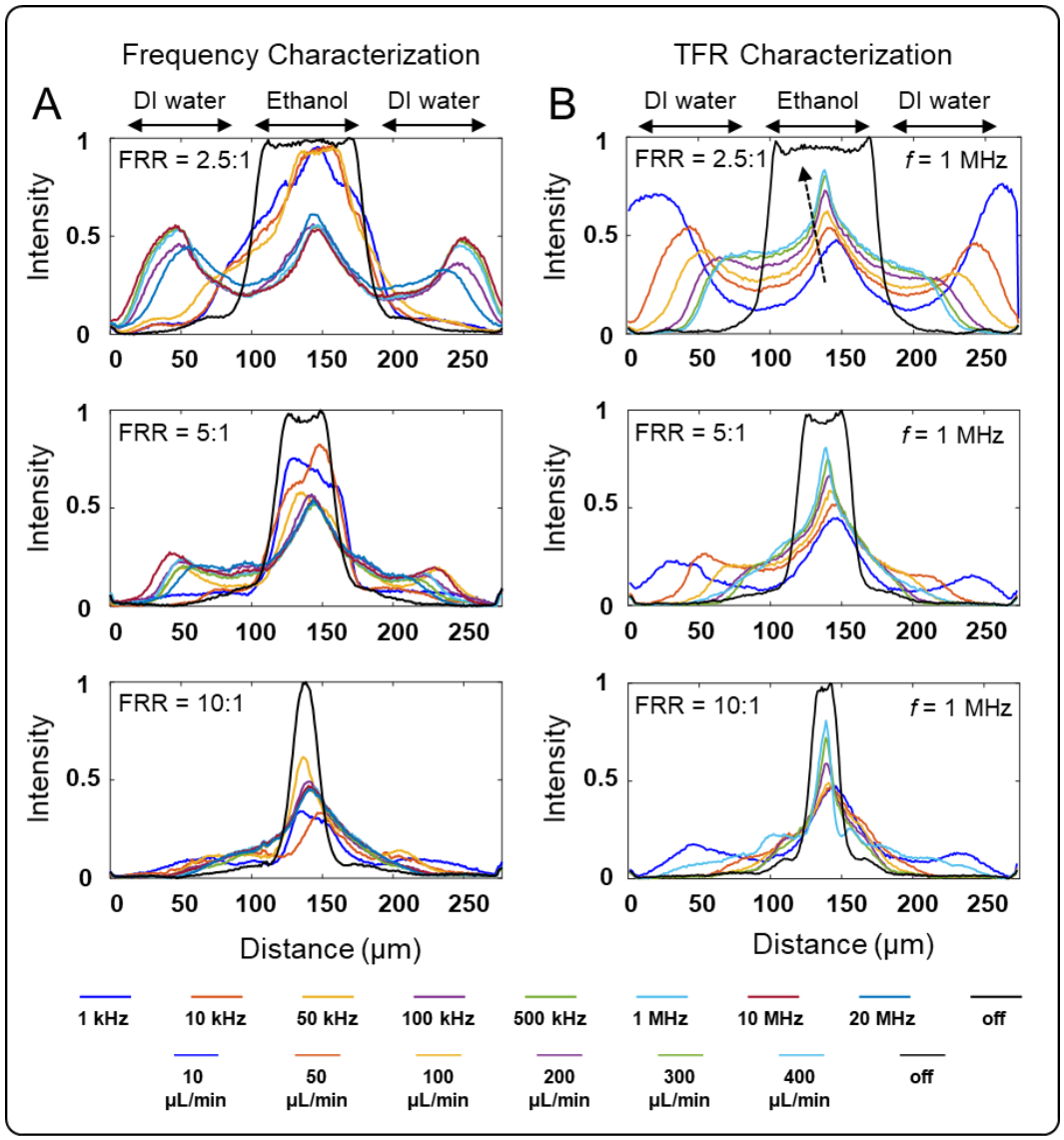

Figure 7. 2 Normalized pixel intensities at the cross-section of channel outlet at different DI water to ethanol FRRs for **A.** different AC signal frequencies ranging from 1 kHz to 20 MHz (TFR = 50 μL/min, V = 10 V_{pp}) and **B.** different volumetric flow rates ranging from 10 to 400 μL/min. Here, the frequency was fixed at 1 MHz with a voltage amplitude of 10 V_{pp}. The arrow direction indicates increasing flow rates.

The mixing dependence on the total flow rate was also investigated by operating the device at 1 MHz frequency and varying the total volumetric flow rate from 10 μL/min up to 400 μL/min. Fig. 7.2A shows the intensity profiles for different TFR values at different FRRs. In general, as the flow rate increased, the electroconvective streams were progressively suppressed yielding more distributed intensity profiles as observed in this figure. To have a quantitative measure of

mixing performance across the experimented frequency and TFR ranges, the mixing indices were calculated as presented in Fig. 7.3A and 3B. According to mixing indices in Fig. 7.3A, frequencies above 100 kHz for all FRRs resulted in optimized mixing. Moreover, mixing indices of larger 0.6 were achieved for all FRRs for up to 200 µL/min TFR with a sharp decrease in mixing degree beyond 200 µL/min TFR. Generally, a mixing index above 0.8 is considered good for most applications. However, for all TFRs and FRRs, the mixing was improved when compared to purely diffusive mixing.

Two major observations were made by mixing ethanol and DI water streams. First, strong fluid actuation was recorded for frequencies up to 20 MHz. The 20 MHz frequency limit was dictated by the function generator upper-frequency limit; thus, the effect of higher frequencies was not explored. The second observation pertains to the unprecedented high volumetric flow rates that could be sustained without entirely suppressing the fluid agitation. These observations can be attributed to two types of different electrokinetic mechanisms, namely ACEO [180] and electrohydrodynamic,[149] that are at play for the frequency ranges examined in this study.

In an AC electroosmotic micromixer, the electric field acts on the self-induced electrical double layer formed on the electrode surfaces to generate electroosmotic slip velocities that are the source of long-range fluid actuation via viscous forces.[367] This type of flow is strongly frequency dependent. At high AC frequencies, the potential drop across the double layer tends to zero ceasing the AC electroosmosis flow. On the contrary, at low AC frequencies, the potential drop takes place entirely across the double layer and tends to zero in the medium. Thus, on the basis of electric field continuity, the tangential electric field on the surface of electrodes also tends to zero yielding no AC electroosmosis flow. Accordingly, the flow velocity profile is zero at low and high frequencies and peaks at an intermediate frequency.[56] The optimized frequency has

experimentally reported to range from 100 Hz up to tens of kHz with complete suppression of the flow in MHz range for aqueous solutions of low conductivity (1 ~ 100 µS/cm).[180, 297, 360] Thus, mixing at frequencies up to few tens of kHz can be attributed to the AC electroosmosis flow that essentially originates from the interaction of an electric field with the double layer. As the frequency increases into the hundreds of kHz and MHz range, for fluid streams of homogenous permittivities and conductivities, no fluid motion is expected unless for high conductivity fluids through ACET phenomenon.[51, 417] However, when fluids with distinct permittivities are present (e.g., organic solvents and DI water), fluid instabilities take place at the interfaces of liquids. The fluid motion is actuated by Maxwell's stresses acting on the interface, where there is a charge accumulation due to the permittivity differences between the fluids. The high frequency (>100 kHz) mixing and high flow rate fluid agitation (up to 400 µl/min) observed in our experiments are ascribed to the electrohydrodynamic effect at the interface of ethanol and DI water streams with very distinct permittivities (ε_{Water}= 80 and $\varepsilon_{Ethanol}$= 24.5).

Fig. 7.3C presents the fluorescent images of the two sheath streams of DI water (black) and the focused stream of ethanol (red) for frequencies of 1 kHz and 1 MHz and flow rates of 10, 200 and 400 µL/min. As illustrated by fluorescent images and quantified by mixing indices, significant changes in intensity profiles were observed at 1 MHz frequency specifically for the 2.5:1 and 5:1 FRRs as a result of electrohydrodynamic mixing at the interface of the ethanol and DI water streams. For the FRR of 10:1, no significant differences were indicated at 1 kHz and 1 MHz frequency. Also, as illustrated in the fluorescent images, the fluid actuation was not inhibited even at the flow rate of 400 µL/min, which is exceptionally high compared to the reported on-chip electrokinetic flows.

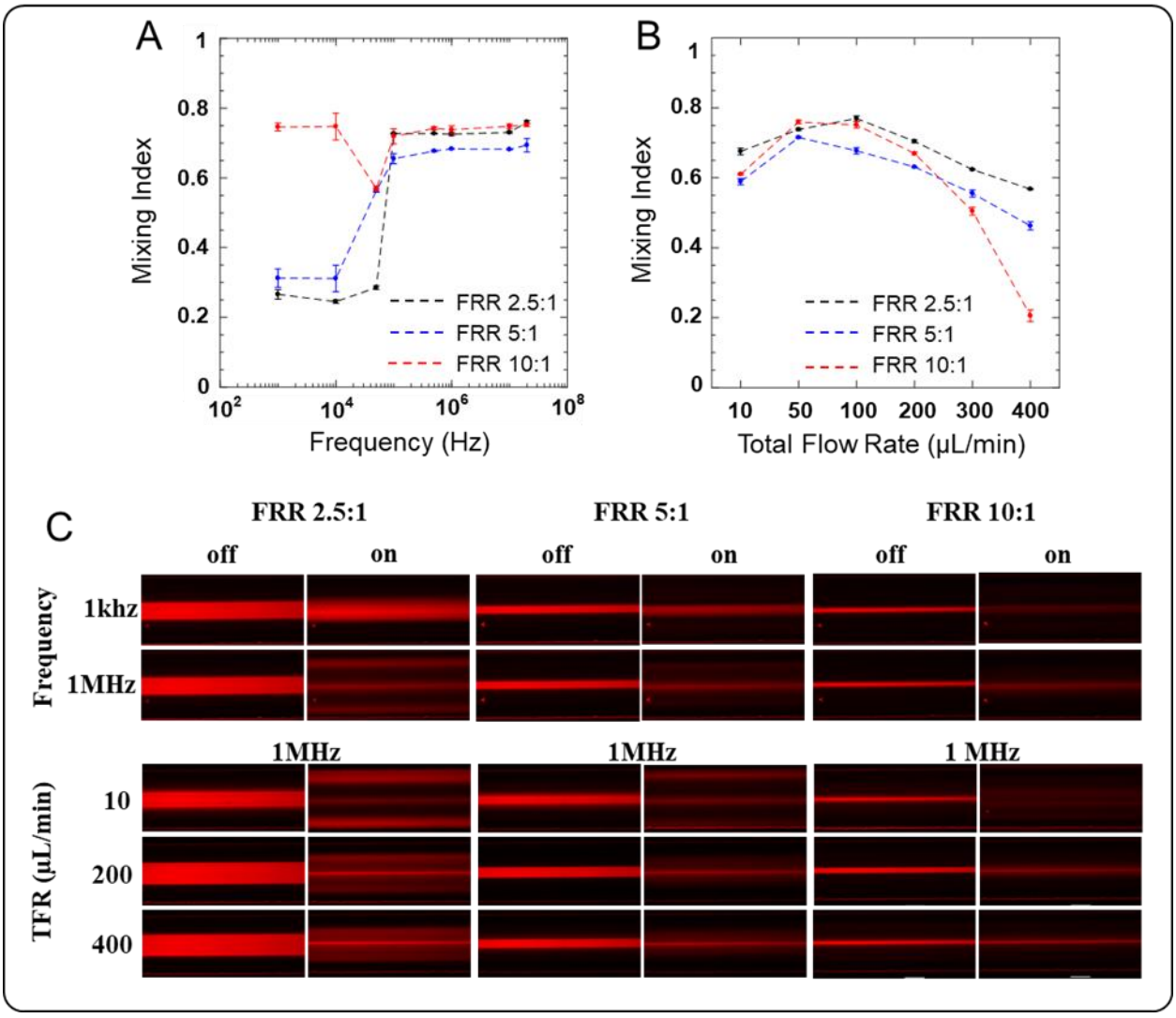

Figure 7. 3 A. Mixing index vs frequency for different FRRs (TFR = 50 μL/min). **B.** Mixing indices vs TFR for different flow rate ratios (f = 1 MHz). **C.** Fluorescent images of DI water streams and ethanol under unmixed (voltage off) and mixed states (voltage on).

7.3.4 Liposome Synthesis

Nanoscale liposomes were synthesized by considering various parameters including FRRs, TFR and initial lipid concentration. The optimized AC voltage frequency (1 MHz) was deduced from the characterization experiments to have maximized mixing at each FRR. Other voltage parameters like voltage amplitude and the phase-shift between electrodes remained unchanged for the synthesis experiments. Liposomal batches' size, size distribution and concentration were measured

using the Nanoparticle Tracking Analysis (NTA) technique as described in the Materials and Methods section.

Three different lipid concentrations of 1, 0.5 and 0.2 mg/ml were prepared for the synthesis of liposomes. Additionally, the effect of flow rate on liposome size was assessed by considering the total volumetric flow rates of 50, 200 and 400 µL/min. As observed in Fig. 7.4A, the size of liposomes had the strongest correlation with the initial lipid concentration and the FRRs. For a concentration of 1 mg/ml, the average size of liposomes ranged from 126.7 ± 0.7 to 165.4 ± 0.9 nm in diameter when water to solvent FRR was changed from 10:1 to 2.5:1 at a TFR of 50 µL/min. A similar trend was also present across other TFRs and lipid concentrations. More specifically, a decrease in the FRR corresponded to larger liposome sizes. A quick look at the mixing indices for different FRR revealed that mixing performances did not predict this trend. For instance, at a TFR of 50 µL/min, the mixing qualities at all FRRs were similar, and at a TFR of 400 µL/min, the smaller ratios resulted in better mixing. Thus, the average size of liposomes did not directly correlate with the mixing performance at different FRRs used in these experiments. Instead, it showed a strong dependence on the proportion of solvent and antisolvent composition in the final dispersive medium. It is understood that at low water to solvent flow rate ratios, few stable nuclei are formed due to the low supersaturation of solution as opposed to a very large number of small nuclei at high superstation at higher ratios with supersaturation defined as the ratio of the actual solute concentration to the equilibrium solubility.[48, 418] This, in turn, yields to larger liposomes at lower water to solvent ratios. Similarly, the experimental results indicated that the quality of mixing was not a major factor affecting the liposome size at low water to solvent ratio since it did not affect the solubility limit of lipids. In contrast, the lipid concentration had a major impact on the liposome size. Overall, a decrease in the initial lipid concentration produced smaller liposomes.

For instance, at a FRR of 10:1, liposomes ranging in size from 126.7 ± 0.7 nm to 79.3 ± 0.3 nm, 145.3 ± 1.6 nm to 103.6 ± 1.4 nm and 148.8 ± 1 nm to 102.8 ± 0.3 nm were synthesized for TFRs of 50, 200 and 400 µL/min, respectively, when lipid concentration was reduced from 1 to 0.2 mg/ml. Both observations were in agreement with what has been defined as the "Ouzo domain" in the ternary hydrophobic solute/solvent/water system to generate nanoparticles of narrow size distribution.[48] The Ouzo domain is a small region between the binodal and spinodal curves at which nanoprecipitation yields nanoparticles of low dispersity beyond which the solvent displacement produces nanoparticles and larger aggregates. More explicitly, the Ouzo domain corresponds to low solute concentrations and low volume ratios of solvent to water.

The concentration of liposomal batches (particles/ml) is presented in Fig. 7.4B. As observed in this figure, the number of synthesized liposomes was reduced as the lipid concentration was reduced. The highest concentration of nanoparticles was achieved at a lipid concentration of 1 mg/ml and a FRR of 2.5:1. Moreover, with the lowest concentration of 0.2 mg/ml, the variation in batch concentrations amongst different FRRs and TFRs were the smallest. Overall, the average concentration was estimated to be about 1×10^{11} particles/ml, which corresponded to 2×10^{10} particles/min considering a total flow rate of 200 µL/min. Finally, the size distribution of liposomal dispersions was assessed for different TFRs across all three concentrations. Fig. 7.5 illustrates the size distribution of liposomes fabricated at a FRR of 10:1. As shown in this figure, the nanoliposomes were highly monodisperse in population and as the TFR decreased, a narrower size distribution was achieved. This was ascribed to improved mixing at lower TFRs. Overall, it can be concluded that the effect of TFR and mixing quality was more pronounced on the size distribution rather than the average diameter of the nanoparticles.

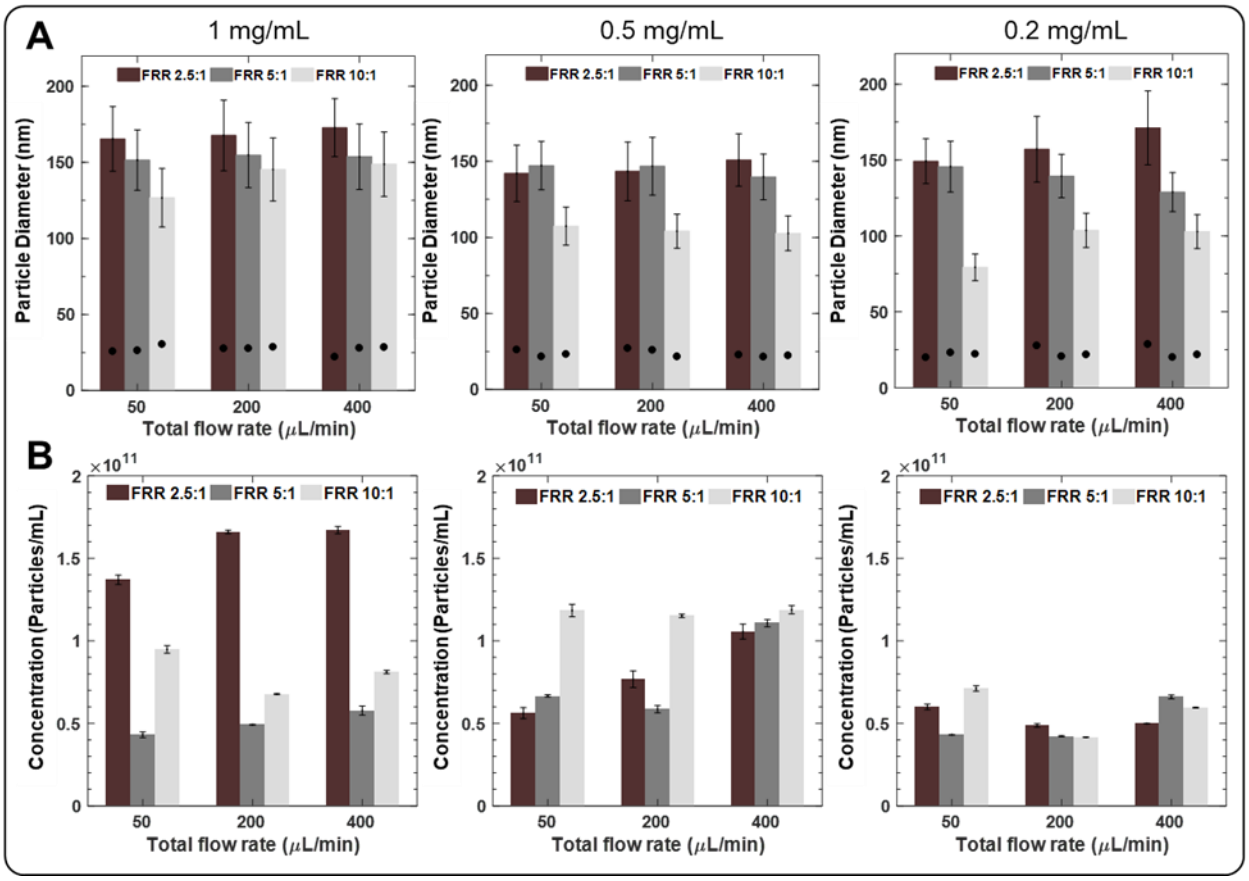

Figure 7. 4 A. Size and **B.** concentration of liposomes for different initial lipid concentrations of 1 mg/ml, 0.5 mg/ml and 0.2 mg/ml. For each initial concentration, the effect of TFR and FRR on the liposome size and final batch concentration were measured. The error bars in size plots indicate the average standard deviations of liposome distributions in a single batch and circle markers are the relative standard deviations indicating the nanoparticles' size spread.

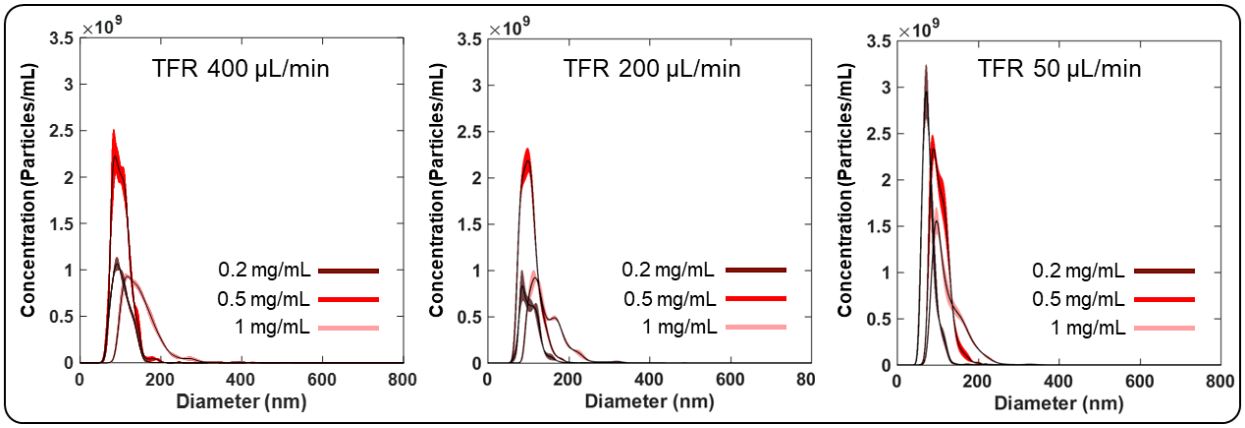

Figure 7. 5 The size distribution of liposomal batches for a FRR of 10:1 at different initial lipid concentrations and TFRs of 400, 200 and 50 μL/min.

We examined the central hypothesis of this study that the induction of fluid instabilities for enhanced mixing should improve the physiochemical characteristics of liposomes by size reduction and monodispersity enhancement. Accordingly, we produced liposomes under electrohydrodynamic-induced flow instabilities and diffusion-assisted flow mixing conditions. In particular, a flow rate of 200 µL/min was selected to synthesize liposomes at different lipid concentrations and FRRs in the presence and the absence of applied voltages. Fig. 7.6A and 6B illustrate the size and concentration of liposomes for these two states. Under the electrohydrodynamic driven flow mixing, smaller liposomes were generated. This was particularly evident for the FRRs of 5:1 and 10:1. Most importantly, higher concentration batches were reproducibly fabricated when the voltage was on. The production of smaller nanoparticles with higher concentrations with the electrohydrodynamic-based synthesis was ascribed to the highly efficient mixing that reduced the time between nucleation and aggregation of nanoliposomes. At last, the effect of electrohydrodynamic-mediated micromixing was manifested in the size distribution of liposomes. Fig. 7.7 delivers the size distribution plots with size mode values that clearly shows higher concentration and monodispersity of liposomes fabricated through the electrohydrodynamic flow micromixing.

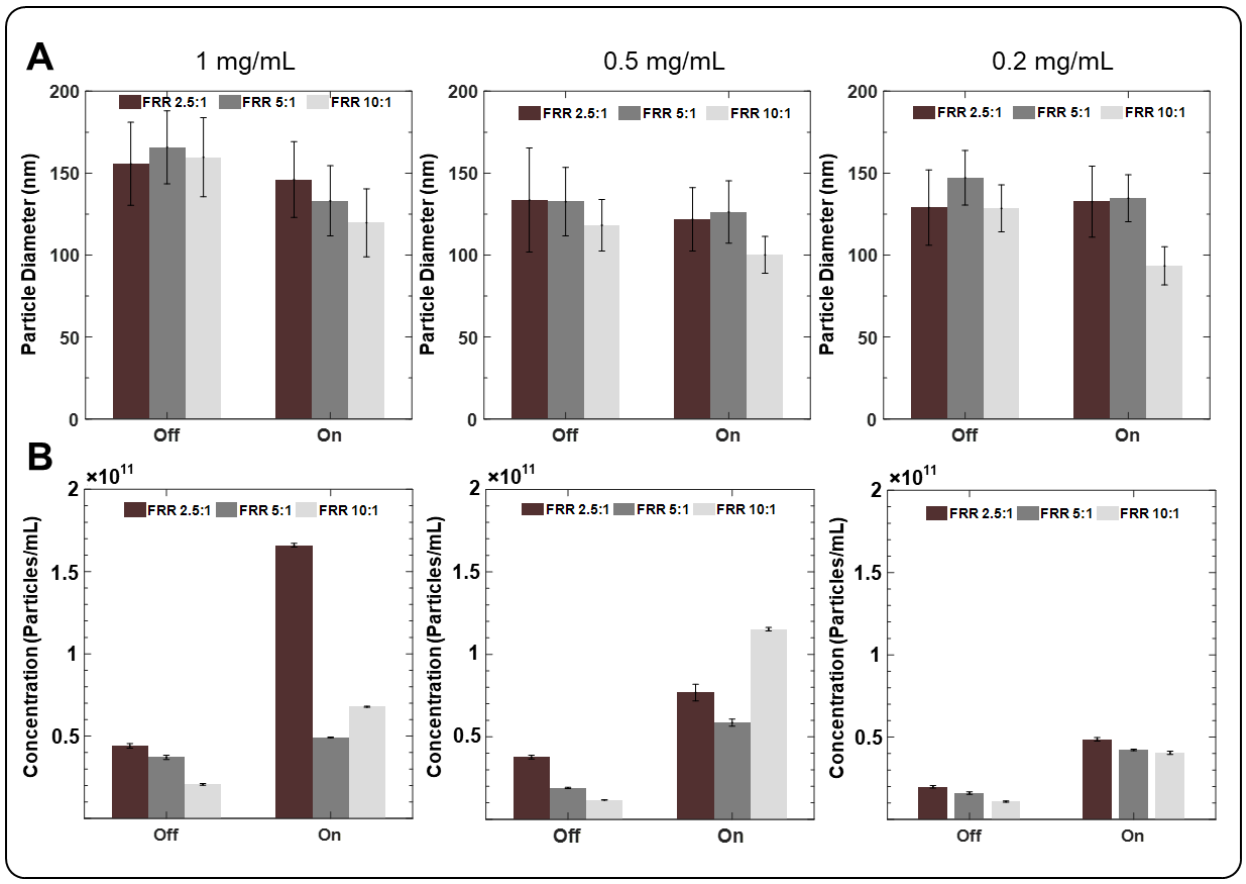

Figure 7. 6 A. Size and **B.** concentration of liposomes for different initial lipid concentrations when the voltage is off and on. The error bars in size plots indicate the average standard deviations of liposomes distribution for each condition.

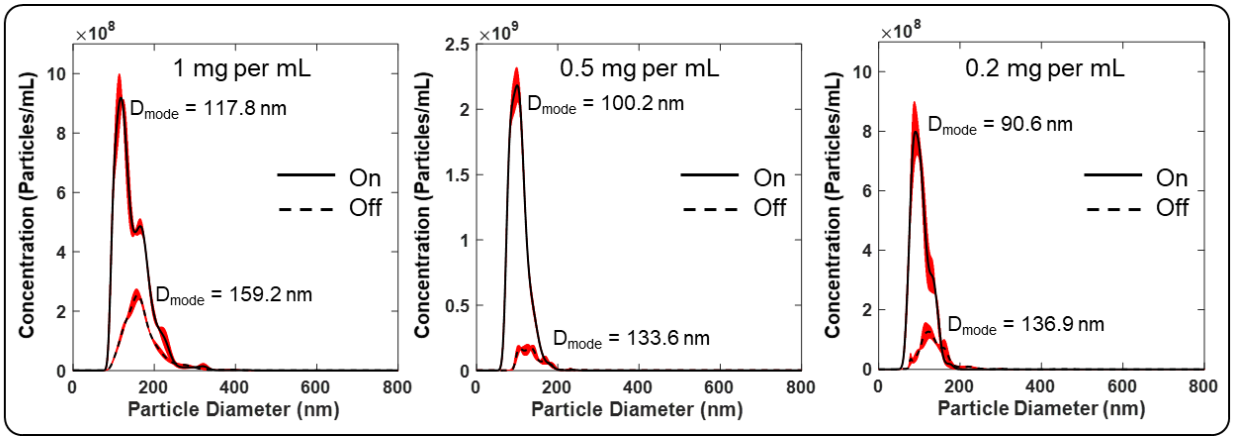

Figure 7. 7 The size distribution of liposomes for different initial lipid concentrations with a TFR of 200 µl/min and a FRR of 10:1. The solid line represents electrohydrodynamic-based synthesis (or voltage on), and the dashed line represents diffusive-based synthesis (or voltage off). In each plot, the mode diameter (D_{mode}) of liposomal batches are reported.

Upon confirming the lipid concentration and flow parameter effects on colloidal liposomal dispersions, we investigated the synthesis of cationic and anionic liposomes through the addition of appropriate precursors, keeping lipid/cholesterol formulation the same. The surface charge of liposomes measured by the colloidal zeta potential is a key indicator of the stability of liposomal dispersions. Large positive (>30 mV) and negative (<−30 mV) zeta potentials generally translate to physically stable colloidal dispersions due to the electrostatic repulsion of individual particles. Aside from physical stability, charged liposomes find applicability to many specific needs of nano-drug delivery systems. Cationic liposomes are increasingly being evaluated as gene-delivery agents due to their ability to form complexes with negatively charged DNA.[419] However, the inactivation of cationic liposomes in the presence of serum and concerns regarding their cytotoxicity have given rise to the use of anionic liposomes for gene delivery despite their limited efficiency. Furthermore, the surface charge of liposomes is an indicator of the circulation and intracellular uptake.[420]

Cationic and anionic formulations were prepared by respectively adding DDAB and DOPG lipids to DPPC/Cholesterol in different weight ratios. Fig. 7.8A shows the zeta potential of liposomal suspensions. All DDAB weight ratios produced highly positive liposomes with a size range of 91.8 ± 4.7 – 109.1 ± 1.7 nm. The most stable anionic liposomes were produced for DPPC:DOPG ratio of 2:1 with a zeta potential of -34.29 mV. Note that neutral liposomes had a zeta potential of approximately 3.2 mV. Fig. 7.8B illustrates the TEM image of anionic liposomes with the inset showing a single liposome. Intact disk-shape liposomes, as well as fractured liposomes, are observed in this image. The appearance of fractured liposomes could be a side effect of negative staining. Negative staining of liposomes often results in artefacts since liposomes are not fixed in their native structure as opposed to protein complexes. The artefacts may give the

appearance of collapsed, distorted and rearranged liposomes. For instance, the interaction of liposomes with carbon film on the imaging grid often leads to spreading of lipids and sometimes recombination of lipids to hydrophilic films or other structures. As a result, some of the distorted structures in the TEM image can be attributed to the negative staining artefacts. However, not all anomalies (i.e. rippled structures, micelles, bicelles, etc.) should be considered as a negative staining issue and need to be confirmed by Cryo-TEM. Cryo-TEM eliminates many negative staining problems since liposomes are preserved in their most native state. The sample is vitrified in a thin layer of solvent and imaged at very low temperatures, such that the medium neither changes phase nor evaporates in the high vacuum. In this study, further imaging analysis was not pursued due to inaccessibility to a Cryo-TEM.

Finally, as depicted in Fig. 7.8C and 8D, the size distribution plots of charged liposomes indicate highly monodisperse populations for both cationic and anionic liposomes (Fig. 7.8C and 8D). Indeed, the size distribution plots directly reflect the overall trend observed for the zeta potentials. Additionally, the cationic and anionic liposomes were smaller in size than their counterpart neutral liposomes.

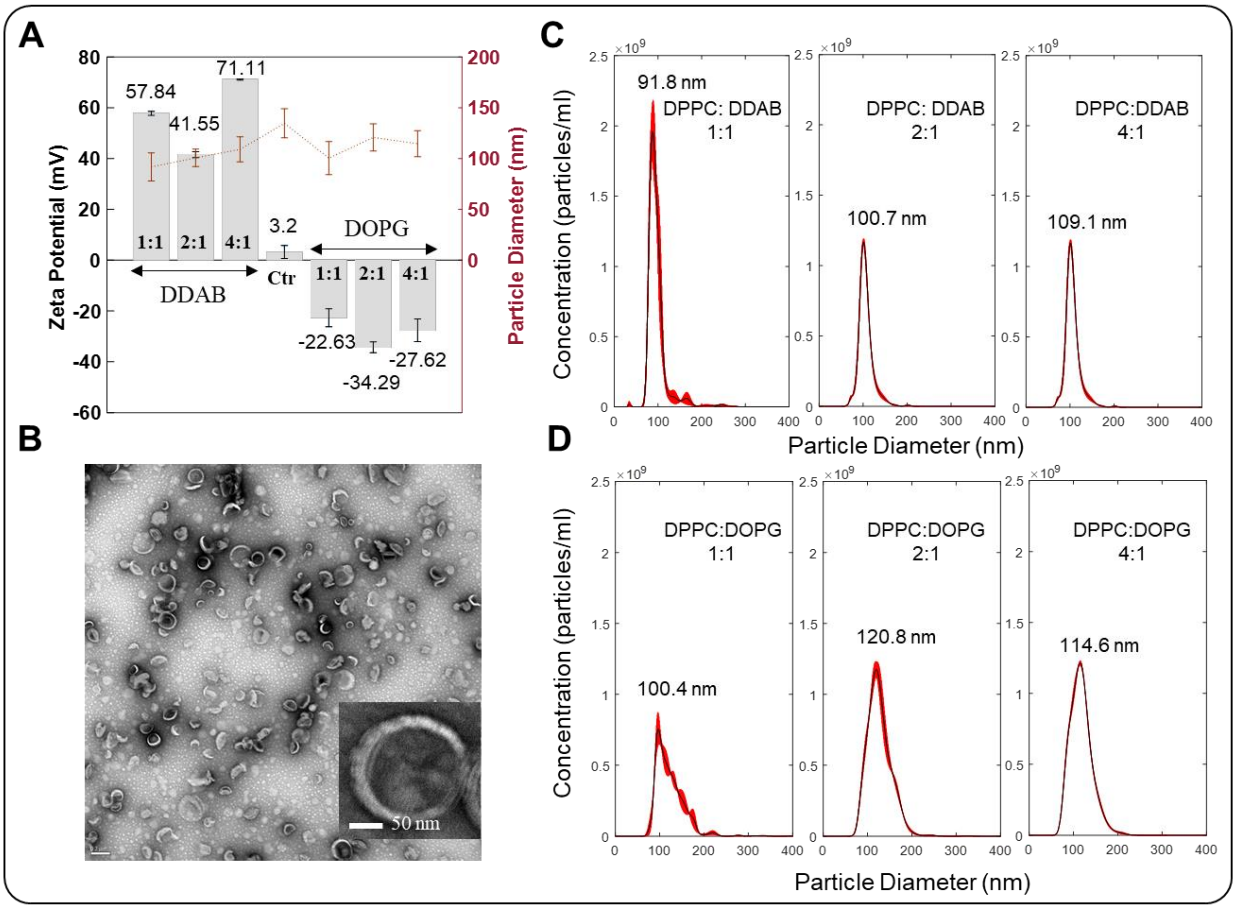

Figure 7. 8 A. Zeta potentials and sizes of liposomal dispersions with different weight ratios of DPPC to precursors DDAB and DOPG. **B.** The TEM images of anionic liposomes. C. The size distribution of cationic liposomes for different formulations with mode values noted. D. The size distribution of anionic liposomes for different formulation with mode values noted. (n=3)

7.4 Discussion

The implications of voltage parameters and media properties on the electrohydrodynamic-assisted nanoparticle synthesis are often materialized through the induction of different micromixing mechanisms and voltage-triggered electroporation of assembled membranes. In this study, an AC signal of 10 V_{pp} amplitude was utilized, which remained constant throughout characterization and synthesis experiments. The effect of AC signal frequency on the mixing performance was studied using a frequency range of 1 kHz up to 20 MHz. Both voltage amplitude and frequency are critical parameters in defining the performance of the proposed

electrohydrodynamic micromixer. In general, the higher the voltage is, the stronger the electric field intensity and the induces flows are, which result in improve mixing. The applied voltage, however, cannot be increased indefinitely as Faradaic charging starts to take place at sufficiently large voltages. Faradaic charging often causes electrolysis and bubble formations that are detrimental to the device operation. At the peak voltage of 10 V_{pp}, bubbles were only observed at frequencies below 1 kHz reaching the DC limit. These bubbles were large enough to clog the channel and severely disturb the flow streams, which required a high-pressure flow to remove them from the mixing channel.

Aside from Faradaic charging, increasing voltage may induce ACET flows in addition to electrohydrodynamic flows. Application of a voltage to electrodes in contact with a liquid can result in Joule heating, which produces a temperature field that depends on liquid conductivity and voltage amplitude through $\Delta T \sim \sigma V^2/2k$, with σ being the liquid conductivity, V being the voltage amplitude, and k being the fluid heat conductivity.[379] The temperature variations within the volume of contained liquid lead to conductivity and permittivity gradients that feed variations in net charge density generating an electrostatic body force. Studies by Green et al.[57] and Castellano et al.[379] suggest that for voltages smaller than 10 V (20 V_{pp}) and conductivities less than approximately 10^{-2} Sm^{-1} (10^{-4} Scm^{-1}), Joule heating is insufficient for the generation of temperature gradients to cause AC electrothermal flows. Another theoretical and experimental investigation of ACET flow by Loire et al. also indicates that, at a conductivity of 40×10^{-4} Scm^{-1} and voltages less than 10 V_{pp}, insignificant flow velocities less than 0.25 μms^{-1} are generated.[380] Noting the experimental conditions in this study (i.e., low conductivity DI water and ethanol solutions and operation voltage of 10 V_{pp}), it is reasonable to assume that ACET phenomenon is not contributing to the observed flows. Nevertheless, if anti-solvent solutions of higher conductivities are utilized, the generation

of Joule heating and the subsequent ACET flow is inevitable even at low voltages. The replacement of anti-solvent solution with common ionic solutions such as phosphate buffered saline (PBS) should generate ACET flows without subsiding the electrohydrodynamic flows. As described earlier, the working mechanism of electrohydrodynamic mixing relies on fluid systems with liquids of distinct electrical permittivities and conductivities. In this study, ethanol and DI water with distinct permittivities but similar conductivities were employed. If DI water is replaced with PBS, there will be significant differences in electrical permittivity as well as conductivity of PBS and the solvent solution, that will produce electrohydrodynamic flow actuation. However, the intensity of the generated flows as well as the frequency response of the system can be different from those observed in this study. Moreover, the contribution of ACET flow to the overall flow is another key question that needs to be answered. Finally, the increased temperature as a result of Joule heating may affect the size and distribution characteristics of liposomal batches.[421] Therefore, further experiments are necessary to find optimized parameters for micromixing and liposome synthesis.

So far, we discussed the effect of voltage on the operation of the proposed platform. The relation between frequency and the resultant flows in terms of strength and the physical mechanism is more complex than that of voltage. From AC electrokinetics studies, it is known that ACEO and ACET are strong functions of frequency. For instance, ACEO flow velocity peaks at a characteristic frequency in the range of the reciprocal charge relaxation time of the fluid (typically in the range of hundreds of Hz to tens of kHz).[180] The dependency on the frequency is attributed to the frequency-dependent formation of an electrical double layer (EDL) on the surface of electrodes. Similarly, the electrohydrodynamic flow velocity is expected to be responsive to frequency variations as described earlier.

Lastly, the electric field strength and duration can affect the chemical structure of lipids and the physical integrity of lipid membranes in formed liposomes. Much of our understanding of the effect of voltage on lipid membranes comes from cell electroporation studies.[422] Exposure of biological cells to sufficiently high electric fields develops an induced transmembrane voltage across the cell membranes that leads to the formation of aqueous pores in the lipid bilayer. The aqueous pores can also develop without the application of external fields. Under certain conditions, for instance, high temperature, surface tension, or both, cell membranes can permeate water and some monoatomic ions due to the formation of aqueous pores in the lipid bilayer. However, an external electric field facilitates the formation of a greater number of pores that are more stable than in the absence of an electric field. The aqueous pores have radii of at most several nanometers and their lifetime (forming and resealing) ranges from milliseconds up to minutes after the field is removed.[423] The first-order approximation of transmembrane voltage (U_m) for a spherical cell of radius R in a uniform electric field of strength E is given by Schwan equation:[424]

$$U_m = fERcos\theta\left(1 - e^{-\frac{t}{\tau}}\right) \tag{7.5}$$

where θ is the angle measured from the center of the cell with respect to the direction of the field, τ is the time constant of membrane charging, and t is the time elapsed since the onset of the field. f is a dimensionless factor reflecting electric and dimensional properties of the cell and the surrounding medium. Eq. 7.5 assumes that the cytoplasm and extracellular medium are purely conductive (i.e. nonzero conductivity, but zero dielectric permittivity) and the membrane is a lossy dielectric (having both nonzero conductivity and permittivity). With those assumptions, eq. 7.5 is generally applicable to rectangular pulses of larger than 1 μs and AC signals of up to 1 MHz.[422] For pulses of shorter time length and AC signals of higher frequencies, the accuracy of the analytical expression in eq. 7.5 becomes progressively questionable as dielectric properties of the

cytoplasm and the extracellular medium gain importance.[425] The expression in eq. 7.5 can be simplified considering that the time constant of the cell membrane is often much smaller than the duration of the electric field ($t \gg \tau$). Thus, the transient term in eq. 7.5 approaches zero giving:

$$U_m = fERcos\theta \tag{7.6}$$

Often a threshold transmembrane voltage must be reached for the electroporation of cells to happen although electroporation threshold shall not be considered as a discrete value at which all cells are either permeabilized or not affected. The threshold transmembrane voltage for various cell lines has reported varying from 0.2 ~ 1 V, conventionally generated by rectangular pulses of micro- or milli-second duration with amplitudes in the range of tenths of kV/cm to few kV/cm for most mammalian cells.[426-427] Further increase in field intensity can induce irreversible electroporation whereby permanent pores are generated that can eventually lead to cell death.

While most of the existing knowledge on electroporation pertains to cells in buffers of physiological properties as described above, general extrapolations can be made to describe the electroporation (reversible or irreversible) of nanoscale liposomes. The effect of voltage on the physicochemical properties of liposomes can be analyzed by considering both electric field intensities as well as the excitation frequency. It has been reported by a few studies that the threshold transmembrane voltage for nanoscale liposomes are relatively smaller than most studied cells.[427-428] For instance, Kakorin and colleagues used a threshold voltage of 0.3 V for electroporating liposomes ranging in diameter from 50 nm to 340 nm, which is slightly smaller than the threshold voltage for cells.[428] On the other hand, the synthesized liposomes in this study varied in size from 70 nm to 180 nm in diameter, that is almost two orders of magnitude smaller than typical cell sizes. Thus, considering both threshold transmembrane voltage as well as their

nanoscale dimensions of liposomes, it is expected that higher field intensities are required to induce electroporation in those liposomes compared to cells or cell-size liposomes.

Studies based on chip-based cell electroporation utilizing AC fields have reported voltages of 8.5 – 10 V (17 V_{pp} – 20 V_{pp}) for cell sizes of about 10 μm in diameter.[429-430] A comparative analysis reveals that at the voltage of 10 V_{pp} and for nanoscale liposomes, the likeliness of electroporation is slim. Nevertheless, if electroporation takes place, it should be reversible upon voltage removal and nondestructive to the liposome structure. Finally, the explored frequencies in this study (up to 20 MHz) is unlikely to induce any structural damage to formed liposomes as those frequencies are routinely employed with cells of various dimensions in dielectrophoresis experiments.

7.5 Conclusion

In this article, we delivered a novel electrohydrodynamic-driven micromixing platform for the synthesis of highly monodisperse liposomes with tremendous potential for drug delivery applications. We applied the proposed setup for the fabrication of neutral, anionic and cationic liposomes, and we proved liposomal batches of higher concentration and narrower size distribution can reproducibly be synthesized using this method compared to passive diffusive mixing. The fundamental basis of electrohydrodynamic-induced fluid mixing relies on multiphase liquid systems with distinct electrical conductivity/permittivity parameters. Intriguingly, these multiphase liquid systems involving solvents and anti-solvents are prevalently utilized in the nanoprecipitation of nanoparticles of different chemistries. As a result, the methods introduced in this article can readily be applied for the generation of other nanoparticles relying on the nonappreciation process. Furthermore, the device fabrication process is simple and accessible requiring only an additional metal deposition step compared to conventional soft-lithographed

microfluidic devices. Finally, the fabricated devices are robust and can be used repeatedly so long as issues with contaminant clogging or liquid leakage do not occur.

7.6 Materials and Methods

7.6.1 Materials

Reagent alcohol (90% Ethanol, 5% Methyl alcohol as denaturant and 5% Isopropyl alcohol as denaturant), 2-proponal alcohol, ethyl acetate, acetone, trichloro (1H, 1H, 2H, 2H-perfluorooctyl) silane, didodecyldimethylammonium bromide (DDAB), 1,2-Dioleoyl-sn-glycero-3-phospho-rac-(1-glycerol) sodium salt (DOPG) and cholesterol were purchased from Sigma-Aldrich (Oakville, On, Canada). 1,2-dipalmitoyl-sn-glycero-3-phosphocholine (DPPC) was purchased from Avanti Polar Lipids Inc. (Alabaster, AL, USA). Dow Corning Sylgard 184 silicon elastomer kits, containing a base and a curing agent of polydimethylsiloxane (PDMS) was obtained from Ellseworth (Germantown, WI, USA).

7.6.2 Device Fabrication

The proposed device consisted of gold electrodes on a glass slide and PDMS fluidic channels. The gold electrodes were patterned by conventional photolithography employing an image reversal process with AZ5214E photoresist. 20 nm of Titanium followed by 80 nm of gold were deposited using e-beam evaporation on the photolithographically-patterned glass substrate. Next, the electrode patterns were emerged by the dissolution of photoresist in Microposit 1165 remover heated to 70 ˚C. The electrode pattern consisted of three parallel rectangular electrodes separated by 20 μm spacings. The center electrode width was 60 μm, and the exposed width of side electrodes inside the fluidic channel was 90 μm each.

The microfluidic channels of 60 μm height and 280 μm width were fabricated using the conventional soft-lithography by patterning SU-8 2015 on a Silicon wafer. The patterned Silicon

wafer was treated with vacuum-deposited trichlorosilane. Then, PDMS (mixed in a 10:1 ratio of PDMS base and the curing agent) was poured over the patterned Silicon wafer followed by degassing to remove bubbles from the surface of PDMS and baking at 80 ˚C for 1 hour in an oven. Next, the cured PDMS was undergone an extraction procedure to remove loose uncross-linked oligomers to avoid product contamination during the synthesis process when PDMS is exposed to solvents. The extraction protocol involved successive immersion of cured PDMS in high-swelling and low-swelling solvents.[431] Specifically, the cured PDMS was extracted by immersion in ethyl acetate for 5 days followed by acetone for 2 days. The residual solvent in PDMS was removed by drying in an oven at 90 ˚C for 24 hrs.

Upon the extraction process, a PDMS slab with microfluidic channels and a glass slide with patterned electrodes were treated with oxygen plasma. Immediately after oxygen plasma, 100 µl of DI water was pipetted onto the PDMS slab to easily slide the PDMS slab when it was brought into contact with the glass slide for the alignment of the fluidic channel with the electrodes under a light microscope. After alignment, the bonding was completed by heating the assembly on a hot plate at 50 ˚C overnight. Finally, Polytetrafluoroethylene (PTFE) tubes were inserted in PDMS inlet/outlet vias for fluid delivery.

7.6.3 Experimental Setup

The mixing characterization experiments were performed by infusing DI water and dyed ethanol solution using a standard infuse/withdraw syringe pump (11 Elite Programmable Syringe Pump, Harvardapparatus, Inc.). The dyed ethanol solution was prepared by dissolving Rhodamine B powder in reagent alcohol with a concentration of 20×10^{-6} Mol L^{-1} followed by filtration using a 0.2 µm membrane syringe filter (Corning, Inc.). The image acquisition setup consisted of an inverted microscope (TE-2000E, Nikon) equipped with a CCD camera (Retiga-2000R, Nikon) and

Nikon NIS-Elements D software. The voltage was supplied by a 2-input/2-output function generator (AFG3200C, Tektronix, Inc.).

The lipid solutions were prepared by dissolving different concentrations of DPPC/Cholesterol in reagent alcohol in 1:0.25 (DPPC:Cholesterol) ratios. This ratio remained constant throughout all experiments. All lipid formulations were stored in glass vials (VWR International Radnor, PA, USA) with aluminum covered caps and stored at 4 ˚C until use. The lipid solutions were brought to room temperature before injection through the microfluidic device.

7.6.4 Nanoparticle Tracking Analysis (NTA)

The size distribution and concentration of nanoliposomes were characterized using a NanoSight NS300 instrument equipped with an sCMOS camera and a Blue 488 laser. The NanoSight NS300 instrument can work with particle concentrations in the range of ~ 10^7 – 10^9 particles/mL, which is approximately 20 – 100 particles in the field of view. Larger particle concentrations within the field of view may prevent accurate particle tracking by the NanoSight software. On the other hand, lower particle concentrations may fail to produce statistically significant results within typical measurement time frames (30 s – 120 s). The reported particles/frame value in multiple frames of a sample video obtained by the NanoSight software was used to decide whether the concentration requirements was met or not. Accordingly, the synthesized liposomes were diluted by 100×, 200×, or 1000× depending on the concentration of initial lipid. All samples were measured under dynamic conditions with the same syringe pump speed level at 100 and at a constant temperature of 25 ˚C. Each sample was analyzed by capturing three videos of 100 s length with camera level and detection threshold of 12-14 and 5, respectively.

The NTA method tracks the individual particle's position on a frame-by-frame basis and then calculates the diffusion coefficient and the size of each particle. This yields a list of single-

particle measurements, which is used to report common statistical measures of a population to represent the final particle size and distribution. These statistical parameters include mean, mode, standard deviation (SD) and median (D50). The standard deviation, reported in nanometer, relates to the absolute width of the distribution. In order to compare the NTA results with the conventional distribution measure (polydispersity index (PDI)) by the dynamic light scattering (DLS), the absolute width of the distribution can be compared to the mean diameter to obtain a relative standard deviation (RSD). RSD is calculated by taking the ratio of SD to mean and multiplying by 100. While a PDI of greater than 0.4 indicates a polydisperse population with DLS, an RSD of greater than 40 represents a polydisperse population with NTA. In the results section, the mean diameter and RSD values were reported to compare batch-to-batch differences for size and population distribution.

7.6.5 Zeta Potential Measurements

The zeta potential of liposomes was measured using a PALS Zeta Potential Analyzer Ver. 3.57 (Brookhaven Instruments Corp.). The measurements were performed by taking 200 µL of liposome samples and diluting it in 1.3 mL of DI water. For each measurement, 10 measurement runs were recorded at a temperature of 25 ˚C, and Smoluchowski model was used for calculating the zeta potential.

7.6.6 Transmission Electron Microscopy

The liposomal dispersions were negatively stained using the single-droplet method. 10 µL of liposome solution was pipetted on a Formvar-carbon coated grid. After approximately 10 s, 10 µL of 2% uranyl acetate was pipetted onto the grid for 30 s. Then the sample on the grid was absorbed with a wedge of filter paper. The grid was allowed to dry at room temperature and imaged with a Philips Tecnai T12 electron microscope at an acceleration voltage of 120 kV.

7.6.7 Mixing Characterization

The mixing performance was characterized by measuring pixel intensities across the width of the channel at a 200 µm distance from where electrodes end and calculating the mixing index (MI) where 1 and 0 represent perfectly mixed and unmixed states, respectively. The MI was computed by taking the ratio of the standard deviation of pixel intensities in the mixed state, σ, to the standard deviation of the pixel intensities in the unmixed state, σ_0 , according to the formula below:

$$MI = 1 - \frac{\sigma}{\sigma_0} = 1 - \frac{\sqrt{\frac{1}{N}\sum_{i=1}^{N}(I_i - \bar{I})^2}}{\sqrt{\frac{1}{N}\sum_{i=1}^{N}(I_{0i} - \bar{I})^2}} \tag{7.7}$$

Where I_i and I_{oi} represents the local pixel intensities for the mixed and unmixed states, respectively. $\bar{I}$ is the average pixel intensity and N is the total number of pixels.

7.8 Supporting Information

7.8.1 Device Geometry

The electrode and microfluidic channel geometrical parameters are detailed in Fig. S7.1 and Table S7.1.

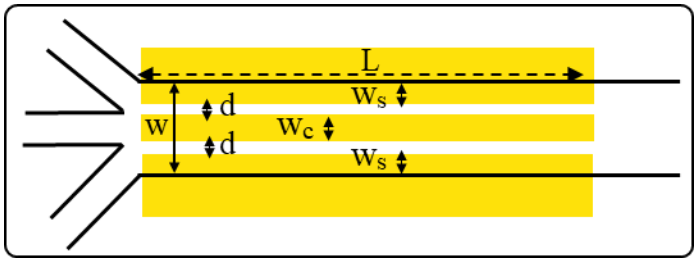

Figure S7.1 Geometrical parameters of the electrohydrodynamic micromixer.

Table S7.1 The geometrical parameter values corresponding to Fig. S7.1.

Parameter	Value (μm)	Description
w_c	60	Center electrode
w_s	90	Side electrode
d	20	Electrode spacing
w	280	Channel width
h	60	Channel height
L	3000	Electrode length

7.8.2 Device Fabrication: PDMS Oligomer Extraction

It is well known that uncross-linked PDMS oligomers in bulk polymerized PDMS can leach in organic solvents providing a source of unaccounted contamination in PDMS-based microdevices.[431] To eliminate the uncross-linked oligomers, an extraction protocol was employed that involved submersion of PDMS pieces in ethyl acetate (5 days) and acetone (2 days) followed by drying at 90 ˚C for 1 day. The degree of PDMS oligomer release was quantified for the raw and extracted PDMS using four common solvents including acetone (Sol1), 2-propanol (Sol2), ethanol (Sol3) and acetonitrile (Sol4). The raw and extracted PDMS pieces (2 cm × 1 cm × 0.3 cm blocks) were weighed and then immersed in 5 mL of each solvent for 6 hours with no agitation at room temperature. Then, the pieces were removed from the solvents and dried in a 90 ˚C oven for 1 day. The weight of PDMS pieces was measured after solvent evaporation and the percent change is reported in Fig. S7.2. The weight reduction is a result of oligomer removal from the PDMS matrix. As illustrated in Fig. S7.2, the extraction protocol employed in this study was quite effective in eliminating unpolymerized oligomers. For instance, the 2% weight reduction for raw PDMS was lowered to 0.04% for the extracted PDMS in acetone. A negligible weight change was observed for ethanol that is less aggressive compared to acetone.[431]

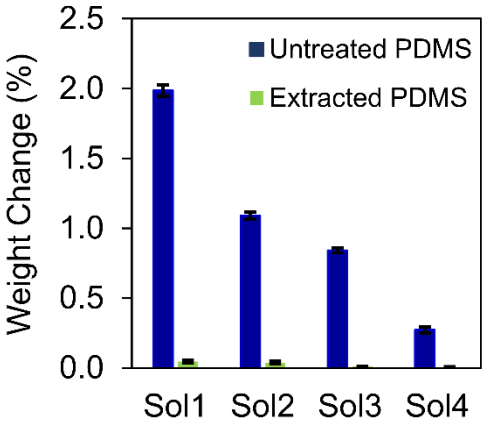

Figure S7.2 Weight percentage change before and after PDMS oligomer extraction. Sol1: acetone, Sol2: 2-propanol, Sol3: ethanol, Sol4: acetonitrile.

7.8.3 Control Experiments

To ensure the liposomal batches were free from contaminates, control experiments were carried out to rule out the presence of any nanoparticle contaminates either due to the ethanol impurities or the metal-generated nanoparticles. [432-433] The control experiments were run by flowing different ratios of DI water to ethanol and measuring the output by the NTA. For comparison, the NTA image snapshots for the liposomal batches of 0.2 mg/mL lipid concentration were contrasted with those of control experiments (Fig. S7.3). In this figure, four randomly selected frames from NTA videos corresponding to each experimental condition are shown. As indicated by Fig. S7.3 and the average number of particles per frame reported by the NTA, the control experiments showed a negligible amount of contaminates.

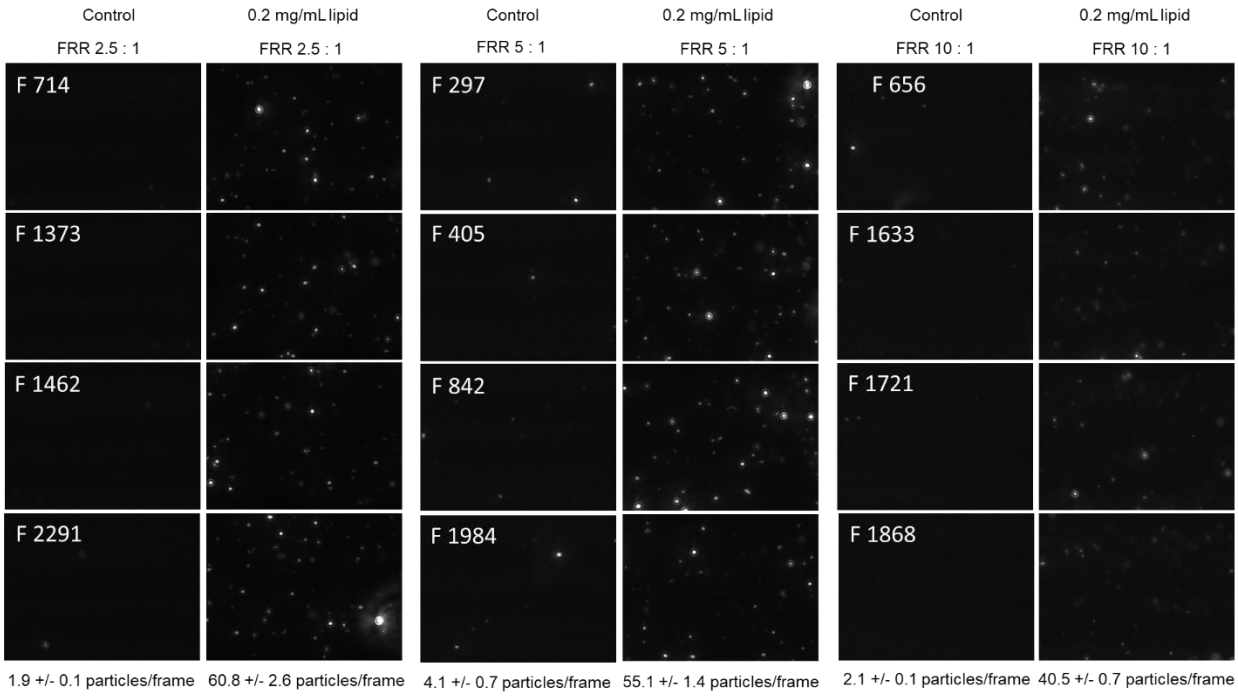

Figure S7.3 Control experiments at different FRR of water to ethanol solutions. For each experimental condition, four randomly chosen frames were selected from NTA videos. The frame numbers are shown on the left top corner of each frame.

Chapter 8. General Discussion and Conclusion

This thesis was concerned with the study of multifaceted applications of electric fields to particles and liquids in microscale fluidic channels. More specifically, we explored various electrically-driven phenomena including dielectrophoresis, AC electroosmosis and electrohydrodynamics to manipulate cells and actuate fluids. Those phenomena can facilely be utilized by the inclusion of microfabricated electrodes in the device structure and the same setup may be used to induce different types of forces. However, for most purposes and applications, one actuation mechanism is dominant considering the involved fluidic/particle parameters.

The current thesis stemmed from three major investigative studies in the field of electrokinetics and electrohydrodynamics. First, the concept of dielectrophoresis was implemented to examine a novel frequency hopping signaling scheme to perform tunable sorting of synthesis particles and cells. This study aimed at knowing whether a hopping frequency AC signal can be utilized to leverage the frequency-dependent behavior of DEP force for a tunable particle sorting. The results of this investigation showed that starting with a heterogeneous population of polystyrene microspheres, the individual size groups can be sorted out from the smallest to the largest size particles. Furthermore, the platform was proven feasible for the isolation of MCF-7 cancer cell line (a model for CTCs) from blood cells. Albeit achieving tunable sorting, particle-particle electrostatic interactions with synthetic polystyrene particles were a hindrance to the recovery of the desired particles.[434] The electrostatic interaction amongst particles often leads to similar or dissimilar particle chains that exhibit different dielectrophoretic behavior than individual entities. To mitigate this challenge, the electric field was momentarily interrupted to dissociate chained particles. Nevertheless, the chain formation is a problem that should tackle either through adjustments to the electric field as stated or particle concentration such that fewer interactions take

place. On the contrary, the particle-particle interactions may provide opportunities for the self-assembly and printing of colloidal particles.[435-436]

Electrically-driven fluid agitation and mixing was another major focus of this thesis. We explored the concept of AC electroosmosis for micromixing of Newtonian aqueous solutions and ways to improve and tune the degree of mixing. Accordingly, for the first time, the concept of phase-controlled field-effect micromixing was introduced and validated through experiments and semi-analytical simulations. It was demonstrated that the operation and optimization of the proposed micromixer can be explained with a simple analogy to field-effect transistor devices by tunning the gate-source and source-drain voltage potentials. This was done by operating the device by exciting the electrodes at constant amplitudes and frequencies with an imposed phase lag. At an optimized flow rate, it was shown the source, gate and drain potentials can be configured such that the micromixer switches from an unmixed state to a completely mixed state by modulating the phase shift between the electrodes.

Finally, we extended our understanding of electrically-induced micromixing to the on-chip synthesis of drug-delivery organic nanoparticles employing the concept of nanoprecipitation. As the nanoprecipitation of nanoparticles necessitates the use of a solvent phase and an aqueous phase, these techniques involve liquids of distinct electrical permittivities and/or conductivities. The application of electric fields across those liquid boundaries induces the electrohydrodynamic instability and fluid motion at the boundaries. Consequently, the proposed platform for the nanoprecipitation experiments that consisted of stratified laminar streams of aqueous, solvent, aqueous phases was thoroughly characterized to uncover the frequency-dependent mixing behavior as well as the optimized flow rate that can be sustained for efficient mixing. Next, the devised platform was used for the synthesis of monodisperse liposomes considering various

parameters such as the overall flow rate, solvent phase to aqueous phase ratio and initial particle concentration.

This study resulted in the first demonstration of the feasibility and applicability of electrically-driven micromixing to the highly demanded chemical synthesis applications. Albeit many existing studies on electrically-forced micromixing focusing on theoretical understanding and experimental validations, a true on-chip application was missing. Moreover, the fluid mixing induced by electrohydrodynamic flow instabilities showed an impressive capability for high flow rate operations at small voltages surpassing other active electrokinetic mechanisms or acoustic-based methodologies. For instance, for all flow rate ratios of water to solvent and at a total flow rate of 200 μL/min, mixing indices of larger than 0.6 were achieved. The ability to enhance mixing at such high flow rates employing an electrical technique provides opportunities for the wider utility of such techniques in synthesis applications.

The introduced concepts in the context of electrohydrodynamic-mediated micromixing only uncovered the basics working mechanism and an immediate application in the field of nanoparticle formation. There is ample opportunities to unravel the theoretical aspects of the experimental observations and to uncover new applications.

Chapter 9. Limitations and Future Perspectives

In this thesis, we covered many different aspects of electrically-driven microfluidic platforms that make them a ubiquitous part of many bioanalytical systems. However, several practical challenges preclude the adoption and widespread use of these methods for bioanalytical devices. Moreover, many facets of the studied platforms were remained unexplored and may serve as rich prospect theoretical or experimental studies. We cover those limitations and future perspectives in a categorized fashion below.

9.1 Limitations

A. Dependency on the liquid's electrical parameters

Electrokinetic and electrohydrodynamic effects are strongly dependent on the electrical permittivity and conductivity of the liquid or liquid systems that they act upon. Changes in conductivity or permittivity of the system will alter the effective force on suspended particles as in dielectrophoresis or on liquids as in AC electroosmosis or electrohydrodynamic.

In dielectrophoresis platforms, the transition from an nDEP to pDEP force is only observed for suspension media of relatively low conductivity (<200 mS/m). At higher conductivities, the cells will solely undergo nDEP force since the cells are always less polarizable than the media. This dependency on conductivity has several major consequences. First, platforms relying on pDEP become ineffective when cells are suspended in buffers at higher conductivities, which make it challenging to differentiate various cells populations. Second, the requirement for low conductivity media often means additional preprocessing steps involving buffer preparation and resuspension of cells. Furthermore, low-conductivity media put cells under stressed conditions that may have adverse effects on their long-term viability. This is especially important if the sorted cells are needed for the downstream processing. On the other hand, suspension in high conductivity

buffers such as PBS introduces other impediments to the facile use of nDEP force for cell manipulation. Electrochemical reactions and bubble formation on the surface of electrodes often lead to electrode corrosion and channel clogging. Moreover, Joule heating of the suspension media is an important stressor to the cells. Passage of electric currents through a conductive medium leads to power dissipation causing joule heating. Temperature elevation due to Joule heating is an important parameter affecting antibody-antigen interaction kinetics. Temperatures a few degree Celcius beyond the physiological temperature of 37 ˚C will lead to protein denaturation or even cell lysis. Accordingly, most platforms employing high conductivity media must consider lowing the voltage amplitude in order to prevent those adverse effects which subsequently lead to weaker DEP forces.

AC electroosmosis-induced flows are also highly dependent on the ionic strength of working liquids. The ACEO flow velocities reduce in magnitude with increasing electrolyte concentration. The flow velocities have shown to be immeasurably small for concentrations in excess of 10 mM. Thus, ACEO flow actuation is entirely non-existent for physiological buffers and is only applicable to dilute solutions, DI water, or alcohols. Nevertheless, the ACEO flow becomes attractive for applications for which dilute and pure aqueous solutions can be used for example for displacing a biological fluid with DI water or exchanging heat for micro-cooling.

Finally, electrohydrodynamic effect modulates with variations in electrical permittivity and conductivity of interfacing liquids. However, the suppression or the amplification of the flow velocities appear to be less sensitive to variations in electrical properties of the liquids as long as a distinct difference in permittivity or conductivity exists between the liquids.

B. Locally-driven Global Effects

With both ACEO and DEP phenomena, the intensity of the force field is strongest near the surface of the electrodes. If the length that characterizes electric field variations is L, then the DEP force scales with L, as $F_{dep} \sim V^2/L^3$. This means that as the distance from the electrodes increases, the DEP force reduces significantly with the cube of the distance. Accordingly, most DEP platforms are limited in how far the channel depth can be increased and for most practical purpose the channel depth ranges from 30 μm to 60 μm in length.

Similarly, the ACEO flow velocities are strongest immediately over electrode surfaces, whose length scales vary in range from 10 μm to 100 μm. Furthermore, the ACEO flow velocities are strongest near the edge of electrodes at the electrode-pair gaps and reduce with distance away from the electrode gaps. Thus, devices based on ACEO flow induction are limited in channel height and width scaling.

9.2 Future Perspectives

In this thesis, three main objectives were pursued involving the use of AC dielectrophoresis, AC electroosmosis and electrohydrodynamic for particle manipulation and fluid handling. Within each objective, there are opportunities for further performance enhancement, extensions to the use of other materials or components and theoretical analysis. The dielectrophoretic platform introduced in this thesis can be studied further to include signals with duty cycles other than 50%. Also, the concept of frequency hopping dielectrophoresis may be used with DEP devices based on lateral displacement employing slanted electrodes. The lateral displacement DEP mechanism for sorting should improve challenges with particle aggregation, and the hopping frequency signalling should improve unspecific particle attachment to the electrodes by allowing cells or particles to dissociate under the release frequency.

The electrohydrodynamic-driven micromixing was proved very efficient and practical considering the fluid systems involving DI water and solvents in the context of nanoprecipitation of nanoparticles. Here, we only covered the fundamental concepts and the feasibility of the proposed platform for nanoparticle synthesis. However, the promising results achieved in those experiments can be extended to fully unravel the effect of using different aqueous solutions and the effect of electric field on drug encapsulation efficiency. For instance, an immediate extension to current study would involve exchanging DI water with aqueous solutions of larger ionic conductivities or even PBS. In this case, the electrohydrodynamic flows still exist but the new fluidic system must be characterized to understand the effect of frequency, total sustainable flow rate and possible generation of Joule heating and the subsequent ACET flows. In this context, the use of high conductivity media such as PBS and the application of proper voltages will induce a temperature increase that may even improve the homogeneity and size distribution of nanoparticle batches.

Another interesting extension to the current study would be studying the effect of electric fields on the drug encapsulation efficiency. One possible mechanism by which electric fields increase encapsulation efficiency is through the generation of nanopores on the lipid membrane of liposomes that would allow the passage of drug-contained extra-vesicular buffer after the liposomes are formed.

Finally, the demonstrated electrohydrodynamic-mixing of the stratified aqueous, solvent, aqueous phase is not supported by any existing rich numerical modelling. Matching the experimental results with theoretical analysis will complement our understanding of electrohydrodynamic-mediated mixing and opens many avenues for it optimization.

References

1. Esmaeeli, A.; Halim, M. A., Electrohydrodynamics of a liquid drop in AC electric fields. *Acta Mech* **2018,** *229* (9), 3943-3962.
2. Samiei, E.; Derby, M. D. D.; Van den Berg, A.; Hoorfar, M., An electrohydrodynamic technique for rapid mixing in stationary droplets on digital microfluidic platforms. *Lab on a Chip* **2017,** *17* (2), 227-234.
3. El Moctar, A. O.; Aubry, N.; Batton, J., Electro-hydrodynamic micro-fluidic mixer. *Lab on a Chip* **2003,** *3* (4), 273-280.
4. Ren, Q. L.; Wang, Y. C.; Lin, X. X.; Chan, C. L., AC electrokinetic induced non-Newtonian electrothermal blood flow in 3D microfluidic biosensor with ring electrodes for point-of-care diagnostics. *J Appl Phys* **2019,** *126* (8).
5. Li, L.; Wang, X. Y.; Pu, Q. S.; Liu, S. R., Advancement of electroosmotic pump in microflow analysis. *Analytica Chimica Acta* **2019,** *1060*, 1-16.
6. Lee, S.; Kim, J.; Wereley, S. T.; Kwon, J. S., Light-actuated electrothermal microfluidic flow for micro-mixing. *Journal of Micromechanics and Microengineering* **2019,** *29* (1).
7. Azizian, P.; Azarmanesh, M.; Dejam, M.; Mohammadi, M.; Shamsi, M.; Sanati-Nezhad, A.; Mohamad, A. A., Electrohydrodynamic formation of single and double emulsions for low interfacial tension multiphase systems within microfluidics. *Chemical Engineering Science* **2019,** *195*, 201-207.
8. Zhang, K. L.; Ren, Y. K.; Hou, L. K.; Feng, X. S.; Chen, X. M.; Jiang, H. Y., An efficient micromixer actuated by induced-charge electroosmosis using asymmetrical floating electrodes. *Microfluidics and Nanofluidics* **2018,** *22* (11).
9. Meng, J.; Li, S.; Li, J.; Yu, C.; Wei, C.; Dai, S., AC electrothermal mixing for high conductive biofluids by arc-electrodes. *Journal of Micromechanics and Microengineering* **2018,** *28* (6), 065004.
10. Wu, Y. P.; Ren, Y. K.; Tao, Y.; Hou, L. K.; Hu, Q. M.; Jiang, H. Y., A novel micromixer based on the alternating current-flow field effect transistor. *Lab on a Chip* **2017,** *17* (1), 186-197.
11. Herzenberg, L. A.; Parks, D.; Sahaf, B.; Perez, O.; Roederer, M.; Herzenberg, L. A., The history and future of the fluorescence activated cell sorter and flow cytometry: a view from Stanford. *Clin Chem* **2002,** *48* (10), 1819-27.
12. Hodne, K.; Weltzien, F.-A., Single-Cell Isolation and Gene Analysis: Pitfalls and Possibilities. *International Journal of Molecular Sciences* **2015,** *16* (11), 26832-26849.
13. Bhagat, A. A.; Bow, H.; Hou, H. W.; Tan, S. J.; Han, J.; Lim, C. T., Microfluidics for cell separation. *Med Biol Eng Comput* **2010,** *48* (10), 999-1014.
14. Miltenyi, S.; Muller, W.; Weichel, W.; Radbruch, A., High-Gradient Magnetic Cell-Separation with Macs. *Cytometry* **1990,** *11* (2), 231-238.
15. Gascoyne, P. R. C.; Vykoukal, J., Particle separation by dielectrophoresis. *Electrophoresis* **2002,** *23* (13), 1973-1983.
16. Wu, M.; Ozcelik, A.; Rufo, J.; Wang, Z.; Fang, R.; Jun Huang, T., Acoustofluidic separation of cells and particles. *Microsyst Nanoeng* **2019,** *5*, 32.
17. Chen, Y. C.; Wu, M. X.; Ren, L. Q.; Liu, J. Y.; Whitley, P. H.; Wang, L.; Huang, T. J., High-throughput acoustic separation of platelets from whole blood. *Lab on a Chip* **2016,** *16* (18), 3466-3472.

18. Shi, J.; Huang, H.; Stratton, Z.; Huang, Y.; Huang, T. J., Continuous particle separation in a microfluidic channel via standing surface acoustic waves (SSAW). *Lab Chip* **2009,** *9* (23), 3354-9.
19. Ashkin, A.; Dziedzic, J. M.; Bjorkholm, J. E.; Chu, S., Observation of a single-beam gradient force optical trap for dielectric particles. *Opt Lett* **1986,** *11* (5), 288.
20. Zhang, H.; Liu, K. K., Optical tweezers for single cells. *J R Soc Interface* **2008,** *5* (24), 671-90.
21. Ashkin, A., Optical trapping and manipulation of neutral particles using lasers. *Proceedings of the National Academy of Sciences of the United States of America* **1997,** *94* (10), 4853-4860.
22. Nieminen, T. A.; Loke, V. L. Y.; Stilgoe, A. B.; Knoner, G.; Branczyk, A. M.; Heckenberg, N. R.; Rubinsztein-Dunlop, H., Optical tweezers computational toolbox. *J Opt a-Pure Appl Op* **2007,** *9* (8), S196-S203.
23. Huang, L. R.; Cox, E. C.; Austin, R. H.; Sturm, J. C., Continuous particle separation through deterministic lateral displacement. *Science* **2004,** *304* (5673), 987-990.
24. Salafi, T.; Zhang, Y.; Zhang, Y., A Review on Deterministic Lateral Displacement for Particle Separation and Detection. *Nano-Micro Letters* **2019,** *11* (1).
25. Inglis, D. W., Efficient microfluidic particle separation arrays. *Appl Phys Lett* **2009,** *94* (1), 013510.
26. Yamada, M.; Nakashima, M.; Seki, M., Pinched flow fractionation: Continuous size separation of particles utilizing a laminar flow profile in a pinched microchannel. *Analytical Chemistry* **2004,** *76* (18), 5465-5471.
27. Wilding, P.; Kricka, L. J.; Cheng, J.; Hvichia, G.; Shoffner, M. A.; Fortina, P., Integrated cell isolation and polymerase chain reaction analysis using silicon microfilter chambers. *Analytical Biochemistry* **1998,** *257* (2), 95-100.
28. Panaro, N. J.; Lou, X. J.; Fortina, P.; Kricka, L. J.; Wilding, P., Micropillar array chip for integrated white blood cell isolation and PCR. *Biomol Eng* **2005,** *21* (6), 157-162.
29. Zheng, S.; Lin, H.; Liu, J. Q.; Balic, M.; Datar, R.; Cote, R. J.; Tai, Y. C., Membrane microfilter device for selective capture, electrolysis and genomic analysis of human circulating tumor cells. *Journal of Chromatography A* **2007,** *1162* (2), 154-161.
30. Yamada, M.; Seki, M., Hydrodynamic filtration for on-chip particle concentration and classification utilizing microfluidics. *Lab on a Chip* **2005,** *5* (11), 1233-1239.
31. Park, J. S.; Song, S. H.; Jung, H. I., Continuous focusing of microparticles using inertial lift force and vorticity via multi-orifice microfluidic channels. *Lab on a Chip* **2009,** *9* (7), 939-948.
32. Kuntaegowdanahalli, S. S.; Bhagat, A. A. S.; Kumar, G.; Papautsky, I., Inertial microfluidics for continuous particle separation in spiral microchannels. *Lab on a Chip* **2009,** *9* (20), 2973-2980.
33. Lenshof, A.; Laurell, T., Continuous separation of cells and particles in microfluidic systems. *Chemical Society Reviews* **2010,** *39* (3), 1203-1217.
34. Lu, L. H.; Ryu, K. S.; Liu, C., A magnetic microstirrer and array for microfluidic mixing. *Journal of Microelectromechanical Systems* **2002,** *11* (5), 462-469.
35. Ahmed, D.; Mao, X. L.; Juluri, B. K.; Huang, T. J., A fast microfluidic mixer based on acoustically driven sidewall-trapped microbubbles. *Microfluidics and Nanofluidics* **2009,** *7* (5), 727-731.

36. Huang, P. H.; Xie, Y. L.; Ahmed, D.; Rufo, J.; Nama, N.; Chen, Y. C.; Chan, C. Y.; Huang, T. J., An acoustofluidic micromixer based on oscillating sidewall sharp-edges. *Lab on a Chip* **2013,** *13* (19), 3847-3852.
37. Chang, C. C.; Yang, R. J., Electrokinetic mixing in microfluidic systems. *Microfluidics and Nanofluidics* **2007,** *3* (5), 501-525.
38. Castellanos, A.; Pérez, A., Electrohydrodynamic Systems. In *Springer Handbook of Experimental Fluid Mechanics*, Tropea, C.; Yarin, A. L.; Foss, J. F., Eds. Springer Berlin Heidelberg: Berlin, Heidelberg, 2007; pp 1317-1333.
39. Shin, S. M.; Kang, I. S.; Cho, Y. K., Mixing enhancement by using electrokinetic instability under time-periodic electric field. *Journal of Micromechanics and Microengineering* **2004,** *15* (3), 455-462.
40. Jahn, A.; Vreeland, W. N.; Gaitan, M.; Locascio, L. E., Controlled vesicle self-assembly in microfluidic channels with hydrodynamic focusing. *Journal of the American Chemical Society* **2004,** *126* (9), 2674-2675.
41. Coleman, J. T.; Sinton, D., A sequential injection microfluidic mixing strategy. *Microfluidics and Nanofluidics* **2005,** *1* (4), 319-327.
42. Buchegger, W.; Wagner, C.; Lendl, B.; Kraft, M.; Vellekoop, M. J., A highly uniform lamination micromixer with wedge shaped inlet channels for time resolved infrared spectroscopy. *Microfluidics and Nanofluidics* **2011,** *10* (4), 889-897.
43. SadAbadi, H.; Packirisamy, M.; Wuthrich, R., High performance cascaded PDMS micromixer based on split-and-recombination flows for lab-on-a-chip applications. *Rsc Advances* **2013,** *3* (20), 7296-7305.
44. Stroock, A. D.; Dertinger, S. K. W.; Ajdari, A.; Mezic, I.; Stone, H. A.; Whitesides, G. M., Chaotic mixer for microchannels. *Science* **2002,** *295* (5555), 647-651.
45. Jahn, A.; Stavis, S. M.; Hong, J. S.; Vreeland, W. N.; Devoe, D. L.; Gaitan, M., Microfluidic Mixing and the Formation of Nanoscale Lipid Vesicles. *Acs Nano* **2010,** *4* (4), 2077-2087.
46. Vauthier, C.; Bouchemal, K., Methods for the preparation and manufacture of polymeric nanoparticles. *Pharm Res* **2009,** *26* (5), 1025-58.
47. Capretto, L.; Carugo, D.; Mazzitelli, S.; Nastruzzi, C.; Zhang, X., Microfluidic and lab-on-a-chip preparation routes for organic nanoparticles and vesicular systems for nanomedicine applications. *Adv Drug Deliv Rev* **2013,** *65* (11-12), 1496-532.
48. Lepeltier, E.; Bourgaux, C.; Couvreur, P., Nanoprecipitation and the "Ouzo effect": Application to drug delivery devices. *Adv Drug Deliver Rev* **2014,** *71*, 86-97.
49. Bazant, M. Z.; Squires, T. M., Induced-charge electrokinetic phenomena: Theory and microfluidic applications. *Phys Rev Lett* **2004,** *92* (6).
50. Modarres, P.; Tabrizian, M., Alternating current dielectrophoresis of biomacromolecules: The interplay of electrokinetic effects. *Sensors and Actuators B-Chemical* **2017,** *252*, 391-408.
51. Ramos, A.; Morgan, H.; Green, N. G.; Castellanos, A., Ac electrokinetics: a review of forces in microelectrode structures. *Journal of Physics D-Applied Physics* **1998,** *31* (18), 2338-2353.
52. Morgan, H.; Green, N. G., *AC electrokinetics : colloids and nanoparticles*. Research Studies Press: Philadelphia, PA, 2003; p xvi, 324 p.
53. Chang, H. C.; Yeo, L. Y., *Electrokinetically driven microfluidics and nanofluidics*. Cambridge University Press: Cambridge ; New York, 2010; p xvi, 508 p., 8 p. of plates.
54. Squires, T. M.; Bazant, M. Z., Induced-charge electro-osmosis. *J Fluid Mech* **2004,** *509*, 217-252.

55. Jones, T. B., Basic theory of dielectrophoresis and electrorotation. *Ieee Eng Med Biol* **2003,** *22* (6), 33-42.
56. Ramos, A.; Morgan, H.; Green, N. G.; Castellanos, A., AC Electric-Field-Induced Fluid Flow in Microelectrodes. *J Colloid Interface Sci* **1999,** *217* (2), 420-422.
57. Green, N. G.; Ramos, A.; Gonzalez, A.; Castellanos, A.; Morgan, H., Electrothermally induced fluid flow on microelectrodes. *Journal of Electrostatics* **2001,** *53* (2), 71-87.
58. J R Melcher, a.; Taylor, G. I., Electrohydrodynamics: A Review of the Role of Interfacial Shear Stresses. *Annual Review of Fluid Mechanics* **1969,** *1* (1), 111-146.
59. Ying, H.; Holzel, R.; Pethig, R.; Wang, X. B., Differences in the Ac Electrodynamics of Viable and Nonviable Yeast-Cells Determined through Combined Dielectrophoresis and Electrorotation Studies. *Phys Med Biol* **1992,** *37* (7), 1499-1517.
60. Li, L.; Li, C.; Zhang, Z.; Alexov, E., On the Dielectric "Constant" of Proteins: Smooth Dielectric Function for Macromolecular Modeling and Its Implementation in DelPhi. *J Chem Theory Comput* **2013,** *9* (4), 2126-2136.
61. Kim, D.; Sonker, M.; Ros, A., Dielectrophoresis: From Molecular to Micrometer-Scale Analytes. *Analytical Chemistry* **2019,** *91* (1), 277-295.
62. Saif, B.; Mohr, R. K.; Montrose, C. J.; Litovitz, T. A., On the mechanism of dielectric relaxation in aqueous DNA solutions. *Biopolymers* **1991,** *31* (10), 1171-80.
63. Tomic, S.; Babic, S. D.; Vuletic, T.; Krca, S.; Ivankovic, D.; Griparic, L.; Podgornik, R., Dielectric relaxation of DNA aqueous solutions. *Phys Rev E* **2007,** *75* (2 Pt 1), 021905.
64. Camacho-Alanis, F.; Ros, A., Protein dielectrophoresis and the link to dielectric properties. *Bioanalysis* **2015,** *7* (3), 353-71.
65. Nakano, A.; Ros, A., Protein dielectrophoresis: advances, challenges, and applications. *Electrophoresis* **2013,** *34* (7), 1085-96.
66. Regtmeier, J.; Eichhorn, R.; Bogunovic, L.; Ros, A.; Anselmetti, D., Dielectrophoretic trapping and polarizability of DNA: the role of spatial conformation. *Anal Chem* **2010,** *82* (17), 7141-9.
67. Regtmeier, J.; Duong, T. T.; Eichhorn, R.; Anselmetti, D.; Ros, A., Dielectrophoretic manipulation of DNA: separation and polarizability. *Anal Chem* **2007,** *79* (10), 3925-32.
68. Bakewell, D. J. E., I.;Morgan, H.;Milner, J.;Feldman, Y., Dielectric relaxation measurements of 12 kbp plasmid DNA. In *Biochimica et Biophysica Acta - Gene Structure and Expression*, 2000; Vol. 1493, pp 151-158.
69. Macaulay, I. C.; Voet, T., Single cell genomics: advances and future perspectives. *PLoS Genet* **2014,** *10* (1), e1004126.
70. Heath, J. R.; Ribas, A.; Mischel, P. S., Single-cell analysis tools for drug discovery and development. *Nat Rev Drug Discov* **2016,** *15* (3), 204-16.
71. Wang, D. J.; Bodovitz, S., Single cell analysis: the new frontier in 'omics'. *Trends in Biotechnology* **2010,** *28* (6), 281-290.
72. Klein, A. M.; Mazutis, L.; Akartuna, I.; Tallapragada, N.; Veres, A.; Li, V.; Peshkin, L.; Weitz, D. A.; Kirschner, M. W., Droplet Barcoding for Single-Cell Transcriptomics Applied to Embryonic Stem Cells. *Cell* **2015,** *161* (5), 1187-1201.
73. Brouzes, E.; Medkova, M.; Savenelli, N.; Marran, D.; Twardowski, M.; Hutchison, J. B.; Rothberg, J. M.; Link, D. R.; Perrimon, N.; Samuels, M. L., Droplet microfluidic technology for single-cell high-throughput screening. *Proceedings of the National Academy of Sciences of the United States of America* **2009,** *106* (34), 14195-14200.

74. Kang, H. M.; Subramaniam, M.; Targ, S.; Nguyen, M.; Maliskova, L.; McCarthy, E.; Wan, E.; Wong, S.; Byrnes, L.; Lanata, C. M.; Gate, R. E.; Mostafavi, S.; Marson, A.; Zaitlen, N.; Criswell, L. A.; Ye, C. J., Multiplexed droplet single-cell RNA-sequencing using natural genetic variation. *Nature Biotechnology* **2018,** *36* (1), 89-+.
75. Kimmerling, R. J.; Szeto, G. L.; Li, J. W.; Genshaft, A. S.; Kazer, S. W.; Payer, K. R.; Borrajo, J. D.; Blainey, P. C.; Irvine, D. J.; Shalek, A. K.; Manalis, S. R., A microfluidic platform enabling single-cell RNA-seq of multigenerational lineages. *Nat Commun* **2016,** *7*.
76. Fan, H. C.; Wang, J. B.; Potanina, A.; Quake, S. R., Whole-genome molecular haplotyping of single cells. *Nature Biotechnology* **2011,** *29* (1), 51-+.
77. Qin, Y.; Wu, L.; Schneider, T.; Yen, G. S.; Wang, J.; Xu, S.; Li, M.; Paguirigan, A. L.; Smith, J. L.; Radich, J. P.; Anand, R. K.; Chiu, D. T., A Self-Digitization Dielectrophoretic (SD-DEP) Chip for High-Efficiency Single-Cell Capture, On-Demand Compartmentalization, and Downstream Nucleic Acid Analysis. *Angew Chem Int Edit* **2018,** *57* (35), 11378-11383.
78. Collins, D. J.; Morahan, B.; Garcia-Bustos, J.; Doerig, C.; Plebanski, M.; Neild, A., Two-dimensional single-cell patterning with one cell per well driven by surface acoustic waves. *Nat Commun* **2015,** *6*.
79. Wu, C. H.; Chen, R. F.; Liu, Y.; Yu, Z. M.; Jiang, Y. W.; Cheng, X., A planar dielectrophoresis-based chip for high-throughput cell pairing. *Lab on a Chip* **2017,** *17* (23), 4008-4014.
80. Kim, S. H.; Antfolk, M.; Kobayashi, M.; Kaneda, S.; Laurell, T.; Fujii, T., Highly efficient single cell arraying by integrating acoustophoretic cell pre-concentration and dielectrophoretic cell trapping. *Lab Chip* **2015,** *15* (22), 4356-63.
81. Kim, S. H.; Fujii, T., Efficient analysis of a small number of cancer cells at the single-cell level using an electroactive double-well array. *Lab on a Chip* **2016,** *16* (13), 2440-2449.
82. Morimoto, A.; Mogami, T.; Watanabe, M.; Iijima, K.; Akiyama, Y.; Katayama, K.; Futami, T.; Yamamoto, N.; Sawada, T.; Koizumi, F.; Koh, Y., High-Density Dielectrophoretic Microwell Array for Detection, Capture, and Single-Cell Analysis of Rare Tumor Cells in Peripheral Blood. *PLoS One* **2015,** *10* (6), e0130418.
83. Sen, M.; Ino, K.; Ramon-Azcon, J.; Shiku, H.; Matsue, T., Cell pairing using a dielectrophoresis-based device with interdigitated array electrodes. *Lab on a Chip* **2013,** *13* (18), 3650-3652.
84. Lownes Urbano, R.; Morss Clyne, A., An inverted dielectrophoretic device for analysis of attached single cell mechanics. *Lab Chip* **2016,** *16* (3), 561-73.
85. Huang, L.; Tu, L.; Zeng, X. Y.; Mi, L.; Li, X. Z.; Wang, W. H., Study of a Microfluidic Chip Integrating Single Cell Trap and 3D Stable Rotation Manipulation. *Micromachines* **2016,** *7* (8).
86. Chung, J.; Chen, Y.; Kim, S. J., High-density impedance-sensing array on complementary metal-oxide-semiconductor circuitry assisted by negative dielectrophoresis for single-cell-resolution measurement. *Sensors and Actuators B-Chemical* **2018,** *266*, 106-114.
87. Nadappuram, B. P.; Cadinu, P.; Barik, A.; Ainscough, A.; Devine, M. J.; Kang, M.; Gonzalez-Garcia, J.; Kittler, J. T.; Willison, K. R.; Vilar, R.; Actis, P.; Wojciak-Stothard, B.; Oh, S. H.; Ivanov, A. P.; Edel, J. B., Nanoscale tweezers for single-cell biopsies. *Nature Nanotechnology* **2019,** *14* (1), 80-+.
88. Barik, A.; Zhang, Y.; Grassi, R.; Nadappuram, B. P.; Edel, J. B.; Low, T.; Koester, S. J.; Oh, S. H., Graphene-edge dielectrophoretic tweezers for trapping of biomolecules. *Nat Commun* **2017,** *8* (1), 1867.

89. Tarhan, M. C.; Lafitte, N.; Tauran, Y.; Jalabert, L.; Kumemura, M.; Perret, G.; Kim, B.; Coleman, A. W.; Fujita, H.; Collard, D., A rapid and practical technique for real-time monitoring of biomolecular interactions using mechanical responses of macromolecules. *Scientific Reports* **2016,** *6*.
90. Tian, K.; Decker, K.; Aksimentiev, A.; Gu, L. Q., Interference-Free Detection of Genetic Biomarkers Using Synthetic Dipole-Facilitated Nanopore Dielectrophoresis. *Acs Nano* **2017,** *11* (2), 1204-1213.
91. Tanaka, S.; Tsutsui, M.; Theodore, H.; Yuhui, H.; Arima, A.; Tsuji, T.; Doi, K.; Kawano, S.; Taniguchi, M.; Kawai, T., Tailoring particle translocation via dielectrophoresis in pore channels. *Sci Rep* **2016,** *6*, 31670.
92. Freedman, K. J.; Otto, L. M.; Ivanov, A. P.; Barik, A.; Oh, S. H.; Edel, J. B., Nanopore sensing at ultra-low concentrations using single-molecule dielectrophoretic trapping. *Nat Commun* **2016,** *7*.
93. Freedman, K. J.; Crick, C. R.; Albella, P.; Barik, A.; Ivanov, A. P.; Maier, S. A.; Oh, S. H.; Edel, J. B., On-Demand Surface- and Tip-Enhanced Raman Spectroscopy Using Dielectrophoretic Trapping and Nanopore Sensing. *Acs Photonics* **2016,** *3* (6), 1036-1044.
94. Ertsgaard, C. T.; Wittenberg, N. J.; Klemme, D. J.; Barik, A.; Shih, W. C.; Oh, S. H., Integrated Nanogap Platform for Sub-Volt Dielectrophoretic Trapping and Real-Time Raman Imaging of Biological Nanoparticles. *Nano Lett* **2018,** *18* (9), 5946-5953.
95. Lesser-Rojas, L.; Ebbinghaus, P.; Vasan, G.; Chu, M. L.; Erbe, A.; Chou, C. F., Low-copy number protein detection by electrode nanogap-enabled dielectrophoretic trapping for surface-enhanced Raman spectroscopy and electronic measurements. *Nano Lett* **2014,** *14* (5), 2242-50.
96. Shi, L. L.; Rana, A.; Esfandiari, L., A low voltage nanopipette dielectrophoretic device for rapid entrapment of nanoparticles and exosomes extracted from plasma of healthy donors. *Scientific Reports* **2018,** *8*.
97. Wu, T. H.; Chen, Y.; Park, S. Y.; Hong, J.; Teslaa, T.; Zhong, J. F.; Di Carlo, D.; Teitell, M. A.; Chiou, P. Y., Pulsed laser triggered high speed microfluidic fluorescence activated cell sorter. *Lab on a Chip* **2012,** *12* (7), 1378-1383.
98. Chen, Y.; Wu, T. H.; Kung, Y. C.; Teitell, M. A.; Chiou, P. Y., 3D pulsed laser-triggered high-speed microfluidic fluorescence-activated cell sorter. *Analyst* **2013,** *138* (24), 7308-7315.
99. Chung, A. J.; Gossett, D. R.; Di Carlo, D., Three Dimensional, Sheathless, and High-Throughput Microparticle Inertial Focusing Through Geometry-Induced Secondary Flows. *Small* **2013,** *9* (5), 685-690.
100. Chen, Y.; Chung, A. J.; Wu, T. H.; Teitell, M. A.; Di Carlo, D.; Chiou, P. Y., Pulsed Laser Activated Cell Sorting with Three Dimensional Sheathless Inertial Focusing. *Small* **2014,** *10* (9), 1746-1751.
101. Yan, S.; Zhang, J.; Li, M.; Alici, G.; Du, H.; Sluyter, R.; Li, W., On-chip high-throughput manipulation of particles in a dielectrophoresis-active hydrophoretic focuser. *Scientific Reports* **2014,** *4* (1), 5060.
102. Mathew, B.; Alazzam, A.; Destgeer, G.; Sung, H. J., Dielectrophoresis based cell switching in continuous flow microfluidic devices. *Journal of Electrostatics* **2016,** *84*, 63-72.
103. Kim, M.; Jung, T.; Kim, Y.; Lee, C.; Woo, K.; Seol, J. H.; Yang, S., A microfluidic device for label-free detection of Escherichia coli in drinking water using positive dielectrophoretic

focusing, capturing, and impedance measurement. *Biosensors & Bioelectronics* **2015,** *74*, 1011-1015.
104. Kung, Y. C.; Huang, K. W.; Chong, W.; Chiou, P. Y., Tunnel Dielectrophoresis for Tunable, Single-Stream Cell Focusing in Physiological Buffers in High-Speed Microfluidic Flows. *Small* **2016,** *12* (32), 4343-8.
105. Brimmo, A. T.; Menachery, A.; Qasaimeh, M. A., Microelectrofluidic probe for sequential cell separation and patterning. *Lab Chip* **2019,** *19* (24), 4052-4063.
106. Lewis, J. M.; Vyas, A. D.; Qiu, Y. Q.; Messer, K. S.; White, R.; Heller, M. J., Integrated Analysis of Exosomal Protein Biomarkers on Alternating Current Electrokinetic Chips Enables Rapid Detection of Pancreatic Cancer in Patient Blood. *Acs Nano* **2018,** *12* (4), 3311-3320.
107. Ibsen, S. D.; Wright, J.; Lewis, J. M.; Kim, S.; Ko, S. Y.; Ong, J.; Manouchehri, S.; Vyas, A.; Akers, J.; Chen, C. C.; Carter, B. S.; Esener, S. C.; Heller, M. J., Rapid Isolation and Detection of Exosomes and Associated Biomarkers from Plasma. *Acs Nano* **2017,** *11* (7), 6641-6651.
108. Sang, S.; Feng, Q.; Jian, A.; Li, H.; Ji, J.; Duan, Q.; Zhang, W.; Wang, T., Portable microsystem integrates multifunctional dielectrophoresis manipulations and a surface stress biosensor to detect red blood cells for hemolytic anemia. *Sci Rep* **2016,** *6*, 33626.
109. Shim, S.; Stemke-Hale, K.; Tsimberidou, A. M.; Noshari, J.; Anderson, T. E.; Gascoyne, P. R., Antibody-independent isolation of circulating tumor cells by continuous-flow dielectrophoresis. *Biomicrofluidics* **2013,** *7* (1), 11807.
110. Pesch, G. R.; Lorenz, M.; Sachdev, S.; Salameh, S.; Du, F.; Baune, M.; Boukany, P. E.; Thoming, J., Bridging the scales in high-throughput dielectrophoretic (bio-)particle separation in porous media. *Sci Rep* **2018,** *8* (1), 10480.
111. Rohani, A.; Sanghavi, B. J.; Salahi, A.; Liao, K. T.; Chou, C. F.; Swami, N. S., Frequency-selective electrokinetic enrichment of biomolecules in physiological media based on electrical double-layer polarization. *Nanoscale* **2017,** *9* (33), 12124-12131.
112. Li, M.; Anand, R. K., High-Throughput Selective Capture of Single Circulating Tumor Cells by Dielectrophoresis at a Wireless Electrode Array. *Journal of the American Chemical Society* **2017,** *139* (26), 8950-8959.
113. Han, S. I.; Kim, H. S.; Han, K. H.; Han, A., Digital quantification and selection of high-lipid-producing microalgae through a lateral dielectrophoresis-based microfluidic platform. *Lab Chip* **2019,** *19* (24), 4128-4138.
114. Song, H.; Rosano, J. M.; Wang, Y.; Garson, C. J.; Prabhakarpandian, B.; Pant, K.; Klarmann, G. J.; Perantoni, A.; Alvarez, L. M.; Lai, E., Continuous-flow sorting of stem cells and differentiation products based on dielectrophoresis. *Lab Chip* **2015,** *15* (5), 1320-8.
115. Luo, T.; Fan, L.; Zeng, Y. X.; Liu, Y.; Chen, S. X.; Tan, Q. L.; Lam, R. H. W.; Sun, D., A simplified sheathless cell separation approach using combined gravitational-sedimentation-based prefocusing and dielectrophoretic separation. *Lab on a Chip* **2018,** *18* (11), 1521-1532.
116. Tirapu-Azpiroz, J.; Temiz, Y.; Delamarche, E., Dielectrophoretic microbead sorting using modular electrode design and capillary-driven microfluidics. *Biomed Microdevices* **2017,** *19* (4), 95.
117. Calero, V.; Garcia-Sanchez, P.; Honrado, C.; Ramos, A.; Morgan, H., AC electrokinetic biased deterministic lateral displacement for tunable particle separation. *Lab Chip* **2019,** *19* (8), 1386-1396.
118. Xing, X.; Ng, C. N.; Chau, M. L.; Yobas, L., Railing cells along 3D microelectrode tracks for continuous-flow dielectrophoretic sorting. *Lab Chip* **2018,** *18* (24), 3760-3769.

119. Zhao, K.; Larasati; Duncker, B. P.; Li, D. Q., Continuous Cell Characterization and Separation by Microfluidic Alternating Current Dielectrophoresis. *Analytical Chemistry* **2019,** *91* (9), 6304-6314.
120. Bazant Mz; Urbanski JP; Levitan JA; Subramanian K; Kilic MS; Jones, A.; Thorsen, T., Electrolyte dependence of AC electro-osmosis. In *Proceedings of 11th international conference on miniaturized systems for chemistry and life sciences (MicroTAS)*, 2007; pp 285-287.
121. Kirby, B., *Micro- and nanoscale fluid mechanics : transport in microfluidic devices*. Cambridge University Press: New York, 2010; p xxiii, 512 p.
122. Garcia-Sanchez, P.; Ramos, A.; Green, N. G.; Morgan, H., Experiments on AC electrokinetic pumping of liquids using arrays of microelectrodes. *Ieee Transactions on Dielectrics and Electrical Insulation* **2006,** *13* (3), 670-677.
123. Ajdari, A., Pumping liquids using asymmetric electrode arrays. *Physical Review E* **2000,** *61* (1), R45-R48.
124. Brown, A. B.; Smith, C. G.; Rennie, A. R., Pumping of water with ac electric fields applied to asymmetric pairs of microelectrodes. *Phys Rev E* **2001,** *63* (1 Pt 2), 016305.
125. Mpholo, M.; Smith, C. G.; Brown, A. B. D., Low voltage plug flow pumping using anisotropic electrode arrays. *Sensors and Actuators B-Chemical* **2003,** *92* (3), 262-268.
126. Ramos, A.; Gonzalez, A.; Castellanos, A.; Green, N. G.; Morgan, H., Pumping of liquids with ac voltages applied to asymmetric pairs of microelectrodes. *Phys Rev E* **2003,** *67* (5 Pt 2), 056302.
127. Huang, C. C.; Bazant, M. Z.; Thorsen, T., Ultrafast high-pressure AC electro-osmotic pumps for portable biomedical microfluidics. *Lab Chip* **2010,** *10* (1), 80-5.
128. Bazant, M. Z.; Kilic, M. S.; Storey, B. D.; Ajdari, A., Towards an understanding of induced-charge electrokinetics at large applied voltages in concentrated solutions. *Adv Colloid Interface Sci* **2009,** *152* (1-2), 48-88.
129. Studer, V.; Pepin, A.; Chen, Y.; Ajdari, A., An integrated AC electrokinetic pump in a microfluidic loop for fast and tunable flow control. *Analyst* **2004,** *129* (10), 944-9.
130. Bazant, M. Z.; Sabri Kilic, M.; Storey, B. D.; Ajdari, A., Nonlinear electrokinetics at large voltages. *New Journal of Physics* **2009,** *11* (7), 075016.
131. Green, N. G.; Ramos, A.; Gonzalez, A.; Morgan, H.; Castellanos, A., Fluid flow induced by nonuniform ac electric fields in electrolytes on microelectrodes. I. Experimental measurements. *Physical Review E* **2000,** *61* (4), 4011-4018.
132. Fuhr, G.; Schnelle, T.; Wagner, B., Traveling Wave-Driven Microfabricated Electrohydrodynamic Pumps for Liquids. *Journal of Micromechanics and Microengineering* **1994,** *4* (4), 217-226.
133. Wu, J.; Lian, M.; Yang, K., Micropumping of biofluids by alternating current electrothermal effects. *Appl Phys Lett* **2007,** *90* (23).
134. Yuan, Q.; Wu, J., Thermally biased AC electrokinetic pumping effect for Lab-on-a-chip based delivery of biofluids. *Biomedical Microdevices* **2013,** *15* (1), 125-133.
135. Lang, Q.; Wu, Y. S.; Ren, Y. K.; Tao, Y.; Lei, L.; Jiang, H. Y., AC Electrothermal Circulatory Pumping Chip for Cell Culture. *Acs Applied Materials & Interfaces* **2015,** *7* (48), 26792-26801.
136. Williams, S. J., Enhanced electrothermal pumping with thin film resistive heaters. *Electrophoresis* **2013,** *34* (9-10), 1400-8.

137. Kwon, J. S.; Wereley, S. T., Light-actuated electrothermal microfluidic motion: experimental investigation and physical interpretation. *Microfluidics and Nanofluidics* **2015,** *19* (3), 609-619.
138. Modarres, P.; Tabrizian, M., Phase-controlled field-effect micromixing using AC electroosmosis. *Microsystems & Nanoengineering* **2020,** *6* (1), 60.
139. Wu, C. C.; Huang, W. C.; Hu, C. C., An ultrasensitive label-free electrochemical impedimetric DNA biosensing chip integrated with a DC-biased AC electroosmotic vortex. *Sensors and Actuators B-Chemical* **2015,** *209*, 61-68.
140. Oueslati, R.; Cheng, C.; Wu, J.; Chen, J. G., Highly sensitive and specific on-site detection of serum cocaine by a low cost aptasensor. *Biosensors & Bioelectronics* **2018,** *108*, 103-108.
141. Cui, H. C.; Cheng, C.; Lin, X. G.; Wu, J.; Chen, J. G.; Eda, S.; Yuan, Q., Rapid and sensitive detection of small biomolecule by capacitive sensing and low field AC electrothermal effect. *Sensors and Actuators B-Chemical* **2016,** *226*, 245-253.
142. Costella, M.; Avenas, Q.; Frenea-Robin, M.; Marchalot, J.; Bevilacqua, P.; Charette, P. G.; Canva, M., Dielectrophoretic cell trapping for improved surface plasmon resonance imaging sensing. *Electrophoresis* **2019,** *40* (10), 1417-1425.
143. Song, Y.; Chen, P.; Chung, M. T.; Nidetz, R.; Park, Y.; Liu, Z.; McHugh, W.; Cornell, T. T.; Fu, J.; Kurabayashi, K., AC Electroosmosis-Enhanced Nanoplasmofluidic Detection of Ultralow-Concentration Cytokine. *Nano Lett* **2017,** *17* (4), 2374-2380.
144. Cheng, I. F.; Chang, H. C.; Chen, T. Y.; Hu, C.; Yang, F. L., Rapid (<5 min) identification of pathogen in human blood by electrokinetic concentration and surface-enhanced Raman spectroscopy. *Sci Rep* **2013,** *3*, 2365.
145. Huang, Y. H.; Chang, J. S.; Chao, S. D.; Wu, K. C.; Huang, L. S., Improving the binding efficiency of quartz crystal microbalance biosensors by applying the electrothermal effect. *Biomicrofluidics* **2014,** *8* (5).
146. Lee, W. C.; Lee, H.; Lim, J.; Park, Y. J., An effective electrical sensing scheme using AC electrothermal flow on a biosensor platform based on a carbon nanotube network. *Appl Phys Lett* **2016,** *109* (22).
147. Yang, K.; Islam, N.; Eda, S.; Wu, J., Optimization of an AC electrokinetics immunoassay lab-chip for biomedical diagnostics. *Microfluidics and Nanofluidics* **2017,** *21* (3).
148. Bazant, M. Z., Electrokinetics meets electrohydrodynamics. *J Fluid Mech* **2015,** *782*, 1-4.
149. Bandopadhyay, A.; Ghosh, U., Electrohydrodynamic Phenomena. *J Indian I Sci* **2018,** *98* (2), 201-225.
150. Saville, D. A., ELECTROHYDRODYNAMICS: The Taylor-Melcher Leaky Dielectric Model. *Annual Review of Fluid Mechanics* **1997,** *29* (1), 27-64.
151. Taylor, G., Studies in Electrohydrodynamics .I. Circulation Produced in a Drop by an Electric Field. *Proc R Soc Lon Ser-A* **1966,** *291* (1425), 159-&.
152. Bhushani, J. A.; Anandharamakrishnan, C., Electrospinning and electrospraying techniques: Potential food based applications. *Trends Food Sci Tech* **2014,** *38* (1), 21-33.
153. Nguyen, D. N.; Clasen, C.; Van den Mooter, G., Pharmaceutical Applications of Electrospraying. *J Pharm Sci-Us* **2016,** *105* (9), 2601-2620.
154. Gryshkov, O.; Muller, M.; Leal-Marin, S.; Mutsenko, V.; Suresh, S.; Kapralova, V. M.; Glasmacher, B., Advances in the application of electrohydrodynamic fabrication for tissue engineering. *International Conference Emerging Trends in Applied and Computational Physics 2019 (Etacp-2019)* **2019,** *1236*.

155. Nikolaou, M.; Krasia-Christoforou, T., Electrohydrodynamic methods for the development of pulmonary drug delivery systems. *Eur J Pharm Sci* **2018,** *113*, 29-40.
156. Jalaal, M.; Khorshidi, B.; Esmaeilzadeh, E., Electrohydrodynamic (EHD) mixing of two miscible dielectric liquids. *Chem Eng J* **2013,** *219*, 118-123.
157. Zahn, J. D.; Reddy, V., Two phase micromixing and analysis using electrohydrodynamic instabilities. *Microfluidics and Nanofluidics* **2006,** *2* (5), 399-415.
158. DePaoli, D. W.; Tsouris, C.; Hu, M. Z. C., EHD micromixing reactor for particle synthesis. *Powder Technology* **2003,** *135*, 302-309.
159. Modarres, P.; Tabrizian, M., Electrohydrodynamic-driven Micromixing for the Synthesis of Highly Monodisperse Nanoscale Liposomes. *ACS Applied Nano Materials* **2020**.
160. Modarres, P.; Tabrizian, M. In *Nanoparticle Synthesis Using an Electrohydrodynamic Micromixer*, 2020 IEEE 33rd International Conference on Micro Electro Mechanical Systems (MEMS), 18-22 Jan. 2020; 2020; pp 1068-1070.
161. Kavehpour, H. P., Coalescence of Drops. *Annual Review of Fluid Mechanics, Vol 47* **2015,** *47*, 245-268.
162. McWilliam, I.; Kwan, M. C.; Hall, D., Inkjet Printing for the Production of Protein Microarrays. *Protein Microarrays: Methods and Protocols* **2011,** *785*, 345-361.
163. Laohalertdecha, S.; Naphon, P.; Wongwises, S., A review of electrohydrodynamic enhancement of heat transfer. *Renew Sust Energ Rev* **2007,** *11* (5), 858-876.
164. Maurmann, N.; Sperling, L. E.; Pranke, P., Electrospun and Electrosprayed Scaffolds for Tissue Engineering. *Adv Exp Med Biol* **2018,** *1078*, 79-100.
165. Huang, Y.; Bu, N.; Duan, Y.; Pan, Y.; Liu, H.; Yin, Z.; Xiong, Y., Electrohydrodynamic direct-writing. *Nanoscale* **2013,** *5* (24), 12007-17.
166. Yeo, L. Y.; Lastochkin, D.; Wang, S. C.; Chang, H. C., A new ac electrospray mechanism by Maxwell-Wagner polarization and capillary resonance. *Phys Rev Lett* **2004,** *92* (13).
167. Yeo, L. Y.; Gagnon, Z.; Chang, H. C., AC electrospray biomaterials synthesis. *Biomaterials* **2005,** *26* (31), 6122-6128.
168. Li, F.; Ozen, O.; Aubry, N.; Papageorgiou, D. T.; Petropoulos, P. G., Linear stability of a two-fluid interface for electrohydrodynamic mixing in a channel. *J Fluid Mech* **2007,** *583*, 347-377.
169. Dienerowitz, M.; Mazilu, M.; Dholakia, K., Optical manipulation of nanoparticles: a review. *J Nanophotonics* **2008,** *2*.
170. Grier, D. G., A revolution in optical manipulation. *Nature* **2003,** *424* (6950), 810-6.
171. Friend, J.; Yeo, L. Y., Microscale acoustofluidics: Microfluidics driven via acoustics and ultrasonics. *Rev Mod Phys* **2011,** *83* (2), 647-704.
172. Sitters, G.; Kamsma, D.; Thalhammer, G.; Ritsch-Marte, M.; Peterman, E. J.; Wuite, G. J., Acoustic force spectroscopy. *Nat Methods* **2015,** *12* (1), 47-50.
173. Gijs, M. A. M., Magnetic bead handling on-chip: new opportunities for analytical applications. *Microfluidics and Nanofluidics* **2004,** *1* (1), 22-40.
174. Haber, C.; Wirtz, D., Magnetic tweezers for DNA micromanipulation. *Rev Sci Instrum* **2000,** *71* (12), 4561-4570.
175. Pohl, H. A., The Motion and Precipitation of Suspensoids in Divergent Electric Fields. *J Appl Phys* **1951,** *22* (7), 869-871.
176. Jones, T. B., *Electromechanics of particles*. Cambridge University Press: Cambridge ; New York, 1995; p xxii, 265 p.

177. Green, N. G., Jones, T. B., Numerical determination of the effective moments of non-spherical particles. *Journal of Physics D-Applied Physics* **2007,** *40* (1), 78-85.
178. Nili, H.; Green, N. G., Higher-order dielectrophoresis of nonspherical particles. *Phys Rev E* **2014,** *89* (6), 063302.
179. Holzel, R., Dielectric and dielectrophoretic properties of DNA. *Iet Nanobiotechnol* **2009,** *3* (2), 28-45.
180. Green, N. G.; Ramos, A.; Gonzalez, A.; Morgan, H.; Castellanos, A., Fluid flow induced by nonuniform ac electric fields in electrolytes on microelectrodes. I. Experimental measurements. *Phys Rev E Stat Phys Plasmas Fluids Relat Interdiscip Topics* **2000,** *61* (4 Pt B), 4011-8.
181. Green, N. G.; Ramos, A.; Gonzalez, A.; Morgan, H.; Castellanos, A., Fluid flow induced by nonuniform ac electric fields in electrolytes on microelectrodes. III. Observation of streamlines and numerical simulation. *Phys Rev E Stat Nonlin Soft Matter Phys* **2002,** *66* (2 Pt 2), 026305.
182. Storey, B. D.; Edwards, L. R.; Sabri Kilic, M.; Bazant, M. Z. High-frequency flow reversal of AC electro-osmosis due to steric effects *ArXiv e-prints* [Online], 2007. http://adsabs.harvard.edu/abs/2007arXiv0711.4812S (accessed November 1, 2007).
183. Lastochkin, D.; Zhou, R. H.; Wang, P.; Ben, Y. X.; Chang, H. C., Electrokinetic micropump and micromixer design based on ac faradaic polarization. *J Appl Phys* **2004,** *96* (3), 1730-1733.
184. Pethig, R., Review article-dielectrophoresis: status of the theory, technology, and applications. *Biomicrofluidics* **2010,** *4* (2).
185. Zhang, C.; Khoshmanesh, K.; Mitchell, A.; Kalantar-Zadeh, K., Dielectrophoresis for manipulation of micro/nano particles in microfluidic systems. *Anal Bioanal Chem* **2010,** *396* (1), 401-20.
186. Khoshmanesh, K.; Nahavandi, S.; Baratchi, S.; Mitchell, A.; Kalantar-zadeh, K., Dielectrophoretic platforms for bio-microfluidic systems. *Biosens Bioelectron* **2011,** *26* (5), 1800-14.
187. Hughes, M. P., Strategies for dielectrophoretic separation in laboratory-on-a-chip systems. *Electrophoresis* **2002,** *23* (16), 2569-82.
188. Jubery, T. Z.; Srivastava, S. K.; Dutta, P., Dielectrophoretic separation of bioparticles in microdevices: a review. *Electrophoresis* **2014,** *35* (5), 691-713.
189. Li, M.; Li, W. H.; Zhang, J.; Alici, G.; Wen, W., A review of microfabrication techniques and dielectrophoretic microdevices for particle manipulation and separation. *Journal of Physics D-Applied Physics* **2014,** *47* (6), 1-29.
190. Regtmeier, J.; Eichhorn, R.; Viefhues, M.; Bogunovic, L.; Anselmetti, D., Electrodeless dielectrophoresis for bioanalysis: theory, devices and applications. *Electrophoresis* **2011,** *32* (17), 2253-73.
191. Washizu, M.; Kurosawa, O., Electrostatic Manipulation of DNA in Microfabricated Structures. *Ieee Transactions on Industry Applications* **1990,** *26* (6), 1165-1172.
192. Washizu, M.; Suzuki, S.; Kurosawa, O.; Nishizaka, T.; Shinohara, T., Molecular Dielectrophoresis of Biopolymers. *Ieee Transactions on Industry Applications* **1994,** *30* (4), 835-843.
193. Kabata, H.; Kurosawa, O.; Arai, I.; Washizu, M.; Margarson, S. A.; Glass, R. E.; Shimamoto, N., Visualization of single molecules of RNA polymerase sliding along DNA. *Science* **1993,** *262* (5139), 1561-3.

194. Asbury, C. L.; van den Engh, G., Trapping of DNA in nonuniform oscillating electric fields. *Biophys J* **1998,** *74* (2 Pt 1), 1024-30.
195. Asbury, C. L.; Diercks, A. H.; van den Engh, G., Trapping of DNA by dielectrophoresis. *Electrophoresis* **2002,** *23* (16), 2658-66.
196. Wong, P. K.; Chen, C. Y.; Wang, T. H.; Ho, C. M., Electrokinetic bioprocessor for concentrating cells and molecules. *Anal Chem* **2004,** *76* (23), 6908-14.
197. Bown, M. R.; Meinhart, C. D., AC electroosmotic flow in a DNA concentrator. *Microfluidics and Nanofluidics* **2006,** *2* (6), 513-523.
198. Cheng, I. F.; Yang, H. L.; Chung, C. C.; Chang, H. C., A rapid electrochemical biosensor based on an AC electrokinetics enhanced immuno-reaction. *Analyst* **2013,** *138* (16), 4656-4662.
199. Wu, J.; Ben, Y. X.; Battigelli, D.; Chang, H. C., Long-range AC electroosmotic trapping and detection of bioparticles. *Ind Eng Chem Res* **2005,** *44* (8), 2815-2822.
200. Du, J. R.; Juang, Y. J.; Wu, J. T.; Wei, H. H., Long-range and superfast trapping of DNA molecules in an ac electrokinetic funnel. *Biomicrofluidics* **2008,** *2* (4), 44103.
201. Du, J. R.; Wei, H. H., Focusing and trapping of DNA molecules by head-on ac electrokinetic streaming through join asymmetric polarization. *Biomicrofluidics* **2010,** *4* (3), 1-13.
202. Dewarrat, F., Calame, M.,Schonenberger, C., Orientation and positioning of DNA molecules with an electric field technique. *Single Mol* **2002,** *3* (4), 189-193.
203. Holzel, R.; Calander, N.; Chiragwandi, Z.; Willander, M.; Bier, F. F., Trapping single molecules by dielectrophoresis. *Phys Rev Lett* **2005,** *95* (12), 128102.
204. Tuukkanen, S.; Kuzyk, A.; Toppari, J. J.; Hytonen, V. P.; Ihalainen, T.; Torma, P., Dielectrophoresis of nanoscale double-stranded DNA and humidity effects on its electrical conductivity. *Appl Phys Lett* **2005,** *87* (18), 1-3.
205. Tuukkanen, S.; Kuzyk, A.; Toppari, J. J.; Hakkinen, H.; Hytonen, V. P.; Niskanen, E.; Rinkio, M.; Torma, P., Trapping of 27 bp-8 kbp DNA and immobilization of thiol-modified DNA using dielectrophoresis. *Nanotechnology* **2007,** *18* (29).
206. Kalyanasundaram, D.; Inoue, S.; Kim, J. H.; Lee, H. B.; Kawabata, Z.; Yeo, W. H.; Cangelosi, G. A.; Oh, K.; Gao, D.; Lee, K. H.; Chung, J. H., Electric field-induced concentration and capture of DNA onto microtips. *Microfluidics and Nanofluidics* **2012,** *13* (2), 217-225.
207. Kalyanasundaram, D.; Kim, J. H.; Yeo, W. H.; Oh, K.; Lee, K. H.; Kim, M. H.; Ryew, S. M.; Ahn, S. G.; Gao, D.; Cangelosi, G. A.; Chung, J. H., Rapid extraction and preservation of genomic DNA from human samples. *Analytical and Bioanalytical Chemistry* **2013,** *405* (6), 1977-1983.
208. Hashiguchi, G.; Goda, T.; Hosogi, M.; Hirano, K.; Kaji, N.; Baba, Y.; Kakushima, K.; Fujita, H., DNA manipulation and retrieval from an aqueous solution with micromachined nanotweezers. *Anal Chem* **2003,** *75* (17), 4347-50.
209. Yamahata, C.; Collard, D.; Legrand, B.; Takekawa, T.; Kunternura, M.; Hashiguchi, G.; Fujita, H., Silicon nanotweezers with subnanometer resolution for the micromanipulation of biomolecules. *Journal of Microelectromechanical Systems* **2008,** *17* (3), 623-631.
210. Yamahata, C.; Collard, D.; Takekawa, T.; Kumemura, M.; Hashiguchi, G.; Fujita, H., Humidity dependence of charge transport through DNA revealed by silicon-based nanotweezers manipulation. *Biophys J* **2008,** *94* (1), 63-70.
211. Kumemura, M.; Collard, D.; Sakaki, N.; Yamahata, C.; Hosogi, M.; Hashiguchi, G.; Fujita, H., Single-DNA-molecule trapping with silicon nanotweezers using pulsed dielectrophoresis. *Journal of Micromechanics and Microengineering* **2011,** *21* (5), 054020.

212. Tuukkanen, S.; Toppari, J. J.; Kuzyk, A.; Hirviniemi, L.; Hytonen, V. P.; Ihalainen, T.; Torma, P., Carbon nanotubes as electrodes for dielectrophoresis of DNA. *Nano Lett* **2006,** *6* (7), 1339-43.
213. Yeo, W. H.; Chung, J. H.; Liu, Y.; Lee, K. H., Size-specific concentration of DNA to a nanostructured tip using dielectrophoresis and capillary action. *J Phys Chem B* **2009,** *113* (31), 10849-58.
214. Yeo, W. H.; Kopacz, A. M.; Kim, J. H.; Chen, X.; Wu, J.; Gao, D.; Lee, K. H.; Liu, W. K.; Chung, J. H., Dielectrophoretic concentration of low-abundance nanoparticles using a nanostructured tip. *Nanotechnology* **2012,** *23* (48), 485707.
215. Maruyama, H.; Nakayama, Y., Trapping Protein Molecules at a Carbon Nanotube Tip using Dielectrophoresis. *Appl Phys Express* **2008,** *1* (12).
216. Kopacz, A. M.; Yeo, W. H.; Chung, J. H.; Liu, W. K., Nanoscale sensor analysis using the immersed molecular electrokinetic finite element method. *Nanoscale* **2012,** *4* (16), 5189-94.
217. Kalyanasundaram, D.; Kim, J. H.; Fotouhi, G.; Lee, H. B.; Hiraiwa, M.; Oh, K.; Lee, K. H.; Chung, J. H., Nanotips for single-step preparation of DNA for qPCR analysis. *Analyst* **2013,** *138* (11), 3135-8.
218. Yeo, W. H.; Chou, F. L.; Oh, K.; Lee, K. H.; Chung, J. H., Hybrid Nanofibril Assembly Using an Alternating Current Electric Field and Capillary Action. *J Nanosci Nanotechno* **2009,** *9* (12), 7288-7292.
219. Tang, J.; Gao, B.; Geng, H.; Velev, O. D.; Qin, L. C.; Zhou, O., Assembly of 1D Nanostructures into Sub-micrometer Diameter Fibrils with Controlled and Variable Length by Dielectrophoresis. *Adv Mater* **2003,** *15* (16), 1352-1355.
220. Suhr, J.; Koratkar, N.; Keblinski, P.; Ajayan, P., Viscoelasticity in carbon nanotube composites. *Nat Mater* **2005,** *4* (2), 134-7.
221. Yamahata, C.; Takekawa, T.; Ayano, K.; Hosogi, M.; Kumemura, M.; Legrand, B.; Collard, D.; Hashiguchi, G.; Fujita, H. In *Silicon Nanotweezers with Adjustable and Controllable Gap for the Manipulation and Characterization of DNA Molecules*, 2006 International Conference on Microtechnologies in Medicine and Biology, 9-12 May 2006; 2006; pp 123-126.
222. Chou, C. F.; Tegenfeldt, J. O.; Bakajin, O.; Chan, S. S.; Cox, E. C.; Darnton, N.; Duke, T.; Austin, R. H., Electrodeless dielectrophoresis of single- and double-stranded DNA. *Biophys J* **2002,** *83* (4), 2170-9.
223. Lapizco-Encinas, B. H.; Ozuna-Chacon, S.; Rito-Palomares, M., Protein manipulation with insulator-based dielectrophoresis and direct current electric fields. *J Chromatogr A* **2008,** *1206* (1), 45-51.
224. Nakano, A.; Chao, T. C.; Camacho-Alanis, F.; Ros, A., Immunoglobulin G and bovine serum albumin streaming dielectrophoresis in a microfluidic device. *Electrophoresis* **2011,** *32* (17), 2314-22.
225. Staton, S. J.; Jones, P. V.; Ku, G.; Gilman, S. D.; Kheterpal, I.; Hayes, M. A., Manipulation and capture of Abeta amyloid fibrils and monomers by DC insulator gradient dielectrophoresis (DC-iGDEP). *Analyst* **2012,** *137* (14), 3227-9.
226. Nakano, A.; Camacho-Alanis, F.; Ros, A., Insulator-based dielectrophoresis with beta-galactosidase in nanostructured devices. *Analyst* **2015,** *140* (3), 860-8.
227. Chaurey, V.; Rohani, A.; Su, Y. H.; Liao, K. T.; Chou, C. F.; Swami, N. S., Scaling down constriction-based (electrodeless) dielectrophoresis devices for trapping nanoscale bioparticles in physiological media of high-conductivity. *Electrophoresis* **2013,** *34* (7), 1097-104.

228. Liao, K. T.; Chou, C. F., Nanoscale molecular traps and dams for ultrafast protein enrichment in high-conductivity buffers. *J Am Chem Soc* **2012,** *134* (21), 8742-5.
229. Liao, K. T.; Tsegaye, M.; Chaurey, V.; Chou, C. F.; Swami, N. S., Nano-constriction device for rapid protein preconcentration in physiological media through a balance of electrokinetic forces. *Electrophoresis* **2012,** *33* (13), 1958-66.
230. Chiou, C. H.; Chien, L. J.; Kuo, J. N., Nanoconstriction-based electrodeless dielectrophoresis chip for nanoparticle and protein preconcentration. *Appl Phys Express* **2015,** *8* (8).
231. Ying, L.; Bruckbauer, A.; Rothery, A. M.; Korchev, Y. E.; Klenerman, D., Programmable delivery of DNA through a nanopipet. *Anal Chem* **2002,** *74* (6), 1380-5.
232. Ying, L.; White, S. S.; Bruckbauer, A.; Meadows, L.; Korchev, Y. E.; Klenerman, D., Frequency and voltage dependence of the dielectrophoretic trapping of short lengths of DNA and dCTP in a nanopipette. *Biophys J* **2004,** *86* (2), 1018-27.
233. Bruckbauer, A.; Ying, L.; Rothery, A. M.; Zhou, D.; Shevchuk, A. I.; Abell, C.; Korchev, Y. E.; Klenerman, D., Writing with DNA and protein using a nanopipet for controlled delivery. *J Am Chem Soc* **2002,** *124* (30), 8810-1.
234. Clarke, R. W.; White, S. S.; Zhou, D.; Ying, L.; Klenerman, D., Trapping of proteins under physiological conditions in a nanopipette. *Angew Chem Int Edit* **2005,** *44* (24), 3747-50.
235. Clarke, R. W.; Piper, J. D.; Ying, L.; Klenerman, D., Surface conductivity of biological macromolecules measured by nanopipette dielectrophoresis. *Phys Rev Lett* **2007,** *98* (19), 198102.
236. Teixidor, G. T.; Gorkin, R. A.; Tripathi, P. P.; Bisht, G. S.; Kulkarni, M.; Maiti, T. K.; Battacharyya, T. K.; Subramaniam, J. R.; Sharma, A.; Park, B. Y.; Madou, M., Carbon microelectromechanical systems as a substratum for cell growth. *Biomed Mater* **2008,** *3* (3).
237. Martinez-Duarte, R.; Camacho-Alanis, F.; Renaud, P.; Ros, A., Dielectrophoresis of lambda-DNA using 3D carbon electrodes. *Electrophoresis* **2013,** *34* (7), 1113-22.
238. Martinez-Duarte, R.; Renaud, P.; Madou, M. J., A novel approach to dielectrophoresis using carbon electrodes. *Electrophoresis* **2011,** *32* (17), 2385-2392.
239. Rouabah, H. A.; Park, B. Y.; Zaouk, R. B.; Morgan, H.; Madou, M. J.; Green, N. G., Design and fabrication of an ac-electro-osmosis micropump with 3D high-aspect-ratio electrodes using only SU-8. *Journal of Micromechanics and Microengineering* **2011,** *21* (3).
240. Hoeb, M.; Radler, J. O.; Klein, S.; Stutzmann, M.; Brandt, M. S., Light-induced dielectrophoretic manipulation of DNA. *Biophys J* **2007,** *93* (3), 1032-8.
241. Chiou, P. Y.; Ohta, A. T.; Jamshidi, A.; Hsu, H. Y.; Wu, M. C., Light-actuated ac electroosmosis for nanoparticle manipulation. *Journal of Microelectromechanical Systems* **2008,** *17* (3), 525-531.
242. Jamshidi, A.; Neale, S. L.; Yu, K.; Pauzauskie, P. J.; Schuck, P. J.; Valley, J. K.; Hsu, H. Y.; Ohta, A. T.; Wu, M. C., NanoPen: Dynamic, Low-Power, and Light-Actuated Patterning of Nanoparticles. *Nano Lett* **2009,** *9* (8), 2921-2925.
243. Washizu, M.; Kurosawa, O.; Arai, I.; Suzuki, S.; Shimamoto, N., Applications of Electrostatic Stretch-and-Positioning of DNA. *Ieee Transactions on Industry Applications* **1995,** *31* (3), 447-456.
244. Ueda, M.; Iwasaki, H.; Kurosawa, O.; Washizu, M., Atomic Force Microscopy Observation of Deoxyribonucleic Acid Stretched and Anchored onto Aluminum Electrodes. *Japanese Journal of Applied Physics* **1999,** *38* (Part 1, No. 4A), 2118-2119.
245. Yamamoto, T., Molecular surgery of DNA based on electrostatic micromanipulation. *IEEE Transactions on Industry Applications* **2000,** *36*, 1010-1017.

246. Nimse, S. B.; Song, K.; Sonawane, M. D.; Sayyed, D. R.; Kim, T., Immobilization techniques for microarray: challenges and applications. *Sensors-Basel* **2014,** *14* (12), 22208-29.
247. Namasivayam, V.; Larson, R. G.; Burke, D. T.; Burns, M. A., Electrostretching DNA molecules using polymer-enhanced media within microfabricated devices. *Anal Chem* **2002,** *74* (14), 3378-85.
248. Holzel, R.; Gajovic-Eichelmann, N.; Bier, F. F., Oriented and vectorial immobilization of linear M13 dsDNA between interdigitated electrodes--towards single molecule DNA nanostructures. *Biosens Bioelectron* **2003,** *18* (5-6), 555-64.
249. Germishuizen, W. A.; Walti, C.; Wirtz, R.; Johnston, M. B.; Pepper, M.; Davies, A. G.; Middelberg, A. P. J., Selective dielectrophoretic manipulation of surface-immobilized DNA molecules. *Nanotechnology* **2003,** *14* (8), 896-902.
250. Venkatesh, A. G.; Herth, S.; Becker, A.; Reiss, G., Orientation-defined alignment and immobilization of DNA between specific surfaces. *Nanotechnology* **2011,** *22* (14).
251. Wälti, C.; Germishuizen, W. A.; Tosch, P.; Kaminski, C. F.; Davies, A. G., AC electrokinetic manipulation of DNA. *Journal of Physics D: Applied Physics* **2007,** *40* (1), 114-118.
252. Germishuizen, W. A.; Tosch, P.; Middelberg, A. P. J.; Walti, C.; Davies, A. G.; Wirtz, R.; Pepper, M., Influence of alternating current electrokinetic forces and torque on the elongation of immobilized DNA. *J Appl Phys* **2005,** *97* (1), 014702.
253. Germishuizen, W. A.; Walti, C.; Tosch, P.; Wirtz, R.; Pepper, M.; Davies, A. G.; Middelberg, A. P., Dielectrophoretic manipulation of surface-bound DNA. *IEE Proc Nanobiotechnol* **2003,** *150* (2), 54-8.
254. Sung, K. E.; Burns, M. A., Optimization of dielectrophoretic DNA stretching in microfabricated devices. *Anal Chem* **2006,** *78* (9), 2939-47.
255. Wälti, C.; Tosch, P.; Davies, A. G.; Germishuizen, W. A.; Kaminski, C. F., Establishment of the ac electrokinetic elongation mechanism of DNA by three-dimensional fluorescent imaging. *Appl Phys Lett* **2006,** *88* (15), 153901.
256. Kawabata, T.; Washizu, M., Dielectrophoretic detection of molecular bindings. *Ieee Transactions on Industry Applications* **2001,** *37* (6), 1625-1633.
257. Sano, H. A.; Kabata, H.; Kurosawa, O.; Washizu, M., Dielectrophoretic chromatography with cross-flow injection. *Proc Ieee Micr Elect* **2002**, 11-14.
258. Viefhues, M.; Regtmeier, J.; Anselmetti, D., Fast and continuous-flow separation of DNA-complexes and topological DNA variants in microfluidic chip format. *Analyst* **2013,** *138* (1), 186-96.
259. Viefhues, M.; Wegener, S.; Rischmuller, A.; Schleef, M.; Anselmetti, D., Dielectrophoresis based continuous-flow nano sorter: fast quality control of gene vaccines. *Lab Chip* **2013,** *13* (15), 3111-8.
260. Sheehan, P. E.; Whitman, L. J., Detection limits for nanoscale biosensors. *Nano Lett* **2005,** *5* (4), 803-7.
261. Cheng, I. F.; Yang, H. L.; Chung, C. C.; Chang, H. C., A rapid electrochemical biosensor based on an AC electrokinetics enhanced immuno-reaction. *Analyst* **2013,** *138* (16), 4656-62.
262. Chuang, C. H.; Du, Y. C.; Wu, T. F.; Chen, C. H.; Lee, D. H.; Chen, S. M.; Huang, T. C.; Wu, H. P.; Shaikh, M. O., Immunosensor for the ultrasensitive and quantitative detection of bladder cancer in point of care testing. *Biosens Bioelectron* **2016,** *84*, 126-32.
263. Kim, H. J.; Kim, J.; Yoo, Y. K.; Lee, J. H.; Park, J. H.; Hwang, K. S., Sensitivity improvement of an electrical sensor achieved by control of biomolecules based on the negative dielectrophoretic force. *Biosensors & Bioelectronics* **2016,** *85*, 977-985.

264. Li, S. S.; Ren, Y. K.; Cui, H. C.; Yuan, Q.; Wu, J.; Eda, S.; Jiang, H. Y., Alternating current electrokinetics enhanced in situ capacitive immunoassay. *Electrophoresis* **2015,** *36* (3), 471-474.
265. Schafer, C.; Kern, D. P.; Fleischer, M., Capturing molecules with plasmonic nanotips in microfluidic channels by dielectrophoresis. *Lab on a Chip* **2015,** *15* (4), 1066-1071.
266. Barik, A.; Otto, L. M.; Yoo, D.; Jose, J.; Johnson, T. W.; Oh, S. H., Dielectrophoresis-Enhanced Plasmonic Sensing with Gold Nanohole Arrays. *Nano Lett* **2014,** *14* (4), 2006-2012.
267. Sharma, A.; Han, C. H.; Jang, J., Rapid electrical immunoassay of the cardiac biomarker troponin I through dielectrophoretic concentration using imbedded electrodes. *Biosensors & Bioelectronics* **2016,** *82*, 78-84.
268. Gong, J. R., Label-free attomolar detection of proteins using integrated nanoelectronic and electrokinetic devices. *Small* **2010,** *6* (8), 967-73.
269. Chuang, C. H.; Wu, T. F.; Chen, C. H.; Chang, K. C.; Ju, J. W.; Huang, Y. W.; Nhan, V. V., Lab on a chip for multiplexed immunoassays to detect bladder cancer using multifunctional dielectrophoretic manipulations. *Lab on a Chip* **2015,** *15* (14), 3056-3064.
270. Puttaswamy, S. V.; Lin, C. H.; Sivashankar, S.; Yang, Y. S.; Liu, C. H., Electrodeless dielectrophoretic concentrator for analyte pre-concentration on poly-silicon nanowire field effect transistor. *Sensors and Actuators B-Chemical* **2013,** *178*, 547-554.
271. Sanghavi, B. J.; Varhue, W.; Rohani, A.; Liao, K. T.; Bazydlo, L. A.; Chou, C. F.; Swami, N. S., Ultrafast immunoassays by coupling dielectrophoretic biomarker enrichment in nanoslit channel with electrochemical detection on graphene. *Lab Chip* **2015,** *15* (24), 4563-70.
272. Swami, N.; Chou, C. F.; Ramamurthy, V.; Chaurey, V., Enhancing DNA hybridization kinetics through constriction-based dielectrophoresis. *Lab Chip* **2009,** *9* (22), 3212-20.
273. Cheng, I. F.; Han, H. W.; Chang, H. C., Dielectrophoresis and shear-enhanced sensitivity and selectivity of DNA hybridization for the rapid discrimination of Candida species. *Biosens Bioelectron* **2012,** *33* (1), 36-43.
274. Cheng, I. F.; Senapati, S.; Cheng, X.; Basuray, S.; Chang, H. C.; Chang, H. C., A rapid field-use assay for mismatch number and location of hybridized DNAs. *Lab Chip* **2010,** *10* (7), 828-31.
275. Ceron-Carrasco, J. P.; Jacquemin, D., Electric-field induced mutation of DNA: a theoretical investigation of the GC base pair. *Phys Chem Chem Phys* **2013,** *15* (13), 4548-53.
276. Ceron-Carrasco, J. P.; Cerezo, J.; Jacquemin, D., How DNA is damaged by external electric fields: selective mutation vs. random degradation. *Physical Chemistry Chemical Physics* **2014,** *16* (18), 8243-8246.
277. Bekard, I.; Dunstan, D. E., Electric field induced changes in protein conformation. *Soft Matter* **2014,** *10* (3), 431-7.
278. Wang, X.; Li, Y.; He, X.; Chen, S.; Zhang, J. Z., Effect of strong electric field on the conformational integrity of insulin. *J Phys Chem A* **2014,** *118* (39), 8942-52.
279. Jarukanont, D.; Coimbra, J. T. S.; Bauerhenne, B.; Fernandes, P. A.; Patel, S.; Ramos, M. J.; Garcia, M. E., Biomolecular structure manipulation using tailored electromagnetic radiation: a proof of concept on a simplified model of the active site of bacterial DNA topoisomerase. *Physical Chemistry Chemical Physics* **2014,** *16* (39), 21768-21777.
280. Kastritis, P. L.; Bonvin, A. M., On the binding affinity of macromolecular interactions: daring to ask why proteins interact. *J R Soc Interface* **2013,** *10* (79), 20120835.

281. Reverberi, R.; Reverberi, L., Factors affecting the antigen-antibody reaction. *Blood Transfus* **2007,** *5* (4), 227-40.
282. Kale, A.; Patel, S.; Hu, G. Q.; Xuan, X. C., Numerical modeling of Joule heating effects in insulator-based dielectrophoresis microdevices. *Electrophoresis* **2013,** *34* (5), 674-683.
283. Giraud, G.; Pethig, R.; Schulze, H.; Henihan, G.; Terry, J. G.; Menachery, A.; Ciani, I.; Corrigan, D.; Campbell, C. J.; Mount, A. R.; Ghazal, P.; Walton, A. J.; Crain, J.; Bachmann, T. T., Dielectrophoretic manipulation of ribosomal RNA. *Biomicrofluidics* **2011,** *5* (2), 24116.
284. Nawarathna, D.; Chang, R.; Nelson, E.; Wickramasinghe, H. K., Targeted messenger RNA profiling of transfected breast cancer gene in a living cell. *Anal Biochem* **2011,** *408* (2), 342-4.
285. Gan, L.; Chao, T. C.; Camacho-Alanis, F.; Ros, A., Six-helix bundle and triangle DNA origami insulator-based dielectrophoresis. *Anal Chem* **2013,** *85* (23), 11427-34.
286. Kuzyk, A.; Yurke, B.; Toppari, J. J.; Linko, V.; Torma, P., Dielectrophoretic trapping of DNA origami. *Small* **2008,** *4* (4), 447-50.
287. Shen, B.; Linko, V.; Dietz, H.; Toppari, J. J., Dielectrophoretic trapping of multilayer DNA origami nanostructures and DNA origami-induced local destruction of silicon dioxide. *Electrophoresis* **2015,** *36* (2), 255-62.
288. Gan, L.; Camacho-Alanis, F.; Ros, A., Polarizability of Six-Helix Bundle and Triangle DNA Origami and Their Escape Characteristics from a Dielectrophoretic Trap. *Analytical Chemistry* **2015,** *87* (24), 12059-12064.
289. Linko, V.; Leppiniemi, J.; Paasonen, S. T.; Hytonen, V. P.; Toppari, J. J., Defined-size DNA triple crossover construct for molecular electronics: modification, positioning and conductance properties. *Nanotechnology* **2011,** *22* (27).
290. Sanghavi, B. J.; Varhue, W.; Chavez, J. L.; Chou, C. F.; Swami, N. S., Electrokinetic Preconcentration and Detection of Neuropeptides at Patterned Graphene-Modified Electrodes in a Nanochannel. *Analytical Chemistry* **2014,** *86* (9), 4120-4125.
291. Uppalapati, M.; Huang, Y. M.; Aravamuthan, V.; Jackson, T. N.; Hancock, W. O., "Artificial mitotic spindle" generated by dielectrophoresis and protein micropatterning supports bidirectional transport of kinesin-coated beads. *Integr Biol (Camb)* **2011,** *3* (1), 57-64.
292. Uppalapati, M.; Huang, Y. M.; Jackson, T. N.; Hancock, W. O., Microtubule alignment and manipulation using AC electrokinetics. *Small* **2008,** *4* (9), 1371-81.
293. Bohm, K. J.; Mavromatos, N. E.; Michette, A.; Stracke, R.; Unger, E., Movement and alignment of microtubules in electric fields and electric-dipole-moment estimates. *Electromagn Biol Med* **2005,** *24* (3), 319-330.
294. Arsenault, M. E.; Zhao, H.; Purohit, P. K.; Goldman, Y. E.; Bau, H. H., Confinement and manipulation of actin filaments by electric fields. *Biophys J* **2007,** *93* (8), L42-4.
295. Huang, L.; Manandhar, P.; Byun, K. E.; Chase, P. B.; Hong, S., Selective assembly and alignment of actin filaments with desired polarity on solid substrates. *Langmuir* **2006,** *22* (21), 8635-8.
296. Asokan, S. B.; Jawerth, L.; Carroll, R. L.; Cheney, R. E.; Washburn, S.; Superfine, R., Two-dimensional manipulation and orientation of actin-myosin systems with dielectrophoresis. *Nano Lett* **2003,** *3* (4), 431-437.
297. Nili, H.; Green, N. G., AC Electrokinetics of Nanoparticles. In *Encyclopedia of Nanotechnology*, Bhushan, B., Ed. Springer: New York, 2012; pp 18-25.
298. Du, J. R.; Juang, Y. J.; Wu, J. T.; Wei, H. H., Long-range and superfast trapping of DNA molecules in an ac electrokinetic funnel. *Biomicrofluidics* **2008,** *2* (4).

299. Wolff, A.; Leiterer, C.; Csaki, A.; Fritzsche, W., Dielectrophoretic manipulation of DNA in microelectrode gaps for single-molecule constructs. *Front Biosci* **2008,** *13*, 6834-40.
300. Bakewell, D. J. G.; Hughes, M. P.; Milner, J. J.; Morgan, H., Dielectrophoretic manipulation of avidin and DNA. *P Ann Int Ieee Embs* **1998,** *20*, 1079-1082.
301. Zheng, L.; Brody, J. P.; Burke, P. J., Electronic manipulation of DNA, proteins, and nanoparticles for potential circuit assembly. *Biosens Bioelectron* **2004,** *20* (3), 606-19.
302. Sonnenberg, A.; Marciniak, J. Y.; Krishnan, R.; Heller, M. J., Dielectrophoretic isolation of DNA and nanoparticles from blood. *Electrophoresis* **2012,** *33* (16), 2482-90.
303. Sonnenberg, A.; Marciniak, J. Y.; McCanna, J.; Krishnan, R.; Rassenti, L.; Kipps, T. J.; Heller, M. J., Dielectrophoretic isolation and detection of cfc-DNA nanoparticulate biomarkers and virus from blood. *Electrophoresis* **2013,** *34* (7), 1076-84.
304. Du, M. L.; Bier, F. F.; Holzel, R., Quantifying DNA dielectrophoresis. *DNA-Based Nanoscale Integration* **2006,** *859*, 65-72.
305. Bakewell, D. J.; Morgan, H., Dielectrophoresis of DNA: time- and frequency-dependent collections on microelectrodes. *IEEE Trans Nanobioscience* **2006,** *5* (2), 139-46.
306. Laux, E. M.; Knigge, X.; Bier, F. F.; Wenger, C.; Holzel, R., Dielectrophoretic immobilization of proteins: Quantification by atomic force microscopy. *Electrophoresis* **2015,** *36* (17), 2094-101.
307. Otto, S.; Kaletta, U.; Bier, F. F.; Wenger, C.; Holzel, R., Dielectrophoretic immobilisation of antibodies on microelectrode arrays. *Lab Chip* **2014,** *14* (5), 998-1004.
308. Laux, E. M.; Knigge, X.; Bier, F. F.; Wenger, C.; Holzel, R., Aligned Immobilization of Proteins Using AC Electric Fields. *Small* **2016,** *12* (11), 1514-20.
309. Chaurey, V.; Polanco, C.; Chou, C. F.; Swami, N. S., Floating-electrode enhanced constriction dielectrophoresis for biomolecular trapping in physiological media of high conductivity. *Biomicrofluidics* **2012,** *6* (1), 12806-1280614.
310. Viefhues, M.; Regtmeier, J.; Anselmetti, D., Nanofluidic devices for dielectrophoretic mobility shift assays by soft lithography. *Journal of Micromechanics and Microengineering* **2012,** *22* (11), 115024.
311. Dalir, H.; Yanagida, Y.; Hatsuzawa, T., Probing DNA mechanical characteristics by dielectrophoresis. *Sensors and Actuators B-Chemical* **2009,** *136* (2), 472-478.
312. Hyun, C.; Kaur, H.; McNabb, D. S.; Li, J., Dielectrophoretic stretching of DNA tethered to a fiber tip. *Nanotechnology* **2015,** *26* (12), 125501.
313. Cristofanilli, M., Circulating tumor cells, disease progression, and survival in metastatic breast cancer. *Semin Oncol* **2006,** *33* (3), S9-S14.
314. Nagrath, S.; Sequist, L. V.; Maheswaran, S.; Bell, D. W.; Irimia, D.; Ulkus, L.; Smith, M. R.; Kwak, E. L.; Digumarthy, S.; Muzikansky, A.; Ryan, P.; Balis, U. J.; Tompkins, R. G.; Haber, D. A.; Toner, M., Isolation of rare circulating tumour cells in cancer patients by microchip technology. *Nature* **2007,** *450* (7173), 1235-U10.
315. Adams, A. A.; Okagbare, P. I.; Feng, J.; Hupert, M. L.; Patterson, D.; Gottert, J.; McCarley, R. L.; Nikitopoulos, D.; Murphy, M. C.; Soper, S. A., Highly efficient circulating tumor cell isolation from whole blood and label-free enumeration using polymer-based microfluidics with an integrated conductivity sensor. *J Am Chem Soc* **2008,** *130* (27), 8633-41.
316. Yoo, C. E.; Park, J. M.; Moon, H. S.; Joung, J. G.; Son, D. S.; Jeon, H. J.; Kim, Y. J.; Han, K. Y.; Sun, J. M.; Park, K.; Park, D.; Park, W. Y., Vertical Magnetic Separation of Circulating Tumor Cells for Somatic Genomic-Alteration Analysis in Lung Cancer Patients. *Sci Rep* **2016,** *6*, 37392.

317. Kang, J. H.; Krause, S.; Tobin, H.; Mammoto, A.; Kanapathipillai, M.; Ingber, D. E., A combined micromagnetic-microfluidic device for rapid capture and culture of rare circulating tumor cells. *Lab Chip* **2012,** *12* (12), 2175-81.
318. Hoshino, K.; Huang, Y. Y.; Lane, N.; Huebschman, M.; Uhr, J. W.; Frenkel, E. P.; Zhang, X. J., Microchip-based immunomagnetic detection of circulating tumor cells. *Lab on a Chip* **2011,** *11* (20), 3449-3457.
319. Chen, P.; Huang, Y. Y.; Hoshino, K.; Zhang, J. X. J., Microscale Magnetic Field Modulation for Enhanced Capture and Distribution of Rare Circulating Tumor Cells. *Scientific Reports* **2015,** *5*.
320. Hyun, K. A.; Kwon, K.; Han, H.; Kim, S. I.; Jung, H. I., Microfluidic flow fractionation device for label-free isolation of circulating tumor cells (CTCs) from breast cancer patients. *Biosens Bioelectron* **2013,** *40* (1), 206-12.
321. Tan, S. J.; Lakshmi, R. L.; Chen, P.; Lim, W. T.; Yobas, L.; Lim, C. T., Versatile label free biochip for the detection of circulating tumor cells from peripheral blood in cancer patients. *Biosens Bioelectron* **2010,** *26* (4), 1701-5.
322. Sarioglu, A. F.; Aceto, N.; Kojic, N.; Donaldson, M. C.; Zeinali, M.; Hamza, B.; Engstrom, A.; Zhu, H.; Sundaresan, T. K.; Miyamoto, D. T.; Luo, X.; Bardia, A.; Wittner, B. S.; Ramaswamy, S.; Shioda, T.; Ting, D. T.; Stott, S. L.; Kapur, R.; Maheswaran, S.; Haber, D. A.; Toner, M., A microfluidic device for label-free, physical capture of circulating tumor cell clusters. *Nature Methods* **2015,** *12* (7), 685-+.
323. Fan, X. Y.; Jia, C. P.; Yang, J.; Li, G.; Mao, H. J.; Jin, Q. H.; Zhao, J. L., A microfluidic chip integrated with a high-density PDMS-based microfiltration membrane for rapid isolation and detection of circulating tumor cells. *Biosensors & Bioelectronics* **2015,** *71*, 380-386.
324. Hernandez-Castro, J. A.; Li, K.; Meunier, A.; Juncker, D.; Veres, T., Fabrication of large-area polymer microfilter membranes and their application for particle and cell enrichment. *Lab on a Chip* **2017,** *17* (11), 1960-1969.
325. Grover, P. K.; Cummins, A. G.; Price, T. J.; Roberts-Thomson, I. C.; Hardingham, J. E., Circulating tumour cells: the evolving concept and the inadequacy of their enrichment by EpCAM-based methodology for basic and clinical cancer research. *Ann Oncol* **2014,** *25* (8), 1506-1516.
326. Shen, Z.; Wu, A.; Chen, X., Current detection technologies for circulating tumor cells. *Chem Soc Rev* **2017,** *46* (8), 2038-2056.
327. Voldman, J., Electrical forces for microscale cell manipulation. *Annu Rev Biomed Eng* **2006,** *8* (1), 425-54.
328. Hussein, M.; Awwad, F.; Jithin, D.; El Hasasna, H.; Athamneh, K.; Iratni, R., Breast cancer cells exhibits specific dielectric signature in vitro using the open-ended coaxial probe technique from 200 MHz to 13.6 GHz. *Scientific Reports* **2019,** *9* (1), 4681.
329. Ahmad, M. A.; Natour, Z. A.; Mustafa, F.; Rizvi, T. A., Electrical Characterization of Normal and Cancer Cells. *IEEE Access* **2018,** *6*, 25979-25986.
330. Alazzam, A.; Mathew, B.; Alhammadi, F., Novel microfluidic device for the continuous separation of cancer cells using dielectrophoresis. *J Sep Sci* **2017,** *40* (5), 1193-1200.
331. Cui, H. H.; Voldman, J.; He, X. F.; Lim, K. M., Separation of particles by pulsed dielectrophoresis. *Lab Chip* **2009,** *9* (16), 2306-12.
332. Guo, X. L.; Zhu, R., Controllably moving individual living cell in an array by modulating signal phase difference based on dielectrophoresis. *Biosensors & Bioelectronics* **2015,** *68*, 529-535.

333. Rohani, A.; Varhue, W.; Su, Y.-H.; Swami, N. S., Electrical tweezer for highly parallelized electrorotation measurements over a wide frequency bandwidth. *ELECTROPHORESIS* **2014,** *35* (12-13), 1795-1802.
334. Urdaneta, M.; Smela, E., Multiple frequency dielectrophoresis. *Electrophoresis* **2007,** *28* (18), 3145-55.
335. Ren, Y. F.; Huang, S. H.; Mosser, S.; Heuschkel, M. O.; Bertsch, A.; Fraering, P. C.; Chen, J. J. J.; Renaud, P., A Simple and Reliable PDMS and SU-8 Irreversible Bonding Method and Its Application on a Microfluidic-MEA Device for Neuroscience Research. *Micromachines* **2015,** *6* (12), 1923-1934.
336. Arnold, W. M.; Schwan, H. P.; Zimmermann, U., Surface Conductance and Other Properties of Latex-Particles Measured by Electrorotation. *J Phys Chem-Us* **1987,** *91* (19), 5093-5098.
337. Weng, P. Y.; Chen, I. A.; Yeh, C. K.; Chen, P. Y.; Juang, J. Y., Size-dependent dielectrophoretic crossover frequency of spherical particles. *Biomicrofluidics* **2016,** *10* (1), 011909.
338. Park, S.; Zhang, Y.; Wang, T. H.; Yang, S., Continuous dielectrophoretic bacterial separation and concentration from physiological media of high conductivity. *Lab Chip* **2011,** *11* (17), 2893-900.
339. Vahey, M. D.; Voldman, J., High-Throughput Cell and Particle Characterization Using Isodielectric Separation. *Analytical Chemistry* **2009,** *81* (7), 2446-2455.
340. Pethig, R., Review-Where Is Dielectrophoresis (DEP) Going? *Journal of the Electrochemical Society* **2017,** *164* (5), B3049-B3055.
341. Techaumnat, B.; Eua-arporn, B.; Takuma, T., Calculation of electric field and dielectrophoretic force on spherical particles in chain. *J Appl Phys* **2004,** *95* (3), 1586-1593.
342. Gascoyne, P.; Satayavivad, J.; Ruchirawat, M., Microfluidic approaches to malaria detection. *Acta Tropica* **2004,** *89* (3), 357-369.
343. Han, A.; Yang, L.; Frazier, A. B., Quantification of the heterogeneity in breast cancer cell lines using whole-cell impedance spectroscopy. *Clin Cancer Res* **2007,** *13* (1), 139-143.
344. Nguyen, N. T.; Huang, X., Mixing in microchannels based on hydrodynamic focusing and time-interleaved segmentation: modelling and experiment. *Lab Chip* **2005,** *5* (11), 1320-6.
345. Lim, T. W.; Son, Y.; Jeong, Y. J.; Yang, D. Y.; Kong, H. J.; Lee, K. S.; Kim, D. P., Three-dimensionally crossing manifold micro-mixer for fast mixing in a short channel length. *Lab on a Chip* **2011,** *11* (1), 100-103.
346. Liu, R. H.; Stremler, M. A.; Sharp, K. V.; Olsen, M. G.; Santiago, J. G.; Adrian, R. J.; Aref, H.; Beebe, D. J., Passive mixing in a three-dimensional serpentine microchannel. *Journal of Microelectromechanical Systems* **2000,** *9* (2), 190-197.
347. Heo, H. S.; Suh, Y. K., Enhancement of stirring in a straight channel at low Reynolds-numbers with various block-arrangement. *Journal of Mechanical Science and Technology* **2005,** *19* (1), 199-208.
348. Yang, J. T.; Huang, K. J.; Tung, K. Y.; Hu, I. C.; Lyu, P. C., A chaotic micromixer modulated by constructive vortex agitation. *Journal of Micromechanics and Microengineering* **2007,** *17* (10), 2084-2092.
349. Cai, G. Z.; Xue, L.; Zhang, H. L.; Lin, J. H., A Review on Micromixers. *Micromachines* **2017,** *8* (9).
350. Harnett, C. K.; Templeton, J.; Dunphy-Guzman, K. A.; Senousy, Y. M.; Kanouff, M. P., Model based design of a microfluidic mixer driven by induced charge electroosmosis. *Lab on a Chip* **2008,** *8* (4), 565-572.

351. Nouri, D.; Zabihi-Hesari, A.; Passandideh-Fard, M., Rapid mixing in micromixers using magnetic field. *Sensor Actuat a-Phys* **2017,** *255*, 79-86.
352. Petkovic, K.; Metcalfe, G.; Chen, H.; Gao, Y.; Best, M.; Lester, D.; Zhu, Y., Rapid detection of Hendra virus antibodies: an integrated device with nanoparticle assay and chaotic micromixing. *Lab on a Chip* **2017,** *17* (1), 169-177.
353. Chen, X. Y.; Zhang, L., A review on micromixers actuated with magnetic nanomaterials. *Microchim Acta* **2017,** *184* (10), 3639-3649.
354. Grumann, M.; Geipel, A.; Riegger, L.; Zengerle, R.; Ducree, J., Batch-mode mixing on centrifugal microfluidic platforms. *Lab Chip* **2005,** *5* (5), 560-5.
355. Lee, S. H.; van Noort, D.; Lee, J. Y.; Zhang, B. T.; Park, T. H., Effective mixing in a microfluidic chip using magnetic particles. *Lab on a Chip* **2009,** *9* (3), 479-482.
356. Luong, T. D.; Phan, V. N.; Nguyen, N. T., High-throughput micromixers based on acoustic streaming induced by surface acoustic wave. *Microfluidics and Nanofluidics* **2011,** *10* (3), 619-625.
357. Choi, E.; Kwon, K.; Lee, S. J.; Kim, D.; Park, J., Non-equilibrium electrokinetic micromixer with 3D nanochannel networks. *Lab on a Chip* **2015,** *15* (8), 1794-1798.
358. Sasaki, N.; Kitamori, T.; Kim, H. B., Fluid mixing using AC electrothermal flow on meandering electrodes in a microchannel. *Electrophoresis* **2012,** *33* (17), 2668-2673.
359. Song, H. J.; Cai, Z. L.; Noh, H.; Bennett, D. J., Chaotic mixing in microchannels via low frequency switching transverse electroosmotic flow generated on integrated microelectrodes. *Lab on a Chip* **2010,** *10* (6), 734-740.
360. Ng, W. Y.; Goh, S.; Lam, Y. C.; Yang, C.; Rodriguez, I., DC-biased AC-electroosmotic and AC-electrothermal flow mixing in microchannels. *Lab on a Chip* **2009,** *9* (6), 802-809.
361. Huang, S. H.; Wang, S. K.; Khoo, H. S.; Tseng, F. G., AC electroosmotic generated in-plane microvortices for stationary or continuous fluid mixing. *Sensors and Actuators B-Chemical* **2007,** *125* (1), 326-336.
362. Sasaki, N.; Kitamori, T.; Kim, H. B., AC electroosmotic micromixer for chemical processing in a microchannel. *Lab on a Chip* **2006,** *6* (4), 550-554.
363. Nampoothiri, K. N.; Seshasayee, M. S.; Srinivasan, V.; Bobji, M. S.; Sen, P., Direct heating of aqueous droplets using high frequency voltage signals on an EWOD platform. *Sensors and Actuators B-Chemical* **2018,** *273*, 862-872.
364. Song, Y. J.; Chen, P. Y.; Chung, M. T.; Nidetz, R.; Park, Y.; Liu, Z. H.; McHugh, W.; Cornell, T. T.; Fu, J. P.; Kurabayashi, K., AC Electroosmosis-Enhanced Nanoplasmofluidic Detection of Ultralow-Concentration Cytokine. *Nano Lett* **2017,** *17* (4), 2374-2380.
365. Hart, R.; Ergezen, E.; Lec, R.; Noh, H., Improved protein detection on an AC electrokinetic quartz crystal microbalance (EKQCM). *Biosensors & Bioelectronics* **2011,** *26* (8), 3391-3397.
366. Green, N. G.; Ramos, A.; Gonzalez, A.; Morgan, H.; Castellanos, A., Fluid flow induced by nonuniform ac electric fields in electrolytes on microelectrodes. III. Observation of streamlines and numerical simulation. *Physical Review E* **2002,** *66* (2).
367. Gonzalez, A.; Ramos, A.; Green, N. G.; Castellanos, A.; Morgan, H., Fluid flow induced by nonuniform ac electric fields in electrolytes on microelectrodes. II. A linear double-layer analysis. *Physical Review E* **2000,** *61* (4), 4019-4028.
368. Wang, Y. N.; Fu, L. M., Micropumps and biomedical applications - A review. *Microelectronic Engineering* **2018,** *195*, 121-138.

369. Ward, K.; Fan, Z. H., Mixing in microfluidic devices and enhancement methods. *J Micromech Microeng* **2015,** *25* (9).
370. Salari, A.; Thompson, M., Recent advances in AC electrokinetic sample enrichment techniques for biosensor development. *Sensors and Actuators B-Chemical* **2018,** *255*, 3601-3615.
371. Mirzajani, H.; Cheng, C.; Wu, J. N.; Ivanoff, C. S.; Aghdam, E. N.; Ghavifekr, H. B., Design and characterization of a passive, disposable wireless AC-electroosmotic lab-on-a-film for particle and fluid manipulation. *Sensors and Actuators B-Chemical* **2016,** *235*, 330-342.
372. Hart, R.; Lec, R.; Noh, H., Enhancement of heterogeneous immunoassays using AC electroosmosis. *Sensors and Actuators B-Chemical* **2010,** *147* (1), 366-375.
373. Yeh, L. H.; Xue, S.; Joo, S. W.; Qian, S.; Hsu, J. P., Field Effect Control of Surface Charge Property and Electroosmotic Flow in Nanofluidics. *Journal of Physical Chemistry C* **2012,** *116* (6), 4209-4216.
374. van der Wouden, E. J.; Heuser, T.; Hermes, D. C.; Oosterbroek, R. E.; Gardeniers, J. G. E.; van den Berg, A., Field-effect control of electro-osmotic flow in microfluidic networks. *Colloids and Surfaces a-Physicochemical and Engineering Aspects* **2005,** *267* (1-3), 110-116.
375. Karnik, R.; Fan, R.; Yue, M.; Li, D. Y.; Yang, P. D.; Majumdar, A., Electrostatic control of ions and molecules in nanofluidic transistors. *Nano Lett* **2005,** *5* (5), 943-948.
376. Buch, J. S.; Wang, P. C.; DeVoe, D. L.; Lee, C. S., Field-effect flow control in a polydimethylsiloxane-based microfluidic system. *Electrophoresis* **2001,** *22* (18), 3902-7.
377. Fu, H.; Liu, X. L.; Li, S. J., Mixing indexes considering the combination of mean and dispersion information from intensity images for the performance estimation of micromixing. *Rsc Advances* **2017,** *7* (18), 10906-10914.
378. Wu, J. T.; Du, J. R.; Juang, Y. J.; Wei, H. H., Rectified elongational streaming due to asymmetric electro-osmosis induced by ac polarization. *Appl Phys Lett* **2007,** *90* (13).
379. Castellanos, A.; Ramos, A.; Gonzalez, A.; Green, N. G.; Morgan, H., Electrohydrodynamics and dielectrophoresis in microsystems: scaling laws. *Journal of Physics D-Applied Physics* **2003,** *36* (20), 2584-2597.
380. Loire, S.; Kauffmann, P.; Mezic, I.; Meinhart, C. D., A theoretical and experimental study of ac electrothermal flows. *Journal of Physics D-Applied Physics* **2012,** *45* (18).
381. Laouini, A.; Jaafar-Maalej, C.; Limayem-Blouza, I.; Sfar, S.; Charcosset, C.; Fessi, H., Preparation, Characterization and Applications of Liposomes: State of the Art. *J Colloid Sci Biotec* **2012,** *1* (2), 147-168.
382. Ding, S. K.; Anton, N.; Vandamme, T. F.; Serra, C. A., Microfluidic nanoprecipitation systems for preparing pure drug or polymeric drug loaded nanoparticles: an overview. *Expert Opin Drug Del* **2016,** *13* (10), 1447-1460.
383. Lu, M. Q.; Ozcelik, A.; Grigsby, C. L.; Zhao, Y. H.; Guo, F.; Leong, K. W.; Huang, T. J., Microfluidic hydrodynamic focusing for synthesis of nanomaterials. *Nano Today* **2016,** *11* (6), 778-792.
384. Wang, J. M.; Li, Y.; Wang, X. Y.; Wang, J. C.; Tian, H. M.; Zhao, P.; Tian, Y.; Gu, Y. M.; Wang, L. Q.; Wang, C. Y., Droplet Microfluidics for the Production of Microparticles and Nanoparticles. *Micromachines* **2017,** *8* (1).
385. Huang, P. H.; Zhao, S. G.; Bachman, H.; Nama, N.; Li, Z. S.; Chen, C. Y.; Yang, S. J.; Wu, M. X.; Zhang, S. P.; Huang, T. J., Acoustofluidic Synthesis of Particulate Nanomaterials. *Adv Sci* **2019**.

386. Mallick, S.; Choi, J. S., Liposomes: Versatile and Biocompatible Nanovesicles for Efficient Biomolecules Delivery. *J Nanosci Nanotechno* **2014,** *14* (1), 755-765.
387. Immordino, M. L.; Dosio, F.; Cattel, L., Stealth liposomes: review of the basic science, rationale, and clinical applications, existing and potential. *Int J Nanomedicine* **2006,** *1* (3), 297-315.
388. Akbarzadeh, A.; Rezaei-Sadabady, R.; Davaran, S.; Joo, S. W.; Zarghami, N.; Hanifehpour, Y.; Samiei, M.; Kouhi, M.; Nejati-Koshki, K., Liposome: classification, preparation, and applications. *Nanoscale Research Letters* **2013,** *8*.
389. Mendez, R.; Banerjee, S., Sonication-Based Basic Protocol for Liposome Synthesis. *Methods Mol Biol* **2017,** *1609*, 255-260.
390. Ong, S. G. M.; Chitneni, M.; Lee, K. S.; Ming, L. C.; Yuen, K. H., Evaluation of Extrusion Technique for Nanosizing Liposomes. *Pharmaceutics* **2016,** *8* (4).
391. Li, L. L.; Li, X. D.; Wang, H., Microfluidic Synthesis of Nanomaterials for Biomedical Applications. *Small Methods* **2017,** *1* (8).
392. Liu, Y.; Jiang, X. Y., Why microfluidics? Merits and trends in chemical synthesis. *Lab on a Chip* **2017,** *17* (23), 3960-3978.
393. Ma, J. P.; Lee, S. M. Y.; Yi, C. Q.; Li, C. W., Controllable synthesis of functional nanoparticles by microfluidic platforms for biomedical applications - a review. *Lab on a Chip* **2017,** *17* (2), 209-226.
394. Ahn, J.; Ko, J.; Lee, S.; Yu, J.; Kim, Y.; Jeon, N. L., Microfluidics in nanoparticle drug delivery; From synthesis to pre-clinical screening. *Adv Drug Deliv Rev* **2018,** *128*, 29-53.
395. Maeki, M.; Kimura, N.; Sato, Y.; Harashima, H.; Tokeshi, M., Advances in microfluidics for lipid nanoparticles and extracellular vesicles and applications in drug delivery systems. *Adv Drug Deliver Rev* **2018,** *128*, 84-100.
396. Elvira, K. S.; Solvas, X. C. I.; Wootton, R. C. R.; deMello, A. J., The past, present and potential for microfluidic reactor technology in chemical synthesis. *Nature Chemistry* **2013,** *5* (11), 905-915.
397. Carugo, D.; Bottaro, E.; Owen, J.; Stride, E.; Nastruzzi, C., Liposome production by microfluidics: potential and limiting factors. *Scientific Reports* **2016,** *6*.
398. Hood, R. R.; DeVoe, D. L., High-Throughput Continuous Flow Production of Nanoscale Liposomes by Microfluidic Vertical Flow Focusing. *Small* **2015,** *11* (43), 5790-5799.
399. Wi, R.; Oh, Y.; Chae, C.; Kim, D. H., Formation of liposome by microfluidic flow focusing and its application in gene delivery. *Korea-Aust Rheol J* **2012,** *24* (2), 129-135.
400. Shah, V. M.; Nguyen, D. X.; Patel, P.; Cote, B.; Al-Fatease, A.; Pham, Y.; Huynh, M. G.; Woo, Y.; Alani, A. W. G., Liposomes produced by microfluidics and extrusion: A comparison for scale-up purposes. *Nanomed-Nanotechnol* **2019,** *18*, 146-156.
401. Kastner, E.; Kaur, R.; Lowry, D.; Moghaddam, B.; Wilkinson, A.; Perrie, Y., High-throughput manufacturing of size-tuned liposomes by a new microfluidics method using enhanced statistical tools for characterization. *Int J Pharmaceut* **2014,** *477* (1-2), 361-368.
402. Kimura, N.; Maeki, M.; Sato, Y.; Note, Y.; Ishida, A.; Tani, H.; Harashima, H.; Tokeshi, M., Development of the iLiNP Device: Fine Tuning the Lipid Nanoparticle Size within 10 nm for Drug Delivery. *Acs Omega* **2018,** *3* (5), 5044-5051.
403. Chen, D. L.; Love, K. T.; Chen, Y.; Eltoukhy, A. A.; Kastrup, C.; Sahay, G.; Jeon, A.; Dong, Y. Z.; Whitehead, K. A.; Anderson, D. G., Rapid Discovery of Potent siRNA-Containing Lipid Nanoparticles Enabled by Controlled Microfluidic Formulation. *Journal of the American Chemical Society* **2012,** *134* (16), 6948-6951.

404. Zhigaltsev, I. V.; Belliveau, N.; Hafez, I.; Leung, A. K. K.; Huft, J.; Hansen, C.; Cullis, P. R., Bottom-Up Design and Synthesis of Limit Size Lipid Nanoparticle Systems with Aqueous and Triglyceride Cores Using Millisecond Microfluidic Mixing. *Langmuir* **2012,** *28* (7), 3633-3640.
405. Cortes-Quiroz, C. A.; Zangeneh, M.; Goto, A., On multi-objective optimization of geometry of staggered herringbone micromixer. *Microfluidics and Nanofluidics* **2009,** *7* (1), 29-43.
406. Rasouli, M. R.; Tabrizian, M., An ultra-rapid acoustic micromixer for synthesis of organic nanoparticles. *Lab on a Chip* **2019**.
407. Roy, P. R.; Tomkins, M. R.; Docoslis, A., Enhancing the Performance of Surface-based Biosensors by AC Electrokinetic Effects - a Review. *Environment* **2004**, 1-22.
408. Lang, Q.; Ren, Y.; Hobson, D.; Tao, Y.; Hou, L.; Jia, Y.; Hu, Q.; Liu, J.; Zhao, X.; Jiang, H., In-plane microvortices micromixer-based AC electrothermal for testing drug induced death of tumor cells. *Biomicrofluidics* **2016,** *10* (6), 064102.
409. Porter, J. M.; Modares, P.; Castiello, F. R.; Tabrizian, M. In *Capacitive Detection of Insulin Antibody enhanced by AC Electrothermal mixing*, 2019 IEEE 6th Portuguese Meeting on Bioengineering (ENBENG), 22-23 Feb. 2019; 2019; pp 1-4.
410. Cui, H.; Cheng, C.; Lin, X.; Wu, J.; Chen, J.; Eda, S.; Yuan, Q., Rapid and sensitive detection of small biomolecule by capacitive sensing and low field AC electrothermal effect. *Sensors and Actuators B: Chemical* **2016,** *226*, 245-253.
411. Lee, W. C.; Lee, H.; Lim, J.; Park, Y. J., An effective electrical sensing scheme using AC electrothermal flow on a biosensor platform based on a carbon nanotube network. *Appl Phys Lett* **2016,** *109* (22), 223701.
412. Lee, K. H.; Yang, G. L. Z.; Wyslouzil, B. E.; Winter, J. O., Electrohydrodynamic Mixing-Mediated Nanoprecipitation for Polymer Nanoparticle Synthesis. *Acs Appl Polym Mater* **2019,** *1* (4), 691-700.
413. Rivas, C. J. M.; Tarhini, M.; Badri, W.; Miladi, K.; Greige-Gerges, H.; Nazari, Q. A.; Rodriguez, S. A. G.; Roman, R. A.; Fessi, H.; Elaissari, A., Nanoprecipitation process: From encapsulation to drug delivery. *Int J Pharmaceut* **2017,** *532* (1), 66-81.
414. Jahn, A.; Vreeland, W. N.; DeVoe, D. L.; Locascio, L. E.; Gaitan, M., Microfluidic directed formation of liposomes of controlled size. *Langmuir* **2007,** *23* (11), 6289-6293.
415. Schnitzer, O.; Yariv, E., The Taylor–Melcher leaky dielectric model as a macroscale electrokinetic description. *J Fluid Mech* **2015,** *773*, 1-33.
416. ElMoctar, A. O.; Peerhossaini, H.; Bardon, J. P., Numerical and experimental investigation of direct electric conduction in a channel flow. *Int J Heat Mass Tran* **1996,** *39* (5), 975-993.
417. Gonzalez, A.; Ramos, A.; Morgan, H.; Green, N. G.; Castellanos, A., Electrothermal flows generated by alternating and rotating electric fields in microsystems. *J Fluid Mech* **2006,** *564*, 415-433.
418. Bally, F.; Garg, D. K.; Serra, C. A.; Hoarau, Y.; Anton, N.; Brochon, C.; Parida, D.; Vandamme, T.; Hadziioannou, G., Improved size-tunable preparation of polymeric nanoparticles by microfluidic nanoprecipitation. *Polymer* **2012,** *53* (22), 5045-5051.
419. Balazs, D. A.; Godbey, W., Liposomes for Use in Gene Delivery. *Journal of Drug Delivery* **2011,** *2011*.
420. Kang, J. H.; Jang, W. Y.; Ko, Y. T., The Effect of Surface Charges on the Cellular Uptake of Liposomes Investigated by Live Cell Imaging. *Pharm Res-Dordr* **2017,** *34* (4), 704-717.

421. Zook, J. M.; Vreeland, W. N., Effects of temperature, acyl chain length, and flow-rate ratio on liposome formation and size in a microfluidic hydrodynamic focusing device. *Soft Matter* **2010,** *6* (6), 1352-1360.
422. Kotnik, T.; Kramar, P.; Pucihar, G.; Miklavcic, D.; Tarek, M., Cell membrane electroporation- Part 1: The phenomenon. *IEEE Electrical Insulation Magazine* **2012,** *28* (5), 14-23.
423. Yarmush, M. L.; Golberg, A.; Sersa, G.; Kotnik, T.; Miklavcic, D., Electroporation-Based Technologies for Medicine: Principles, Applications, and Challenges. *Annu Rev Biomed Eng* **2014,** *16*, 295-320.
424. Kotnik, T.; Bobanovic, F.; Miklavcic, D., Sensitivity of transmembrane voltage induced by applied electric fields - a theoretical analysis. *Bioelectrochemistry and Bioenergetics* **1997,** *43* (2), 285-291.
425. Kotnik, T.; Miklavcic, D., Second-order model of membrane electric field induced by alternating external electric fields. *IEEE Trans Biomed Eng* **2000,** *47* (8), 1074-81.
426. Retelj, L.; Pucihar, G.; Miklavcic, D., Electroporation of Intracellular Liposomes Using Nanosecond Electric Pulses-A Theoretical Study. *Ieee T Bio-Med Eng* **2013,** *60* (9), 2624-2635.
427. Weaver, J. C., Electroporation of biological membranes from multicellular to nano scales. *Ieee Transactions on Dielectrics and Electrical Insulation* **2003,** *10* (5), 754-768.
428. Kakorin, S.; Liese, T.; Neumann, E., Membrane curvature and high-field electroporation of lipid bilayer vesicles. *J Phys Chem B* **2003,** *107* (37), 10243-10251.
429. Sedgwick, H.; Caron, F.; Monaghan, P. B.; Kolch, W.; Cooper, J. M., Lab-on-a-chip technologies for proteomic analysis from isolated cells. *Journal of the Royal Society Interface* **2008,** *5*, S123-S130.
430. Lu, H.; Schmidt, M. A.; Jensen, K. F., A microfluidic electroporation device for cell lysis. *Lab Chip* **2005,** *5* (1), 23-9.
431. Lee, J. N.; Park, C.; Whitesides, G. M., Solvent compatibility of poly(dimethylsiloxane)-based microfluidic devices. *Analytical Chemistry* **2003,** *75* (23), 6544-6554.
432. Alheshibri, M.; Craig, V. S. J., Generation of nanoparticles upon mixing ethanol and water; Nanobubbles or Not? *Journal of Colloid and Interface Science* **2019,** *542*, 136-143.
433. Rak, D.; Ovadova, M.; Sedlak, M., (Non)Existence of Bulk Nanobubbles: The Role of Ultrasonic Cavitation and Organic Solutes in Water. *J Phys Chem Lett* **2019,** *10* (15), 4215-4221.
434. Chen, Q.; Yuan, Y. J., A review of polystyrene bead manipulation by dielectrophoresis. *RSC Advances* **2019,** *9* (9), 4963-4981.
435. Rozynek, Z.; Han, M.; Dutka, F.; Garstecki, P.; Jozefczak, A.; Luijten, E., Formation of printable granular and colloidal chains through capillary effects and dielectrophoresis. *Nat Commun* **2017,** *8*.
436. Zhou, P. L.; Yu, H. B.; Yang, W. G.; Wen, Y. D.; Wang, Z. D.; Li, W. J.; Liu, L. Q., Spatial Manipulation and Assembly of Nanoparticles by Atomic Force Microscopy Tip-Induced Dielectrophoresis. *Acs Applied Materials & Interfaces* **2017,** *9* (19), 16715-16724.